UNIWERSYTET
IM. ADAMA MICKIEWICZA
W POZNANIU

Doctoral thesis

Mathieu Moalic

Numerical Investigations of Collective Spin-Wave Dynamics in Complex Magnetic Textures and Patterned Ferromagnetic Films

Supervisor: **Prof. dr hab. Maciej Krawczyk**

Assistant supervisor: **Dr Mateusz Zelent**

Faculty of Physics and Astronomy
Institute of Spintronics and Quantum Information
Adam Mickiewicz University, Poznań

Poznań 2025

To my wonderful fiancée, Ewa, and my devoted parents, Laurent and Sophie — thank you for your endless love and support throughout this journey.

Declaration

Declaration of the author of this dissertation:

I hereby declare that except where specific reference is made to the work of others, the contents of this dissertation are original and have not been submitted in whole or in part for consideration for any other degree or qualification in this, or any other university. This dissertation is my own work and all the contents of the dissertation have been obtained by legal means.

Mgr **Mathieu Moalic**

Declaration of the thesis Supervisor:

This dissertation is ready to be reviewed.

Prof. dr hab. Maciej Krawczyk

Abstract

Electronic computing units continue to shrink, but further scaling looks increasingly constrained by high power densities and operating voltages. Spin waves (magnons), by contrast, carry information with very little energy, and at microwave frequencies their wavelengths can be on the order of a few hundred down to a few tens of nanometres, enabling nanoscale components that consume far less power than conventional electronics. Thus, magnons in ferromagnets have emerged as a promising route to low-power information processing.

Magnetic materials themselves have been known for millennia and underpin everyday technologies —from motors and sensors to computers and even simple fridge magnets. Over the last two decades, researchers have focused on building the fundamental blocks of magnonic circuitry: directional couplers, diodes, transistors, and logic gates. To fully exploit spin-wave behaviour in such systems, precise control of the interactions between individual elements, particularly on the sub-micrometre scale, is essential.

In this thesis, I study ferromagnetic thin films with complex patterns and magnetic textures that can find applications in magnonic systems. The central aim is to establish design rules and numerical tools for deterministic control of spin-wave spectra, mode profiles, and interactions in sub-micrometre patterned films.

I begin the thesis with the foundations of magnetism, followed by an explanation of micromagnetism, the interactions governing magnetic systems, magnetisation textures, and spin waves. I conclude the background with topics currently under intensive study: magnonic crystals and spin-wave computing. I then present the software developed during this research. I developed the micromagnetic simulation tool “Amumax” and a data post-processing package, “Pyzfn,” for space- and time-efficient analysis of large datasets, enabling simulations of previously intractable systems.

In the first part of the research, I investigate thin films with perpendicular magnetic anisotropy (PMA) that are patterned with antidots whose are surrounded by rims which have reduced PMA, forming in-plane magnetised regions. The first paper shows that controlled softening of the magnetisation in the in-plane magnetised rims in the antidot lattice tailors spin-wave spectra, creating rim-localised edge modes, edge-mode–bulk-mode hybrids, magnonic bandgaps, and history-dependent non-reciprocity —thereby establishing anisotropy engineering as a reconfigurable spin-wave control knob. Building on this, I combine the out-of-plane magnetised bulk of the ferromagnetic film with the in-plane-magnetised rims in the antidot lattice to realise strong, exchange-mediated magnon–magnon coupling between confined and propagating modes—a pathway to programmable interactions relevant for coherent magnonics and hybrid quantum technologies. I then harness nonlinearity in a lithographically simple architecture composed of an in-plane-magnetised nanosized element immersed in an out-of-plane magnetised ferromagnetic strip to up-converts a uniform microwave pump into coherent propagating plane spin waves with sub-300-nm wavelength and doubled frequency. The emission frequency and efficiency of the second-harmonic generation scale with the magnetic field magnitude and the nanoelement width. Furthermore, the concept can be readily extended to two-dimensional systems, providing a compact, tunable source of exchange-dominated waves suitable for spin-wave-based realisation of artificial neural networks.

In parallel, I explore deterministic, hierarchical confinement of spin waves at the nanoscale using Sierpiński-triangle networks based on ferromagnetic film, motivated as a generalisation of antidot-lattice concepts to multiscale patterns. The fractal’s nested quantisation lengths generate tunable magnonic minibands and bandgaps—adjustable geometrically or by rotating the bias magnetic field—offering broadband spectral agility for multiplexing and routing of spin waves without changing the

material. Finally, in collaboration with the experimental group in Vienna, we study a one-dimensional yttrium iron garnet (YIG), hole-based one-dimensional magnonic nanocrystal and demonstrate spin-wave bandgaps, slow-mode plateaus, and defect cavities, validating the routing and filtering concepts in a sub-micrometre, low-loss ferromagnetic platform.

The results have been published in four papers and one preprint and the developed software is open source and publicly available. Together, these studies articulate a framework for programmable magnonics based on three complementary control knobs—anisotropy, geometry, and nonlinearity —implemented in lithography-friendly thin-film platforms. They deliver reconfigurable spin-wave edge–bulk hybridisation and magnonic bandgap formation, strong exchange-mediated magnon modes coupling tunable by magnetic field magnitude and its history, a compact frequency-doubling source of sub-300-nm spin waves, and hierarchical spectral control in deterministic fractal networks, with experimental validation in low-loss YIG nanocrystals. Thus, this work charts a viable path to practical, ultra-low-power magnonic processors by delivering controllable spin-wave spectra, interactions, and on-chip spin-wave frequency conversion in manufacturable thin-film platforms.

Abstrakt

Elektroniczne układy obliczeniowe wciąż są miniaturyzowane, jednak dalsze skalowanie wydaje się coraz bardziej ograniczane przez wysokie gęstości mocy i stosowane napięcia. Natomiast, fale spinowe (magnony) przenoszą informację przy bardzo niewielkim zużyciu energii, a przy częstotliwościach mikrofalowych ich długości fal mogą wynosić od kilkuset do kilkudziesięciu nanometrów, co umożliwia tworzenie elementów w nanoskali zużywających znacznie mniej energii niż konwencjonalna elektronika. Dlatego magnony, w szczególności w ferromagnetykach, wyłaniają się jako obiecująca droga do niskoenergetycznego przetwarzania informacji.

Materiały magnetyczne są znane od tysiącleci i stanowią podstawę wielu technologii codziennego użytku — od silników i czujników po komputery, a nawet zwykłe magnesy na lodówce. W ciągu ostatnich dwóch dekad badacze koncentrowali się również na budowie podstawowych elementów układów magnonicznych: sprzęgaczy kierunkowych, diod, tranzystorów i bramek logicznych. Aby w pełni wykorzystać właściwości fal spinowych w takich systemach, kluczowa jest precyzyjna kontrola oddziaływań między poszczególnymi elementami, szczególnie w skali submikrometrowej.

W niniejszej pracy badam cienkie warstwy ferromagnetyczne o złożonych teksturach magnetyzacji i złożonej strukturalizacji w nanoskali, które mogą znaleźć zastosowanie w systemach magnonicznych. Głównym celem pracy doktorskiej jest wyznaczenie podstawowych zasad projektowych i opracowanie narzędzi numerycznych do deterministycznej kontroli widm fal spinowych, profili modów i ich wzajemnych oddziaływań w strukturalizowanych w skali submikrometrów warstwach ferromagnetycznych.

Pracę doktorską rozpoczynam od przedstawienia podstaw magnetyzmu, a następnie omawiam mikromagnetyzm; oddziaływania rządzące układami magnetycznymi; tekstury namagnesowania oraz fale spinowe. Wprowadzenie kończę opisem obecnie intensywnie badanych tematów: kryształów magnonicznych i obliczeń z użyciem fal spinowych. Następnie przedstawiam oprogramowanie rozwinięte w trakcie badań. Opracowałem narzędzie do symulacji mikromagnetycznych „Amumax" oraz pakiet postprocessingu danych „Pyzfn" do oszczędnej przestrzennie i czasowo analizy dużych zbiorów danych, umożliwiające symulacje wcześniej praktycznie nieosiągalnych systemów.

W pierwszej części badań analizuję cienkie warstwy ferromagnetyczne z prostopadłą anizotropią magnetyczną (PMA), strukturyzowane siecią anty-kropek, których obrzeża mają zredukowane PMA, tworząc pierścienie namagnesowane w płaszczyźnie. Pierwsza praca pokazuje, że kontrolowane mięknięcie namagnesowania w obszarach brzegowych sieci anty-kropek kształtuje widmo fal spinowych, tworząc mody zlokalizowane na obrzeżach, hybrydy modów brzegowych i objętościowych, magnoniczne przerwy pasmowe oraz zależną od historii namagnesowania niewzajemność — wskazując inżynierię anizotropii jako wydajny sposób umożliwiający sterowanie falami spinowymi. To połączenie objętościowej części strukturyzowanej warstwy ferromagnetycznej z PMA z obszarami brzegowymi namagnesowanymi w płaszczyźnie wykorzystuję, aby zademonstrować silne, z wykorzystaniem oddziaływań wymiennych, sprzężenie magnon–magnon między modami związanymi i biegnącymi. Otwiera to drogę do programowalnych oddziaływań istotnych dla rozwoju koherentnej magnoniki i hybrydowych technologii kwantowych. Następnie, wykorzystuję nieliniowość dynamiki magnetyzacji występującą w litograficznie prostej strukturze, złożonej z nano-obszaru namagnesowanego w płaszczyźnie i osadzonego w ferromagnetycznym pasku namagnesowanym prostopadle do płaszczyzny paska, który przekształca sygnał jednorodnego pola mikrofalowego w spójne, biegnące płaskie fale spinowe o częstotliwości dwa razy większej i długości fali poniżej 300 nm. Częstotliwość emisji i sprawność generacji drugiej harmonicznej skalują się z polem oraz szerokością nanoelementu, a koncepcję można łatwo rozszerzyć na układy dwu-wy-mia-ro-we, dostarczając tym samym zwarte,

przestrajalne źródło fal spinowych, zdominowanych przez oddziaływania wymienne, odpowiednie do realizacji magnonicznych sztucznych sieci neuronowych.

Równolegle, badałem deterministyczne, hierarchiczne związanie fal spinowych w nanoskali z użyciem struktury trójkąta Sierpińskiego, jako uogólnienie koncepcji sieci antykropek na wzory wieloskalowe. Zagnieżdżone długości kwantyzacji fali spinowej w strukturze fraktalnej generują przestrajalne mini-pasma i magnoniczne przerwy pasmowe — kontrolowane geometrią lub poprzez obrót zewnętrznego pola magnetycznego — oferując szerokopasmową elastyczność spektralną fal spinowych do multi-pleksowania i sterowania sygnałów, bez konieczności zmiany materiału. Wreszcie, we współpracy z grupą eksperymentalną z Wiednia, badamy jednowymiarowy, oparty na łańcuchu anty-kropek nanokryształ magnoniczny wytworzony na bazie wąskiego, sub-mikro-metro-wego, paska z granatu itrowo-żelazowego (YIG). Wykazujemy możliwość otrzymania przerw pasmowych dla fal spinowych, plato modów wolnych oraz wnęk rezonansowych na defektach, potwier-dzając koncepcje małostratnego trasowania i filtrowania fal spinowych w skali podmikrometrowej, opartej o platformę na bazie ferromagnetycznego dielektryka.

Praca doktorska wytycza realną ścieżkę do praktycznych, niskoenergetycznych procesorów mag-no-nicz-nych, dostarczając sposobu na kontrolowalne widma fal spinowych i oddziaływania oraz konwersję częstotliwości na chipie wytwarzalnych na platformach cienkowarstwowych. Wyniki opublikowano w czterech artykułach naukowych oraz jednym preprincie będącym obecnie w recenzji, a opracowane oprogramowanie jest upublicznione z otwartym kodem źródłowym. Łącznie, zaprezentowane badania przedstawiają ramy programowalnej mag-no-ni-ki oparte na trzech komplementarnych elementach sterujących — anizotropii, geometrii i nieliniowości — wdrożonych w przyjaznych litograficznie platformach cienkowarstwowych. Dostarczają one metody na przełączalną hybrydyzację fal spinowych brzeg–objętość, silnego sprzężenia modów fal spinowych przestrajalnych polem magnetycznym i historią namagnesowania, formowania magnonicznych przerw pasmowych, zwartego źródła krótkich fal spinowych podwajającego częstotliwość wzbudzających je mikrofal oraz hierarchicznej kontroli spektralnej.

Short note about the author

The author completed a Bachelor's degree in Physics at the University of Rennes 1 in 2018. This was followed by a Double Diploma Master's programme, combining studies in Nanoscience and Nanotechnology at Rennes 1 with the Physics of Advanced Materials for Energy Processing programme at Adam Mickiewicz University (AMU) in Poznań, Poland. Doctoral research was carried out as a PhD candidate in the Nanomaterials Physics Division.

The author served as the principal investigator for a research project funded by the National Science Centre (NCN), titled Designing an experimentally feasible two-dimensional magnonic crystal to demonstrate topologically protected spin waves (NCN PRELUDIUM, 2024–2025, Grant No. 2023/49/N/ST3/03538). In addition, they received two short-term internship grants from the "Inicjatywa Doskonałości – Uczelnia Badawcza" programme, supporting two-week research stays at the University of Vienna, in the group of Prof. Chumak and the University of Porto in the group of Prof. Kakazei. Beyond this, the author has contributed to several other national and international research projects as a team member or investigator.

The list of projects and scholarships includes:

- NCN SHENG, "Spin Waves in Magnetic Skyrmion Crystals", Grant No. UMO-2018/30/Q/ST3/00416.
- NCN OPUS, "New Platform for Study Wave Phenomenon – Reconfigurable Topological Properties and Frustrated Ground States in Magnonics", Grant No. UMO-2020/37/B/ST3/03936
- NCN PRELUDIUM, "Designing an experimentally feasible two-dimensional magnonic crystal for the demonstration of topologically protected spin waves", Grant No. 2023/49/N/ST3/03538
- Horizon Europe, MANNGA, "Magnonic Artificial Neural Networks and Gate Arrays", Grant No. 101070347
- Scholarship funded by the Adam Mickiewicz University Foundation.
- Computational simulations performed at the Poznań Supercomputing and Networking Center (Grant No. pl0095-01).

Throughout their academic career, the author has delivered twenty presentations at national and international conferences across the world. They have published thirteen scientific papers in peer-reviewed journals or as preprints. Of these, eight were authored as first, second, or corresponding author, and five form the foundation of this dissertation. These works have been published or are currently under review in leading journals including Scientific Reports, Journal of Physics: Condensed Matter, Journal of Applied Physics, APL Materials, Journal of Magnetism and Magnetic Materials, Nanoscale, Solid State Physics, and Small Structures.

In addition to teaching courses on micromagnetic simulations, the author has co-supervised five Master's theses.

Author publication list

- *Stabilization and racetrack application of asymmetric Néel skyrmions in hybrid nanostructures*,
  M. Zelent, **M. Moalic**, M. Mruczkiewicz, X. Li, Y. Zhou, M. Krawczyk.
  Scientific Reports, **13** (1), 13572 (2023).
- *Spin-wave spectra in antidot lattice with inhomogeneous perpendicular magnetic anisotropy*,
  M. Moalic, M. Krawczyk, M. Zelent.
  Journal of Applied Physics, **132** (21), 213901 (2022).
- *Tunability of spin-wave spectra in a 2D triangular shaped magnonic fractals*,
  R. Mehta, **M. Moalic**, M. Krawczyk, S. Saha.
  Journal of Physics: Condensed Matter, **35** (32), 324002 (2023).
- *The role of non-uniform magnetisation texture for magnon-magnon coupling in an antidot lattice*,
  M. Moalic, M. Zelent, K. Szulc, M. Krawczyk.
  Scientific Reports, **14** (1), 11501 (2024).
- *Scattering of spin waves in a multimode waveguide under the influence of confined magnetic skyrmion*,
  K. A. Kotus, **M. Moalic**, M. Zelent, M. Krawczyk, P. Gruszecki.
  APL Materials, **10** (9), 091101 (2022).
- *Control of vortex chirality in a symmetric ferromagnetic ring using a ferromagnetic nanoelement*,
  U. Makartsou, **M. Moalic**, M. Zelent, M. Mruczkiewicz, M. Krawczyk.
  Nanoscale, **15** (31), 13094–13101 (2023).
- *Unidirectional spin wave emission by traveling pair of magnetic field profiles*,
  G. Philippe, **M. Moalic**, J. W. Kłos.
  Journal of Magnetism and Magnetic Materials, **587**, 171359 (2023).
- *Spin dynamics in patterned magnetic multilayers with perpendicular magnetic anisotropy*,
  M. Zelent, P. Gruszecki, **M. Moalic**, O. Hellwig, A. Barman, M. Krawczyk.
  Solid State Physics, **73**, 51 (2022).
- *Enhancement of dynamical coupling in artificial spin-ice systems by incorporating perpendicularly magnetised ferromagnetic matrix*,
  S. S. Kunnath, M. Zelent, **M. Moalic**, M. Krawczyk.
  Small Structures, 2400627 (2024).
- *Angle-dependent resonant dynamics of stripes and skyrmions in Re/Co/Pt multilayers*,
  S. K. Jena, K. Lenz, M. Zelent, **M. Moalic**, A. Lynnyk, A. Pietruczik, P. Aleszkiewicz, E. Milińska, J. Lindner, A. Wawro.
  arXiv preprint, 2501.06865 (2025).
- *1D YIG hole-based magnonic nanocrystal*,
  K.O. Levchenko, K. Davídková, R.O. Serha, **M. Moalic**, A.A. Voronov, C. Dubs, O. Surzhenko, M. Lindner, J. Panda, Q. Wang, O. Wojewoda, B. Heinz, M. Urbánek, M. Krawczyk, A.V. Chumak.
  Applied Physics Letters, **127**, 172401 (2025).
- *Efficient generation of second-harmonic propagating spin waves in a thin, out-of-plane-magnetised ferromagnetic film*,
  M. Moalic, Y. Patat, M. Zelent, M. Krawczyk.
  arXiv preprint, 2509.07705 (2025).

- *Controlling spin textures of magnetic nanodots using an antidot matrix*,
  S.A. Bunyaev, G.O. Kharchenko, R.V. Verba, **M. Moalic**, M. Krawczyk, M. Urbánek, K.Y. Guslienko, G.N. Kakazei.
  Low Temperature Physics, 51.8: 1017-1022 (2025).

Author publications and preprints included into thesis

- *Spin-wave spectra in antidot lattice with inhomogeneous perpendicular magnetic anisotropy*,
  M. Moalic, M. Krawczyk, M. Zelent.
  Journal of Applied Physics, **132** (21), 213901 (2022).
- *The role of non-uniform magnetisation texture for magnon-magnon coupling in an antidot lattice*,
  M. Moalic, M. Zelent, K. Szulc, M. Krawczyk.
  Scientific Reports, **14** (1), 11501 (2024).
- *Efficient generation of second-harmonic propagating spin waves in a thin, out-of-plane-magnetised ferromagnetic film*,
  M. Moalic, Y. Patat, M. Zelent, M. Krawczyk.
  arXiv preprint, 2509.07705 (2025).
- *Tunability of spin-wave spectra in a 2D triangular shaped magnonic fractals*,
  R. Mehta, **M. Moalic**, M. Krawczyk, S. Saha.
  Journal of Physics: Condensed Matter, **35** (32), 324002 (2023).
- *1D YIG hole-based magnonic nanocrystal*,
  K.O. Levchenko, K. Davídková, R.O. Serha, **M. Moalic**, A.A. Voronov, C. Dubs, O. Surzhenko, M. Lindner, J. Panda, Q. Wang, O. Wojewoda, B. Heinz, M. Urbánek, M. Krawczyk, A.V. Chumak
  Applied Physics Letters, **127**, 172401 (2025).

Software developed during the PhD

- **Amumax**: A fork of mumax3 aimed at enhancing Python workflow integration. Includes improved WebUI and uses pyzfn to leverage Zarr-formatted data, making output processing significantly more efficient. [https://github.com/MathieuMoalic/amumax]
- **Pyzfn**: A Python library for post-processing micromagnetic simulation data generated by Amumax, a fork of mumax3. It is designed for use with Zarr-backed datasets and supports spatially resolved frequency-domain analysis, visualization, and export of magnetization dynamics. [https://github.com/MathieuMoalic/pyzfn]

Introduction

The arc of digital computing is approaching a plateau[1]. Shrinking gate lengths no longer follow the blistering pace of past decades, and pushing them further runs into hard limits—soaring power densities and the need for higher operating voltages[2,3]. Even if some forecasts suggest semiconductor technology can keep improving for roughly another decade, the slowdown of electronics-based progress looks ultimately unavoidable[4].

This reality has researchers worldwide hunting for successors—or at least powerful companions—to traditional silicon[4]. For years, complementary metal–oxide–semiconductor (CMOS) technology and its transistor paradigm defined the cutting edge, propelling the rapid rise of computing. Now, with conventional scaling faltering, the quest is on for approaches that can overtake or substantially augment CMOS, opening new paths for performance growth beyond what classic semiconductor engineering can deliver[4,5].

Among the candidates to push computing beyond CMOS, magnonics stands out. Spin waves carry information through the collective precession of spins rather than by shuttling electrons, which means far less energy is dissipated than in conventional charge-based circuits[6,7]. Their natural operating band is extremely high—typically gigahertz and, in favourable regimes, reaching into the terahertz—and these frequencies correspond to nanometer-scale wavelengths, a sweet spot for fast operations packed into tiny footprints[7,8]. Crucially, spin waves respond readily to both magnetic and electric fields, offering rich, low-power control knobs[9].

Because spin waves are wave phenomena, their dynamics don't mirror electronic charge transport. That mismatch isn't a bug—it's an invitation to rethink computation itself. Logic families need not be strictly Boolean; analogue signal processing, non-Boolean interference-based logic, and unconventional paradigms—including neural-network-style processing and even quantum-computing–adjacent concepts—may map more naturally onto magnonic hardware[10–12].

Realising this promise demands groundwork: deep study of spin-wave physics, concrete proposals for logic elements, and practical design of integrated spin-wave circuits. With those pieces in place, magnonics has a credible path to becoming a key building block of future computing architectures.

Building on this vision, the main goal of my thesis is to study collective spin-wave dynamics in complex magnetic textures and patterned ferromagnetic films, which motivates the following open questions:

- Can modifying the magnetic anisotropy locally be used to tailor spin-wave excitations in a reconfigurable magnonic crystal for the demonstration of topologically protected spin waves
- How tunable is the hybridisation and strong coupling between rim modes and extended bulk modes via magnetic field history, rim width, or material contrast?
- Do patterned lattices with inhomogeneous anisotropy support reconfigurable magnonic band structures that switch between metastable states?
- Can a locally confined, in-plane-magnetised mode serve as an efficient pump for nonlinear frequency doubling, launching coherent second-harmonic spin waves with wavelength below 300 nm?
- Can fractals create geometry-controlled frequency bandgaps and minibands that remain adjustable by external magnetic field orientation?
- Do one-dimensional yttrium iron garnet (YIG) hole-based magnonic nanocrystals support distinct spin-wave modes and provide geometry- and field-tunable control of propagation—manifested as magnonic bandgaps, slow-mode plateaus, and defect cavities?

These hypotheses are supported by my thesis, which is built around five research papers on which I serve as the lead author: four are published in peer-reviewed physics journals, and the remaining one is available as a preprint and currently under review.

The thesis is organised into five chapters. Chapter 1 introduces the foundations of magnetism, including the history of magnetic materials, their classification, and the properties of ferromagnets. Chapter 2 outlines micromagnetic theory and numerical methods. Chapter 3 presents the custom software (Amumax and Pyzfn) that I developed throughout my PhD, enabling efficient computation and analysis of the magnetic systems considered in this work. Chapter 4 gathers the five core publications: *Spin-wave spectra in antidot lattice with inhomogeneous perpendicular magnetic anisotropy*; *The role of non-uniform magnetisation texture for magnon-magnon coupling in an antidot lattice*; *Efficient generation of second-harmonic propagating spin waves in a thin, out-of-plane-magnetised ferromagnetic film*; *Tunability of spin-wave spectra in a 2D triangular shaped magnonic fractals*; and *1D YIG hole-based magnonic nanocrystal*. Chapter 5 provides an outlook for reprogrammable, low-power magnonic signal-processing devices and lists the conferences I have attended and helped organize, the awards, grants and scholarships I received, the scientific visits I did and students I co-supervised.

Table of contents

1 Foundations of Magnetism 1
1.1 History of Magnetic Knowledge 1
1.2 Microscopic Origins of Magnetic Behaviour 1
1.3 Classification of Magnetic Responses 1
1.4 Properties of Ferromagnetic Materials 2
2 Micromagnetic simulations 4
2.1 Magnetic Interactions 4
2.1.1 Exchange Interaction 5
2.1.2 Dipolar Interaction 6
2.1.3 Zeeman Interaction 7
2.1.4 Anisotropy 7
2.2 The Landau-Lifshitz-Gilbert Equation 7
2.2.1 Magnetisation 7
2.2.2 Gyromagnetic Ratio 8
2.2.3 The Landau-Lifshitz Equation 8
2.2.4 The Landau-Lifshitz-Gilbert (LLG) Equation 8
2.3 Magnetisation Configurations 9
2.3.1 Magnetic Domains 9
2.3.2 Domain Walls 9
2.3.3 Vortices 10
2.4 Spin-Waves and Magnonics 10
2.4.1 Ferromagnetic Resonance 10
2.4.2 Propagation of Spin-Waves in Thin Films 11
2.4.3 Magnonic Crystals 12
2.4.4 Magnon-magnon coupling 12
2.4.5 Ion-beam tailoring of ultrathin magnets 13
3 Software Development 14
3.1 Amumax 14
3.1.1 Python Integration with Zarr Format 14
3.1.2 Enhanced WebUI 14
3.1.3 Template System for Parameter Sweeps 17
3.1.4 Chunking and Data Management 18
3.1.5 Optimised Mesh Definition 18
3.1.6 Enhanced Command Line Interface and Usage 18
3.2 Pyzfn 18
3.2.1 Snapshots 20
3.2.2 Interactive Spectral Analysis 21
4 Main research topics 22
4.1 Spin-wave spectra in antidot lattice with inhomogeneous perpendicular magnetic anisotropy 23
4.1.1 Introduction 23
4.2 The role of non-uniform magnetisation texture for magnon-magnon coupling in an antidot lattice 31
4.2.1 Introduction 31
4.3 Efficient generation of second-harmonic propagating spin waves in a thin, out-of-plane-magnetised ferromagnetic film 43
4.3.1 Introduction 43

4.4 Tunability of spin-wave spectra in a 2D triangular shaped magnonic fractals 66
4.4.1 Introduction 66
4.5 1D YIG hole-based magnonic nanocrystal 79
4.5.1 Introduction 79
4.6 Outlook 99
4.7 Other research 100
5 About the author 102
5.1 Conferences 102
5.1.1 Oral Presentations 102
5.1.2 Poster Presentations 102
5.1.3 Organization 103
5.2 Awards, grants and scholarships 103
5.3 Research Projects 104
5.4 Scientific visits 104
5.5 Student co-supervision 104

Chapter 1

Foundations of Magnetism

1.1 History of Magnetic Knowledge

The study of magnetism dates back to antiquity, where natural lodestones were observed to attract iron[13]. The term "magnet" derives from the Greek *magnētis lithos*, or "Magnesian stone." Early accounts include Thales of Miletus in Greece and references in Indian medical texts like the *Sushruta Samhita*, which describe the use of magnetite for extracting metallic objects[13].

During the Middle Ages, the magnetic compass—originating in China and later adopted across the Islamic world and Europe—transformed navigation[14,15]. In 1269, Petrus Peregrinus' Epistola de magnete offered the first systematic experimental account of magnetic polarity and compass construction[16]. In 1600, William Gilbert's De Magnete established an experimental science of magnetism, introduced the terrella, and argued that Earth is a giant magnet, thereby explaining compass behaviour[17].

A major shift occurred in the 19$^{\text{th}}$ century, beginning with Ørsted's discovery that electric currents produce magnetic fields[18]. Faraday[19] and Ampère formalised these interactions, leading to Maxwell's equations[20], which unified electricity and magnetism. These ideas were later absorbed into Einstein's theory of relativity[21] and modern quantum electrodynamics[22], where magnetism remains central to fundamental physics.

1.2 Microscopic Origins of Magnetic Behaviour

At its most fundamental level, magnetism originates from quantum mechanical properties of subatomic particles[23]. Protons, neutrons, and electrons all possess an intrinsic magnetic moment, but it is the electrons, particularly those in partially filled outer orbitals, that dominate magnetic behaviour in solids due to their significantly larger magnetic moments.

According to Hund's rules[24] and the Pauli exclusion principle[25], electrons in inner atomic shells pair up with opposing magnetic moments, resulting in no net contribution. Conversely, unpaired electrons in outer shells contribute to a material's net magnetic moment, making magnetism an emergent property linked to atomic structure[23].

1.3 Classification of Magnetic Responses

Materials respond differently to external magnetic fields based on their electronic structure[26]:

- **Diamagnetism** – a weak, universal response where magnetic fields induce a moment opposite to the applied field; dominant in materials with fully paired electrons. Notably, superconductors show perfect diamagnetism (the Meissner effect): magnetic flux is expelled by screening currents of the Cooper-pair condensate, a macroscopic quantum state distinct from ordinary orbital diamagnetism[27].
- **Paramagnetism** – observed in substances with unpaired electrons. These align with an external field but lose alignment upon field removal due to thermal agitation. Above the Curie temperature, ordered magnets lose long-range order and become paramagnetic (Curie–Weiss behaviour)[26].
- **Magnetic Ordering** – in some materials, magnetic interactions overcome thermal disturbances, resulting in long-range magnetic order even without an external field.

Within ordered systems, a few behaviours are identified:

- **Ferromagnetism**: all magnetic moments align in the same direction.
- **Antiferromagnetism**: neighbouring moments align in opposite directions and cancel out.

- **Ferrimagnetism**: opposing but unequal magnetic moments produce a net magnetisation.
- **Altermagnetism**: zero net magnetisation, yet crystal symmetry makes spins alternate in momentum space, yielding ferromagnet-like transport effects[28].

In amorphous materials, analogous states include asperomagnetism and speromagnetism[26].

1.4 Properties of Ferromagnetic Materials

Ferromagnetism is a collective quantum-mechanical effect that sets in when the exchange interaction between neighbouring 3d or 4f electrons outweighs thermal agitation, below the Curie temperature[26], forcing their spins to align parallel. Elemental iron, cobalt, and nickel are the textbook cases, but in practice most technologically important ferromagnets are alloys or compounds engineered for specific magnetic and electronic properties:

- Permalloy ($Ni_{80}Fe_{20}$) – the canonical soft-magnetic alloy. Its nearly vanishing magnetocrystalline anisotropy, high permeability, and very low Gilbert damping (~10^{-3}) make it ideal for microwave spin-wave experiments, magnetic cores, and sensors[29].
- Fe-Co alloys (e.g., $Fe_{65}Co_{35}$) – exhibit the highest known saturation magnetisation (~2.45 T) among room-temperature ferromagnets, useful for high-density recording heads and spin-transfer-torque devices[30].
- Heusler and half-Heusler alloys (e.g., Co_2MnSi, CoFeAl) – nearly half-metallic, offering high spin polarisation for spin valves and magnetic tunnel junctions[31].
- Rare-earth hard magnets (e.g., $Nd_2Fe_{14}B$, $SmCo_5$) – very large magnetocrystalline anisotropy and coercivity yield square hysteresis and record energy products, enabling compact permanent magnets for motors, generators, and actuators[32–34].
- Yttrium Iron Garnet ($Y_3Fe_5O_{12}$, YIG) – formally a ferrimagnetic oxide, but widely treated as a "ferromagnetic insulator" in magnonics because its two Fe sublattices couple strongly, yielding an ultralow effective damping (~10^{-5}) and long (cm-scale) spin-wave propagation lengths[35]. YIG films and waveguides serve as gold-standard platforms for studying coherent magnon transport and magnon-photon hybridisation.

In all these systems, spontaneous spin alignment partitions the crystal into magnetic domains separated by domain walls; applying an external field moves or annihilates these walls, producing the characteristic hysteresis loop[36]. At the nanoscale, however, deliberate nanostructuring—patterning elements below the single-domain size and imparting strong shape anisotropy—can suppress domain-wall formation so that isolated nanomagnets remain uniformly magnetised at remanence (i.e., single-domain without an applied field)[37–40]. Tailoring elemental composition, crystallographic order, microstructure, and geometry controls exchange strength, anisotropy, and damping, enabling ferromagnetic materials—from Permalloy nanostrips to epitaxial YIG films—to underpin everything from hard-disk write heads to quantum magnonic circuits.

A key quantity describing the magnetic state of a material is the *magnetisation* $\boldsymbol{M}$, defined as the magnetic moment per unit volume:

$$\boldsymbol{M} = \frac{\mathrm{d}\boldsymbol{m}}{\mathrm{d}V}$$

where $\boldsymbol{m}$ is the total magnetic moment contained in volume V. The SI unit of magnetisation is amperes per metre (A/m)[41].

Ferromagnetic materials are characterised by high magnetic permeability, which quantifies the ease with which a material becomes magnetised in response to an applied magnetic field $\boldsymbol{H}$. At low fields, the relationship between magnetisation and field is described by the magnetic susceptibility χ:

$$\boldsymbol{M} = \chi \boldsymbol{H}$$

although this relation is linear only in paramagnetic materials. In ferromagnets, due to the presence of spontaneous magnetisation, $\boldsymbol{M}$ is non-zero even when $\boldsymbol{H} = 0$. The system exhibits a non-linear and history-dependent response, forming what is known as a *hysteresis loop*[13]. This loop illustrates how the magnetisation depends not only on the current field but also on the magnetic history of the material.

The total magnetic flux density $\boldsymbol{B}$ in the material is given by:

$$\boldsymbol{B} = \mu_0(\boldsymbol{H} + \boldsymbol{M})$$

where μ_0 is the vacuum permeability. Introducing the relative permeability $\mu_r = 1 + \chi$, we also write:

$$\boldsymbol{B} = \mu_0 \mu_r \boldsymbol{H} = \mu \boldsymbol{H}$$

with μ representing the absolute magnetic permeability of the material.

Coercive field H_c (coercivity) is the magnitude of the reverse applied field needed to drive the magnetisation M of a previously saturated ferromagnet to zero, i.e., a measure of resistance to demagnetisation[13,38]. Ferromagnets are therefore grouped as follows:

- **Soft ferromagnets**, such as annealed iron or Permalloy ($Ni_{80}Fe_{20}$), have low coercivity and are easily magnetised and demagnetised[13]. These materials are used in applications requiring rapidly changing magnetic fields (e.g., transformers, sensors, magnonics).
- **Hard ferromagnets**, such as $Nd_2Fe_{14}B$, $SmCo_5$, or hard ferrites (e.g., $BaFe_{12}O_{19}$), have high coercivity and retain their magnetisation, making them suitable for permanent magnets[32–34].

In practical terms, "soft" typically means $H_c \lesssim 1\text{–}10\ \mathrm{kA{\cdot}m^{-1}}$ (i.e., $\mu_0 H_c \lesssim 1\text{–}10$ mT), whereas "hard" commonly implies $H_c \gtrsim 100\ \mathrm{kA{\cdot}m^{-1}}$ (i.e., $\mu_0 H_c \gtrsim 0.1$ T); intermediate values are often termed semi-hard[34,38].

Chapter 2

Micromagnetic simulations

2.1 Magnetic Interactions

The magnetic behaviour of ferromagnetic materials is governed by a range of fundamental interactions that collectively determine the structure and dynamics of the magnetisation field $\boldsymbol{M}(\boldsymbol{r}, t)$, where $\boldsymbol{r}$ is the position vector and t is time. These interactions contribute to the system's total free energy. Since many depend not only on the local orientation of the magnetisation but also on its spatial variation, the total energy E_{total} is expressed as a functional of $\boldsymbol{M}$ and its spatial derivatives $\partial_{x,y,z}\boldsymbol{M}$. It can be decomposed into several distinct energy terms, each corresponding to a specific physical mechanism:

$$E_{\text{total}} = E_{\text{ex}} + E_{\text{demag}} + E_Z + E_{\text{anis}} + ...$$

Here:

- E_{ex} is the *exchange energy*, the interaction that encourages neighboring spins to adopt a common direction; with a positive exchange constant it drives ferromagnetism (parallel alignment), whereas a negative exchange constant favours antiferromagnetism (antiparallel alignment)[26,37].
- E_{demag} is the *magnetostatic (demagnetisation) energy*, accounting for long-range interactions between magnetic dipoles;
- E_Z is the *Zeeman energy*, representing the interaction of the magnetisation with an external magnetic field;
- E_{anis} denotes the *magnetic anisotropy energy* which stems from spin–orbit coupling and crystal symmetry, and it also can have a magnetoelastic contribution: magnetostriction couples magnetisation to strain, so internal strain or applied stress produces stress-induced anisotropy that favours particular directions[26,38,42].

In addition to these, other interactions such as the *Dzyaloshinskii–Moriya interaction* (antisymmetric exchange that favours chiral spin canting)[43,44], the *Ruderman–Kittel–Kasuya–Yosida* (RKKY) indirect exchange mediated by conduction electrons[45–47], magnetoelastic coupling that links magnetisation to strain[38,42], long-range magnetostatic/electromagnetic fields relevant to micromagnetics[36,37], and spin-transfer torque from spin-polarised currents[48,49] are acknowledged in the broader context of magnetisation dynamics but are not directly relevant to the simulations and results presented in this thesis.

Thermal fluctuations are omitted in the deterministic micromagnetic framework adopted here; while temperature effects can be incorporated via stochastic extensions of the Landau–Lifshitz–Gilbert equation, such as Brown's thermal field or Langevin dynamics, the present work focuses on zero-temperature dynamics[50,51].

The effective magnetic field $\boldsymbol{H}_{\text{eff}}$, which governs the dynamics of the magnetisation, is defined as the variational derivative of the total energy functional with respect to the magnetisation:

$$\boldsymbol{H}_{\text{eff}} = -\frac{1}{\mu_0}\frac{\delta E_{\text{total}}}{\delta \boldsymbol{M}}$$

The effective field encapsulates all internal and external interactions acting on the magnetisation and serves as the driving term in the Landau-Lifshitz-Gilbert (LLG) equation which describes the time

evolution of the system and is further detailed in Section 2.2. In this way, the energy landscape directly determines the dynamics and equilibrium states observed in micromagnetic simulations.

2.1.1 Exchange Interaction

The exchange interaction is a fundamental quantum mechanical effect that underlies the spontaneous alignment of magnetic moments in ferromagnetic and antiferromagnetic materials. It originates from the interplay between the Pauli exclusion principle and the Coulomb repulsion of electrons. When two electrons possess parallel spins, the antisymmetry of the total wavefunction required for fermions increases their spatial separation, thereby reducing their Coulomb repulsion. Conversely, antiparallel spins may occupy the same spatial orbital, leading to increased electrostatic repulsion. This energetic difference between spin configurations gives rise to an effective interaction which favours parallel alignment in ferromagnets and antiparallel alignment in antiferromagnets[52].

The exchange interaction was first formalised by Heisenberg in 1928[52], and is commonly described within a semi-classical framework using the Heisenberg Hamiltonian:

$$\hat{H}_{\text{ex}} = -\sum_{\langle i,j \rangle} J_{ij} \;\; \boldsymbol{S}_i \cdot \boldsymbol{S}_j$$

where $\boldsymbol{S}_i$ and $\boldsymbol{S}_j$ are the spin vectors at lattice sites i and j, respectively, and J_{ij} denotes the exchange integral or exchange constant between these sites. The summation is typically limited to nearest neighbours due to the rapidly decaying nature of the interaction with distance. A positive exchange constant ($J_{ij} > 0$) leads to ferromagnetic ordering, while a negative value promotes antiferromagnetic or ferrimagnetic alignment.

Many metallic magnets (Fe, Co, Ni) however, are better described in an itinerant "band" framework: spin polarisation trades kinetic-energy cost against exchange-energy gain. In the Stoner mean-field theory, ferromagnetism appears when $I, N(E_F) > 1$, where I is an exchange parameter and $N(E_F)$ the density of states at the Fermi level[53]. Microscopically, the Hubbard model adds an on-site repulsion U to a tight-binding band; in-mean field it reproduces the Stoner criterion and beyond mean field it captures correlation-driven magnetism and the crossover between itinerant and local-moment behaviour[54].

In the micromagnetic continuum approximation, which is valid when the magnetisation varies slowly over distances large compared to the atomic lattice constant, the discrete spin Hamiltonian is replaced by a continuous energy functional. The exchange energy density for uniform M_s in this framework is given by:[36,37]

$$E_{\text{ex}} = \frac{A_{\text{ex}}}{M_s^2} \int_V (\nabla \boldsymbol{M})^2 \;\; \mathrm{d}^3 r$$

where M_s is the saturation magnetisation (the maximum magnetisation a magnetic material can attain when all its atomic magnetic moments are fully aligned), and A_{ex} is the exchange stiffness constant, a material-dependent parameter typically on the order of 10^{-11} J/m for ferromagnets. This expression penalises spatial inhomogeneities in the magnetisation, thereby favouring collinear spin configurations[38,55]. In such an approximation, the exchange stiffness is defined as $A_{\text{ex}} = \frac{S^2}{2dV_a} \sum_j J_{\text{ij}} r_{\text{ij}}^2$ where S is the spin quantum number, d is the dimensionality of the system (1, 2, or 3), V_a is the atomic volume, and r_{ij} is the distance between spins at sites i and j[26,37].

It is also useful to introduce the characteristic exchange length, defining a natural length scale for variations in the magnetisation due to the competition between exchange and magnetostatic energy. The exchange length is given by:

$$\ell_{\mathrm{ex}} = \sqrt{\frac{2A_{\mathrm{ex}}}{\mu_0 M_s^2}}$$

Typical values of ℓ_{ex} range from a few nanometres in metallic ferromagnets to tens of nanometres in magnetic insulators such as YIG.

It is worth mentioning that in mean-field theory for a nearest-neighbour Heisenberg ferromagnet, the Curie temperature scales linearly with the exchange constant: $T_{\mathrm{C}} \propto J$[23,26].

It is worth noting that for standard magnonic materials used here T_C lies well above room temperature —for example YIG has $T_C \approx 560$ K and Permalloy ($Ni_{80}Fe_{20}$) has $T_C \approx 850$ K —so over typical operating ranges (270 ± 30 K) the variation of M_s is small and can be neglected for our purposes.

In summary, the exchange interaction is a short-range, isotropic quantum mechanism that aligns neighbouring spins and, when it dominates over thermal fluctuations, establishes long-range magnetic order; in the continuum it enforces spatial coherence by penalising rapid magnetisation variations and sets the key energetic and spatial scales of micromagnetics via the exchange stiffness and exchange length[26,36,37].

2.1.2 Dipolar Interaction

The dipolar interaction, also referred to as the magnetostatic or demagnetising interaction, arises from the magnetic field produced by a magnetic moment acting on other moments within the system. Unlike the exchange interaction, which is short-ranged and quantum mechanical in origin, the dipolar interaction is classical, long-ranged, and inherently non-local, decaying with the cube of the distance between magnetic moments[36,37,56].

For two point dipoles $\boldsymbol{\mu}_1$ and $\boldsymbol{\mu}_2$ separated by a displacement vector $\boldsymbol{r}$, the dipolar interaction energy is given by:

$$E_{\mathrm{demag}} = \frac{\mu_0}{4\pi|\boldsymbol{r}|^3}\left[\boldsymbol{\mu}_1 \cdot \boldsymbol{\mu}_2 - 3\frac{(\boldsymbol{\mu}_1 \cdot \boldsymbol{r})(\boldsymbol{\mu}_2 \cdot \boldsymbol{r})}{|\boldsymbol{r}|^2}\right]$$

This interaction tends to align magnetic moments into configurations that minimise the magnetic stray field—the magnetostatic field that leaks from a magnetised body due to uncompensated surface or volume poles—often opposing the uniform alignment favoured by the exchange interaction[36,37].

The dipolar interaction plays a critical role in shaping complex magnetisation textures by driving the system towards configurations that minimise the net stray field. This promotes domain formation and magnetic-closure structures such as Landau patterns or vortices. In systems with non-uniform magnetisation, the dipolar energy becomes especially influential, as the resulting stray fields reshape the overall magnetic landscape. Uniaxial magnetic anisotropy adds a competing energy term that favours alignment along a preferred axis; its balance with dipolar and exchange energies determines whether domains, vortices, or stripe patterns emerge[36,57–59]. Consequently, in thin films and nanostructures the combined effects of dipolar, exchange, and anisotropy energies set the equilibrium domain size, domain walls, vortex cores, and even the stability ranges of topological textures such as skyrmions[60–62].

To efficiently compute the long-range dipolar (demagnetising) field in micromagnetic simulations, a common approach is to exploit the convolution theorem by expressing the field calculation as a convolution between the magnetisation and a demagnetisation kernel. This convolution can be accelerated using the fast Fourier transform (FFT), reducing the computational complexity from $\mathcal{O}(N^2)$ to $\mathcal{O}(N \log N)$ for a grid with N cells. When implemented on modern graphics processing units (GPUs), FFT-based convolution methods achieve significant speedups by leveraging parallel processing and highly optimised libraries (e.g., cuFFT). This approach enables the real-time computation of non-

local fields in large-scale simulations, making GPU-accelerated micromagnetics a powerful tool for modelling large complex magnetisation dynamics[63–66].

2.1.3 Zeeman Interaction

The Zeeman interaction describes the coupling between the magnetic moments of a system and an external magnetic field, forcing the magnetisation to align with the applied field and thus contributing to the total magnetic energy[37,38,56]. The total Zeeman energy E_Z for a body of volume V is

$$E_Z = -\mu_0 \int_V \boldsymbol{H}_{\text{ext}} \cdot \boldsymbol{M} \ \mathrm{d}^3 r$$

where $\boldsymbol{H}_{\text{ext}}$ is the applied field, and $\boldsymbol{M}$ the local magnetisation[36,37,56]. Competition between this term and exchange, dipolar, and anisotropy energies determines the equilibrium magnetisation configuration[26,42].

2.1.4 Anisotropy

Anisotropy in magnetic materials is the tendency for the magnetisation to favour certain directions because different microscopic mechanisms break rotational symmetry in specific ways[37,38,42]. Key sources and the anisotropy types they most often generate are:

- Crystal-lattice symmetry (spin–orbit coupling) – orbital–spin locking in cubic lattices yields cubic anisotropy; in lower-symmetry lattices (hexagonal, tetragonal, orthorhombic) it produces a single uniaxial easy axis[26,38,42]. Microscopic links between orbital moments and magnetocrystalline anisotropy are well established in theory and ab-initio studies[67–69].
- Shape (included in the demagnetising field) – elongated grains, wires, or thin films develop uniaxial shape anisotropy with the easy axis along the longest dimension[36,70,71].
- Surface / interface effects – broken inversion symmetry and hybridisation at film interfaces typically reinforce a perpendicular uniaxial anisotropy, for example in Co/Pt or CoFeB/MgO multilayers[68,72,73].
- Strain (magnetoelastic coupling) – applied or epitaxial strain lowers symmetry and can convert a nominally cubic system into one with a dominant uniaxial easy axis[74–76].

Uniaxial anisotropy therefore appears across diverse scenarios—from hexagonal Co to thin Fe films and even shape-defined nanowires. Its energy density is

$$w_{\text{anis}} = K_u \left(1 - \left(\boldsymbol{u} \cdot \frac{\boldsymbol{M}}{M_s} \right)^2 \right)$$

where K_u is the uniaxial anisotropy constant. This anisotropy contributes to the alignment of the magnetisation along the direction of $\boldsymbol{u}$, which is the easy axis[37,38,42].

2.2 The Landau-Lifshitz-Gilbert Equation

The Landau-Lifshitz-Gilbert (LLG) equation, named after Lev Landau, Evgeny Lifshitz, and T. L. Gilbert, is a cornerstone differential equation in the field of micromagnetics. It describes the time evolution of the magnetisation vector $\boldsymbol{M}$ within a solid material, particularly its precessional motion under the influence of an effective magnetic field $\boldsymbol{H}_{\text{eff}}$ and accounting for damping effects[50,77–79].

2.2.1 Magnetisation

In micromagnetics, the magnetisation is defined as the dipole moment density:

$$\boldsymbol{M} = \frac{1}{V} \sum_i \boldsymbol{\mu_i} = -\frac{1}{V} \sum_i \gamma_i J_i$$

and the magnetic moment $\boldsymbol{\mu}$ is related to the total angular momentum $\boldsymbol{J}$ (orbital $\boldsymbol{L}$ plus spin $\boldsymbol{S}$) by the gyromagnetic ratio γ, such that[50,78,79] $\boldsymbol{\mu} = -\gamma \boldsymbol{J}$.

2.2.2 Gyromagnetic Ratio

For free electrons, the gyromagnetic ratio γ_e (where $\mu = -\gamma_e S$) is calculated as $\gamma_e = \frac{g_e \, |q_e|}{2m_e}$, where q_e is the elementary charge, m_e is the electron mass, and $g_e \approx 2$ is the electron g-factor; this gives $\gamma_e \approx 28.025 \;\; \mathrm{GHz/T}$ (or $\approx 1.7595 \cdot 10^{11}$ rad $\mathrm{s^{-1}T^{-1}}$). In real ferromagnets, the measured gyromagnetic ratio γ deviates slightly from this free-electron value because spin–orbit interaction couples the electron spin to the crystal lattice and admixes finite orbital angular momentum into the total magnetic moment, so γ must be treated as an effective, material-specific parameter—typically a few percent above γ_e for 3d transition-metal alloys[80,81].

2.2.3 The Landau-Lifshitz Equation

Neglecting any energy dissipation (damping), the equation of motion for the magnetisation $\boldsymbol{M}$ in an effective magnetic field $\boldsymbol{H}_{\text{eff}}$ is given by:

$$\frac{\partial \boldsymbol{M}}{\partial t} = -\gamma \mu_0 \boldsymbol{M} \times \boldsymbol{H}_{\text{eff}}$$

This equation, sometimes referred to as the Landau-Lifshitz equation in its undamped form, describes a perpetual precession of the magnetisation vector $\boldsymbol{M}$ around the effective magnetic field vector $\boldsymbol{H}_{\text{eff}}$.[50,82]. Note that here we only consider the Landau-Lifshitz torque but the Zhang-Li spin-transfer torque and Slonczewski torque could also be included[48,83].

2.2.4 The Landau-Lifshitz-Gilbert (LLG) Equation

In real magnetic systems, energy dissipates through multiple channels—most of them rooted in spin–orbit interaction (e.g., magnon–phonon coupling, magnon–electron coupling in metals, and magnon–magnon processes)—driving the magnetisation to align with the effective field. Landau and Lifshitz first introduced a phenomenological damping term in 1935 but in 1955, T. L. Gilbert proposed an alternative, and often preferred, form for the damping term. His modification results in the Landau-Lifshitz-Gilbert (LLG) equation:

$$\frac{d\boldsymbol{M}}{dt} = \boldsymbol{T} + \boldsymbol{T_d} = (-\gamma \mu_0 \boldsymbol{M} \times \boldsymbol{H}_{\text{eff}}) + \left(\frac{\alpha}{M_s} \boldsymbol{M} \times \frac{d\boldsymbol{M}}{dt} \right)$$

In this equation, α is the dimensionless Gilbert damping parameter, which is a phenomenological constant characteristic of the material. It quantifies the rate at which energy is dissipated from the magnetic system. The first term, $\boldsymbol{T}$, is from the Landau-Lifshitz equation. The second term, $\boldsymbol{T_d}$, is the Gilbert damping torque, which is directed towards the equilibrium direction and causes the magnetisation to spiral inwards towards $\boldsymbol{H}_{\text{eff}}$. A schematic of the torques is shown in Figure 1.

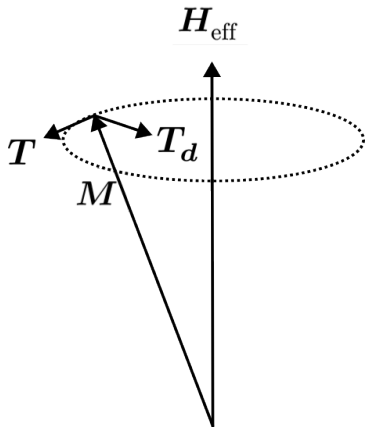

Figure 1: Schematic of spin precession described by the Landau-Lifshitz-Gilbert equation.

Note that this form of the equation, in particular the damping term, is specially formulated to keep $|M|$ constant[50,78,79].

2.3 Magnetisation Configurations

Magnetisation configurations arise from the delicate balance and competition between several fundamental micromagnetic interactions[50,84]. The exchange interaction favours parallel or antiparallel alignment of neighboring magnetic moments[84], as discussed in Section 2.1.1. Concurrently, the Zeeman and uniaxial anisotropy interactions attempt to align magnetic moments along external fields and preferred crystalline axes, respectively, and the long-range, shape-dependent dipolar interaction adds further complexity[70,71,85].

The interplay of these competing forces dictates the equilibrium states of magnetisation, leading to diverse configurations that we will explore in this section.[86,87]. The study of these magnetic configurations, particularly in patterned films and artificial structures like magnonic crystals, reveals rich physical phenomena and holds significant promise for future technological advancements[6,7,88,89].

2.3.1 Magnetic Domains

A fundamental characteristic of ferromagnetic materials is their spontaneous formation of spatially ordered magnetisation patterns[42,86]. Within these patterns, a magnetic domain is defined as a uniformly magnetised region[84,86]. The existence and characteristics of magnetic domains are a direct consequence of the competition between various energy contributions, primarily anisotropy, dipolar (magnetostatic), and exchange interactions[50,84,85].

The system finds an energy minimum by partitioning into domains, thereby reducing the overall magnetostatic energy at the cost of introducing domain walls, which possess associated exchange and anisotropy energies[86,87,90]. The final domain structure is also influenced by the sample's magnetic history[42,85,91].

2.3.2 Domain Walls

Domain walls are the non-uniformly magnetised regions that separate adjacent magnetic domains[36,37]. Within a domain wall, the magnetisation vector gradually rotates from the orientation of one domain to that of its neighbor[36]. The theoretical study of these transitional regions dates back to pioneering work by Bloch, Landau and Lifshitz, and Néel, who established the foundational understanding of their internal magnetisation structures[77,92,93].

Two primary types of 180° domain walls are distinguished based on the magnetisation rotation within the wall[36]. In a Bloch domain wall, the magnetisation rotates in a plane perpendicular to the plane defined by the magnetisation of the two adjacent domains[36]. In contrast, a Néel domain wall involves

magnetisation rotation within the plane containing the magnetisation vectors of the domains[36,93]. Bloch walls are typically observed in bulk materials and thicker films, while Néel walls are more prevalent in very thin films, generally with thickness less than the exchange length l_{ex} [36,37]. Whether a Bloch or a Néel configuration minimises the total energy in a thin-film ferromagnet is dictated by the balance between exchange, anisotropy, and magnetostatic terms[36,94,95].

The width of a domain wall is primarily determined by the competition between the exchange interaction and uniaxial anisotropy[36,37]. A very narrow wall minimises anisotropy energy but maximizes exchange energy due to abrupt spin changes[36]. Conversely, a very wide wall minimises exchange energy but increases anisotropy energy as more spins are oriented away from the easy axis[36]. The equilibrium domain wall width (δ_{DW}) minimises the sum of these energies and is approximately given by[36,37]:

$$\delta_{\text{DW}} = \pi\sqrt{\frac{A_{\text{ex}}}{K_u}}$$

The domain wall width is typically on the order of a few nanometers, depending on the material properties and the specific anisotropy contributions[36,37]. In real materials, additional factors such as defects, impurities, and external fields can further influence the domain wall structure and create more complex configurations, including vortex walls and cross-tie walls[36,95].

2.3.3 Vortices

A magnetic vortex is a stable, flux-closure magnetisation pattern common in confined ferromagnets (e.g., nanodisks/dots), where moments curl in-plane clockwise or counter-clockwise to minimise stray fields and magnetostatic energy[36,37,96]. It forms from the competition between exchange (favouring parallel alignment) and magnetostatic energies in small geometries[37,97]. To avoid the prohibitive exchange cost of a point singularity at the centre, the magnetisation in a tiny core tilts out of plane[36,98].

Thus, a magnetic vortex is characterized by two independent binary descriptors[36]: Chirality: the sense of the in-plane curl, clockwise ($c = -1$) or counter-clockwise ($c = +1$)[96]. Polarity: the direction of the out-of-plane magnetisation of the vortex core, up ($p = +1$) or down ($p = -1$)[96,98].

These two binary properties mean that a single magnetic vortex can exist in one of four stable states ($c = \pm 1$, $p = \pm 1$)[36]. Their intrinsic stability and unique dynamics—most notably the low-frequency gyrotropic motion of the vortex core—make vortices attractive for fundamental studies and spintronic applications[97,99,100]. The ability to control and switch chirality and/or polarity using external magnetic fields or spin-polarized currents has been demonstrated and remains an active research area[101,102].

2.4 Spin-Waves and Magnonics

In this section, we will focus on a compact set of ingredients—ferromagnetic resonance as a spectroscopic baseline, dipole–exchange spin-wave propagation in thin films, magnonic crystals, controlled magnon–magnon coupling, and ion-beam tailoring of ultrathin magnets. The selected topics provide the minimal background and notation needed for the results presented in my publications.

2.4.1 Ferromagnetic Resonance

Ferromagnetic Resonance (FMR) is a phenomenon characterized by the coupling between an electromagnetic wave and the magnetisation of a ferromagnetic medium. This coupling leads to a significant absorption of the wave's power. The energy is absorbed by the precessing magnetisation (Larmor precession) of the material[103,104]. This effect has found diverse applications, ranging from spectroscopic techniques for probing material properties to the design of microwave devices and studying SWs[103,105–109]. In cavity FMR, the nearly uniform microwave field couples predominantly to the spatially uniform ($k \simeq 0$) precession, whereas broadband FMR using microstrip or coplanar-waveguide transducers

generates strongly non-uniform near fields that can excite and detect both the uniform mode and finite-k, propagating SWs[103,106,108].

For a thin uniformly magnetised film without anisotropy and with an externally applied magnetic field $\boldsymbol{B}_{\mathrm{ext}}$ parallel to its plane, the resonant frequency f can be described by the Kittel formula[110]:

$$f = \frac{\gamma}{2\pi}\sqrt{B(B+\mu_0 M_s)}$$

In 1948, Charles Kittel developed a more general formula for the FMR frequency under a homogeneous excitation. His derivation, which accounted for both the external magnetic field and a sample's internal magnetic properties, was specifically applicable to homogeneously magnetised materials with an ellipsoidal shape. For such samples, the demagnetising field is uniform, which simplified the calculations and allowed for a precise formula:

$$f = \frac{\gamma}{2\pi}\sqrt{(B+\mu_0(N_x-N_z)M_s)\big(B+\mu_0\big(N_y-N_z\big)M_s\big)}$$

Here, N_x, N_y, and N_z are the diagonal components of the demagnetising tensor in the x, y, and z directions, respectively[70,71,111]. This dependence of the uniform precession frequency on the saturation magnetisation is widely exploited in experiments to determine the M_s value of a sample by measuring its FMR frequency. A key aspect of this uniform precession is that its frequency does not depend on the exchange stiffness, as all magnetic moments are oriented identically and precess in phase, resulting in zero net exchange interaction energy. This simplification is often referred to as the macrospin approximation and is commonly used in analytical treatments of FMR.

2.4.2 Propagation of Spin-Waves in Thin Films

In extended thin films, SW dynamics are well captured by the linearised LLG equation (cf.[89]; see also[77];[78]), which yields plane-wave solutions

$$\boldsymbol{m}(\boldsymbol{r},t) \propto e^{i(\boldsymbol{k}\cdot\boldsymbol{r}-\omega t)}$$

with in-plane wave-vector $\boldsymbol{k}$, angular frequency $\omega = 2\pi f$, and dynamic magnetisation amplitude $\boldsymbol{m} \| M_s$. The resulting dispersion relations reflect the competition between exchange, dipolar and anisotropy fields and depend on the film thickness δ, the propagation direction relative to the equilibrium magnetisation $\boldsymbol{M_0}$, and the boundary conditions at the surfaces[7,89,112].

2.4.2.1 Dipole–exchange dispersion (in-plane magnetised films)

For a uniformly magnetised film of thickness δ with the static field in the plane and the wave-vector making an angle φ to $\boldsymbol{M_0}$, the fundamental thickness mode ($n = 0$) has the canonical Kalinikos–Slavin dipole–exchange form[89,112]:

$$\omega^2(k,\varphi) = \left[\omega_H + \omega_M l_{\mathrm{ex}}^2 k^2 + \omega_M (1-P)\sin^2\varphi\right]\left[\omega_H + \omega_M l_{\mathrm{ex}}^2 k^2 + \omega_M P \sin^2\varphi\right]$$

where $\omega_H = \gamma\mu_0 H_{\mathrm{ext}}$, $\omega_M = \gamma\mu_0 M_s$ and $P = P(|k|\ \delta) = 1 - \frac{1-e^{\{-|k|\ \delta\}}}{|k|\ \delta}$ is the dynamic demagnetising factor capturing the finite thickness[89,112]. Two limiting propagation geometries are particularly important:

- **Damon–Eshbach (DE) surface waves** ($\varphi = 90°$): $\boldsymbol{k} \perp \boldsymbol{M_0}$. They are magnetostatic surface modes localised at one film surface over a depth $\propto \frac{1}{|k|}$ and exhibit large group velocities[89,113].
- **Backward-volume (BV) waves** ($\varphi = 0°$): $\frac{\boldsymbol{k}}{M_s}$. In the long-wavelength limit they show **negative** dispersion ($\frac{\partial\omega}{\partial k} < 0$), hence the name "backward"[89].

In a symmetric film (identical top/bottom interfaces and no chiral interactions) the frequency dispersion is reciprocal, $\omega(+k) = \omega(-k)$, but DE modes are non-reciprocal in profile: the $+k$ and $-k$ waves

are localised at opposite surfaces, which leads to direction-dependent coupling and attenuation in asymmetric stacks or with different surface damping[88,113].

For short wavelengths ($|k|\delta \gg 1$) the dipolar term saturates ($P \to 1$) and the dispersion crosses over to the exchange-dominated limit where, to leading order, all geometries tend towards a quadratic stiffening with k[89] :

$$\omega \approx \gamma\mu_0 \left(H_{\text{ext}} + \frac{2A_{\text{ex}}}{\mu_0 M_s} k^2 \right)$$

2.4.3 Magnonic Crystals

Magnonic crystals (MCs) are artificially engineered ferromagnetic media whose magnetic parameters —typically the saturation magnetisation M_s, the exchange stiffness A_{ex}, or the anisotropy K_u — or geometries are modulated with a spatial periodicity a on the order of the relevant spin-wave wavelengths[7,114]. This periodicity gives rise to a Bloch-type band structure for spin waves, featuring Bragg-scattering induced bandgaps at the Brillouin-zone boundaries or centers where the condition for constructive or destructive interference is fulfilled[115,116]. As a consequence, MCs act as frequency-selective materials that can filter, reflect, or localise spin-wave modes in much the same way that photonic crystals manipulate light[6,117]. Practically, the periodicity can be realised by lithographically patterning antidot lattices[118,119], modulating film thicknesses (surface/step MCs)[120,121], depositing multilayer or bicomponent stripes[122,123], or exploiting strain-induced anisotropy variations—for example by ion bombarding[124–126]. The bandwidth and centre frequency of the magnonic bandgaps are tunable through the lattice constant, the modulation depth[114], an externally applied magnetic field B_{ext}[127], or even electric-field control in multiferroic heterostructures[128,129]. Because MCs support reconfigurable, low-dissipation signal propagation in the gigahertz range, they are regarded as key components for on-chip microwave filters, phase shifters, and logic elements in magnon-based information processing architectures[117,130–132].

2.4.4 Magnon-magnon coupling

Magnon–magnon coupling arises when two spin-wave modes approach each other in frequency–wave-vector space: if their dynamic magnetisations are orthogonal the dispersions cross, but finite overlap of stray- or exchange-fields hybridises the modes and produces an anticrossing with a gap Δf. This hybridisation reorganises the spectrum—opening tunable gaps, flattening branches, and suppressing group velocity—so waves can be localised and guided near the anticrossing, as demonstrated in patterned YIG waveguides[133].

Concrete platforms span from interlayer-exchange–coupled synthetic antiferromagnets, where tilting the in-plane bias field breaks symmetry and opens a gap that exceeds individual linewidths, placing the system in the strong-coupling regime[134], to antidot lattices with rim–bulk anisotropy contrast, where exchange-mediated mixing between bulk and rim modes yields pronounced avoided crossings and strongly mixed eigenvectors such as the ones studied in Section 4.2[135]. Pushing into the ultrastrong regime, multilayered three-dimensional spin-vortex ice exhibits dynamically mediated inter-layer dipolar coupling and enables selective control of vortex chirality via mode hybridisation[136]. Ultrastrong coupling has likewise been realised in van der Waals antiferromagnets, where temperature-tunable exchange reveals signatures of the deep-strong regime[137], and related self-hybridisation in layered systems enables electrical control over the number and strength of avoided crossings[138].

Controlled hybridisation is valuable both fundamentally and for devices. By engineering dispersions and slow magnons, it enables on-chip localisation, delays, and frequency-selective transport[114,133,139]. In multi-mode or multilayer systems it supports coherent energy exchange and mode conversion, providing routes to multiplexing, routing, and frequency conversion[134,139,140]. Because the gap size and

eigenvector mixing depend on field angle, geometry, and magnetic microstate, coupling offers an in-situ knob to reprogram pass-/stop-bands and redistribute spectral weight[114,134,138]. The k-dependent anticrossing gaps also act as spectroscopy of interactions—distinguishing dipolar from exchange channels and probing interlayer exchange in complex heterostructures[134,138]. Finally, coupled-mode platforms naturally realise non-Hermitian and topological wave physics (parity–time symmetry, exceptional points), enabling mode switching and high-sensitivity responses, and they underpin reconfigurable magnonic crystals, filters, interconnects, and other signal-processing elements envisioned in magnon-computing roadmaps[114,139,141–144].

2.4.5 Ion-beam tailoring of ultrathin magnets

Ion bombardment with light ions (He^+, Ne^+, Ga^+, Ar^+) modifies interface chemistry, crystal order, and strain without adding topography, turning a uniform ferromagnetic film into a lithographically defined landscape of magnetic constants on demand[145,146].

The saturation magnetisation M_s, perpendicular anisotropy K_u, exchange stiffness A_{ex}, and many other magnetic properties can be tuned by carefully dosing the ions[146,147]. For example, at a given dose, ferromagnetic-resonance linewidths show that Gilbert damping α changes by < 10% in Co/Pd/Co/Ni multilayers with perpendicular anisotropy irradiated with helium ions[147].

Analogous fluence windows exist in ferrimagnetic garnets: He^+ doses of 10^{14}–$10^{15}\mathrm{cm}^{-2}$ quench the perpendicular anisotropy of Bi-YIG yet preserve its sub-milli damping, allowing irradiated stripes to act as low-loss spin-wave lenses and flat-band magnonic crystals envisioned in recent road-maps[148,149].

Since the modification is subsurface, no physical relief is added, so microwave losses tied to roughness are minimised and magnon channels/lenses can be written directly[148,149]. Focused He^+ beams achieve 10-nm spatial precision (Ga^+: few-tens of nm), enabling deterministic skyrmion nucleation sites and nanotracks[149–151]. Ion species and energy set the modified depth profile—from interfacial mixing to tens of nanometres—guided by stopping-range simulations[145].

Chapter 3

Software Development

3.1 Amumax

During my PhD, I built Amumax[152], a fork of mumax3[153],[154]. A software fork is a copy of an existing software project that is developed independently, often to add new features, fix bugs, or change its direction. The development of mumax3 had stalled since the release of version 3.10 in 2020. However, the hardware (specifically NVIDIA GPUs) was getting more performant and a better data saving scheme was needed to allow for larger simulations. Among the many new features that I added to Amumax, the most notable ones are the integration of the Zarr format for storing simulation data, an enhanced WebUI, a template system for parameter sweeps, chunking and data management, optimised mesh definition and an enhanced command line interface and usage.

It is available as an open source project; anybody is welcome to use and/or contribute to the software available at https://github.com/MathieuMoalic/amumax.

3.1.1 Python Integration with Zarr Format

A significant improvement in Amumax is the integration of the Zarr format for storing simulation data. Zarr allows efficient chunked and compressed storage of n-dimensional arrays, which facilitates faster access to specific parts of the simulation data. This is particularly advantageous for large-scale simulations, as users can access only the parts of the data they need, reducing memory usage and improving performance.

Additionally, the integration with the Python ecosystem through Pyzfn, a library that I wrote alongside Amumax, enables seamless analysis and processing of simulation data directly in Python, leveraging tools like NumPy[155], Dask[156], and xarray[157] for data manipulation and visualisation.

3.1.2 Enhanced WebUI

Amumax provides a more intuitive WebUI compared to mumax. A WebUI is a web-based graphical user interface that allows users to interact with the software through a web browser. The new interface is designed to simplify the interaction with the simulation, including progress tracking, job management, and output visualisation. Users can launch simulations, monitor their progress, and visualize 3D data through an interactive browser session, which provides a user-friendly alternative to the command line.

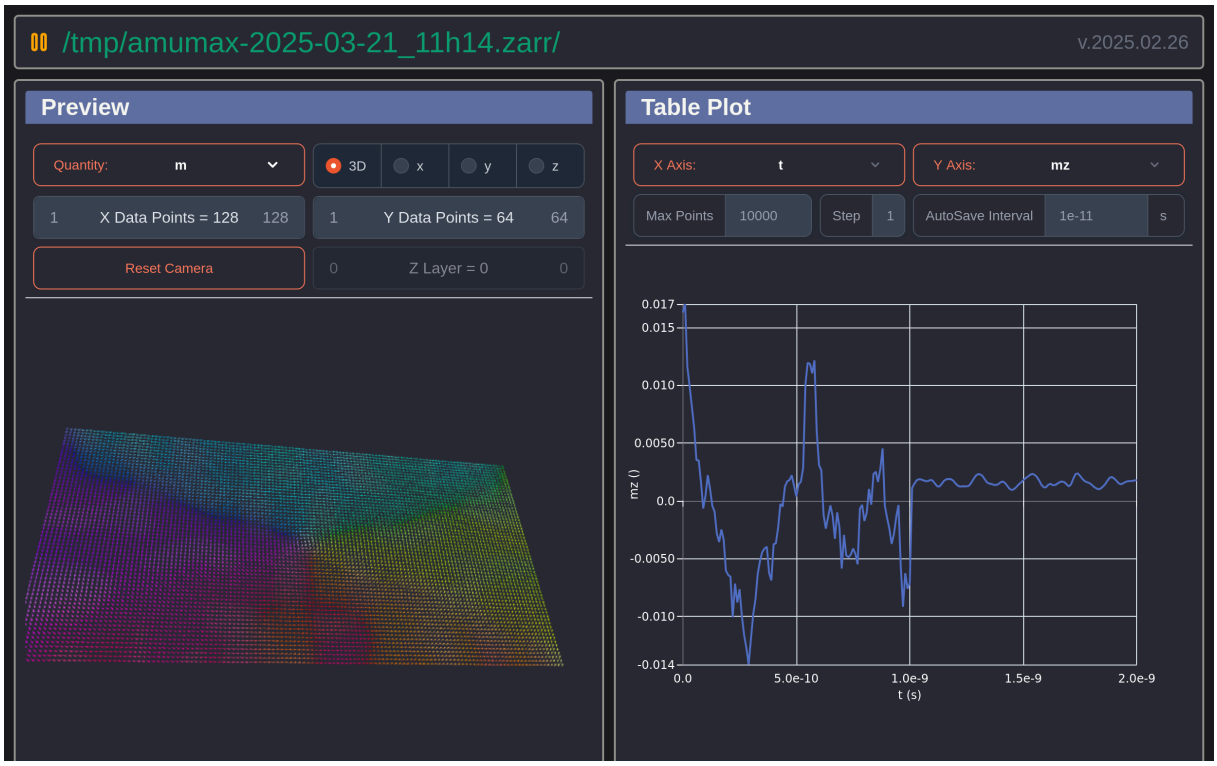

Figure 2: Amumax WebUI: The Preview on the left allows for live preview in 3D or 2D of the quantity. The table plot allows plotting 1D data relative to each other.

The 3D preview shown in Figure 2 (left column) was built on top of the powerful hardware accelerated Three.js[158] library which allows the user to visualise thousands of arrows at a time, with a colour scheme that reflects their orientation. This preview can be used to visualise the magnetisation or any other vector field such as torque, demagnetisation field etc. There is also a 2D preview that uses Chart.js[159] which allows the user to hover over a cell of the mesh with their mouse cursor and get a reading of the value of the particular quantity they are observing such as damping, exchange energy, magnetisation along an axis, etc.

The table plot on the right hand side of Figure 2 is used for 1D quantities that are saved in the table. The x and y axes can take any value, although it is very common to have the x axis represent the simulation time. Once again, a precise value can be easily read by hovering the plot with the mouse cursor.

Figure 3: Amumax WebUI: The console and Solver

Further down the WebUI, we can find the console Figure 3 (left column), which shows any command being run, so that we can easily keep track of the progress of the simulation. There is also an input field to run any command at any time. The console output text is coloured to make reading easier.

On the right, the solver panel shows crucial solver commands and metrics that should be monitored regularly to make sure that the underlying Runge-Kutta based micromagnetic solver stays within error. There are also buttons for common simulation commands such as *run*, *run steps*, *relax*, etc.

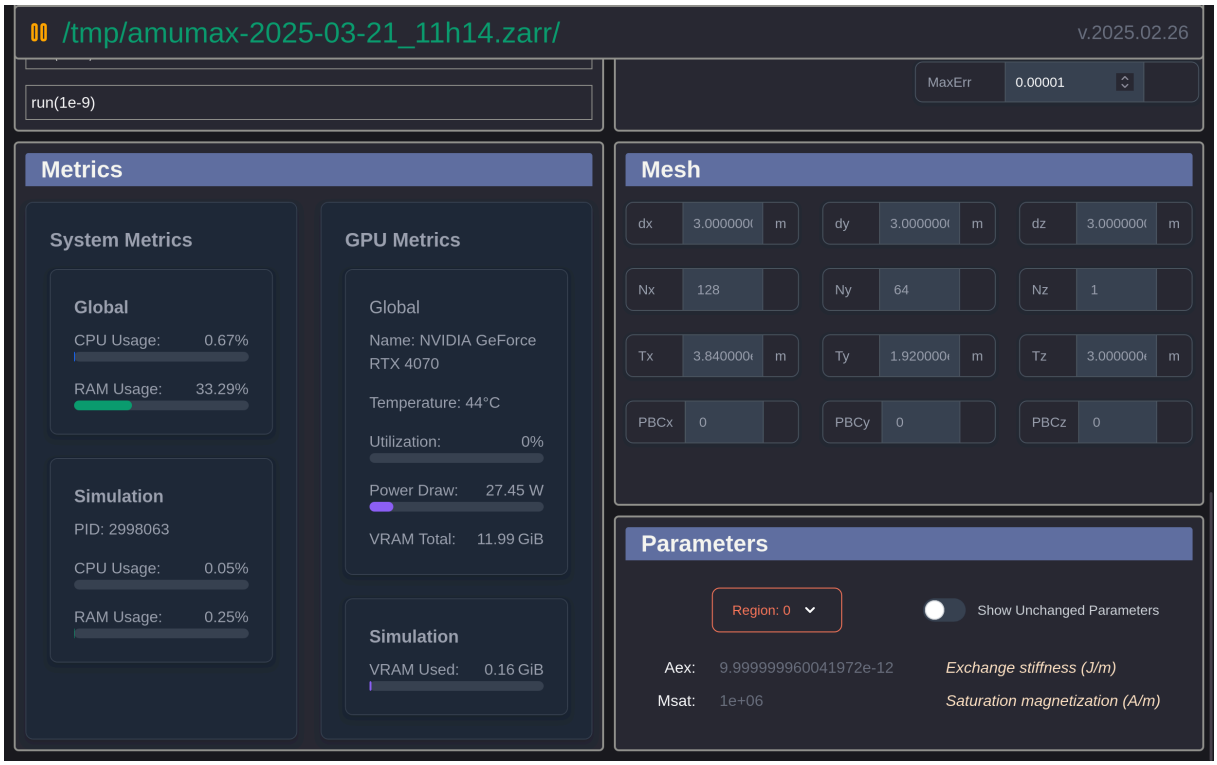

Figure 4: Amumax WebUI: The Metrics, Mesh and Parameters

The bottom panels, as seen in Figure 4, show information that is used less frequently but can still be useful. The Metrics show CPU, GPU and RAM usage, which can help identify potential hardware limitations which can lead to unnecessarily slow simulations.

On the right, the Mesh panel shows the dimensions of the system. Often the simulations are defined using expressions such as `$ Tx = 50 \times a $` if you want the length of the system to be 50 times a lattice constant a. In this case, it can sometimes be useful to know the computed length of your system.

Finally, the Parameters panel informs us about any material parameters, coupling constant, electrical current density, etc. in any region of our system.

3.1.3 Template System for Parameter Sweeps

Amumax integrates a flexible template system that supports the automated generation of simulation input files based on user-defined parameter sweeps. This feature is particularly valuable in high-throughput computational studies, where repeated simulations across systematically varied parameters are required. Instead of modifying each file manually, users define parameter placeholders in a single template. These placeholders are replaced programmatically to produce a collection of simulation-ready input files, each corresponding to a unique parameter set.

The syntax for defining parameter variations is concise and expressive, relying on key-value pairs enclosed in a structured string. Parameters can be specified as explicit arrays of values, or through ranges defined by start, end, and step values or a fixed count of intermediate values. Additional keys allow for customization of output file names through formatting, prefixes, and suffixes. This structure not only improves the clarity and traceability of simulation results but also ensures consistent naming conventions that support automated post-processing.

To illustrate, consider the following minimal example: Aex := “{start=0;end=2;step=1}” This declaration instructs the template system to generate three simulation files in which the exchange constant `Aex` takes on the values 0, 1, and 2, respectively. The resulting files are named accordingly (`0.mx3`, `1.mx3`, `2.mx3`), and the corresponding values are automatically substituted into the input scripts.

The template mechanism supports the generation of multidimensional sweeps by combining multiple parameters within the same template file. In such cases, Amumax evaluates all combinations of parameter values, producing a Cartesian product of simulation configurations. For added flexibility, users can control whether output files are organized in nested directories or flattened into a single folder, depending on the needs of their workflow.

Overall, the template system provides an efficient, scalable, and reproducible way to manage large sets of simulations. By abstracting the generation of input files into a declarative specification, it reduces manual overhead and minimises the risk of user error—an essential requirement in research workflows involving large parameter spaces or iterative optimisation.

3.1.4 Chunking and Data Management

Amumax introduces the concept of chunking for storing simulation data in smaller, more manageable pieces. This is particularly useful when working with large datasets, as it allows users to read and write specific parts of the data without loading the entire dataset into memory. Chunking also enables parallel processing, further improving the efficiency of large-scale simulations. Pyzfn utilizes the chunking of the Amumax output extensively to access simulation data efficiently.

3.1.5 Optimised Mesh Definition

Amumax's performance is largely dictated by Fast Fourier Transform (FFT) computations, which rely heavily on the `cuFFT` library[160]. Optimal performance is achieved when the FFT dimensions are powers of two. Acceptable performance can also be expected for so-called 7-smooth numbers, which are integers composed only of the prime factors 2, 3, 5, and 7. In contrast, grid sizes with prime factors outside this set should generally be avoided, as they tend to incur significant performance penalties, potentially up to an order of magnitude. For this reason, it may be advantageous to slightly oversize the simulation grid to match a smoother and more FFT-friendly configuration.

Furthermore, simulations that employ periodic boundary conditions tend to run significantly faster than those with non-periodic boundaries. This performance gain is attributed to the elimination of zero-padding, which effectively halves the FFT size in each periodic direction. Additionally, periodic simulations consume less memory. However, they do come with the trade-off of a longer initialization time, as multiple repeated image kernels must be computed at the start of the simulation.

In Amumax, mesh parameters such as cell size and grid size are defined directly through variables like `Nx`, `Ny`, and `Nz`, eliminating the need to call specific functions to define the mesh. The mesh can be automatically optimised for FFT performance, following the rules defined above, ensuring that simulations are as fast as possible without compromising accuracy.

3.1.6 Enhanced Command Line Interface and Usage

The main way to start simulations is through the command line interface. A number of flags and arguments can be used to fine tune the simulation we want to perform. I have added many such flags and added a user friendly help command which lists all of the available parameters.

3.2 Pyzfn

I also created Pyzfn[161], a Python-based post-processing library tailored for micromagnetic simulations, specifically designed to analyse and visualise the output data produced by Amumax, a performance-optimised fork of the widely-used mumax micromagnetic simulator. The library provides a structured and extensible interface for interacting with simulation results stored in the `Zarr` data format, which is particularly well-suited for large, multidimensional datasets. By leveraging the capabilities of Zarr, Pyzfn supports efficient disk-based access to data, enabling workflows that are not limited by memory constraints. It is available as an open source project; anybody is welcome to use and/or contribute to the library available at https://github.com/MathieuMoalic/pyzfn.

The core objective of Pyzfn is to facilitate post-simulation analysis through a combination of data access utilities, spectral processing tools, and visualisation methods. It allows researchers to inspect and manipulate magnetisation fields and related quantities without having to manually parse raw data formats. In this context, Pyzfn plays a crucial role in bridging the gap between high-performance simulation and meaningful physical interpretation.

Among its capabilities, Pyzfn includes functionality for computing dispersion relations and identifying spin wave modes—tasks that are central to the analysis of magnetisation dynamics in confined magnetic systems. These operations are optimised to exploit the structure of the underlying simulation data, enabling scalable analysis even in three-dimensional systems with time-resolved dynamics.

Beyond numerical processing, the library also incorporates lightweight visualisation tools. These allow researchers to generate snapshots of magnetisation configurations, or to produce interactive spectral plots for qualitative analysis. The inclusion of such tools makes it possible to obtain immediate visual feedback on the effects of varying physical parameters or boundary conditions.

Internally, Pyzfn is structured around object-oriented abstractions that reflect the logical structure of micromagnetic simulations. Metadata associated with simulations—such as spatial discretization, field parameters, or boundary conditions—are exposed through accessible interfaces. This design encourages both programmatic interaction and integration into larger automated pipelines.

Although Pyzfn is usable out-of-the-box, its implementation encourages extensibility. Advanced users can override slicing behaviour, customize post-processing algorithms, or integrate third-party libraries for further statistical or topological analyses. This makes it suitable not only for one-off analysis but also for systematic studies, such as parameter sweeps or comparative evaluations.

In addition, Pyzfn provides utilities for interoperability with other micromagnetic tools. For example, it supports importing and exporting data in the OOMMF OVF format, which remains a de facto standard within the micromagnetics community. This feature enhances its applicability in multi-tool workflows and comparative benchmarking.

3.2.1 Snapshots

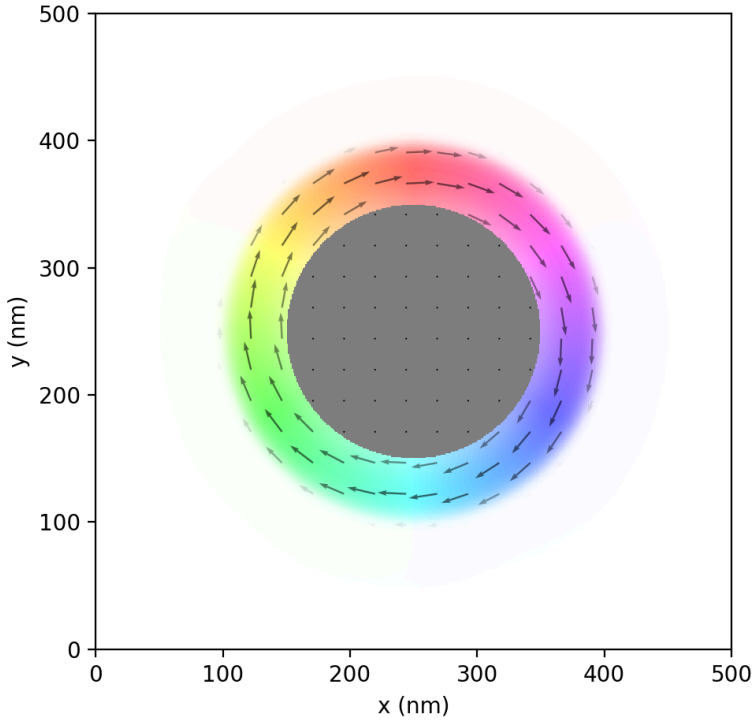

Figure 5: The snapshot preview function of an antidot with reduced perpendicular magnetic anisotropy in its rims, allowing for a vortex-like state to form.

One of the most common tasks when working with micromagnetic simulation data is the visualisation of magnetisation, which is inherently a three-dimensional vector field. Representing such a 3D field in a 2D image requires dimensional reduction, and the choices made in this process can significantly affect both the clarity and interpretability of the visualisation. The approach adopted here is intentionally tailored to the context of magnetic thin films, where magnetisation dynamics are predominantly two-dimensional.

The `snapshot` function utilizes `matplotlib`, a Python plotting library, to generate a 2D visual representation of the 3D magnetisation field, as shown in Fig.Figure 5. This is achieved by encoding all three magnetisation components using a combination of colour and vector glyphs:

- The **z**-component of the magnetisation (m_z) is mapped to the *value* (brightness) channel in HSL colour space, such that regions magnetised strongly along the $+z$ direction appear white, and those along the $-z$ direction appear black.
- The **in-plane components** (m_x, m_y) are represented in two complementary ways:
  - The *hue* channel encodes the in-plane angle, calculated as $\varphi = \arg\big(m_x + i m_y\big)$.
  - A quiver plot is overlaid to show the local direction and relative magnitude of the in-plane magnetisation.
- The **saturation** channel is fixed at its maximum value (1) to ensure that colours remain vivid, making the hue information easier to interpret.
- **Non-magnetic regions**—such as antidots—are masked and shown in grey to distinguish them from active magnetic areas.

Additionally, the function supports periodic tiling of the magnetisation field via the `repeat` parameter. This feature is particularly useful for visualising extended periodic structures, such as antidot lattices, where repeating units enhance the visual context.

3.2.2 Interactive Spectral Analysis

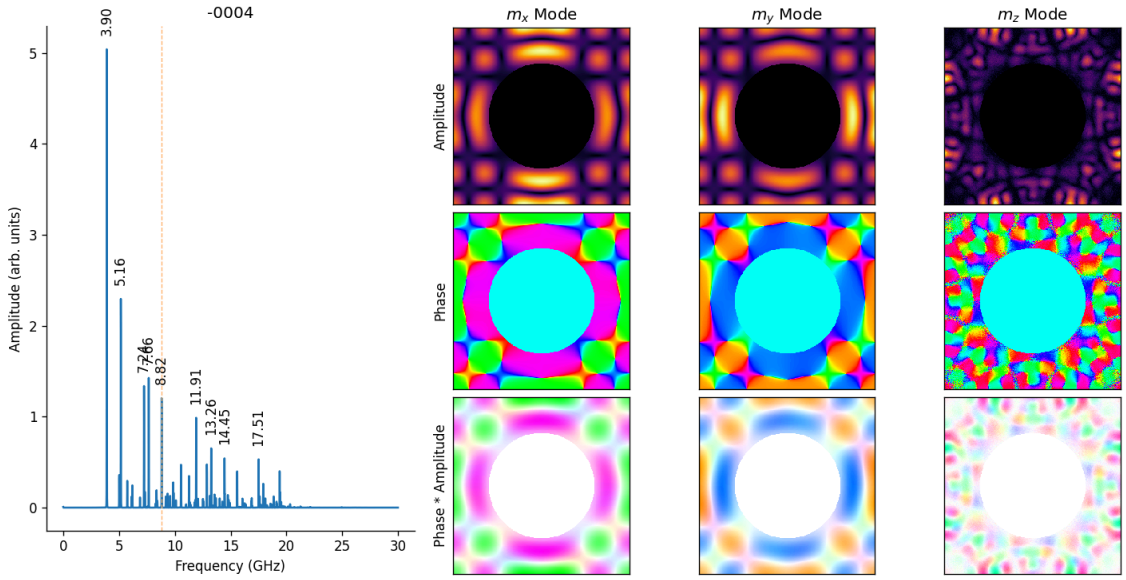

Figure 6: The interactive spectrum preview function of Pyzfn, the structure being visualised is a thin film with a hole (antidot) in the middle

The `ispec` function provides an intuitive and interactive tool for exploring the frequency spectrum of spin-wave modes in micromagnetic simulations. Its purpose is to help identify and visualise resonant modes in a magnetic system, based on the results of a Fourier transform.

When executed, the function displays a figure with two main panels as seen in Fig.Figure 6. The left panel shows the spectral amplitude as a function of frequency, highlighting the most prominent peaks. The right panel is initially blank but becomes active through user interaction.

By clicking on the spectrum plot, the user can select a frequency of interest. This triggers the computation and visualisation of the corresponding spin-wave mode at that frequency. The selected mode is then displayed as a set of colour plots, which illustrate both the amplitude and phase of the magnetisation components. Right-clicking on a peak will automatically snap the selection to the nearest detected resonance, making it easier to analyse specific modes.

This function is especially useful for quickly inspecting how the spin-wave response is distributed across frequencies and for understanding the spatial structure of individual modes in complex magnetic textures.

Overall, Pyzfn is designed to support a reproducible, scalable, and physically meaningful analysis of micromagnetic simulation results. Its architecture reflects the demands of modern computational magnetism research, where high-throughput simulation must be matched by robust and interpretable post-processing. I have used Pyzfn in all of my research projects, and it has proven to be an invaluable tool for extracting insights from complex micromagnetic phenomena.

Chapter 4

Main research topics

In this chapter, I present the results of my research on collective spin-wave dynamics in complex magnetic textures and patterned ferromagnetic films. The findings are structured around five research articles, each preceded by an introductory section that outlines the main results and clarifies my individual contributions.

4.1 Spin-wave spectra in antidot lattice with inhomogeneous perpendicular magnetic anisotropy

- *Spin-wave spectra in antidot lattice with inhomogeneous perpendicular magnetic anisotropy*,
  M. Moalic, M. Krawczyk, M. Zelent.
  Journal of Applied Physics, **132** (21), 213901 (2022).

4.1.1 Introduction

This article explores the collective dynamics of spin waves in patterned ferromagnetic thin films with complex magnetic textures. In particular, it addresses one of the central hypotheses of the thesis: that modifying the magnetic anisotropy locally—especially around the rims of antidots—can be used to tailor spin-wave excitations to offer reconfigurable magnonic crystals. By investigating the spin-wave spectra in antidot lattices formed from multilayer thin films with PMA, we explicitly introduce a narrow rim of reduced PMA at antidot edges and map the resulting modes. We identify robust edge-localized excitations confined to the low-PMA rims and show that their frequencies and spatial profiles can be tuned by the rim width and the anisotropy contrast. As these rim modes approach extended bulk modes, we observe clear hybridization—manifested by avoid-crossings and open, GHz-scale frequency gaps—which demonstrates controlled coupling between localized and delocalized excitations. Together, these results lay a foundation for understanding and engineering magnetisation textures that support reprogrammable, anisotropy-driven magnonic responses.

While the study is performed for a specific parameter set (one multilayer stack, antidot geometry, and an out-of-plane bias field), the mechanisms we uncover—edge-mode formation from local PMA reduction and tunable bulk–edge hybridization via anisotropy contrast and rim width—are generic. We therefore expect the same qualitative behavior to appear in other PMA multilayers and patterned films where anisotropy can be locally engineered (e.g., by interfacial modification or focused-ion irradiation), as well as in related magnonic crystals with comparable symmetry and length scales.

4.1.1.1 Contribution of the Author

In this publication, I conducted all numerical simulations using the Amumax software, analysed the resulting data, prepared the first draft of the manuscript, prepared all the figures except Figure 1, contributed to the writing and critical review of the manuscript and was responsible for compiling the supplementary materials. I was also responsible for submission, and contacts with the editor and editorial staff.

Journal of Applied Physics

Spin-wave spectra in antidot lattice with inhomogeneous perpendicular magnetic anisotropy

Cite as: J. Appl. Phys. **132**, 213901 (2022); https://doi.org/10.1063/5.0128621
Submitted: 29 September 2022 • Accepted: 13 November 2022 • Published Online: 01 December 2022

M. Moalic, M. Krawczyk and M. Zelent

AIP Publishing

Journal of Applied Physics ARTICLE scitation.org/journal/jap

Spin-wave spectra in antidot lattice with inhomogeneous perpendicular magnetic anisotropy

Cite as: J. Appl. Phys. **132**, 213901 (2022); doi: 10.1063/5.0128621
Submitted: 29 September 2022 · Accepted: 13 November 2022 ·
Published Online: 1 December 2022

M. Moalic,[a] M. Krawczyk,[b] and M. Zelent[c]

AFFILIATIONS

Institute of Spintronics and Quantum Information, Faculty of Physics, Adam Mickiewicz University, Poznan, Poland

Note: This paper is part of the Special Topic on Recent Advances in Magnonics.
[a]**Electronic mail:** matmoa@amu.edu.pl
[b]**Author to whom correspondence should be addressed:** krawczyk@amu.edu.pl
[c]**Electronic mail:** mateusz.zelent@amu.edu.pl

ABSTRACT

Magnonic crystals are structures with periodically varied magnetic properties that are used to control collective spin-wave excitations. With micromagnetic simulations, we study spin-wave spectra in a 2D antidot lattice based on a multilayered thin film with perpendicular magnetic anisotropy (PMA). We show that the modification of the PMA near the antidot edges introduces interesting changes to the spin-wave spectra, even in a fully saturated state. In particular, the spectra split into two types of excitations: bulk modes with amplitude concentrated in a homogeneous part of the antidot lattice and edge modes with an amplitude localized in the rims of reduced PMA at the antidot edges. Their dependence on the geometrical or material parameters is distinct, but at resonance conditions fulfilled, we found strong hybridization between bulk and radial edge modes. Interestingly, the hybridization between the fundamental modes in bulk and rim is of magnetostatic origin, but the exchange interactions determine the coupling between higher-order radial rim modes and the fundamental bulk mode of the antidot lattice.

I. INTRODUCTION

Magnonic crystals (MCs), analogous to photonic crystals that have a periodic modulation of the refractive index to control the propagation of electromagnetic waves, are magnetic structures with a periodicity of material properties relevant to spin-wave (SW) propagation.[1,2] The main feature of MCs is appearance of bands of collective SW excitations and the separating them magnonic bandgaps, which is useful for applications to guide and control spin waves.[3–7] The basic types of MCs are artificial crystals formed by periodic arrangement of two different materials.[4] Those can be two ferromagnetic materials, like in bicomponent MCs,[8] ferromagnetic and nonmagnetic materials like in an array of ferromagnetic dots in nonmagnetic matrix,[9–11] or the inverse structures,[12,13] i.e., an array of holes in a ferromagnetic matrix, antidot lattices (ADLs).[14]

Periodic modulation of SW-relevant parameters can be introduced not only in the patterning process[15,16] but also at a later stage. For instance, it's possible to modify the magnetic properties of the exposed areas by ion irradiation of the ferromagnetic film or a multilayered structure.[17–21] Recently, another promising idea has been explored, that is, the formation of periodicity by regular change of the magnetization orientation in a homogeneous thin film.[22] The basic examples are the periodic stripe domains, which can be considered as 1D MCs[23,24] or skyrmion lattices, which also form a kind of 2D MC.[25–28] These structures have an important property; their magnetization structure is reconfigurable and sensitive to the external bias magnetic field; in this way, the magnonic band structure can be programmed after the manufacturing of the device, depending on the actual needs.[22] Nevertheless, the structures combining both patterning and magnetization texture are not yet well explored, in particular, in the context of MCs and magnonics.

In recent studies, ADL based on multilayers with perpendicular magnetic anisotropy (PMA) has been indicated as a system hosting periodic magnetization texture with interesting properties

and potential applications.[29–31] The results of time-resolved magneto-optical Kerr effect (TR-MOKE) microscopy measurements of SW excitations in ADL based on $[Co/Pd]_8$ multilayers were interpreted with micromagnetic simulations.[29] To explain low frequency mode in the spectra, the authors assumed that around the holes there is a rim with modified magnetic properties formed during the patterning process, i.e., Ga ions used in the focused ion beam (FIB) in the patterning process penetrate larger area than the antidots. In the rims around the antidots, the dose is sufficient to disturb the interfaces between Co and Pd and so the PMA, which originates from the interfaces in the multilayer. The absence or reduced PMA in the rims results in the in-plane alignment of magnetization in the rims at remanence.[30] The MC composed of two areas of different magnetization orientations, out-of-plane in the bulk and in-plane in the rims, makes the SW spectra complex, with bulk modes localized in the ferromagnetic matrix, as in standard ADLs, and the additional modes localized in the rims, with possible hybrid excitations. Such structures open the prospects for the magnonic band structure with sub-bands sensitive to external stimuli in different ways, e.g., different dependences on a magnetic field, the property, which can be exploited for developing new phenomena and applications.

In this paper, we study the SW spectra in the ADL lattice based on the multilayer thin film with PMA with the rims around the antidots, where the PMA is reduced. In particular, we study the dependence of the spectra on the rim anisotropy value, rim width, and antidot diameter under a perpendicular magnetic field, fully saturating the sample. We show that the variation of these properties affects mainly the edge-localized modes but additionally may introduce or control a hybridization between the radial modes of the rim and the bulk excitations of the ADL. This offers a possibility to control collective SWs by tuning magnetic properties only in selected areas.

The paper is organized as follows. In Sec. II, we introduce the structure and the micromagnetic model used in simulations. In Sec. III, we present the simulation results of SW spectra in dependence on the anisotropy strength in the rim, antidot diameter, and finally rim width, and interpret the obtained results. In Sec. IV, we summarize the results.

II. STRUCTURE AND METHODOLOGY

For our numerical investigations, we selected a structuralized Co/Pd multilayer with high PMA (with the anisotropy constant $K_{u,bulk}$) and reduced anisotropy around the antidots, already investigated in Ref. 30. The schematic of the unit cell of the studied structure is shown in Fig. 1. The structure is made up of eight repetitions of Co (0.75 nm thickness) and Pd (0.9 nm) bilayers with a total thickness of 13.2 nm. Around the antidot of diameter d is a rim of width w with reduced PMA, $K_{u,rim}$. In our study, we will change these three parameters. The antidots form a square lattice on the (x, y) plane with a lattice constant $a = 500$ nm. To maintain the same static magnetization configuration of the system, i.e., to maintain a full saturation of magnetization in the out-of-plane direction, we perform numerical simulations using a sufficiently strong external magnetic field $\mu_0 H_{ext} = 1$ T directed along the z axis. We do not study SW propagation; hence, the wavevector of all considered SWs is 0, $k = 0$.

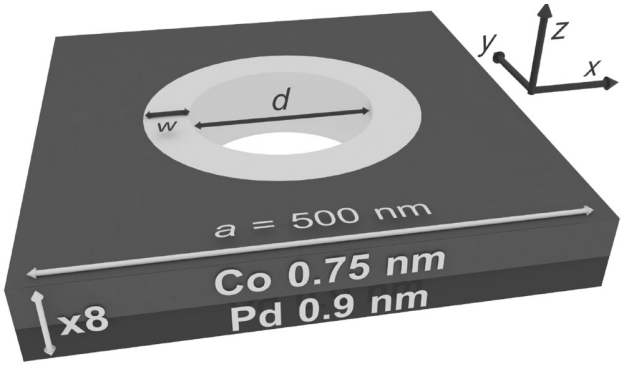

FIG. 1. Schematic illustration of the investigated structure showing the Co/Pd supercell of ADL. Note that the figure is not to scale. The bright color around the hole represents the rim with the reduced PMA.

We use micromagnetic simulations with Mumax3 software,[32,33] which solves the Landau–Lifshitz–Gilbert equation for magnetization vector $\mathbf{M}$,

$$\frac{d\mathbf{m}}{dt} = \gamma\mu_0 \frac{1}{1+\alpha^2}(\mathbf{m}\times\mathbf{H}_{eff}) + \alpha\mu_0(\mathbf{m}\times(\mathbf{m}\times\mathbf{H}_{eff})), \quad (1)$$

where $\mathbf{m} = \mathbf{M}/M_S$ is the normalized magnetization, M_S is the magnetization saturation, H_{eff} is the effective magnetic field acting on magnetization, $\gamma = -187$ rad GHz/T is the gyromagnetic ratio, and α is the damping constant. The following components were considered in the effective magnetic field $\mathbf{H}_{eff}$: demagnetizing field H_d, exchange field H_{exch}, PMA field H_{Ku}, and external magnetic field; thermal effects were neglected. Thus, the effective field is expressed as

$$\mathbf{H}_{eff} = \mathbf{H}_d + \mathbf{H}_{exch} + \mathbf{H}_{ext} + \mathbf{H}_{Ku} + \mathbf{h}_{mf}, \quad (2)$$

where the last term, $\mathbf{h}_{mf}$, is a microwave magnetic field used for SW excitation. The exchange and anisotropy fields are defined as

$$\mathbf{H}_{exch} = \frac{2A_{ex}}{\mu_0 M_S}\Delta\mathbf{m}, \quad \mathbf{H}_{Ku} = \frac{2K_{u,bulk(rim)}}{\mu_0 M_S}(\mathbf{u}\cdot\mathbf{m})\mathbf{u}, \quad (3)$$

where $\mathbf{u}$ is the unit vector that indicates the direction of anisotropy and A_{ex} is the exchange constant.

To simplify the micromagnetic simulations of the multilayered ADL system, we used the effective thickness approach, which involves the effective, experimentally measured, values of the magnetic parameters for single discretization through the thickness of the magnetic multilayer.[34] In the simulations, we used 512 cells across the x and y axes, which bring the cell size to around 0.97 nm in-plane and 13.2 nm for the z axis. To mimic a periodic structure, we used 32 repetitions of Mumax3 periodic boundary conditions, along the x and y axes. The effective magnetic parameters for the Co/Pd multilayer are taken from Ref. 30; they are $K_{u,bulk} = 4.5 \times 10^5$ J/m^3,

$M_S = 0.81 \times 10^6$ A/m, and $A_{ex} = 1.3 \times 10^{-11}$ J/m. We used a low damping constant $\alpha = 1 \times 10^{-7}$ to simulate sharp SW spectra.

To obtain the full SW spectra first, we relax the system, then we implement a special distribution of the external microwave magnetic field for SW excitation, $\mathbf{h}_{mf}$. Using the Voronoi tessellation algorithm, we divided the ADL unitcell area into small random sub-areas, about 30 nm wide each, effectively acting as SW point sources (nanoantennas). Each of these nanoantennas is assigned the same amplitude of a microwave magnetic field, but a random phase offset was used in the system's excitation by an in-plane magnetic field oriented parallel to the line $y = x$ on the positive direction. To excite SWs in a wide frequency range, we used a *sinc* function to apply a time modulation of the microwave field, which has a maximum amplitude of 0.5 mT, a cutoff frequency of 40 GHz, and a sampling rate of 8.3 ps. The magnetic field pumps the system for 1 ns and stops before any data are recorded. The time-resolved, space-dependent magnetization was then saved over 8.3 ns and processed by the fast Fourier transform (FFT) to get 2D visualization of all SW modes. To obtain the SW spectra, we applied a Hanning window to the time dimension of the data before using the FFT. We then found for each frequency, the cell in the system that had the highest amplitude and used it as the FFT amplitude in the spectra. This approach to calculate the SW spectra has the benefit of not favoring the extended SW modes, as is in the case of the homogeneous microwave field.

To refer to a particular SW mode, we use the M_{mnb} notation, where we identify the radial n, azimuthal m, and bulk b numbers, which represent the order of the modes in the rim along the radial and azimuthal directions and in the bulk, respectively. For bulk, by the mode order, we took the number of nodal points along the line connecting neighboring antidots minus one. For instance, a homogeneous in space mode, a fundamental mode, which has a pinned magnetization at the edges of the antidots, we will have the order number $b = 1$. A bulk mode with one more nodal point between antidots, i.e., in total three nodes, is a second-order bulk mode with $b = 2$. When a number is not applicable, we replace it with the "−" symbol. The radial mode order is defined as a number of amplitude quantizations in the rim along the radial direction, where $n = 1$ means a fundamental mode with only partial pinning at the rim edges and no nodes between, then $n = 2$ represents a mode with 1 node between the rim edges. For azimuthal modes, the value of the number m defines the number of full phase rotations along the circumference, where $m = 1$ means a 2π phase change along the circumference of the rim.

III. RESULTS

Initially, we simulate the ADL with an antidot diameter of $d = 200$ nm and a rim width of $w = 50$ nm in dependence on the anisotropy value in the rim. As the $\mathbf{H}_{ani}$ is parallel to $\mathbf{H}_{ext}$, a local reduction in the anisotropy field should result in a decrease in the resonant frequencies of SWs confined in these areas. Indeed, Fig. 2(a) shows the dependence of the SWs spectrum on the

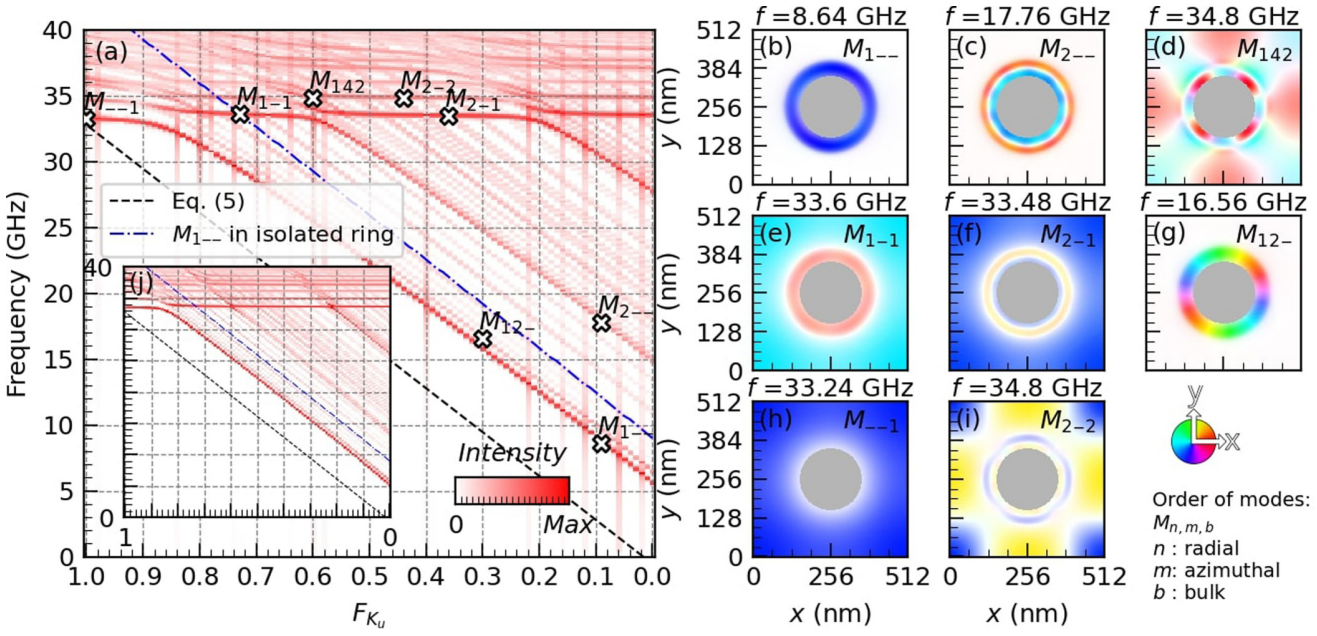

FIG. 2. (a) SW spectrum dependent on the reduced anisotropy strength F_{Ku}, by changing $K_{u,rim}$. The intensity of the SW spectra has been presented in a logarithmic scale colormap. The black-dashed line represents the analytically calculated ferromagnetic resonance frequency of the uniform thin film, Eq. (5). The blue-dashed-dotted line represents the resonance frequency of the fundamental mode in the isolated ring. The markers indicate the SW modes illustrated in the right panels (b)–(i). Here, the color saturation indicates the mode intensity and the hue indicates the phase of the mode, according to the diagram in the right bottom corner. Inset (j) presents analogous dependence to panel (a), but with rim-matrix exchange interactions disabled.

reduced PMA factor F_{Ku},

$$F_{Ku} = \frac{K_{\mathrm{u,rim}}}{K_{\mathrm{u,bulk}}}, \tag{4}$$

which reveals two distinct groups of modes. One group with frequencies linearly decreasing as F_{Ku} does, and the second one, only weakly dependent on the anisotropy in the rim, which corresponds to the ADL modes in the rim and bulk, respectively. The representative eight modes are marked in Fig. 2(a), and their in-plane spatial profiles are shown in Figs. 2(b)–2(i).

For a uniform distribution of anisotropy, $F_{Ku} = 1$, the lowest frequency mode is a fundamental bulk mode M_{-1} at the frequency of 33.24 GHz, as illustrated in Fig. 2(h). The modes of higher frequencies are the higher-order bulk modes. The reduction in the anisotropy in the rims leads to transition of a homogeneous ADL to a structuralized bicomponent system with different magnetic parameters and to isolate edge-localized radial and azimuthal modes. Therefore, with decreasing F_{Ku}, the frequencies of these two types of modes decrease and crossover the bulk modes. At some F_{Ku}, we observe strong hybridization, manifested with opening gaps, in particular, at crossings of the fundamental bulk mode M_{-1} at $F_{Ku} = 0.86$, 0.59, and 0.21 for 34 GHz. The visualizations of modes presented in Figs. 2(e) and 2(f) show that these hybridizations are between the mode M_{-1} and the radial modes of the rim: M_{1-}, M_{2-}, and M_{3-} (profile not shown). The first two radial modes are shown in Figs. 2(b) and 2(c), and their hybridizations with the fundamental bulk mode in (e) and (f), respectively. Also, higher order bulk modes hybridize with the rim modes, although with smaller strength. For example, the hybridization of the second-order radial mode M_{2-} with the second-order bulk mode M_{-2} is clearly seen in the profile of the M_{2-2} mode shown in Fig. 2(i). The hybridization of the modes M_{-2} and M_{14-} is visible in the profile of M_{142} mode as shown in Fig. 2(d), which clearly demonstrates the hybridization of the bulk modes also with the azimuthal modes of the rim.

At frequencies smaller than 33.24 GHz, we see the parallel lines of different intensities. The intensive lines have already been identified as radial modes of the rim; small intensity lines are azimuthal modes, for example, at 16.56 GHz is the M_{12-} mode presented in Fig. 2(g). The first-order radial mode in the rim M_{1-} is analogous to the bulk fundamental mode but restricted in space to the rim. Thus, the M_{1-} and M_{-1} are two fundamental excitations of our ADL. Their mode frequencies are influenced by the anisotropy, exchange, and magnetostatic fields. To analyze the role of individual interactions on the coupling between the modes, we make a comparison of the full spectra, Fig. 2(a), with the spectra of simplified structures.

To clarify the direct effect of the anisotropy field on the system, we calculate the ferromagnetic resonance frequency of a homogeneous film by varying the anisotropy field. We use Kittel's formula,[35]

$$f_0 = \frac{|\gamma|\mu_0(H_{\mathrm{ani}} + H_{\mathrm{d}} + H_{\mathrm{Ku}})}{2\pi}, \tag{5}$$

with f_0 being the mode frequency, $H_{\mathrm{d}} = -M_{\mathrm{S}}$, and H_{Ku} as defined in Eq. (3). The function $f_0(F_{Ku})$ is shown with the black-dashed line in Fig. 2(a). When $F_{Ku} = 1$, f_0 and the resonance frequency for the simulated ADL are only 400 MHz apart. This means that an ADL with an antidot diameter of $a = 200$ nm at full saturation has a minor effect on the resonant frequency of the fundamental bulk mode. However, as F_{Ku} is reduced, the fundamental mode of the ADL smoothly transforms into a radial mode M_{1-} in the rim. At $F_{Ku} = 0.84$, we observe a strong hybridization between both modes; see also the mode M_{1-1} in Fig. 2(e). With further reduction in anisotropy in the rim, the frequency difference increases, reaching a stable frequency separation of 6.20 GHz between f_0 and the M_{1-} mode. This difference between frequencies is mainly due to shape anisotropy of the rim, which rises the rim mode frequencies.

If we compare the frequencies of the M_{1-} mode with those of the isolated ring (obtained from independent micromagnetic simulations, keeping parameters of the rim), the green-dashed line in Fig. 2(a), we can see that the frequency of the fundamental mode of the rim is constantly lower by 3.59 GHz. This means that the magnetostatic field from the ADL bulk and a side contact of the rim with the ADL, effectively lowers the internal demagnetizing field in the rim, lowering its mode frequencies.

So far in this study, the exchange interaction has been homogenous throughout the system. Now, we wanted to find out if the hybridization between SW modes is due to dipolar or exchange interactions between the bulk and the rim. To do that in the micromagnetic simulations, we simply add a 2 nm nonmagnetic spacer between the rim and the bulk, which brakes the exchange interaction at the interface of these two regions. The result is presented in Fig. 2(j). We notice that the frequency of the fundamental bulk mode M_{-1} at $F_{Ku} = 0.85$ only slightly rises from 32.88 to 33.48 GHz. Thus, the hybridization strength has slightly decreased with the exchange decoupling of the rim from the bulk. For hybridization of the M_{-1} mode with higher order radial modes, at $F_{\mathrm{Ku}} = 0.59$, and 0.21, the frequency difference does not exceed 300 MHz in Fig. 2(j), indicating very weakly coupled modes, when the exchange between the rim and bulk is excluded. This clearly indicates that these hybridizations are driven by the exchange interactions. Thus, we can conclude that the hybridization of fundamental bulk mode with fundamental rim mode has a magnetostatic character, while the hybridizations with higher order radial modes have a strong exchange character.

For further analysis, we performed micromagnetic simulations of the system in dependence on the antidot diameter d in 2 nm steps in the range from 200 to 0 nm. At last value of d, there is no antidot and only a circular area with reduced anisotropy. The other parameters are fixed, i.e., $F_{\mathrm{Ku}} = 0$ and $w = 50$ nm. The results are shown in Fig. 3(a). As expected, the diameter of the antidot only weakly affect the frequency of the fundamental bulk mode [see the mode M_{3-1} and Fig. 3(f)] and the higher-order bulk modes [e.g., M_{2-2} and Fig. 3(i)]. Unexpectedly, we do not observe avoid-crossings as d changes, although many crossings between different types of modes are visible. On the other hand, Fig. 3(f) clearly indicates the hybrydisation occuring between the fundamental bulk mode and the radial rim modes.

The frequency of the rim radial modes shows a slight decrease with decreasing d [see the modes M_{1-}, M_{2-}, and M_{3-} and their profiles in Figs. 3(b), 3(d), and 3(e), respectively]. But at an antidot

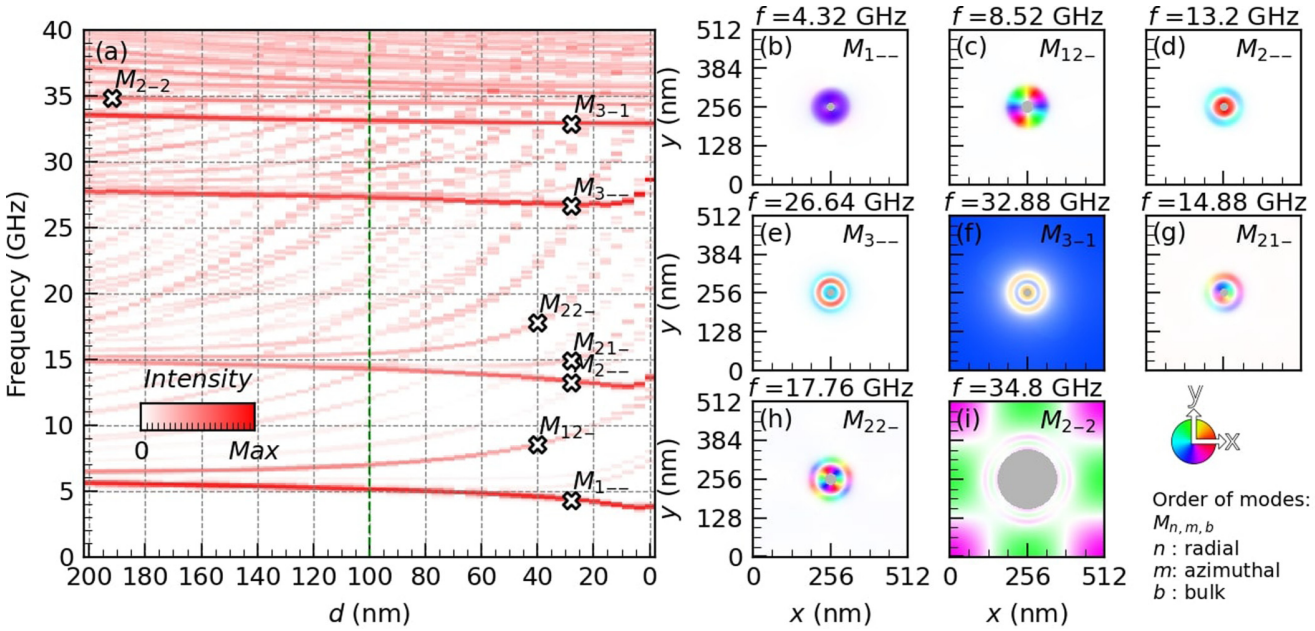

FIG. 3. (a) The spin-wave spectrum in dependence on the antidot diameter d. The green-dashed line represents the antidot diameter $d = 100$ nm used in Figs. 2 and 4. (b)–(i) Visualization of spin-wave modes for selected frequencies and antidot diameters marked in (a). The saturation indicates the intensity and the hue indicates the phase of the mode, according to the diagram in the right bottom corner.

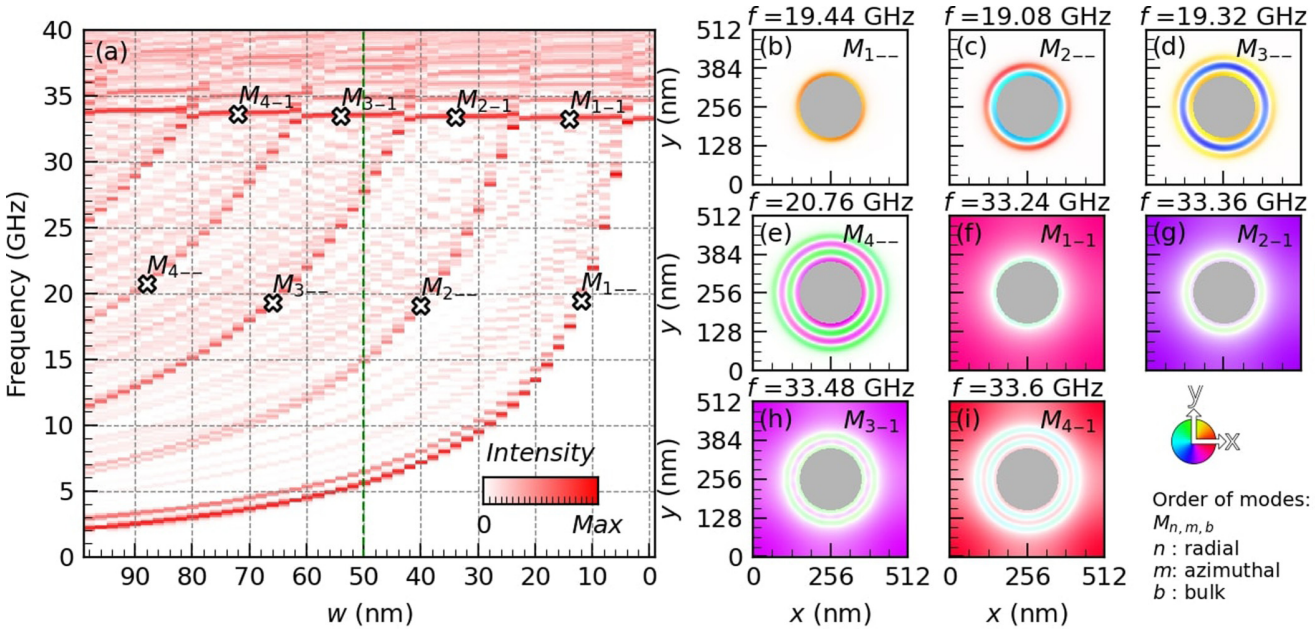

FIG. 4. (a) Spin-wave spectrum in dependence on rim width, w. The green-dashed line represents the rim width used in previous investigations. (b)–(i) Visualization of spin-wave modes at selected frequencies and antidot diameters marked in (a). The color saturation indicates the mode intensity and the hue indicates the phase of the mode, according to the diagram in the right bottom corner.

diameter of about 10 nm, the frequency of these modes starts to increase. It is caused by a change in the topology of the ADL geometry. The structure changes from an array of antidots to a full ferromagnetic layer. There are strong dipole interactions on opposite sides of the small antidot at this diameter range, which result in a change of effective demagnetizing factors and an increase in mode frequency.[36] The frequency of the second and higher-order azimuthal modes linearly increases at high rates, for example, the frequency of the second-order azimuthal mode M_{12-} and M_{22-} [Figs. 3(c) and 3(h)] increases from 6.5 GHz at $d = 200$ nm up to 10 GHz at 20 nm antidots. This is due to reduction in circumference of the antidot rim that contains the wavelength of the azimuthal mode to decrease, resulting in an increase in frequency.

The other important parameter that affects the resonance spectrum of SWs is the width of the rim w. We performed micromagnetic simulations with a varied width of the reduced anisotropy region from 0 to 100 nm for a fixed antidot diameter ($d = 200$ nm) (see Fig. 4). The results show that the width of the rim significantly affects the frequency of radial and azimuthal modes [see modes $n = 1 \cdots 4$ and their profiles in Figs. 4(b)–4(e)] but having no significant effect on the frequency of bulk modes (e.g., see the frequency of the fundamental bulk mode M_{n-1}). As the rim area decreases, the frequency of azimuthal and radial modes in the rim increases, although at different rates. For example, the frequency of the mode M_{1-} increases from about 2.04 to 33.24 GHz, where the hybridization with the fundamental bulk mode M_{-1} occurs; see the hybridized mode M_{1-1} in Fig. 4(f). Interestingly, there are hybridizations between the M_{-1} mode and the radial modes M_{n-} of the rim, but unexpectedly, the strength of these hybridizations increases with n. However, we need to keep in mind that this is associated with the increasing width of the rim.

IV. CONCLUSIONS

We have studied the SW spectrum in an ADL made of Pd/Co multilayers with PMA at full saturation induced by a PMA and an out-of-plane oriented external magnetic field. A characteristic feature of the structure under investigation is a region around the antidots, a rim, in which the anisotropy was reduced. We have shown that in such a system there are extended bulk modes, radial, and azimuthal excitations. The last two are confined to the rim area and they are very sensitive to variation of the local rim parameters. In particular, the frequency of the azimuthal modes increases with decreasing antidot size, while the dependence of the radial modes is not monotonous in that case. Both types of SWs decrease the frequency with decreasing anisotropy in the rim or with increasing rim width.

Interestingly, it is possible to achieve strong interaction between bulk modes of the ADL and the rim localized modes. Particularly, strong hybridization has been found between the fundamental mode of ADL and the radial excitation of the rim, reaching a value of 1.5 GHz. Importantly, such a coupling is realized by magnetostatic interaction between fundamental modes of the bulk and the rim, while mainly by the local exchange coupling between the rim area and the bulk of ADL for hybridizations with higher order radial modes. This opens the way for designing magnonic crystals with hybridized localized and extended modes, scaled to the deep nanoscale and properties controlled locally at the rim areas.

Our research is the next step toward the use of ADL based on PMA multilayers in magnonic applications. Additionally to the two sets of modes, edge and volume waves, on the same platform, an additional degree of freedom, i.e., the magnetization configuration in the rims at remanence, can be exploited in these materials. Thus, the system offers a platform for studying a wide variety of physical phenomena as well as for multifunctional SW devices with the designed global microwave response and local tuning of channels for SW propagation.

ACKNOWLEDGMENTS

The research has received funding from the National Science Centre of Poland, Grant No. UMO–2020/37/B/ST3/03936. The simulations were partially performed at the Poznan Supercomputing and Networking Center (Grant No. 398).

AUTHOR DECLARATIONS

Conflict of Interest

The authors have no conflicts to disclose.

Author Contributions

M. Moalic: Formal analysis (lead); Investigation (lead); Software (equal); Visualization (lead); Writing – original draft (lead); Writing – review & editing (equal). **M. Krawczyk:** Conceptualization (equal); Funding acquisition (lead); Supervision (equal); Writing – original draft (equal); Writing – review & editing (equal). **M. Zelent:** Formal analysis (equal); Investigation (equal); Methodology (equal); Supervision (equal); Visualization (equal); Writing – original draft (equal); Writing – review & editing (equal).

DATA AVAILABILITY

The data that support the findings of this study are available from the corresponding author upon reasonable request.

REFERENCES

[1]Y. V. Gulyaev and S. A. Nikitov, "Magnonic crystals and spin waves in periodic structures," Dokl. Phys. **46**, 687 (2001).
[2]H. Puszkarski and M. Krawczyk, "Magnonic crystals—The magnetic counterpart of photonic crystals," Solid State Phenom. **94**, 125 (2003).
[3]B. Lenk, H. Ulrichs, F. Garbs, and M. Münzenberg, "The building blocks of magnonics," Phys. Rep. **507**, 107–136 (2011).
[4]M. Krawczyk and D. Grundler, "Review and prospects of magnonic crystals and devices with reprogrammable band structure," J. Phys.: Cond. Matter **26**, 123202 (2014).
[5]S. A. Nikitov, D. V. Kalyabin, I. V. Lisenkov, A. Slavin, Y. N. Barabanenkov, S. A. Osokin, A. V. Sadovnikov, E. N. Beginin, M. A. Morozova, Y. A. Filimonov, Y. V. Khivintsev, S. L. Vysotsky, V. K. Sakharov, and E. S. Pavlov, "Magnonics: A new research area in spintronics and spin wave electronics," Phys.-Usp. **58**, 1002 (2015).
[6]J. Rychły, P. Gruszecki, M. Mruczkiewicz, J. W. Kłos, S. Mamica, and M. Krawczyk, "Magnonic crystals—prospective structures for shaping spin waves in nanoscale," Low Temp. Phys. **41**, 745–759 (2015).

4.2 The role of non-uniform magnetisation texture for magnon-magnon coupling in an antidot lattice

- *The role of non-uniform magnetisation texture for magnon-magnon coupling in an antidot lattice*, **M. Moalic**, M. Zelent, K. Szulc, M. Krawczyk.
  Scientific Reports, **14** (1), 11501 (2024).

4.2.1 Introduction

This article continues our previous work with the same material system and parameters, advancing the thesis's central theme: collective spin-wave dynamics in patterned magnetic systems with complex, non-uniform magnetisation textures. It focuses on an antidot lattice based on multilayer ferromagnetic thin films with PMA and modified rims around the antidots, where non-collinear textures—out-of-plane-magnetised bulk regions and in-plane-magnetised rims—produce distinct spin-wave modes and clear hybridization effects. We show strong magnon–magnon coupling between bulk and rim-localised modes, quantified by large anti-crossings (~380 MHz at $B_{\mathrm{ext,z}} \simeq 0.354$ T) and a cooperativity C≈4.7 for the interaction between the fundamental bulk mode and second-order radial rim modes. We demonstated that inserting a thin non-magnetic spacer which breaks bulk–rim exchange collapses the gap to ~50 MHz, confirming that the coupling is exchange-dominated. This research was later continued in another paper: *Enhancement of dynamical coupling in artificial spin-ice systems by incorporating perpendicularly magnetised ferromagnetic matrix*, by S. S. Kunnath, M. Zelent, **M. Moalic**, M. Krawczyk in **Small Structures**, 2400627 (2024).

4.2.1.1 Contribution of the Author

In this publication, I conducted all numerical simulations using the Amumax software, analysed the resulting data, prepared all the figures except for Figure 1.a, wrote the first draft of the manuscript, contributed to the writing and critical review of the manuscript, and was responsible for compiling the supplementary materials. I was also responsible for submission, and contacts with the editor and editorial staff.

scientific reports

Check for updates

OPEN

The role of non-uniform magnetization texture for magnon–magnon coupling in an antidot lattice

Mathieu Moalic✉, Mateusz Zelent, Krzysztof Szulc & Maciej Krawczyk

We numerically study the spin-wave dynamics in an antidot lattice based on a Co/Pd multilayer structure with reduced perpendicular magnetic anisotropy at the edges of the antidots. This structure forms a magnonic crystal with a periodic antidot pattern and a periodic magnetization configuration consisting of out-of-plane magnetized bulk and in-plane magnetized rims. Our results show a different behavior of spin waves in the bulk and in the rims under varying out-of-plane external magnetic field strength, revealing complex spin-wave spectra and hybridizations between the modes of these two subsystems. A particularly strong magnon–magnon coupling, due to exchange interactions, is found between the fundamental bulk spin-wave mode and the second-order radial rim modes. However, the dynamical coupling between the spin-wave modes at low frequencies, involving the first-order radial rim modes, is masked by the changes in the static magnetization at the bulk–rim interface with magnetic field changes. The study expands the horizons of magnonic-crystal research by combining periodic structural patterning and non-collinear magnetization texture to achieve strong magnon–magnon coupling, highlighting the significant role of exchange interactions in the hybridization.

Magnonic crystals (MCs) are a type of magnetic meta-material characterized by the periodicity of some material properties that cause the formation of an artificially tailored spin-wave (SW) band structure[1–7]. These crystals are analogous to photonic crystals, which utilize periodic modulation of the refractive index to control the propagation of electromagnetic waves[8]. MCs provide guidance and control over SWs, promising them for a variety of applications[4,7]. They can be created by the periodic arrangement of two different materials, which can be two ferromagnetic materials[9], ferromagnetic and non-magnetic, i.e., an array of ferromagnetic dots in a non-magnetic matrix[10–12], or inverse structures, i.e., an array of holes in a ferromagnetic matrix, also known as antidot lattices (ADLs)[13,14].

Periodic modulation of SW-relevant parameters can be introduced during the patterning process[15,16], but also through post-fabrication techniques such as ion irradiation, which selectively modifies the magnetic properties of targeted regions in ferromagnetic films and multilayers[17–21]. A recent promising concept involves the formation of periodicity by a regular change of magnetization orientation in a homogeneous thin film[22]. This is exemplified by periodic stripe domains, which can be considered as one-dimensional MCs[23,24], or skyrmion lattices, which form 2D MCs[25–28]. These structures possess a crucial feature of reconfigurable magnetization texture that is sensitive to an external bias magnetic field, allowing the magnonic band structure to be programmed and tuned after device fabrication to suit actual requirements[22]. Nevertheless, there is still a lack of understanding of structures that combine both patterning and magnetization texture, especially in the context of SW dynamics.

Recent explorations in magnon–magnon coupling have revealed diverse mechanisms across various systems. In synthetic antiferromagnets and nanomagnonic devices, studies such as *Chen et al.*[29], *Sud et al.*[30] and *Shiota et al.*[31] have demonstrated strong interlayer coupling, influenced by both interlayer exchange and dynamical dipolar interactions, with tunability via external parameters like magnetic-field orientation. This coupling manifests as mode splitting and large anticrossing gaps, pivotal for advanced device applications[32]. Additionally, the works of *Dai et al.*[33] and *Shiota et al.*[31] specifically address the coupling between acoustic and optic magnon modes in synthetic antiferromagnets, highlighting the role of bias-field tuning and symmetry breaking in achieving strong-coupling regimes. In single-system contexts, such as magnetic skyrmions, different internal mode couplings (e.g., gyrotropic and azimuthal modes) primarily occur through direct exchange interactions, as discussed in

Institute of Spintronics and Quantum Information, Faculty of Physics, Adam Mickiewicz University, Poznan, Poland. ✉email: matmoa@amu.edu.pl

Li et al.[34]. However, the coupling between the SWs of the two domains, which provides both magnetostatic and exchange interactions mediated by the domain wall, remains unexplored.

In our previous studies, we have shown that multilayer ADLs with perpendicular magnetic anisotropy (PMA) have the potential to be promising patterned systems with periodic magnetization texture to control SW propagation[35–37]. Micromagnetic simulations were used to interpret time-resolved magneto-optical Kerr effect microscopy measurements of SW spectra in ADLs based on $[Co/Pd]_8$ multilayers[35]. The low-frequency mode observed in the spectra has been attributed to a rim formed during the focused ion-beam patterning process at the antidots' edges (see Fig. 1). The rims exhibit modified magnetic properties due to the area penetrated by Ga^+ ions being larger than antidots. Consequently, at remanence, the magnetization assumes an in-plane alignment, generating an MC composed of two regions with different magnetization orientations[36]. This arrangement gives rise to complex SW spectra consisting of bulk modes confined to the ferromagnetic matrix and various modes localized in the rims, with the potential for their hybrid excitations. However, the hybridization of SWs confined to different areas, particularly those with varying magnetization orientations, within the magnetic conduit has not been explored to date.

In this paper, we focus on a SW spectrum in ADL with modified rims (ADL-MR) based on $[Co/Pd]_8$ multilayers[36,38] as a function of the strength of an external magnetic field, which is perpendicular to the multilayer plane. We show that magnetic field variation affects bulk- and rim-localized modes in different ways, thereby creating good conditions for bulk and edge mode hybridization. We explain the nature of the bulk–rim interactions resulting in magnon–magnon coupling and formulate conditions for its existence. This discovery unlocks possibilities for hybridizing different modes in ADL, exploring new collective SW phenomena, and advancing practical applications of magnonics.

The structure of the paper is as follows: The next section introduces the system and micromagnetic model utilized in the simulations. Following that, in the Results section, we present the hysteresis of the system, the SW modes in dependence on the magnetic field, the bulk–rim static coupling at low frequencies and the

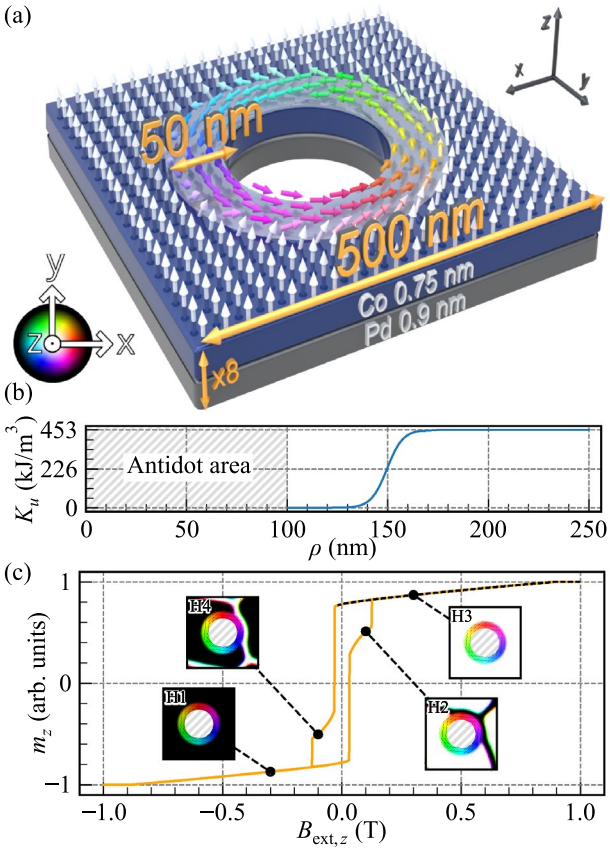

Figure 1. (**a**) Schematic illustration of the investigated structure showing the Co/Pd unit cell of the ADL-MR. Note that the figure is not to scale. The light gray area around the hole represents the rim with the reduced PMA. The arrows roughly indicate the orientation of the magnetization for $B_{\mathrm{ext},z} = 0$ T. (**b**) Variation of the PMA constant along the radial direction, starting at the center of the antidot. (**c**) Hysteresis loop along the z-axis. The dashed black line marks the regime where the demagnetization process is reversible, and within which the SW spectra are calculated. In the insets, the static magnetization configuration at selected field values is illustrated. The non-magnetic areas are hatched in gray. (**a**) and (**c**) The hue represents the in-plane orientation of the magnetization, while the brightness indicates the out-of-plane value, with black being fully down and white fully up.

magnon–magnon coupling between second-order radial rim modes and the bulk modes. Finally, we summarize the findings.

Structure and methodology

We are investigating a multilayered $[Co/Pd]_8$ sample containing a square lattice of antidots with a 200 nm diameter, oriented on the *xy*-plane with a lattice constant of 500 nm. The magnetic structure is defined with an effective-medium approach, where the 8 repetitions of the Co/Pd bilayer stack, consisting of Co (0.75 nm) and Pd (0.9 nm) layers are simulated as a single 13.2 nm-thick layer of Co with effective material parameters[39], according to the approach described in Ref.[40]. We used the following parameters[36]: PMA constant $K_{u,bulk} = 4.5 \times 10^5\,\mathrm{J/m^3}$, saturation magnetization $M_S = 0.81 \times 10^6\,\mathrm{A/m}$, exchange constant $A_{ex} = 1.3 \times 10^{-11}\,\mathrm{J/m}$. In most simulations, we used a low damping constant $\alpha = 1 \times 10^{-7}$ to get a sharp SW spectrum.

We discretized the system with 256 cuboids along the *x*- and *y*-axes in the square-lattice unit cell shown in Fig. 1a, each cuboid being $1.94 \times 1.94 \times 13.2\,\mathrm{nm^3}$ for a total of $500 \times 500 \times 13.2\,\mathrm{nm^3}$. We also tested with up to 8 cells across the thickness and the results were largely the same in the considered frequency range, with the mode frequency difference not exceeding 10%, but at a significant cost in simulation time. Therefore, for efficiency, we modeled only a single lattice unit cell, but with periodic boundary conditions (32 repetitions along the *x*- and *y*-directions) to recreate the square lattice, and with the single cell across the thickness.

We assume that each antidot is surrounded by a 50 nm-wide rim, wherein the PMA constant reduces to zero at the antidot edge. A hyperbolic tangent function is utilized to model the transition of the PMA value from the bulk value to 0:

$$K_u(\rho) = \left(\frac{1}{2}\tanh\left(\frac{\rho - \rho_{edge}}{8}\right) + \frac{1}{2}\right) K_{u,bulk}$$

for $\rho > 100$ nm, where ρ is a radial coordinate relative to the center of antidot, $\rho_{edge} = 150$ nm is the rim edge position, as plotted in Fig. 1b. This function serves as an approximate representation of the anisotropy-reduction profile that is likely to be encountered in experimental samples.

For micromagnetic simulations, we use own our version of Mumax3[41,42], called Amumax[43], which solves the Landau–Lifshitz–Gilbert equation:

$$\frac{d\mathbf{m}}{dt} = \frac{\gamma\mu_0}{1+\alpha^2}(\mathbf{m} \times \mathbf{H}_{eff} + \alpha\mathbf{m} \times (\mathbf{m} \times \mathbf{H}_{eff})), \tag{1}$$

where $\mathbf{m} = \mathbf{M}/M_S$ is the normalized magnetization, $\mathbf{H}_{eff}$ is the effective magnetic field acting on the magnetization, $\gamma = 187\,\mathrm{rad/(s \cdot T)}$ is the gyromagnetic ratio, μ_0 is the vacuum permeability. The following components were considered in the effective magnetic field $\mathbf{H}_{eff}$: demagnetizing field $\mathbf{H}_d$, exchange field $\mathbf{H}_{exch}$, uniaxial magnetic anisotropy field $\mathbf{H}_{anis}$, and external magnetic field $\mathbf{H}_{ext}$. Thermal effects were neglected. Thus, the effective field is expressed as:

$$\mathbf{H}_{eff} = \mathbf{H}_d + \mathbf{H}_{exch} + \mathbf{H}_{ext} + \mathbf{H}_{anis} + \mathbf{h}_{mf}, \tag{2}$$

where the last term, $\mathbf{h}_{mf}$ is a microwave magnetic field used for SW excitation. The exchange and anisotropy fields are defined as

$$\mathbf{H}_{exch} = \frac{2A_{ex}}{\mu_0 M_S}\Delta\mathbf{m}, \quad \mathbf{H}_{anis} = \frac{2K_{u,bulk}}{\mu_0 M_S} m_z \hat{\mathbf{z}}, \tag{3}$$

where A_{ex} is the exchange constant.

During the simulations, we first relax the magnetization in the system until we reach the ground state. We then excite the SWs with a global microwave magnetic field along the *x*-axis, uniform in space, with a *sinc* temporal profile, a cut-off frequency of 20 GHz, and a peak amplitude of 5×10^{-4} T. The excitation field is applied for 1 ns, and we sample the magnetization dynamics at intervals of 16.66 ps over a period of 100 ns.

To acquire the SW spectrum, we took the space- and time-resolved in-plane magnetization and applied a Hanning window along the time axis. We then computed the real discrete Fourier transform using the fast Fourier transform (FFT) algorithm along the time axis for each cuboid composing the system. After this process, for every discrete frequency, we pinpointed the cell exhibiting the maximum amplitude. This step was repeated iteratively for each frequency to progressively construct the spectrum. By selecting the highest amplitude rather than the average, the strongly-localized mode is emphasized over the modes that are spread over a wide area, such as the bulk modes. This procedure is applied to each simulation, where the external magnetic field value varies. The SW spectral response (Figs. 2, 3, 4, and 5) in dependence on the external magnetic field directed along the *z*-axis were calculated for values from 1 T to −0.014 T in decrements of 2 mT. To prevent numerical artifacts arising from a super-symmetry of the spins, we angle the external field by 0.0001 degrees from the *z*-axis. To generate the mode visualizations, we separately took each cuboid making up the system and we calculated the FFT of the in-plane magnetization over time. Then, for a selected frequency, we map the modulus of the complex number to a saturation value between 0 and 1 and the argument of the complex number to a hue where it is red if the argument is 0. This process is repeated for each cuboid in the system.

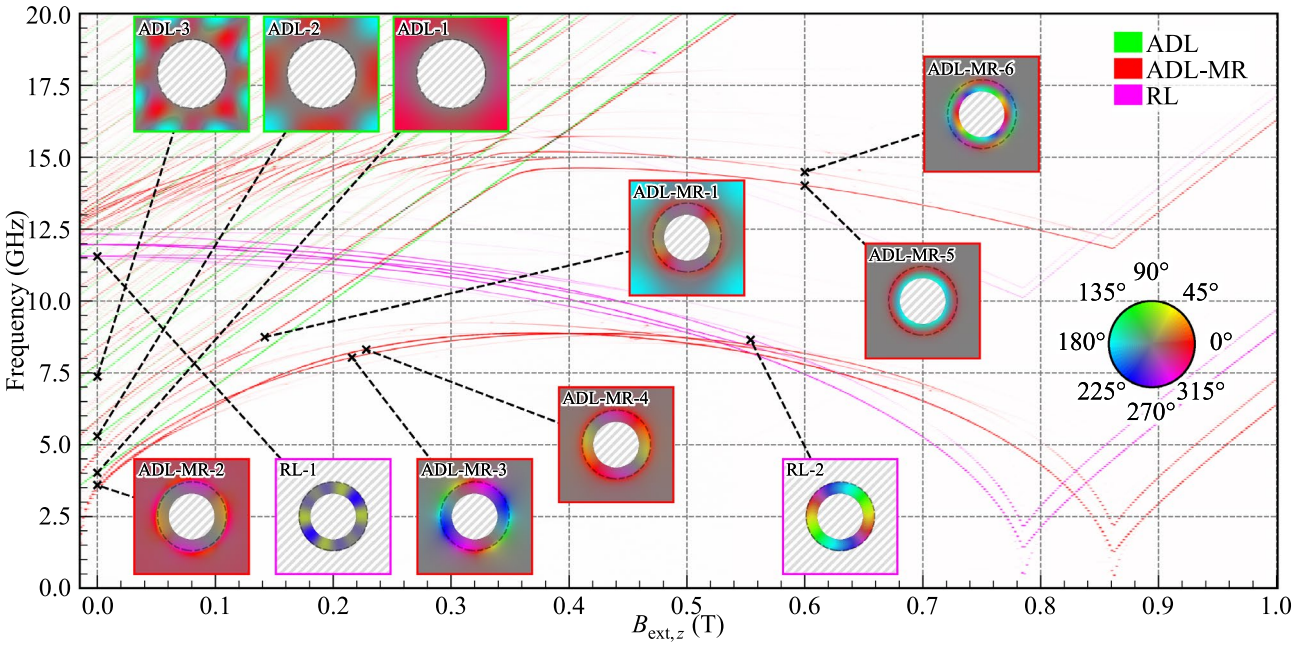

Figure 2. Evolution of the SW resonance spectra for the RL, ADL, and ADL-MR in dependence on the external out-of-plane magnetic field. The line intensity correlates with the SW amplitude. In the insets, the hue represents the phase of the in-plane dynamic magnetization, while the saturation indicates its spatial amplitude. The circular dashed line represents the outer edge of the modified rim. The border color of each inset specifies the corresponding geometry. Non-magnetic areas are hatched in gray. A colorblind-accessible version of this figure is available in the supplementary material.

Results

Hysteresis

First, we study the change of the static magnetization configuration in ADL-MR with the magnetic field applied out of the plane. The hysteresis loop along this direction, changing the magnetic field intensity from $B_{\text{ext},z} = \mu_0 H_{\text{ext},z} = -1$ T to 1 T and back is shown in Fig. 1c. At the remanence, the bulk magnetization keeps an out-of-plane saturation, while in the rim area, it stabilizes into a vortex-like state. Upon switching the external magnetic field, domain walls emerge within the bulk starting at $B_{\text{ext},z} = \pm 0.014$ (see, states *H2* and *H4*). Consequently, at field $B_{\text{ext},z} = \pm 0.124$ T, the domain evolves to full saturation in the opposite direction (*H1* and *H3*). The rim magnetization reaches full saturation when the magnetic field intensity exceeds $B_{\text{ext},z} = 0.86$ T or falls below $B_{\text{ext},z} = -0.86$ T, resulting in an out-of-plane saturation. In the following section, we will examine the SW dynamics in the field range marked by the dashed line in Fig. 1c (i.e., between 1 and −0.014 T), which signifies the full saturation of the bulk. The static magnetization can be in a clockwise (CW) or counter-clockwise (CCW) vortex-like state in the rims. These two states are degenerated, therefore this chirality do not affect the frequencies of the azimuthal modes within the rims. For this reason, when not saturated out of the plane, the magnetization in the rims was chosen to be in the CCW vortex-like state in the rest of this paper.

SW modes in dependence on the magnetic field

Before examining the field dependence of SWs in ADL-MR, we analyze the spectra of two complementary subsystems: a square lattice of rings (RL) with a width of 50 nm but without PMA, plotted in purple in Fig. 2; and a simplified ADL utilizing PMA but without rims, with an antidot diameter of 300 nm plotted in green in Fig. 2 and marked as ADL. The other geometric and material parameters for subsystems remain the same as in ADL-MR. The spatial amplitude distribution of the SW modes is presented in insets adjacent to the spectra. The color of each inset's boundary and label indicates its affiliation with a specific system. Colorblind-accessible visualizations of the ADL, RL and ADL-MR spectra are provided in the supplementary material in Fig. S1, S3, and S2 respectively and a detailed visualization of all the modes from Fig. 2 are displayed in Fig. S7. At remanence in the ADL system, we found the fundamental mode *ADL-1* (the mode numbering refers to the order of modes appearing in the discussion) at $f = 4.02$ GHz and a multitude of higher-order bulk modes, such as *ADL-2* and *ADL-3*, at $f = 5.29$ and 7.37 GHz, respectively. The system is characterized by a standard linear relationship between the SW frequency and the external field[35]. Therefore, as the field increases, no interaction between the modes is observed.

In the RL system with a CCW vortex-like magnetization texture, all the modes have an azimuthal component. At $B_{\text{ext},z} = 0$ T, the three modes of lowest frequency are at $f = 11.55$ (*RL-1*), 11.94 and 12.32 GHz, and correspond to the 3rd, 1st, and 5th order azimuthal modes, respectively. These modes are standing modes resulting from the degeneration of CW and CCW azimuthal modes of the same order. A non-zero value of the magnetic field leads to the splitting of this degeneration[44] and a monotonous decrease in the frequency of the modes with increasing magnetic field, until the magnetization saturates out of plane for 0.78 T. The second-order radial modes

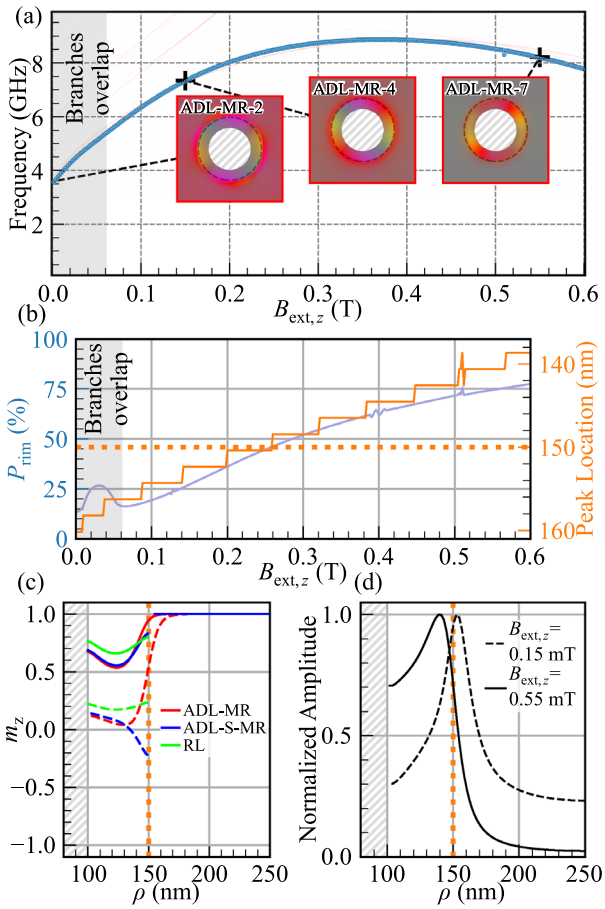

Figure 3. (**a**) Evolution of the SW resonance spectra for the ADL-MR in dependence on the external out-of-plane magnetic field. The line intensity correlates with the SW amplitude. The branch highlighted in blue corresponds to the first-order CW azimuthal mode considered in (**b**) and (**d**). The static configuration shown in (**c**) and the modes in (**d**) are marked by black crosses. (**b**) Rim/bulk mode intensity ratio (in blue) and peak maximum location (in orange) in dependence on the external out-of-plane magnetic field. The light gray areas in (**a**) and (**b**) represent the magnetic field values where the first- and fourth-order azimuthal branches overlap. (**c**) Profile of the out-of-plane static magnetization for $B_{ext,z} = 0.150$ T (dashed lines) and $B_{ext,z} = 0.550$ T (solid lines) for 3 systems (ADL-MR, ADL-S-MR and RL). (**d**) Amplitude profile of the marked modes from (a). The dotted orange line indicates the boundary between the rim and the bulk.

start at around 17.5 GHz at remanence and decrease frequency to 10 GHz at the magnetization reorientation field. All SWs increase in frequency as the magnetic field continues to increase above 0.78 T.

The SW spectrum as a function of the external magnetic field for ADL-MR is plotted in red in Fig. 2. By comparison with the spectra of ADL and RL, we can distinguish two main groups of branches that are related to: (i) the bulk modes that are similar to those in the ADL system, and exhibit a linear frequency increase trend with an increasing magnetic field (compare the branches *ADL-MR-1* and *ADL-1*); (ii) rim modes, like *ADL-MR-2*, *ADL-MR-3*, and *ADL-MR-4*, which exhibit a non-monotonic frequency response to changes in the applied magnetic field. Rim modes are similar to those in the RL system at large fields, $B_{ext,z} \gtrsim 0.4$ T (e.g., *ADL-MR-2* is analogous to *RL-2*). Here, however, the degeneration of the CW and CCW azimuthal modes is broken even for $B_{ext,z} = 0$ T because of the dipolar field generated by the out-of-plane bulk magnetization. Beyond $B_{ext,z} = 0.4$ T, these branches decrease in frequency due to the SW-mode softening until they reach a phase transition at $B_{ext,z} = 0.862$ T. Subsequently, the frequency of these branches increases as the magnetic-field strength continues to increase.

Although the behavior of the two complementary systems, ADL and RL, merge in the ADL-MR system's spectra, some effects remain distinct to ADL-MR. Specifically, we can identify two frequency ranges where collective bulk–rim effects occur. The first range (i) spans low frequencies from 3 to 12.5 GHz, characterized by first-order radial modes in the rims, i.e., modes whose phase does not change sign along the radial direction in the rim (e.g., *ADL-MR-2*, *ADL-MR-3*, and *ADL-MR-4*). The second range (ii) 12.5-17.5 GHz is where the second-order radial modes are in the rim (e.g., *ADL-MR-5* and *ADL-MR-6*). In (i), the bulk modes dependence on $B_{ext,z}$ deviates from a straight-line relationship (see *ADL-MR-1*), and the branches of the rim modes (e.g., *ADL-MR-2* and *ADL-MR-3*) gain dependencies similar to the bulk modes at low field values, leading to a decrease in frequency as the magnetic field decreases starting at $B_{ext,z} \lesssim 0.4$ T. In turn, regarding the (ii) range, there are multiple points of intersection between the bulk and rim modes resulting in anti-crossings.

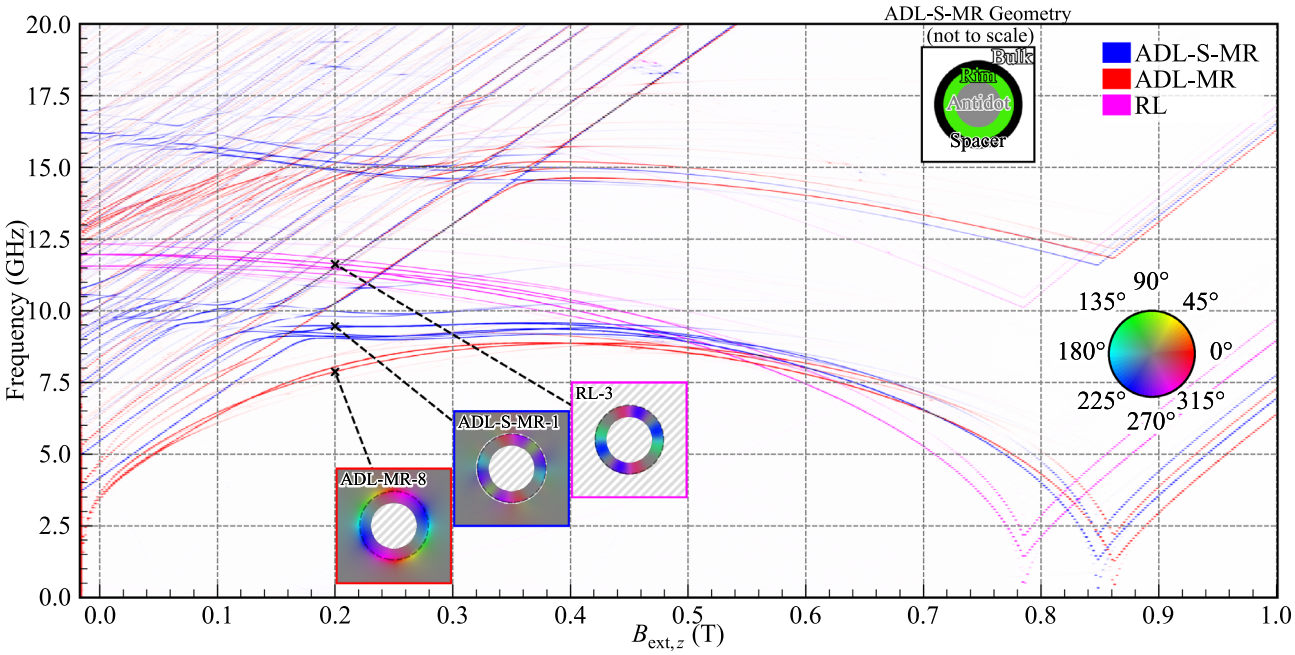

Figure 4. Evolution of the SW resonance spectra for the ADL-MR, ADL-S-MR, and RL in dependence on the external out-of-plane magnetic field. The line intensity correlates with the maximal SW amplitude. In the insets, the hue represents the phase of the in-plane dynamic magnetization, while the saturation indicates its spatial amplitude. The circular dashed line represents the outer edge of the modified rim. The border color of each inset specifies the corresponding geometry. Non-magnetic areas are hatched in gray. A colorblind-accessible version of this figure is available in the supplementary material.

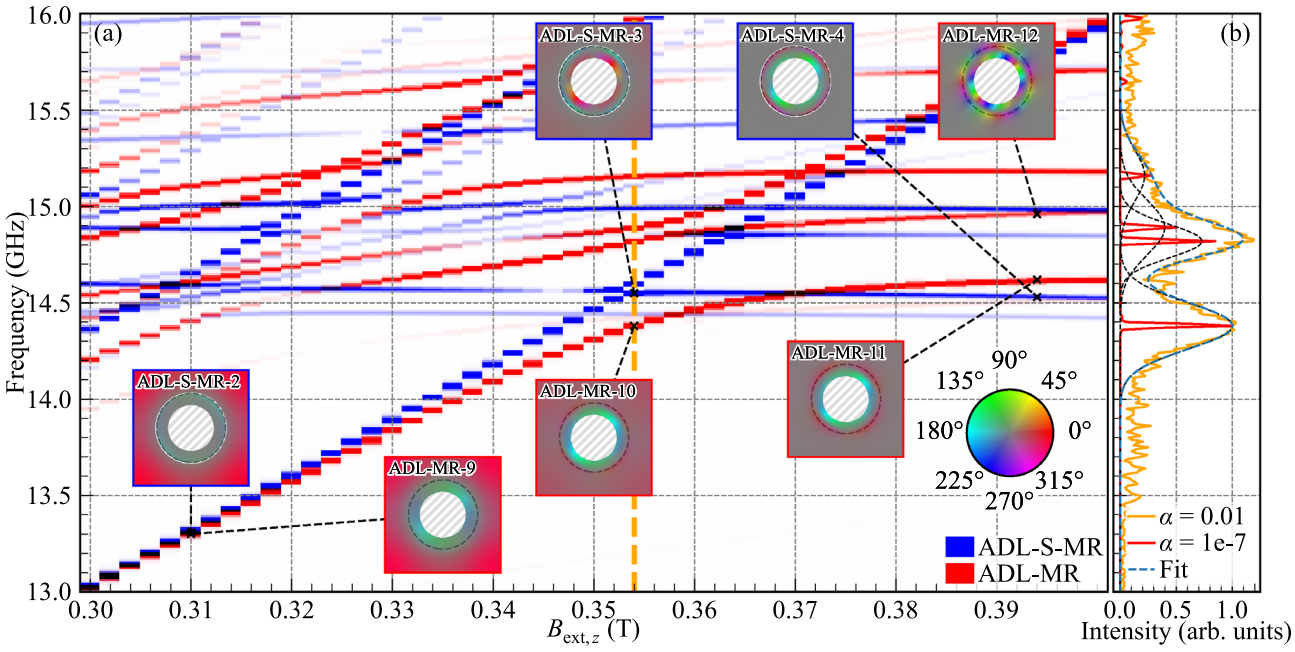

Figure 5. (**a**) A zoom-in part of Fig. 4, which shows the evolution of the SW resonance spectra for the ADL-MR and ADL-S-MR in dependence on the external out-of-plane magnetic field at a higher-frequency range. The vertical dashed orange line indicates the value for which (**b**) was plotted. The line intensity correlates with the SW amplitude. In the insets, the hue represents the phase of the in-plane dynamic magnetization, while the saturation indicates its spatial amplitude. The circular dashed line represents the outer edge of the modified rim. The border color of each inset specifies the corresponding geometry. Non-magnetic areas are hatched in gray. (b) Ferromagnetic resonance spectra of ADL-MR for $B_{ext,z}$ = 0.354 T with low damping in red and realistic damping ($\alpha = 0.01$) in orange. The dashed lines are Gaussian fits of the peaks with frequencies 14.38, 14.82, 14.89, and 15.16 GHz. A colorblind-accessible version of this figure is available in the supplementary materials.

The aforementioned effects of ADL-MR indicate a magnetic coupling between bulk and rim, which is the focus of this paper. However, these effects are influenced by several factors: the gradual change of the magnetization orientation within the rims from an in-plane to an out-of-plane configuration with $B_{\mathrm{ext},z}$ change (see the hysteresis loop in Fig. 1a), the change of the magnetization gradient between rim and bulk, the static stray magnetic field of the bulk area on the rim, and finally the dynamical coupling between bulk and rim SW modes. In the next two sections, the effects found in the ADL-MR are discussed separately for the first- and second-order radial rim modes, i.e., at low (3-12.5 GHz) and high (12.5-17.5 GHz) frequency ranges.

Bulk–rim coupling at low frequencies: first-order radial modes

Our results have shown that the frequencies of the first-order radial modes in the rim are significantly influenced by the interaction with the bulk part of the ADL-MR. The effects of this interaction are also visible in the azimuthal mode profiles shown in Fig. 2, *ADL-MR-2, 3, 4*. They show the transition of the mode localization, where at low magnetic field amplitudes, the mode is predominantly located in the bulk (*ADL-MR-2*) and then gradually shifts its position towards the edge region (*ADL-MR-4*). To explain this bulk–rim coupling, our subsequent analysis will focus on the first-order CW azimuthal mode (i.e., the mode where the m_z component undergoes a phase change of 2π along the path encircling the rim, as illustrated in Figs. S7–S10 in the supplementary material). This mode is highlighted in blue in Fig. 3a, where profiles at three selected values of $B_{\mathrm{ext},z}$, namely *ADL-MR-2*, *ADL-MR-4*, and *ADL-MR-7*, are also depicted. A detailed visualization of all the modes from Fig. 3a are displayed in Fig. S8 in the supplementary material.

We evaluate the spatial distribution of this mode's amplitude, particularly its concentration in bulk or rim. To quantify the extent of concentration, we define the parameter $P_{\mathrm{rim}} = A_{\mathrm{rim}}/A_{\mathrm{unit}}$, where A_{rim} and A_{unit} denote the integrated amplitude profiles within the rim and the unit cell defined as $A_{\mathrm{rim}} = \int_{100}^{150}\int_{0}^{2\pi} \mathrm{FFT}(\mathbf{m}(\rho))^2\, d\rho d\phi$ and $A_{\mathrm{unit}} = \int_{0}^{500}\int_{0}^{500} \mathrm{FFT}(\mathbf{m}(x,y))^2\, dxdy$ with the integration over the surface of the rim and the surface of the unit cell excluding the antidot, respectively. P_{rim} as a function of $B_{\mathrm{ext},z}$ is visualized in blue in Fig. 3b. A P_{rim} value of 0 and 100% indicates that the mode is entirely concentrated within the bulk and the rim, respectively. At the remanence, the mode concentrates predominantly in the bulk as $P_{\mathrm{rim}} = 14\%$, the intensity is equally distributed between the rim and the bulk at 0.282 T, and, at higher fields, this mode is predominantly concentrated in the rim. The peak around $B_{\mathrm{ext},z} = 0.03$ T, which breaks the monotonic dependence of $P(B_{\mathrm{ext},z})$, corresponds to the first- and fourth-order CW azimuthal branches overlapping in this frequency range, which makes the P_{rim} parameter extracted from the simulations (i.e., from profiles of the degenerate modes) inaccurate in this region.

We also quantify the shift of the amplitude maximum of this mode as a function of $B_{\mathrm{ext},z}$, as shown in orange in Fig. 3b. Starting at 160 nm at remanence, i.e., in the bulk of the ADL-MR, the position of the peak moves towards the rim as the magnetic field increases. It reaches the rim edge (150 nm) at 0.2 T and moves into the rim region at higher fields. Confirmation of this behavior is shown in Fig. 3d, which shows the normalized amplitude profiles of the mode, marked by black crosses in Fig. 3a, at $B_{\mathrm{ext},z}$ values of 0.15 and 0.55 T. As $B_{\mathrm{ext},z}$ is increased, not only does the amplitude maximum of the mode move to the rim, but the profile undergoes a transformation, becoming less localized in the domain wall and exhibiting a flattened distribution within the rim region. The radial cross-section of the m_z component of the static magnetization, starting from the antidot edge ($\rho = 100$ nm), is presented for the ADL-MR and the RL configurations in Fig. 3c. The dependencies are depicted for two distinct external field strengths, $B_{\mathrm{ext},z} = 0.15$ T (dashed lines) and $B_{\mathrm{ext},z} = 0.55$ T (solid lines). Notably, the RL configuration exhibits a larger out-of-plane magnetization component compared to the other structures, attributable to the absence of a static stray magnetic field from the bulk of the ADL. In addition, the magnetization gradient of the out-of-plane component, between the bulk and the rim, shifts toward the rim region with increasing $B_{\mathrm{ext},z}$, while the gradient strength decreases due to the decreasing difference between the out-of-plane magnetization component in the rim and the bulk. The position of the mode-intensity maximum follows the position of the largest magnetization gradient. It is because the gradient of m_z (a domain wall) softens the stiffness of the magnetization, allowing for SWs of high amplitude.

The consequence of changing the magnetization texture at small $B_{\mathrm{ext},z}$, apart from the change in the location and concentration of the azimuthal modes, discussed above (see also Fig. 3b–d), is a significant frequency reduction compared to the RL reference system. Mode softening is an effect characteristic of systems with magnetization gradients such as domain walls, vortices, and skyrmions[45]. In such regions, the effective field and energy are reduced (due to compensation of the exchange and anisotropy contributions) so that the magnetic moment requires less energy to precess.

To further pinpoint the origins of the observed bulk–rim interactions shown in Figs. 2 and 3, we conducted simulations of the ADL-MR with a 5.82 nm-wide non-magnetic spacer between the rim and the bulk (ADL-S-MR), see the structure schema in the inset in Fig. 4. The SW spectrum in dependence on $B_{\mathrm{ext},z}$ is depicted in blue in Fig. 4. Colorblind-accessible visualizations of the ADL-S-MR, RL, and ADL-MR spectra are provided in Figs. S4, S3, and S2, respectively, and detailed visualization of all the modes from Fig. 4 is displayed in Fig. S9 in the supplementary material. This approach effectively nullifies the exchange interaction between the rim and the bulk, thereby isolating the dipolar interaction as the only carrier of the bulk–rim interactions. Consequently, the introduction of this spacer eliminates the large magnetization gradient that existed between the bulk and the rim in ADL-MR (see Fig. 3c). Nevertheless, the magnetic configuration inside the rim is different from that of the RL. This is due to the stray field from the bulk of the ADL in the case of ADL-S-MR.

Within the field range from $B_{\mathrm{ext},z} = 0$ to 0.5 T, the ADL-S-MR system exhibits higher frequencies relative to those in the ADL-MR system, and their field dependence resembles that of the RL system, although with lower frequencies. Interestingly, the azimuthal modes of the rim in the ADL-S-MR system are coupled with the bulk modes, as indicated by anti-crossings (see range 8.5-10.5 GHz in Fig. 4). Due to separated rim and bulk parts, this interaction is attributed to dipolar coupling. The large differences between the ADL and ADL-S-MR observed in

Fig. 4 indicate that the exchange interaction between the bulk and the rim in ADL-MR has a significant impact on the azimuthal modes of the rim. We select the first-order azimuthal CW modes at 0.2 T for the ADL-MR, ADL-S-MR, and RL systems, at 7.87, 9.46, and 11.63 GHz, respectively, to visualize their amplitude distribution, which is shown in Fig. 4 in the insets with labels *ADL-MR-8*, *ADL-S-MR-1* and *RL-3*, respectively. These modes and their CCW counterparts are the most intense and robust branches as they have a strong intensity even for higher fields and after saturation. Comparing *ADL-MR-8* with *ADL-S-MR-1*, we see higher SW amplitude in the bulk in ADL-MR system, which indicates that the exchange coupling between the rim and the bulk increases the dynamic coupling between the rim and bulk magnons.

The observations discussed above show that the presence of a static magnetization gradient, its evolution, and the reorientation of the magnetization in the rim with a change in the magnetic field intensity are the most important factors influencing the SW spectra, in particular, mode softening in ADL-MR at low frequencies and low magnetic fields. On top of this, there is a dynamical magnon–magnon coupling, which is clearly evidenced by the amplitude profiles of the predominantly bulk (*ADL-MR-1* and *ADL-MR-2*) and rim (*ADL-MR-4*) modes, which have properties of both the fundamental bulk mode and the first-order azimuthal CW mode (see Fig. 2 and S7 in the supplementary material). However, the overlap of the static magnetization deformation and the dynamical coupling change with the external magnetic field makes the estimation of the dynamical-coupling strength difficult.

Magnon–magnon coupling between second-order radial rim modes and the bulk modes

Let us now move on to analyzing the higher-frequency spectrum, where the interaction between the second-order radial rim modes and the bulk modes exists. The detailed spectra are shown in Fig. 5, which is a zoom-in part of Fig. 4. Colorblind-accessible visualizations of the zoomed-in ADL-MR and ADL-S-MR spectra are provided in Figs. S5 and S6 respectively and a detailed visualization of all the modes from Fig. 5a are displayed in Fig. S10 in the supplementary material. Here, the horizontal branches are related to the azimuthal SW modes concentrated in the rim, which have a π phase change along the radial direction (see the insets and figures in the supplementary material), while the lines with a non-zero slope originate from the bulk modes of the ADL. Comparing the spectra of ADL-MR (in red) with the ADL-S-MR (in blue), it is evident that the ADL-MR exhibits a number of hybridizations between selected bulk modes and second-order radial rim modes, as evidenced by large anti-crossing gaps between the branches, and a strong deviation from the linear dependencies $f(B_{\mathrm{ext},z})$. Conversely, the ADL-S-MR system demonstrates crossings with only tiny gaps, especially between fundamental bulk mode (blue line along the diagonal of the plot in Fig. 5) and second-order radial rim modes, as indicated by vertical orange line at $B_{\mathrm{ext},z} = 0.354$ T. Considering that the only difference between ADL-MR and ADL-S-MR systems is the break of the exchange interaction between the rim and the bulk of the ADL in the latter, we can conclude that the exchange interaction is responsible for the strong magnon–magnon coupling observed in the former system. Nevertheless, it is still the hybrid coupling in ADL-MR, involving dynamical magnon–magnon coupling, dominating in this range of fields and frequencies but modified by the magnetization texture with a change of $B_{\mathrm{ext},z}$.

We aim to understand why some rim and bulk modes show large anticrossing and some do not in ADL-MR. To find the matching condition, we compare the *ADL-MR-9/10/11* modes shown in Fig. 5a, which correspond to the bulk mode, bulk+rim mode, and rim mode, respectively. From there, we can see the smooth transition of the amplitude of the mode as we increase the field. From *ADL-MR-9* to *ADL-MR-10*, we see the bulk part of the mode which is first outside of the rim for $B_{\mathrm{ext},z} = 0.31$ T to partly inside the rim for $B_{\mathrm{ext},z} = 0.354$ T while the rim amplitude increases. The azimuthal homogeneous nature of the outer ring of the rim mode can still be found at $B_{\mathrm{ext},z} = 0.394$ T for *ADL-MR-11* while the amplitude in the bulk is close to null. In comparison, *ADL-MR-12* has a second-order quantization in the azimuthal direction and we observe the crossing of its branch and a fundamental bulk mode at $B_{\mathrm{ext},z} = 0.37$ T for $f = 15.16$ GHz. A deeper analysis of the mode profiles indicates the capability of coupling between rim and bulk modes if the number of azimuthal order of these modes is the same after modulo 4 operation. Such a nature of coupling is strictly connected with the fact that the symmetry of bulk modes is governed by the fourfold symmetry of the square lattice.

As mentioned above, for ADL-S-MR we find a much reduced anti-crossing gap of 50 MHz for $B_{\mathrm{ext},z} = 0.352$ T compared to 380 MHz for ADL-MR. Similarly, as for ADL-MR, we can look at the evolution of the mode profile as we increase the field. The modes *ADL-MR-9/10/11* are taken to be analogous to *ADL-S-MR-2/3/4* for the same branches and the same fields. Removing the exchange interaction between the rim and the bulk had an effect on the expansion of the bulk mode into the rim area, which is not present in the middle of the hybridization on *ADL-S-MR-3* as it is for *ADL-MR-10*. We can then confirm that the exchange interaction is responsible for this particular hybridization.

In Fig. 5b showing the ferromagnetic-resonance spectrum at 0.354 T, we demonstrate that the hybridization under consideration in the ADL-MR system is still visible when using a realistic damping value of $\alpha = 0.01$[36], which is close to the experimental value for Co/Pd multilayers. We fitted the resonant modes of frequencies $f = 14.38, 14.82, 14.89$ and 15.16 GHz with the four Gaussian curves. Based on this, we estimate the cooperativity of the bulk magnon–rim magnon coupling between $f_{\mathrm{high}} = 14.82$ GHz and $f_{\mathrm{low}} = 14.38$ GHz. The strength of the coupling, g, is defined as half of the minimal peak-to-peak frequency spacing in the anti-crossing, it is $g = 220$ MHz at 0.354 T. The half width at half maximum for both peaks is $\kappa_{f_{\mathrm{low}}} = 120$ MHz and $\kappa_{f_{\mathrm{high}}} = 86$ MHz. Using these values, we calculate the cooperativity

$$C = \frac{g^2}{\kappa_{f_{\mathrm{low}}} \times \kappa_{f_{\mathrm{high}}}} = 4.698.$$

Even though the system was not optimized for it, this value of the cooperativity indicates a strong magnon–magnon coupling in the ADL-MR between the second-order radial, first-order azimuthal rim mode and the fundamental bulk ADL mode.

We can compare this cooperativity with the values given for various systems presented in the literature. For instance, Chen et al.[29] report $C = 0.38$ and $C = 21$ in ferromagnetic metallic nanowires magnetized in parallel or antiparallel order, respectively, which are forming an array deposited on YIG film. In the single planar ferromagnetic nanoelement with optimized ends, Dai et al.[33] achieved $C = 60.1$ for the hybridization between the bulk and the edge SW modes. Adhikari et al.[46] reports the coupling between magnons in $Ni_{80}Fe_{20}$ nanocross with cooperativity $C = 0.28$, which can be enhanced to 2.5 by making a hole in the nanocross[47]. Synthetic antiferromagnets are also considered for exploitation of the magnon–magnon coupling. Here, the coupling strength depends directly on the RKKY interaction strength between the ferromagnetic layers (controlled by the thickness of the non-magnetic interlayer) but also on the external magnetic field, which changes the relative orientation of the magnetizations in the layers. Depending on materials used, the reported values are $C = 25.0$[48], $C = 5.26$ [49] or $C = 8.4$[50]. Just recently, Dion et al.[51] achieved probably the largest magnon-magnon cooperativity so far $C = 126.4$ in finite-size magnetostatically-coupled ferromagnetic bilayers, thus combining inter-element coupling and the finite size to enhance the coupling between magnons in both layers. In the context presented, the coupling between rim and bulk modes in the ADL-MR system based on PMA material, as demonstrated above, explores a new type of rather strong dynamic coupling between planar regions of non-collinear magnetization, which is mainly mediated by exchange interactions and turns on a higher-order azimuthal mode. The influence of the lattice type, as indicated by the hybridization selection rules, suggests a possibility for further optimization of the coupling strength, not only by changing the material but also by changing the geometry of the ADL.

Conclusions

Using micromagnetic simulations, we study the SW dynamics in a PMA thin film magnonic crystal consisting of antidots with rims around the antidot edges with in-plane magnetization (ADL-MR) as a function of the out-of-plane magnetic field strength. Through comparative studies with its complementary subsystems, i.e. pure ADL and the rim lattice, we have shown that the interactions between the subsystems significantly modify the spectrum of the collective SWs and its dependence on the magnetic field. The study reveals SW hybridizations between different waves concentrated in the rim and the bulk, which depend on the mode type and the out-of-plane magnetic field strength and are additionally modified by the associated changes in the magnetization state at the interface between the subsystems.

We show that in our system a strong magnon–magnon coupling between the fundamental bulk mode and the second-order radial azimuthal mode is present. It is characterized by a cooperativity of $C = 4.698$, which is competitive compared to the other magnon–magnon couplings reported so far in the literature. We show that this coupling is mainly determined by the exchange interactions between the bulk and the rim, which are mediated by the domain wall. In addition, it is influenced by the lattice type, which in combination with the lattice and material parameters opens a wide field for further optimization and exploitation of the collective hybrid dynamics in such systems. Thus, the demonstrated properties are pivotal for the development of magnonic applications and devices, including hybrid and quantum magnonics.

Data availability

The simulations input files and post processing code are available publicly at https://doi.org/10.5281/zenodo.10531882.

Received: 12 February 2024; Accepted: 3 May 2024
Published online: 20 May 2024

References

1. Gulyaev, Y. V. & Nikitov, S. A. Magnonic crystals and spin waves in periodic structures. *Dokl. Phys.* **46**, 687 (2001).
2. Puszkarski, H. & Krawczyk, M. Magnonic crystals-the magnetic counterpart of photonic crystals. *Solid State Phenom.* **94**, 125 (2003).
3. Lenk, B., Ulrichs, H., Garbs, F. & Münzenberg, M. The building blocks of magnonics. *Phys. Rep.* **507**, 107–136. https://doi.org/10.1016/j.physrep.2011.06.003 (2011).
4. Krawczyk, M. & Grundler, D. Review and prospects of magnonic crystals and devices with reprogrammable band structure. *J. Phys. Condens. Matter* **26**, 123202 (2014).
5. Nikitov, S. A. *et al.* Magnonics: A new research area in spintronics and spin wave electronics. *Phys. Uspekhi* **58**, 1002 (2015).
6. Rychły, J. *et al.* Magnonic crystals-prospective structures for shaping spin waves in nanoscale. *Low Temp. Phys.* **41**, 745–759. https://doi.org/10.1063/1.4932348 (2015).
7. Chumak, A. V., Serga, A. A. & Hillebrands, B. Magnonic crystals for data processing. *J. Phys. D Appl. Phys.* **50**, 244001. https://doi.org/10.1088/1361-6463/AA6A65 (2017).
8. Joannopoulos, J., Johnson, S. G., Winn, J. N. & Meade, R. D. *Photonic Crystals: Molding the Flow of Light* (Princeton University Press, 2008).
9. Tacchi, S. *et al.* Forbidden band gaps in the spin-wave spectrum of a two-dimensional bicomponent magnonic crystal. *Phys. Rev. Lett.* **109**, 137202. https://doi.org/10.1103/PhysRevLett.109.137202 (2012).
10. Kruglyak, V. V. *et al.* Imaging collective magnonic modes in 2D arrays of magnetic nanoelements. *Phys. Rev. Lett.* **104**, 027201. https://doi.org/10.1103/PhysRevLett.104.027201 (2010).
11. Tacchi, S. *et al.* Band diagram of spin waves in a two-dimensional magnonic crystal. *Phys. Rev. Lett.* **107**, 127204. https://doi.org/10.1103/PhysRevLett.107.127204 (2011).
12. Saha, S. *et al.* Tunable magnonic spectra in two-dimensional magnonic crystals with variable lattice symmetry. *Adv. Funct. Mater.* **23**, 2378–2386. https://doi.org/10.1002/adfm.201202545 (2013).
13. Kostylev, M. *et al.* Propagating volume and localized spin wave modes on a lattice of circular magnetic antidots. *J. Appl. Phys.* **103**, 07C507. https://doi.org/10.1063/1.2831792 (2008).

14. Mandal, R. *et al.* Effects of antidot shape on the spin wave spectra of two-dimensional Ni80Fe20 antidot lattices. *Appl. Phys. Lett.* **103**, 262410. https://doi.org/10.1063/1.4860959 (2013).
15. Martin, J., Nogués, J., Liu, K., Vicent, J. & Schuller, I. K. Ordered magnetic nanostructures: Fabrication and properties. *J. Magn. Magn. Mater.* **256**, 449–501. https://doi.org/10.1016/S0304-8853(02)00898-3 (2003).
16. Lau, J. W. & Shaw, J. M. Magnetic nanostructures for advanced technologies: Fabrication, metrology and challenges. *J. Phys. D Appl. Phys.* **44**, 303001. https://doi.org/10.1088/0022-3727/44/30/303001 (2011).
17. Carter, R. L., Owens, J. M., Smith, C. V. & Reed, K. W. Ion-implanted magnetostatic wave reflective array filters. *J. Appl. Phys.* **53**, 2655–2657. https://doi.org/10.1063/1.330928 (1982).
18. Urbánek, M. *et al.* Research Update: Focused ion beam direct writing of magnetic patterns with controlled structural and magnetic properties. *APL Mater.* **6**, 060701. https://doi.org/10.1063/1.5029367 (2018).
19. Fassbender, J. *et al.* Introducing artificial length scales to tailor magnetic properties. *New J. Phys.* **11**, 125002. https://doi.org/10.1088/1367-2630/11/12/125002 (2009).
20. Obry, B. *et al.* A micro-structured ion-implanted magnonic crystal. *Appl. Phys. Lett.* **102**, 202403. https://doi.org/10.1063/1.4807721 (2013).
21. Wawro, A. *et al.* Magnetic properties of coupled Co/Mo/Co structures tailored by ion irradiation. *Phys. Rev. Appl.* **9**, 014029. https://doi.org/10.1103/PhysRevApplied.9.014029 (2018).
22. Yu, H., Xiao, J. & Schultheiss, H. Magnetic texture based magnonics. *Phys. Rep.* **905**, 1–59. https://doi.org/10.1016/j.physrep.2020.12.004 (2021).
23. Banerjee, C. *et al.* Magnonic band structure in a Co/Pd stripe domain system investigated by Brillouin light scattering and micromagnetic simulations. *Phys. Rev. B* **96**, 024421. https://doi.org/10.1103/PHYSREVB.96.024421/FIGURES/3/MEDIUM (2017).
24. Szulc, K. *et al.* Reconfigurable magnonic crystals based on imprinted magnetization textures in hard and soft dipolar-coupled bilayers. *ACS Nano* **16**, 14168–14177. https://doi.org/10.1021/acsnano.2c04256 (2022).
25. Diáz, S. A., Hirosawa, T., Klinovaja, J. & Loss, D. Chiral magnonic edge states in ferromagnetic skyrmion crystals controlled by magnetic fields. *Phys. Rev. Res.* **2**, 013231. https://doi.org/10.1103/PHYSREVRESEARCH.2.013231 (2020).
26. Chen, Z. & Ma, F. Skyrmion based magnonic crystals. *J. Appl. Phys.* **130**, 090901. https://doi.org/10.1063/5.0061832 (2021).
27. Takagi, R. *et al.* Hybridized magnon modes in the quenched skyrmion crystal. *Phys. Rev. B* **104**, 144410. https://doi.org/10.1103/PHYSREVB.104.144410 (2021).
28. Bassotti, M., Silvani, R. & Carlotti, G. From the spin eigenmodes of isolated Néel skyrmions to the magnonic bands of skyrmionic crystals: a micromagnetic study as a function of the interfacial Dzyaloshinskii-Moriya interaction and the exchange constants. *IEEE Magn. Lett.* **13**, 6101505. https://doi.org/10.1109/LMAG.2021.3136152 (2022).
29. Chen, J. *et al.* Strong interlayer magnon-magnon coupling in magnetic metal-insulator hybrid nanostructures. *Phys. Rev. Lett.* **120**, 217202 (2018).
30. Sud, A. *et al.* Tunable magnon-magnon coupling in synthetic antiferromagnets. *Phys. Rev. B* **102**, 100403 (2020).
31. Shiota, Y., Taniguchi, T., Ishibashi, M., Moriyama, T. & Ono, T. Tunable magnon-magnon coupling mediated by dynamic dipolar interaction in synthetic antiferromagnets. *Phys. Rev. Lett.* **125**, 017203 (2020).
32. Li, Y. *et al.* Hybrid magnonics: Physics, circuits, and applications for coherent information processing. *J. Appl. Phys.* **128**, 130902 (2020).
33. Dai, C., Xie, K., Pan, Z. & Ma, F. Strong coupling between magnons confined in a single magnonic cavity. *J. Appl. Phys.* **127**, 203902 (2020).
34. Li, Z., Ma, M., Chen, Z., Xie, K. & Ma, F. Interaction between magnon and skyrmion: Toward quantum magnonics. *J. Appl. Phys.* **132**, 210702 (2022).
35. Pal, S. *et al.* Optically induced spin wave dynamics in $[Co/Pd]_8$ antidot lattices with perpendicular magnetic anisotropy. *Appl. Phys. Lett.* **105**, 162408. https://doi.org/10.1063/1.4898774 (2014).
36. Pan, S. *et al.* Edge localization of spin waves in antidot multilayers with perpendicular magnetic anisotropy. *Phys. Rev. B* **101**, 014403. https://doi.org/10.1103/PhysRevB.101.014403 (2020).
37. Mantion, S. & Biziere, N. Influence of Ga+ milling on the spin waves modes in a Co_2MnSi Heusler magnonic crystal. *J. Appl. Phys.* **131**, 113905. https://doi.org/10.1063/5.0085623 (2022).
38. Moalic, M., Krawczyk, M. & Zelent, M. Spin-wave spectra in antidot lattice with inhomogeneous perpendicular magnetic anisotropy. *J. Appl. Phys.* **132**, 213901 (2022).
39. Lemesh, I. & Beach, G. S. Twisted domain walls and skyrmions in perpendicularly magnetized multilayers. *Phys. Rev. B* **98**, 104402 (2018).
40. Woo, S. *et al.* Observation of room-temperature magnetic skyrmions and their current-driven dynamics in ultrathin metallic ferromagnets. *Nat. Mater.* **15**, 501–506. https://doi.org/10.1038/nmat4593 (2016).
41. Vansteenkiste, A. *et al.* The design and verification of MuMax3. *AIP Adv.* **4**, 107133. https://doi.org/10.1063/1.4899186 (2014).
42. Leliaert, J. *et al.* Fast micromagnetic simulations on GPU–recent advances made with mumax3. *J. Phys. D Appl. Phys.* **51**, 123002. https://doi.org/10.1088/1361-6463/aaab1c (2018).
43. Moalic, M. & Zelent, M. Mathieumoalic/amumax: 2023.10.26, https://doi.org/10.5281/zenodo.10043142 (2023).
44. Dugaev, V. K., Bruno, P., Canals, B. & Lacroix, C. Berry phase of magnons in textured ferromagnets. *Phys. Rev. B* **72**, 024456. https://doi.org/10.1103/PhysRevB.72.024456 (2005).
45. Varentcova, A. S. *et al.* Toward room-temperature nanoscale skyrmions in ultrathin films. *npj Computational Materials* **6**, 193 (2020).
46. Adhikari, K., Sahoo, S., Mondal, A. K., Otani, Y. & Barman, A. Large nonlinear ferromagnetic resonance shift and strong magnon-magnon coupling in $Ni_{80}Fe_{20}$ nanocross array. *Phys. Rev. B* **101**, 054406 (2020).
47. Adhikari, K., Choudhury, S., Barman, S., Otani, Y. & Barman, A. Observation of magnon-magnon coupling with high cooperativity in $Ni_{80}Fe_{20}$ cross-shaped nanoring array. *Nanotechnology* **32**, 395706 (2021).
48. Dai, C. & Ma, F. Strong magnon-magnon coupling in synthetic antiferromagnets. *Appl. Phys. Lett.* **118**, 112405 (2021).
49. Ma, K., Li, C., Hao, Z., Ong, C. & Chai, G. Strong magnon-magnon coupling between ferromagnetic resonances in $Co_{90}Zr_{10}$/Ta/$Fe_{20}Ni_{80}$ multilayers. *Phys. Rev. B* **108**, 094422 (2023).
50. Hayashi, D. *et al.* Observation of mode splitting by magnon-magnon coupling in synthetic antiferromagnets. *Appl. Phys. Express* **16**, 053004 (2023).
51. Dion, T. *et al.* Ultrastrong magnon-magnon coupling and chiral spin-texture control in a dipolar 3d multilayered artificial spin-vortex ice. *Nat. Commun.* **15**, 4077 (2024).

Acknowledgements

The research has received funding from the National Science Centre of Poland, Grant No. UMO-2020/37/B/ST3/03936 and 2023/49/N/ST3/03538. The simulations were partially performed at the Poznan Supercomputing and Networking Center (Grant No. 398).

Author contributions

M.M. ran the simulations, processed the data, prepared the figures, and drafted the manuscript. All authors wrote and reviewed the manuscript.

Competing interests

The authors declare no competing interests.

Additional information

Supplementary Information The online version contains supplementary material available at https://doi.org/10.1038/s41598-024-61246-5.

Correspondence and requests for materials should be addressed to M.M.

Reprints and permissions information is available at www.nature.com/reprints.

Publisher's note Springer Nature remains neutral with regard to jurisdictional claims in published maps and institutional affiliations.

4.3 Efficient generation of second-harmonic propagating spin waves in a thin, out-of-plane-magnetised ferromagnetic film

- *Efficient generation of second-harmonic propagating spin waves in a thin, out-of-plane-magnetised ferromagnetic film*,
  M. Moalic, Y. Patat, M. Zelent, M. Krawczyk.
  arXiv preprint, 2509.07705 (2025).

4.3.1 Introduction

This article aims to create a new scheme to generate compact, on-chip sources of exchange-dominated spin waves with sub-300 nm wavelengths. Building on the concept of anisotropy-engineered magnonic hybrids developed in the preceding publications in Section 4.1 and Section 4.2, the study introduces a lithographically simple architecture: a region with reduced anisotropy and strip with PMA in which a uniform microwave pump drives a localised fundamental mode that is up-converted to its second harmonic. Micromagnetic simulations reveal that the resulting $2f_0$ signal is emitted as a coherent, freely propagating spin wave in the adjacent Co/Pd strip, with the launching efficiency increasing with the pump amplitude. Two independent tuning knobs — the static bias field B_0 and the rim width w — enable continuous frequency control, while extension to a two-dimensional disk geometry demonstrates radial emission from a central antidot. Together, these results complement the earlier work on antidot lattices by providing a reconfigurable, frequency-doubling source that can be integrated into the magnonic circuits explored throughout the thesis. Potential applications include energy-efficient on-chip frequency doubling and short-wavelength spin-wave emitters for magnonic logic and RF signal processing, neuromorphic (artificial-neural-network) hardware, and integration with cavity–magnonic platforms for coherent microwave conversion and control.

4.3.1.1 Contribution of the Author

In this publication, I conducted all numerical simulations using the Amumax software, analysed the resulting data, prepared all the figures, prepared the first draft of the manuscript, contributed to the writing and critical review of the manuscript, and was responsible for compiling the supplementary materials. I also co-supervised the master student, Y. Pattat, in his work on the preliminary concept of using the PMA and rim system to generate spin waves. I was also responsible for submission, and contacts with the editor and editorial staff.

Efficient Generation of Second-Harmonic Propagating Spin Waves in a Thin, Out-of-Plane-Magnetized Ferromagnetic Film

Mathieu Moalic,* Youenn Patat, Mateusz Zelent, and Maciej Krawczyk

Institute of Spintronics and Quantum Information, Faculty of Physics and Astronomy, Adam Mickiewicz University, 61-614 Poznań, Poland

E-mail: matmoa@amu.edu.pl

Abstract

Spin waves are attractive information carriers owing to their gigahertz-to-terahertz frequencies, nanometric wavelengths, and negligible Joule heating. However, efficiently exciting short-wavelength, high-frequency spin waves and exploiting nonlinear effects remains challenging. We propose a hybrid ferromagnetic structure consisting of an in-plane-magnetized nanosized area (a magnonic nanocavity) that is exchange-coupled to an out-of-plane magnetized film or stripe. Micromagnetic simulations show that a spatially uniform out-of-plane microwave field only excites the fundamental mode of the nanocavity. Its second harmonic is then coherently and efficiently launched into the extended part of the ferromagnet, yielding propagating spin waves. This process can be achieved with stripe or extended film geometries, which excite plane waves or radial spin waves, respectively. Given the straightforward fabrication process, which involves degrading the anisotropy of a ferromagnetic layer with perpendicular magnetic anisotropy using an ion beam, it becomes possible to shape the spin-wave wavefront to a great extent by adjusting the nanocavity geometry. The conversion efficiency grows

nonlinearly with the pump amplitude and improves further when the frequency of a higher-order standing spin wave in the nanocavity matches the second-harmonic frequency. The emission frequency is tunable via the bias magnetic field or the width of the nanocavity. These findings suggest a compact route toward on-chip, short-wavelength, high-frequency nonlinear spin-wave sources for artificial neural networks.

Introduction

Although the first demonstration of microwave frequency doubling in ferrites dates back to the 1950s,[1] second-harmonic generation (SHG) and, more generally, multi-harmonic generation of spin waves (SWs) have advanced rapidly over the past decade. This progress is mainly due to their potential applications in magnonic neuromorphic computing,[2–5] because–as with any neural network, a nonlinear response to the pump amplitude is a crucial property.

It has been shown that edge SWs, which are confined by an inhomogeneous demagnetizing field,[6] and oscillations of a pinned domain wall,[7] can act as nonlinear emitters that radiate SWs at twice the drive frequency. Domain walls and related magnetic textures (e.g., vortices and skyrmions), in addition to serving as guides for short-wavelength magnons,[8,9] act as natural loci of broken symmetry that enhance frequency multiplication.[10] However, in most cases, the SWs generated in the SHG process remain confined to the magnetic textures.[9] More recently, dispersion- and symmetry-engineered nanowaveguides have enabled phase-matched, resonant SHG of propagating magnons.[11,12] The anisotropic dispersion relation of magnetostatic SWs[13] allows for SHG of SWs with positive[11] or negative[12] group velocities in the Damon–Eshbach configuration (magnetization perpendicular to the wave vector) and the backward-volume configuration (magnetization parallel to the wave vector), respectively. In parallel, hybrid quantum cavity–magnonic systems have shown that magnon nonlinearities support coherent harmonic generation and broadband microwave frequency conversion—with phase-preserving harmonics and multiwave mixing—highlighting opportunities for on-chip signal processing and quantum control.[14,15]

There are also many other methods for generating short SWs (i.e., sub-100 nm) using linear processes, which are desirable for analog and binary magnonic devices.[16] Existing strategies include (a) microwave nanostrip antennas,[17] (b) magnetic solitons such as domain walls and vortices,[18–20] (c) magnetostatic coupling from ferromagnetic stripes or nanocontacts,[21] (d) two-dimensional grating couplers,[22] and (e) internal-field engineering via lithographic modulation of demagnetizing fields.[23] Most of these approaches face trade-offs: they either operate at relatively low frequencies, require large DC currents, or impose stringent lithographic constraints. Even the recent demagnetizing-field–modulation technique in fully perpendicular films has reached wavelengths down to 200 nm only at modest frequencies and in carefully tailored geometries.[24] Harnessing nonlinear harmonic conversion may circumvent these limitations,[25] especially when implemented in a lithographically simple geometry.

Results and Discussion

We unveil a strategy to locally excite coherent, high-frequency, propagating SWs through SHG, driven by a simple, uniform, out-of-plane microwave field. The key idea lies in a hybrid nanostructure engineered to have two distinct magnetic regions: a nanosized "Excitation Region" (ER) with in-plane magnetization and an extended "Propagation Region" (PR) with perpendicular magnetic anisotropy (PMA). These regions are connected by a 90° domain wall. Importantly, these structures can be fabricated using a focused beam of Ga[26] or He[27,28] ions to degrade the anisotropy locally and form an ER in a thin PMA ferromagnetic film. We demonstrate that this effect exists in a 2D geometry, yielding radially propagating SWs from a centrally localized, in-plane-magnetized rim (Fig. 1), and in 1D geometries, resulting in the emission of plane waves (Fig. 2). This demonstrates flexibility in forming wave fronts of excited SWs, by simple changing the shape of the ER. A detailed analysis reveals that the in-plane–magnetized ER acts as a nonlinear nanocavity that up-converts the uniform drive at f_0 to $2f_0$, while the ER–PR interface efficiently couples out the resulting wave into

the PR. SHG is particularly effective when the width and bias magnetic field are tuned to match the formation of standing SWs in the nanocavity at $2f_0$. This provides a direct and simply route for the local nonlinear generation of technologically vital, high-frequency, short-wavelength magnons, especially promising for realization of magnonic artificial neural networks and quantum magnonics.

For this study, we selected a $[\mathrm{Co/Pd}]_8$ multilayered film of 13.2 nm thickness in which we introduced two distinct regions differing only in their PMA. The first region, ER, lacks uniaxial anisotropy and exhibits in-plane magnetization at remanence (see the green area in Fig. 1(a) and Fig. 2(a)). The second region, PR, exhibits sufficiently strong PMA to saturate the magnetization out of plane (see the blue area in Fig. 1(a) and Fig. 2(a)). The PMA profile is engineered to transition smoothly from zero to the bulk value over a 50 nm region; this profile is shown in Fig. 2(a) as the red dashed line (the same profile is applied radially in the 2D system).

A bias magnetic field B_0 was applied perpendicular to the film plane (along the z-axis) up to 0.6 T. Within this field range, the magnetization in the ER gradually cants away from the in-plane orientation, changing from 7.1° at $B_0 = 200$ mT to 36° at $B_0 = 600$ mT. The two regions are connected by an approximately 90° domain wall at remanence. The material parameters and the effective model used to simulate the multilayer are described in the Methods section.

To study SW dynamics, we applied a microwave magnetic field (b) oriented out of plane (along the z-axis). This induces a torque that acts only on the magnetization in the ER and the domain wall while leaving the PR unexcited. Simulations were conducted using Amumax,[29] our fork of MuMax3, to solve the Landau–Lifshitz–Gilbert equation. Details of the simulations are provided in the Methods section.

We started the simulations with the film shaped as a thin disk (radius 2.5 µm) containing a central antidot (hole) with a diameter of 80 nm, surrounded by a rim (an in-plane-magnetized ER of width $w = 40$ nm). A high-damping region with a width of 500 nm was included near

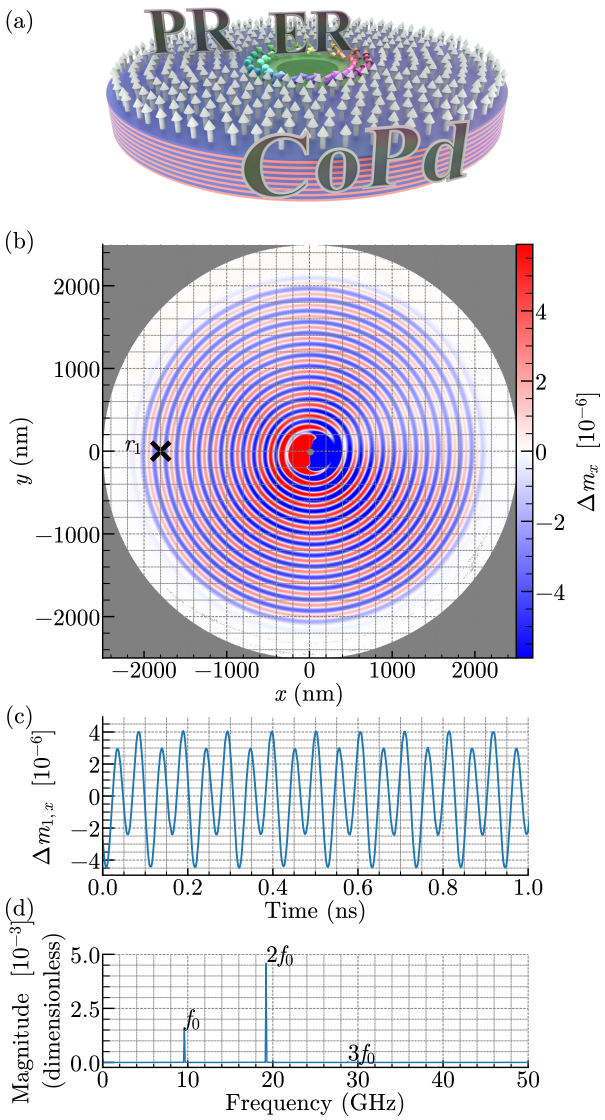

Figure 1: (a) Schematic illustration of the investigated structure showing a Co/Pd disk. Note that the figure is not to scale. The green area around the hole represents the ER with reduced PMA. The arrows indicate the orientation of the magnetization. (b) Snapshot of the two-dimensional simulation at steady state for an excitation frequency of $f = 8.60\,\mathrm{GHz}$. (c) Time evolution of the magnetization at point r_1, indicated in panel (b). (d) Discrete Fourier transform of the magnetization signal at r_1 over time.

the outer edge of the disk to suppress SW reflections.

Under an external magnetic field of $B_0 = 354\,\mathrm{mT}$, the lowest resonant mode in the PR appeared at 13.90 GHz. However, lower-frequency modes still existed within the ER. A sinc-type microwave field was first applied along the z-axis with cutoff frequency $f_{\mathrm{cut}} = 10\,\mathrm{GHz}$

and a peak magnitude of 10 mT to excite SWs. The only peak below f_{cut} was found at $f_0 = 8.60$ GHz. We then ran a steady-state simulation with a sinusoidal excitation at f_0 and a microwave field amplitude of $b = 100\,\mu\mathrm{T}$. Figure 1(b) presents a snapshot of the magnetization deviation from the ground state, Δm_x, over the whole sample, revealing radially propagating SWs, i.e., a pattern similar to that observed in the disk in the vortex state, excited by vortex gyration.[19,20]

To analyze the spectral content, we monitored the dynamical component of the reduced magnetization along x, Δm_x (defined as the deviation from the ground-state magnetization), over time at a point r_1 located 1800 nm from the disk center. The resulting time trace is shown in Fig. 1(c), and its discrete Fourier transform is presented in Fig. 1(d). This confirms that the dominant radiation frequency is $2f_0$ (magnitude of 4.6×10^{-3}), with much weaker components at f_0 (1.6×10^{-3}) and $3f_0$ (0.1×10^{-3}), respectively. Because the excitation frequency lay below the ferromagnetic resonance (FMR) of the PR, the signal at f_0 is an evanescent wave; the strong $2f_0$ signal is therefore notable given the moderate excitation amplitude. This behavior contrasts with SW emission from the vortex core at the pumped frequency.[19,20]

To explain the mechanisms behind higher-order SW generation, we simplified the system by designing a one-dimensional geometry of length 3600 nm along the x-axis, with a single simulation cell along y and periodic boundary conditions implemented as 1,000 replicas on each side. The width of the ER was $w = 70$ nm, which was sufficient to ensure that the magnetization remained mostly in plane and aligned along the $+y$ axis (Fig. 2(a)).

From simulations at a static magnetic field $B_0 = 354$ mT with the sinc-type excitation and the out-of-plane-oriented microwave magnetic field b, we found that the strongest response in the ER, which dominated the spectrum, occurred at $f_0 = 8.60$ GHz (the spectrum is shown in Fig. S1 of the Supporting Information, SI).

We then performed steady-state simulations using a sinusoidal microwave field of frequency $f_0 = 8.60$ GHz and amplitude $b = b_1 = 60\,\mu\mathrm{T}$. Although this excitation frequency

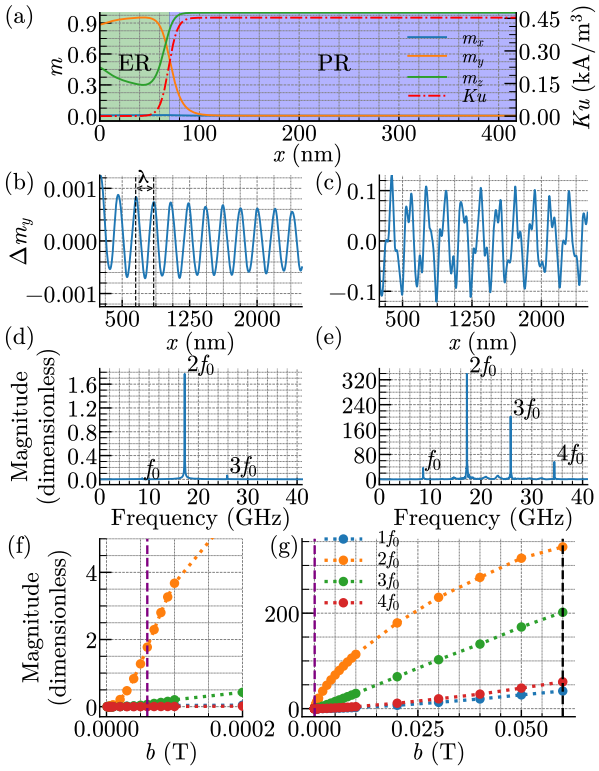

Figure 2: (a) Static magnetization components and out-of-plane anisotropy value along the x axis (for $x < 400\,\text{nm}$). (b) Dynamical y-component of the magnetization along the waveguide under a uniform out-of-plane drive at $f_0 = 8.60\,\text{GHz}$ with microwave magnetic field amplitude $b_1 = 60\,\mu\text{T}$. The wavelength λ corresponds to the $2f_0$ component. (c) Same as (b), but with an amplitude of $b_2 = 60\,\text{mT}$. (d) Discrete Fourier transform of the y-component of the magnetization in a cell located $2\,\mu\text{m}$ from the excitation source, for excitation amplitude b_1. (e) Same as (d), but for b_2. (f,g) Magnitudes of the Fourier transform peaks at $2f_0$, $3f_0$, and $4f_0$ as a function of b. The values b_1 and b_2, used in panels (b,d) and (c,e) respectively, are marked with dashed lines.

lay below the FMR of the PR (i.e., 13.90 GHz), a strong $2f_0$ SW signal was observed propagating in the PR along the x-axis with wavelength $\lambda = 261\,\text{nm}$, as shown in Fig. 2(b). The discrete Fourier transform of the magnetization at $x = 2\,\mu\text{m}$ (Fig. 2(d)) revealed a pronounced peak at $2f_0$ and very weak contributions at f_0 and $3f_0$, in agreement with the 2D system.

To further probe the nonlinear-dynamics regime, we repeated the simulation with a stronger excitation field, $b = b_2 = 60\,\text{mT}$ (an increase by a factor of 1,000), as shown in Fig. 2(c). In this case, the system generated a more complex signal that propagated in the

PR. In addition to the dominant peak at $2f_0$ (magnitude 340 arb. units), higher-frequency harmonics appeared in the spectrum at $3f_0$ (200 arb. units) and $4f_0$ (60 arb. units), as shown in Fig. 2(e).

Figure 2(f,g) shows how the amplitudes of the harmonics generated in the PR evolved as the excitation amplitude increased from 1 µT to 60 mT ($2f_0$, $3f_0$, and $4f_0$). The second-harmonic amplitude increased quadratically with b up to $b = 0.1$ mT, indicating a thresholdless process, similar to other SHG scenarios.[30,31] For larger microwave amplitudes, the amplitude of the $2f_0$ wave scaled as $\sqrt{b}$ and saturated at high b. This behavior indicates the onset of additional threshold processes, which became relevant when the magnetic field exceeded 0.1 mT, as evidenced by the multiple low-intensity peaks visible in Fig. 2(e), generated in higher-order nonlinear processes.[15,32] At these excitation levels, the amplitudes of the third and fourth harmonics increased significantly, narrowing the gap relative to the $2f_0$ wave. This demonstrates the potential for enhancing the amplitude of propagating SWs at twice the frequency of the pumping microwave field, although the saturation mechanism becomes significant at larger excitation amplitudes.

We also studied the effect of damping (see Fig. S2 in the SI) and found that increasing the damping from $\alpha = 1 \times 10^{-3}$ to $\alpha = 1 \times 10^{-2}$ fully suppressed higher-harmonic generation. Raising the driving field from 6 µT to 60 µT restored a clean $2f_0$ response. In metallic PMA multilayers (e.g., Pt/Co, Co/Ni, Co/Pd, CoFeB/Au), room-temperature Gilbert damping is typically of order 10^{-2} and often $\alpha \approx 0.01$–0.05; it is due to interfacial spin–orbit and spin-pumping contributions.[33–37] By contrast, YIG films routinely show $\alpha \sim 10^{-4}$ and can approach a few $\times 10^{-5}$ in thicker or optimized samples.[38–40] Thus our baseline $\alpha = 10^{-3}$ is optimistic for Co/Pd by one order of magnitude but higher than low-loss garnets. This means that, experimentally, similar $2f_0$ emission in metallic stacks, as presented above, will generally require larger drive fields and/or materials optimization to reduce α.

We the adjusted the static external field B_0 and varying the ER width w to explore strategies for controlling the SW generation frequency f_0 and its second harmonic. Figure 3(a)

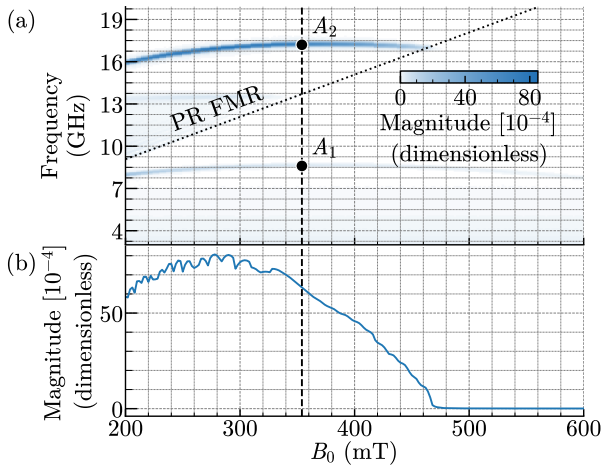

Figure 3: (a) Spin-wave spectrum in the propagation region (PR) recorded at $x = 2000\,\mathrm{nm}$ while sweeping the bias field B_0. For each B_0, the system is driven by a uniform out-of-plane sinusoidal field at the ER fundamental frequency $f_0(B_0)$ with fixed amplitude $b = 100\,\mu\mathrm{T}$; the dotted line marks the PR FMR. The vertical dashed line indicates the operating field used elsewhere in the paper ($B_0 = 354\,\mathrm{mT}$). Markers A_1 and A_2 denote SW modes that are analyzed in Fig. 4. (b) Magnitude of the $2f_0$ Fourier component at $x = 2000\,\mathrm{nm}$ versus B_0 under the same uniform out-of-plane sinusoidal drive at $f_0(B_0)$ with $b = 100\,\mu\mathrm{T}$.

shows the PR spectrum at $x = 2000\,\mathrm{nm}$ as B_0 was ramped from 200 mT to 600 mT. For each B_0, we recomputed the ER fundamental $f_0(B_0)$ and drove the system with a uniform out-of-plane sinusoid at this frequency with fixed amplitude $b = 100\,\mu\mathrm{T}$—that is, only the pump frequency changed with B_0; b was kept constant. Within this field interval, the domain-wall center, defined as the point where $m_z = 0.5$ (i.e., halfway between in-plane and out-of-plane), shifted from $x = 58\,\mathrm{nm}$ to $x = 64\,\mathrm{nm}$. We recorded the PR response at $x = 2000\,\mathrm{nm}$, i.e., far away from the ER. The PR FMR (dotted line) stays above f_0 throughout. The $2f_0$ branch tracks f_0, increasing from 16.0 GHz to 17.25 GHz as B_0 rises from 200 mT to 354 mT, then bending down and crossing the PR FMR at B_0 =464 mT ($2f_0 = 16.5\,\mathrm{GHz}$). For higher B_0, $2f_0$ falls below the PR cutoff and the corresponding wave in the PR becomes evanescent. One interesting feature is how the magnitude of the $2f_0$ branch changes with increasing B_0. As shown in Fig. 3(b), it increases from 60 [arb. units] to a maximum of 81 [arb. units] at $B_0 = 354\,\mathrm{mT}$. As B_0 increases further and approaches the FMR frequency of the PR at $B_0 = 464\,\mathrm{mT}$, the SW amplitude decreases. At this frequency, the SW in the PR has

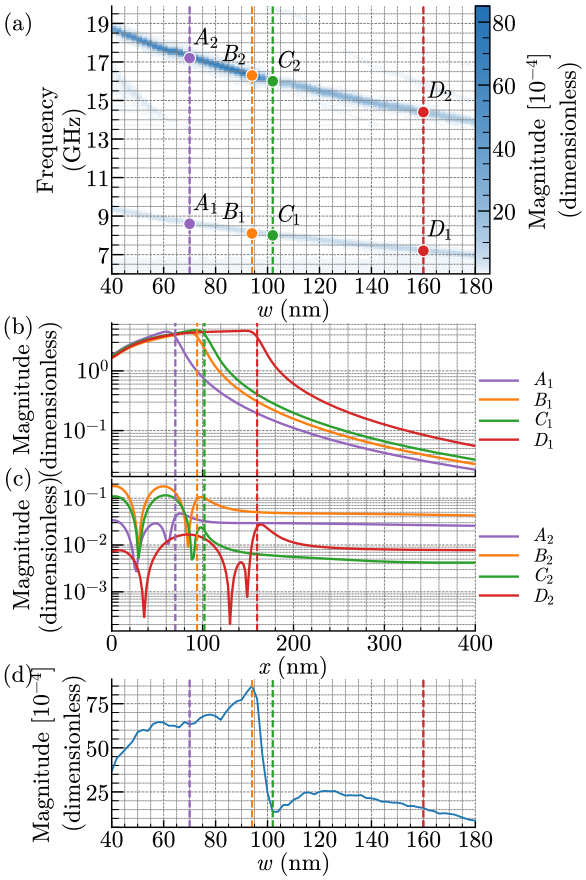

Figure 4: (a) Evolution of the SW spectrum in the PR as a function of the ER width w. (b) Spatial profiles of the normalized SW amplitude corresponding to the f_0 modes at different values of w as marked in panel (a). The dashed lines represent the corresponding ER length w. (c) Same as (b) but for the $2f_0$ frequency. (d) Magnitude of the $2f_0$ peak in the PR, for $x = 2000\,\text{nm}$ as w is increased. The results are obtained with bias magnetic field $B_0 = 354\,\text{mT}$, excited with the sine microwave magnetic field of magnitude $b = 100\,\mu\text{T}$.

an infinite wavelength, which causes its excitation efficiency to drop to zero. This approach offers only moderate $2f_0$ tunability: a 1.25 GHz range for a 160 mT change in the bias field, accompanied by concurrent moderate changes in the emitted intensity.

A complementary tuning route is shown in Fig. 4(a): we fixed $B_0 = 354\,\text{mT}$ and varied the ER width, w, from 40 nm to 180 nm. In these simulations, for each value of w we recomputed the ER fundamental resonance f_0, drove the system with a sinusoid at that frequency with fixed amplitude $b = 100\,\mu\text{T}$, and recorded the PR response at $x = 2000\,\text{nm}$. As w increases from 70 nm to 160 nm, f_0 decreases from 8.60 GHz to 7.44 GHz (and thus $2f_0$ from 17.20 GHz

to 14.88 GHz).

In Fig. 4(d), we show the magnitude of the $2f_0$ branch as a function of w. The magnitude first grows with w —rising from 36×10^{-4} at $w = 40\,\text{nm}$ to 85×10^{-4} at $w = 94\,\text{nm}$—then drops to 14×10^{-4} at $w = 102\,\text{nm}$ and thereafter increases but remains below 26×10^{-4}. Unlike Fig. 3(b), the FMR frequency of the PR is essentially independent of w, so $2f_0$ remains above the PR FMR across the entire range considered. This non-monotonicity of the second-harmonic intensity therefore points to a resonance in the ER, with a maximum near $w = 94\,\text{nm}$ (i.e., point B_2).

To clarify the origin of the f_0 and $2f_0$ modes, we plot in Fig. 4(b) and (c) log-scaled maps of the SW-amplitude spatial distribution for the f_0 and $2f_0$ branches, respectively, at the ER widths marked in Fig. 4(a). The fundamental f_0 modes—A_1 ($f = 8.60\,\text{GHz}$, $w = 70\,\text{nm}$), B_1 ($f = 8.08\,\text{GHz}$, $w = 94\,\text{nm}$), C_1 ($f = 8.00\,\text{GHz}$, $w = 102\,\text{nm}$), and D_1 ($f = 7.20\,\text{GHz}$, $w = 160\,\text{nm}$)—exhibit essentially the same spatial pattern for all w (Fig. 4(b)): the amplitude is tightly confined to the ER, resembling a quarter wavelength, peaks at the domain wall, and decays monotonically into the PR, as expected for f_0 lying below the FMR frequency of the PR. This invariance and below-cutoff character rule out the directly pumped f_0 mode as the source of the observed resonance at $w = 94\,\text{nm}$. The resonant response must therefore be associated with the $2f_0$ mode.

To support this hypothesis, we show the $2f_0$ mode profiles in Fig. 4(c): A_2 ($f = 17.2\,\text{GHz}$, $w = 70\,\text{nm}$), B_2 ($f = 16.16\,\text{GHz}$, $w = 94\,\text{nm}$), C_2 ($f = 16.00\,\text{GHz}$, $w = 102\,\text{nm}$), and D_2 ($f = 14.40\,\text{GHz}$, $w = 160\,\text{nm}$). Unlike the f_0 modes, the $2f_0$ modes have nodal points in the ER. Clearly, the SW magnitude is highest at $w = 94\,\text{nm}$, in both the ER and the PR. Moreover, this is the only case in which the maximal amplitudes are formed at both edges of the ER. This confirms the formation of a standing wave at $2f_0$ and a resonant condition at $w = 94\,\text{nm}$. This conclusion is further supported by tracking the evolution of this standing mode with changes in w, as shown in Fig. 3 of the SI. We attribute the asymmetric profile of the standing wave to the continuous variation in the static magnetization orientation in

the ER.

Another interesting aspect of the dependence shown in Fig. 4(c) is the drastic decrease in the $2f_0$-mode magnitude at $w = 102\,\mathrm{nm}$, i.e., just after resonant excitation. Such a dependence resembles a Fano resonance—i.e., a resonant interaction between a confined mode and a continuous band—widely explored in photonics.[41] However, in our case it would arise from the interaction of the bound SW generated in the SHG process in the ER with the continuous band of propagating SWs in the PR.

To further ensure that the higher-frequency generation is due to a cavity effect in the ER rather than domain-wall excitation, as in other studies,[7–10] we ran a simulation with frozen spins (after relaxation) in the left part of the ER ($x < 40\,\mathrm{nm}$) for $w = 70\,\mathrm{nm}$ (see Fig. S1 in the SI). The spectral plot shows no higher-harmonic generation, allowing us to conclude that the nanocavity formed by the ER plays a crucial role between the ferromagnetic edge and the domain wall.

These results allow us to conclude that the discovered process exists in both 1D and 2D systems and enables the excitation of propagating SWs in the form of radial or plane waves, respectively. The fundamental (pumped) mode is spatially trapped in the ER and peaks at the ER–PR interface, decaying evanescently into the PR. By contrast, the second harmonic is a propagating mode in the PR that carries energy across the entire waveguide. Crucially, the ER acts as a resonant nanocavity, accumulating energy from the uniform pump at the fundamental mode frequency f_0, which up-converts the pumped energy nonlinearly to $2f_0$ (or higher multiples of f_0) and efficiently launches it into the adjacent PR. This process becomes especially efficient when the $2f_0$ frequency matches that of a higher-order standing wave of the nanocavity.

In summary, we have demonstrated, through comprehensive micromagnetic simulations, a compact scheme for generating coherent, propagating SWs at the second harmonic of the pumping microwave field in a hybrid structure composed of two orthogonally magnetized parts: a nanocavity and an extended part. The key ingredients—a uniform out-of-plane

microwave pump, an in-plane-magnetized ER, and an adjacent out-of-plane-magnetized PR—cooperate to (i) confine the fundamental pumping energy in the ER, (ii) up-convert its energy to $2f_0$ inside a nanocavity region, and (iii) launch the resulting short-wavelength wave into the PR. Crucially, the emission frequency can be tuned continuously either by sweeping the bias field B_0 or by adjusting the ER width w, while the conversion efficiency increases nonlinearly with the pump amplitude. The concept extends naturally from one- to two-dimensional geometries, where radially propagating second-harmonic waves emerge from an in-plane-magnetized rim of the central antidot. This suggests that we can manipulate the wavefront of the emitted surface waves by altering the shape of the ER area. This method is similar to the one used with microstrip lines, as described in Ref.,[42] but it eliminates the need for an additional lithographic process and operates on a deep sub-micrometer scale.

The proposed hybrid structure can be fabricated using any ferromagnetic thin film with PMA, e.g., metallic multilayers[43] or garnet thin films,[44] with an in-plane-magnetized nanocavity formed using one of the existing methods that allow the reduction of PMA locally. Examples of these methods include already mentioned ion irradiation,[44,45] but also oxidation,[46] direct-write laser exposure annealing,[47] or even local electric-field modulation.[48] The final method suggests that the nanocavity may be tunable not only by an external magnetic bias field, as shown in our study, but also locally and in a more integrated way. Thus, our results point to a lithographically simple, energy-efficient pathway toward on-chip sources of nonlinearly generated SWs with sub-300 nm wavelengths—an essential building block for next-generation magnonic logic, signal processing, and hybrid magnonic–quantum platforms. Future work will focus on optimizing material stacks to reduce damping (e.g., doped-yttrium iron garnet films), investigating the role of domain-wall chirality, and integrating the proposed emitter with magnonic networks and cavity–magnonic devices.

Methods

Material Parameters. We modeled a multilayered $[\mathrm{Co/Pd}]_8$ system as a 13.2 nm-thick effective Co layer with parameters taken from the literature:[49,50] $K_\mathrm{u} = 4.5 \times 10^5\,\mathrm{J\,m^{-3}}$, $M_\mathrm{s} = 0.81 \times 10^6\,\mathrm{A\,m^{-1}}$, $A_\mathrm{ex} = 1.3 \times 10^{-11}\,\mathrm{J\,m^{-1}}$. To facilitate the observation of coherent SW propagation over several microns, the Gilbert damping was artificially reduced to $\alpha = 1 \times 10^{-3}$. A discretization of 2 nm was used for one-dimensional simulations, and 4 nm × 4 nm for two-dimensional simulations to reduce computational cost. Periodic boundary conditions were applied in the y-direction in the one-dimensional case to emulate a semi-infinite film.

Simulation Setup. Simulations were conducted using Amumax,[29] our fork of MuMax3,[51] solving the Landau–Lifshitz–Gilbert equation. SWs were excited by a uniform microwave field along z with either a sinc-type profile (10 GHz cutoff) or a steady-state sine wave. Magnetization dynamics were sampled every 16.66 ps for 100 ns and processed via fast Fourier transform to extract spatial-frequency-resolved SW spectra. More details on the simulations and post-processing are available in the SI.

Associated content

The data that support the findings of this study are available at: https://doi.org/10.5281/zenodo.17068975

The following files are available free of charge.

- 'si.pdf' : Extended Methods; Spectral response inside the excitation region; Short study on the effect of damping; High-frequency branch crossing

Acknowledgment

The research has received funding from the National Science Centre of Poland, Grant No. UMO-2020/37/B/ST3/03936 and 2023/49/N/ST3/03538, and the EU Research and Innovation Programme Horizon Europe (HORIZON-CL4-2021-DIGITAL-EMERGING-01) under grant agreement no. 101070347 (MANNGA). MM acknowledges funding from the Adam Mickiewicz University Foundation.

Author Information

Corresponding Author

* E-mail: matmoa@amu.edu.pl

Author Contributions

M.M. acquired funding, conceived the study, performed simulations, processed the data, interpreted the results, wrote the manuscript and create the figures. Y.P. assisted with the initial simulations and data analysis. M.Z. reviewed the final manuscript. M.K. acquired funding, conceived the study, supervised the project, interpreted the results, wrote and reviewed the manuscript.

Notes

The authors declare no competing financial interest.

References

(1) Ayres, W. P.; Vartanian, P. H.; Melchor, J. L. Frequency Doubling in Ferrites. *Journal of Applied Physics* **1956**, *27*, 188–189.

(2) Papp, Á.; Porod, W.; Csaba, G. Nanoscale neural network using non-linear spin-wave interference. *Nature Communications* **2021**, *12*, 6422.

(3) Körber, L.; Heins, C.; Hula, T.; Kim, J.-V.; Thlang, S.; Schultheiss, H.; Fassbender, J.; Schultheiss, K. Pattern recognition in reciprocal space with a magnon-scattering reservoir. *Nature Communications* **2023**, *14*, 3954.

(4) Fripp, K. G.; Au, Y.; Shytov, A. V.; Kruglyak, V. V. Nonlinear chiral magnonic resonators: Toward magnonic neurons. *Applied Physics Letters* **2023**, *122*, 172403.

(5) Marrows, C. H.; Barker, J.; Moore, T. A.; Moorsom, T. Neuromorphic computing with spintronics. *npj Spintronics* **2024**, *2*, 12.

(6) Sebastian, T.; Brächer, T.; Pirro, P.; Serga, A. A.; Hillebrands, B.; Kubota, T.; Naganuma, H.; Oogane, M.; Ando, Y. Nonlinear Emission of Spin-Wave Caustics from an Edge Mode of a Microstructured $Co_2Mn_{0.6}Fe_{0.4}Si$ Waveguide. *Phys. Rev. Lett.* **2013**, *110*, 067201.

(7) Hermsdoerfer, S. J.; Schultheiss, H.; Rausch, C.; Schäfer, S.; Leven, B.; Kim, S.-K.; Hillebrands, B. A spin-wave frequency doubler by domain wall oscillation. *Applied Physics Letters* **2009**, *94*, 223510.

(8) Wagner, K.; Kákay, A.; Schultheiss, K.; Henschke, A.; Sebastian, T.; Schultheiss, H. Magnetic domain walls as reconfigurable spin-wave nanochannels. *Nature Nanotechnology* **2016**, *11*, 432–436.

(9) Rodrigues, D.; Nothhelfer, J.; Mohseni, M.; Knapman, R.; Pirro, P.; Everschor-Sitte, K. Nonlinear Dynamics of Topological Ferromagnetic Textures for Frequency Multiplication. *Phys. Rev. Appl.* **2021**, *16*, 014020.

(10) Sluka, V. et al. Emission and propagation of 1D and 2D spin waves with nanoscale wavelengths in anisotropic spin textures. *Nature Nanotechnology* **2019**, *14*, 328–333.

(11) Nikolaev, K. O.; Lake, S. R.; Schmidt, G.; Demokritov, S. O.; Demidov, V. E. Resonant generation of propagating second-harmonic spin waves in nanowaveguides. *Nature Communications* **2024**, *15*, 1827.

(12) Nikolaev, K. O.; Lake, S. R.; others Resonant inter-mode second-harmonic generation of spin waves. *Applied Physics Letters* **2025**, *126*, 082408.

(13) Stancil, D. D.; Prabhakar, A. *Spin Waves: Theory and Applications*; Springer: New York, 2009.

(14) Wu, J.; Liu, J.; Ren, Z.; Leung, M. Y.; Leung, W. K.; Ho, K. O.; Wang, X.; Shao, Q.; Yang, S. Wideband coherent microwave conversion via magnon nonlinearity in a hybrid quantum system. *npj Spintronics* **2024**, *2*, 30.

(15) Lan, Y.; others Coherent harmonic generation of magnons. *Nature Communications* **2025**, *16*, 1178.

(16) Chumak, A. V. et al. Advances in Magnetics Roadmap on Spin-Wave Computing. *IEEE Transactions on Magnetics* **2022**, *58*, 1–72.

(17) Ciubotaru, F.; Devolder, T.; Manfrini, M.; Adelmann, C.; Radu, I. P. All electrical propagating spin wave spectroscopy with broadband wavevector capability. *Applied Physics Letters* **2016**, *109*, 012403.

(18) Woo, S.; Delaney, T.; Beach, G. S. D. Magnetic domain wall depinning assisted by spin wave bursts. *Nature Physics* **2017**, *13*, 448–454.

(19) Wintz, S.; Tiberkevich, V.; Weigand, M.; Raabe, J.; Lindner, J.; Erbe, A.; Slavin, A.; Fassbender, J. Magnetic vortex cores as tunable spin-wave emitters. *Nature Nanotechnology* **2016**, *11*, 948–953.

(20) Dieterle, G. et al. Coherent Excitation of Heterosymmetric Spin Waves with Ultrashort Wavelengths. *Phys. Rev. Lett.* **2019**, *122*, 117202.

(21) Liu, C. et al. Long-distance propagation of short-wavelength spin waves. *Nature Communications* **2018**, *9*, 738.

(22) Yu, H.; Allivy Kelly, O.; Cros, V.; Bernard, R.; Bortolotti, P.; Anane, A.; Brandl, F.; Heimbach, F.; Grundler, D. Approaching soft X-ray wavelengths in nanomagnet-based microwave technology. *Nature Communications* **2016**, *7*, 11255.

(23) Mushenok, F. B.; Dost, R.; Davies, C. S.; Allwood, D. A.; Inkson, B. J.; Hrkac, G.; Kruglyak, V. V. Broadband conversion of microwaves into propagating spin waves in patterned magnetic structures. *Applied Physics Letters* **2017**, *111*, 042404.

(24) Wang, Q.; Verba, R.; Heinz, B.; Schneider, M.; Wojewoda, O.; Davídková, K.; Levchenko, K.; Dubs, C.; Mauser, N. J.; Urbanek, M.; Pirro, P.; Chumak, A. V. Deeply nonlinear excitation of self-normalized short spin waves. *Science Advances* **2023**, *9*, eadg4609.

(25) Kumar, N.; Gruszecki, P.; Gołębiewski, M.; Kłos, J. W.; Krawczyk, M. Exciting High-Frequency Short-Wavelength Spin Waves using High Harmonics of a Magnonic Cavity Mode. *Advanced Quantum Technologies* **2024**, *7*, 2400015.

(26) Fassbender, J.; Ravelosona, D.; Samson, Y. Tailoring magnetism by light-ion irradiation. *Journal of Physics D: Applied Physics* **2004**, *37*, R179.

(27) Chappert, C.; Bernas, H.; Ferré, J.; Kottler, V.; Jamet, J.-P.; Chen, Y.; Cambril, E.; Devolder, T.; Rousseaux, F.; Mathet, V.; Launois, H. Planar Patterned Magnetic Media Obtained by Ion Irradiation. *Science* **1998**, *280*, 1919–1922.

(28) Jiang, S.; Khymyn, R.; Chung, S.; Le, T. Q.; Diez, L. H.; Houshang, A.; Zahedinejad, M.; Ravelosona, D.; Åkerman, J. Reduced spin torque nano-oscillator linewidth using He+ irradiation. *Applied Physics Letters* **2020**, *116*, 072403.

(29) Moalic, M.; Zelent, M. MathieuMoalic/amumax: 2023.10.26. 2023; https://doi.org/10.5281/zenodo.10043142.

(30) Demidov, V. E.; Kostylev, M. P.; Rott, K.; Krzysteczko, P.; Reiss, G.; Demokritov, S. O. Generation of the second harmonic by spin waves propagating in microscopic stripes. *Phys. Rev. B* **2011**, *83*, 054408.

(31) Cheng, C.; Bailey, W. E. High-efficiency gigahertz frequency doubling without power threshold in thin-film Ni81Fe19. *Applied Physics Letters* **2013**, *103*, 242402.

(32) Schultheiss, H.; Vogt, K.; Hillebrands, B. Direct observation of nonlinear four-magnon scattering in spin-wave microconduits. *Phys. Rev. B* **2012**, *86*, 054414.

(33) Kato, T.; Nozaki, Y.; Matsuyama, K.; Fujiwara, H.; Yuasa, H.; Ando, H. Perpendicular anisotropy and Gilbert damping in sputtered Co/Pd multilayers. *IEEE Trans. Magn.* **2012**, *48*, 3288–3291.

(34) Song, C.; Cui, B.; Wang, L.; Liu, Q.; Zeng, F.; Pan, F. Observation of the intrinsic Gilbert damping in Co/Ni films with perpendicular anisotropy. *Appl. Phys. Lett.* **2013**, *102*, 102401.

(35) Barati, E.; Cinal, M.; Edwards, D. M.; Umerski, A. Gilbert damping in magnetic layered systems. *Phys. Rev. B* **2017**, *96*, 014420.

(36) Kuświk, P.; Głowiński, H.; Coy, E.; Dubowik, J.; Stobiecki, F. Perpendicularly magnetized Co20Fe60B20 layer sandwiched between Au with low Gilbert damping. *Journal of Physics: Condensed Matter* **2017**, *29*, 435803.

(37) Janardhanan, S.; Mielcarek, S.; Głowiński, H.; Kowacz, M.; Kuświk, P.; Krawczyk, M.; Trzaskowska, A. Investigation of spin wave dynamics in Au/CoFeB/Au multilayers with perpendicular magnetic anisotropy. *Scientific Reports* **2023**, *13*, 22494.

(38) Sun, Y.; Song, Y.-Y.; Chang, H.; Kabatek, M.; Jantz, M.; Schneider, W.; Wu, M.; Schultheiss, H.; Hoffmann, A. Growth and ferromagnetic resonance properties of nanometer-thick yttrium iron garnet films. *Appl. Phys. Lett.* **2012**, *101*, 152405.

(39) Hauser, C.; Richter, T.; Homonnay, N.; Eisenschmidt, C.; Qaid, M.; Deniz, H.; Huebl, T.; Grundler, D.; Huebl, H.; Albrecht, M. Yttrium Iron Garnet Thin Films with Very Low Damping. *Sci. Rep.* **2016**, *6*, 20827.

(40) Soumah, L.; Beaulieu, N.; Qassym, L.; Carrétéro, C.; Jacquet, E.; Lebourgeois, R.; Youssef, J. B.; Bortolotti, P.; Cros, V.; Anane, A. Ultra-low damping insulating magnetic thin films get perpendicular. *Nat. Commun.* **2018**, *9*, 3355.

(41) Limonov, M. F.; Rybin, M. V.; Poddubny, A. N.; Kivshar, Y. S. Fano resonances in photonics. *Nature Photonics* **2017**, *11*, 543–554.

(42) Temdie, L.; Castel, V.; Jungfleisch, M.; Bernard, R.; Majjad, H.; Stoeffler, D.; Henry, Y.; Bailleul, M.; Vlaminck, V. Probing Spin Wave Diffraction Patterns of Curved Antennas. *Phys. Rev. Appl.* **2024**, *21*, 014032.

(43) Sbiaa, R.; Meng, H.; Piramanayagam, S. N. Materials with perpendicular magnetic anisotropy for magnetic random access memory. *physica status solidi (RRL) – Rapid Research Letters* **2011**, *5*, 413–419.

(44) Das, S.; Mansell, R.; Flajsman, L.; Yao, L.; van der Jagt, J. W.; Chen, S.; Ravelosona, D.; Herrera Diez, L.; van Dijken, S. Tuning of perpendicular magnetic anisotropy in Bi-substituted yttrium iron garnet films by He^+ ion irradiation. *Phys. Rev. Mater.* **2024**, *8*, 114419.

(45) Wawro, A.; Kurant, Z.; Jakubowski, M.; Tekielak, M.; Pietruczik, A.; Böttger, R.; Maziewski, A. Magnetic Properties of Coupled Co/Mo/Co Structures Tailored by Ion Irradiation. *Phys. Rev. Appl.* **2018**, *9*, 014029.

(46) Luo, Z.; Dao, T. P.; Hrabec, A.; Vijayakumar, J.; Kleibert, A.; Baumgartner, M.; Kirk, E.; Cui, J.; Savchenko, T.; Krishnaswamy, G.; Heyderman, L. J.; Gambardella, P. Chirally coupled nanomagnets. *Science* **2019**, *363*, 1435–1439.

(47) Riddiford, L. J.; Brock, J. A.; Murawska, K.; Hrabec, A.; Heyderman, L. J. Grayscale control of local magnetic properties with direct-write laser annealing. *arXiv preprint arXiv:2401.09314* **2024**,

(48) Rana, B.; Otani, Y. Towards magnonic devices based on voltage-controlled magnetic anisotropy. *Communications Physics* **2019**, *2*, 90.

(49) Lemesh, I.; Beach, G. S. Twisted domain walls and skyrmions in perpendicularly magnetized multilayers. *Phys. Rev. B* **2018**, *98*, 104402.

(50) Pan, S.; Mondal, S.; Zelent, M.; Szwierz, R.; Pal, S.; Hellwig, O.; Krawczyk, M.; Barman, A. Edge localization of spin waves in antidot multilayers with perpendicular magnetic anisotropy. *Phys. Rev. B* **2020**, *101*, 014403.

(51) Vansteenkiste, A.; Leliaert, J.; Dvornik, M.; Helsen, M.; Garcia-Sanchez, F.; Van Waeyenberge, B. The design and verification of MuMax3. *AIP Adv.* **2014**, *4*, 107133.

TOC Graphic

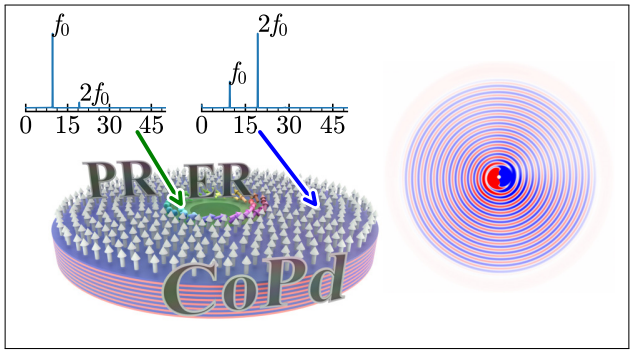

4.4 Tunability of spin-wave spectra in a 2D triangular shaped magnonic fractals

- *Tunability of spin-wave spectra in a 2D triangular shaped magnonic fractals*,
  R. Mehta, **M. Moalic**, M. Krawczyk, S. Saha.
  Journal of Physics: Condensed Matter, **35** (32), 324002 (2023).

4.4.1 Introduction

This publication is part of an international collaboration with the Department of Physics at Ashoka University, India. It explores the control of collective spin-wave dynamics in deterministic magnonic fractals, with a particular focus on the Sierpinski triangle geometry. Within the scope of my doctoral research, this study aligns with the overarching objective of understanding how geometric confinement and symmetry influence spin-wave modes in patterned ferromagnetic systems. Using micromagnetic simulations, we investigate how variations in fractal iteration and external magnetic field orientation affect the spectral features of spin waves. The results demonstrate the emergence of tunable frequency gaps and mini-bandgaps that are characteristic of the self-similar fractal structure. These findings contribute to the broader aim of this thesis by highlighting new pathways for designing reconfigurable, aperiodic magnonic crystals with potential applications in nanoscale signal processing.

4.4.1.1 Contribution of the Author

In this publication, I ran detailed simulations using Amumax for the Sierpinski triangle structures seen in Figure 5 and ran the post-processing of the data such as calculating the spin wave spectra and the spatial amplitude of the spin wave modes. I also contributed to writing the manuscript, and answering the reviewers comments.

PAPER

Tunability of spin-wave spectra in a 2D triangular shaped magnonic fractals

IOP Publishing Journal of Physics: Condensed Matter
J. Phys.: Condens. Matter **35** (2023) 324002 (11pp) https://doi.org/10.1088/1361-648X/acd15f

Tunability of spin-wave spectra in a 2D triangular shaped magnonic fractals

R Mehta[1], M Moalic[2], M Krawczyk[2] and S Saha[1,*]

[1] Department of Physics, Ashoka University, Sonipat, Haryana 131029, India
[2] Institute of Spintronic and Quantum Information, Faculty of Physics, Adam Mickiewicz University, Poznan, Uniwersytetu Poznanskiego 2, Poznan PL-61-614, Poland

E-mail: susmita.saha@ashoka.edu.in

Received 26 December 2022, revised 21 April 2023
Accepted for publication 28 April 2023
Published 12 May 2023

Abstract

Reprogramming the structure of the magnonic bands during their operation is important for controlling spin waves in magnonic devices. Here, we report the tunability of the spin-wave spectra for a triangular shaped deterministic magnonic fractal, which is known as Sierpinski triangle by solving the Landau–Lifshitz–Gilbert equation using a micromagnetic simulations. The spin-wave dynamics change significantly with the variation of iteration number. A wide frequency gap is observed for a structure with an iteration number exceeding some value and a plenty of mini-frequency bandgaps at structures with high iteration number. The frequency gap could be controlled by varying the strength of the magnetic field. A sixfold symmetry in the frequency gap is observed with the variation of the azimuthal angle of the external magnetic field. The spatial distributions of the spin-wave modes allow to identify the bands surrounding the gap. The observations are important for the application of magnetic fractals as a reconfigurable aperiodic magnonic crystals.

Supplementary material for this article is available online

Keywords: spin wave, magnetization dynamics, magnonics, LLG equation, magnetic fractal, micro-magnetic simulation

(Some figures may appear in colour only in the online journal)

1. Introduction

The research on magnetic nanostructures is popular because of their potential applications in information storage, e.g. in magnetic random-access memory [1], heat-assisted magnetic recording [2], magnetic racetrack memory [3], patterned magnetic media [4], and also in magnetic logic devices [5]. Periodic magnetic nanostructures are also a potential candidate for signal processing with spin waves, which are high frequency collective magnetic excitations. Ferromagnetic nanostructures ordered periodically in one, two or three dimensions are known as magnonic crystals (MCs) [6–11]. In case of MCs based on nanostructures, individual elements are strongly magnetostatically coupled with each other. When such a system is thermally, optically, or electrically pumped, spin waves are excited. The wavelengths of spin waves can be orders of magnitude shorter than light waves operating at the same frequency range (i.e. at 20 GHz microwave has 3 cm in air, while the spin-wave wavelength can be shorter than 100 nm), which makes them a suitable candidate for nanoscale on chip microwave signal processing with nano-magnonic devices, including already demonstrated magnonic waveguides [12, 13], filters [14], splitters, phase shifters [15], spin-wave emitters [16, 17] and other logic elements [18]. Thus, a new field of research is introduced named as magnonics, which holds the promise of a new generation of energy efficient devices based on spin waves with significant

* Author to whom any correspondence should be addressed.

impact on the information technology [19, 20]. The dispersion relation of spin waves is quadratic in nature for the short wavelength limit and linear in the long wavelength limit. In MCs this leads to the formation of magnonic minibands with allowed states separated by forbidden band gaps, similarly to electronic band structure in semiconductors. The magnonic band gaps, as well as the spin-wave dynamics, can be tuned by modifying various physical and geometrical parameters [21, 22] not only to answer fundamental questions concerning magnonics but also to provide a new generation of devices to magnonic applications, like spin-wave logic devices [23], and spin-wave multiplexers [24].

The challenge in magnonics research is fine-tuning of the magnonic band structure [25] for applications in future devices. Therefore, the dynamics of spin waves in MCs is being intensively studied. In particular, the tunability of the spin-wave band structure by varying the lattice symmetry [26] and the shape [27, 28] of the nano-element are intensively studied. The spin-wave dynamics in aperiodic MCs such as quasicrystals [29–32] are also investigated. The magnetic properties such as the hysteresis loop [33], the magnonic band structure, and the spin-wave localization strongly depends on the periodicity or aperiodicity of the MCs [34]. In this work, we are interested in studying the tunability of the spin waves in a MC that exhibits fractal-like behavior. Fractals [35, 36] are composed of self-similar structures across different length scales, which look similar under different magnifications. This property is known as dilation symmetry. They also possess a non-integer dimension with a self-similarity and scale invariance, which is commonly referred to as the Hausdorff dimension [37] or fractal dimension. There are two different kinds of fractals namely, random fractal and deterministic fractals. Romanesque cauliflower, fern, or frost, snowflakes are popular examples of naturally observed random fractals. The existence of fractons [38, 39], which are low frequency vibrational excitations and diffusion limited aggregation of dendrites, is a characteristic feature of the random fractal structures. However, in case of deterministic fractals, the self-similarity is not statistically distributed. After every magnification, a part of the structure would be found that is similar to the whole structure. Sierpinski carpets and gaskets are popular examples of deterministic fractals. The concept of deterministic fractals namely, Sierpinski square [40] and triangle [33] are implemented in magnetic systems to study the modification of spin-wave dynamics. Here, the spin-wave dynamic gets modified depending on the change in the demagnetization field due to the structuring of the system. Recently, the magnetostatic mode formation in the Sierpinski square and triangle was reported, where it was shown that the mode formation is related to the geometric scaling of the fractal structure [41]. But the main challenge in magnonics, which is the regulation of spin-wave propagation in magnonic fractal systems, remains unexplored.

In this work, we aim to demonstrate control of the collective spin-wave dynamics in the Sierpinski triangle by varying the strength and orientation of the external magnetic field. The magnetization dynamics of Sierpinski triangles with different iteration numbers are simulated for different strengths as well as for different azimuthal angles (φ) of the external magnetic field. A complex evolution of the spin-wave modes has been observed as the iteration number increased. At a particular iteration, two distinct frequency bands are observed with the presence of a frequency gap. This frequency gap is modified as the strength and the azimuthal angle of the external magnetic field change. Moreover, a number of mini-frequency gaps are found at higher iteration numbers and the localized character of the amplitude distribution of the modes. These two features clearly distinguish the Sierpinski fractal from the triangle with a periodic array. Our simulation results point to the possible application of Sierpinski triangles as a novel multi-functional nano-magnonic devices.

2. Micromagnetic simulations

Time-dependent magnetization dynamics were calculated by solving the Landau–Lifshitz–Gilbert equation by using the public domain software called object oriented micromagnetic framework [42]

$$\frac{d\boldsymbol{m}}{dt} = \gamma\mu_0\,(\boldsymbol{m}\times\boldsymbol{H}_{\text{eff}}) + \alpha\mu_0\,(\boldsymbol{m}\times(\boldsymbol{m}\times\boldsymbol{H}_{\text{eff}}))\,.$$

Here, $\boldsymbol{m}$ is the normalized magnetization vector. α and γ are damping coefficient and gyromagnetic ratio respectively. $\boldsymbol{H}_{\text{eff}}$ is the effective field, which could be written as

$$\boldsymbol{H}_{\text{eff}} = \boldsymbol{H}_{\text{Zeeman}} + \boldsymbol{H}_{\text{demag}} + \boldsymbol{H}_{\text{ex}} + \boldsymbol{H}_{\text{anis}}.$$

Here, $\boldsymbol{H}_{\text{Zeeman}}$, $\boldsymbol{H}_{\text{demag}}$, $\boldsymbol{H}_{\text{ex}}$ and $\boldsymbol{H}_{\text{anis}}$ are the Zeeman field, dynamic demagnetization field, exchange field, and anisotropy field, respectively. The samples are divided into three-dimensional arrays of cuboidal cells with dimensions of $5 \times 5 \times 20$ nm^3, along the *x, y* and *z* axis, respectively. The linear dimensions of the cells are comparable to the exchange length, $\lambda_{\text{ex}} = \sqrt{\frac{A}{2\pi M_s^2}}$, where A is the exchange stiffness constant, and M_{s} is the saturation magnetization. The smaller cell size of $2 \times 2 \times 20$ nm^3 was also taken into account in the simulations, but although the intensity of the spin-wave modes changes for the smaller cell size, the mode frequencies remained almost the same. So, to save the simulation time, simulations are performed with the cell size of $5 \times 5 \times 20$ nm^3.

The parameters used for the simulations considering Py ($Ni_{80}Fe_{20}$) are $M_{\text{s}} = 760 \times 10^3$ Am^{-1}, $A = 13 \times 10^{-12}$ Jm^{-1} ($\lambda_{\text{ex}} = 5$ nm), anisotropy field $\boldsymbol{H}_{\text{anis}} = 0$, gyromagnetic ratio $\gamma = 17.6$ MHzOe^{-1} and damping coefficient $\alpha = 1.0$ (to find out the static ground state configuration). For the magnetization dynamic calculation, damping coefficient $\alpha = 0.006$, a square pulsed magnetic field with rise-time of 20 ps and peak amplitude of 20 Oe, was applied perpendicular to the sample plane. The dynamic magnetization and magnetic fields averaged over the entire sample volume were saved for a total duration of 10 ns at intervals of 10 ps.

For Sierpinski triangles, an equilateral triangle of the side length 2.85 μm is taken, which is named as TRI-0 with iteration number 0 as shown in figure 1(a). Then the iteration number is increased from 0 to 1 by removing an equilateral triangle of side length 1.42 μm and TRI-1 is obtained. In TRI-1

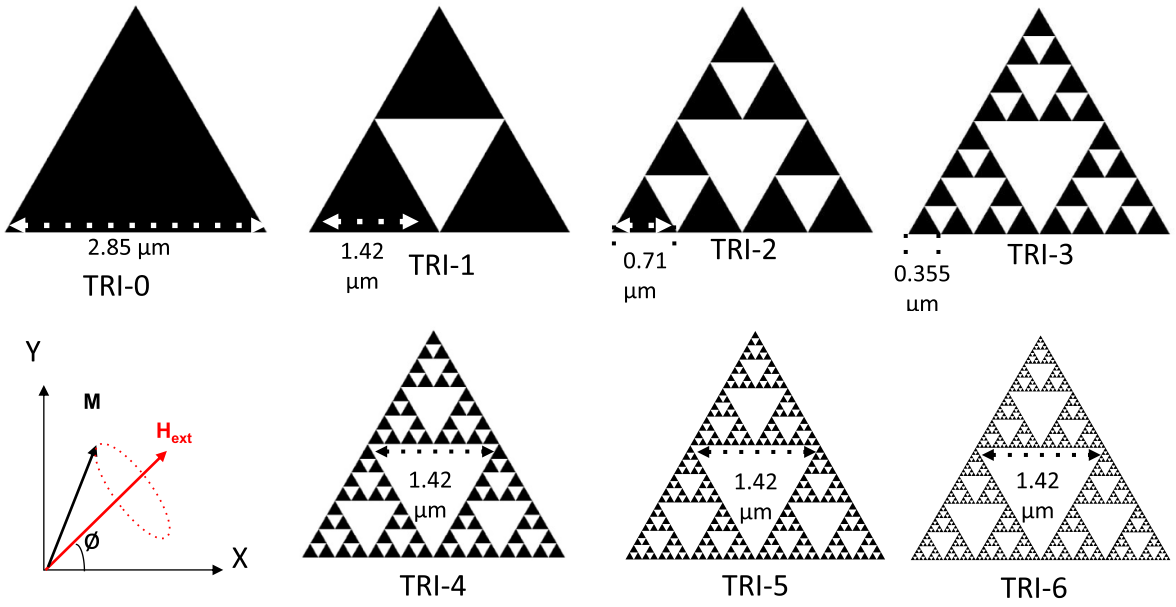

Figure 1. Schematic of the Sierpinski triangles of different iterations with geometrical scaling factor $1/2$. The dimension of the individual building block is shown for four different iterations namely iteration number 0, 1, 2 and 3. The same process is used for higher iterations with number 4, 5, 6 and 7 (not shown here). For higher iterations (4, 5 and 6) the length of the center empty triangle is only shown as it is difficult to point out the individual building blocks. The schematic of the applied external magnetic field ($\boldsymbol{H}_{\text{ext}}$) and the magnetization precession ($\boldsymbol{M}$) are also shown.

(see figure 1(b)), three individual triangles of side length of 1.42 μm are present. For iteration number 2, the central triangular hole of side length of 1.42 μm is still present but triangular holes of side length 0.71 μm are introduced and TRI-2 is obtained (see figure 1(c)). The side length of the smallest triangular hole for TRI-2 is then 0.71 μm. In TRI-3, this process is repeated but now the side length of the smallest triangular hole is 0.355 μm as shown in figure 1(d). Therefore, as the iteration number increases, the size of the triangular holes reduced with a scaling factor of $1/2$ [1.42 μm (for TRI-1 with iteration—1), 0.71 μm (for TRI-2 with iteration—2), 0.355 μm (for TRI-3 with iteration—3), 0.18 μm (for TRI-4 with iteration—4), 90 nm (for TRI-5 with iteration—5), 44.5 (for TRI-6 with iteration—6) and 22 nm (for TRI-7 with iteration—7)] as shown in figure 1.

3. Result and discussions

3.1. Magnetization dynamics

3.1.1. The magnetization dynamics of a single triangle with different sizes. The micromagnetic simulations are performed to study the magnetization dynamics of the individual triangular building block with different sizes down to base length of 20 nm as shown in figure 2. The first one is a single triangle with base length of 2.85 μm (TR-0), which is nothing but the TRI-0 in our Sierpinski triangle. The base length is reduced further to 1.42 μm (TR-1), 0.72 μm (TR-2), 0.36 μm (TR-3), 0.18 μm (TR-4), 90 nm (TR-5), 50 nm (TR-6) and 20 nm (TR-7), which are approximately the same size of the building blocks of TRI-1, TRI-2, TRI-3, TRI-4, TRI-5, TRI-6 and TRI-7, respectively. For TR-0, four spin-wave modes are observed with highest intensity around 9 GHz. As the base length reduced to 1.42 μm (TR-1), a complex multimode spin-wave spectra with frequency range from 6.5 GHz to 11 GHz are observed. With the further reduction of the base length to TR-2 and TR-3 the complexity of the spin-waves between 7.5 GHz and 12 GHz increases but a small peak at lower frequency namely, M1 for TR-2 and TR-3 starts to appear. The complexity in the spin-wave spectra around 6–11 GHz reduced significantly for TR-4 and TR-5 and the lower frequency mode namely M1 is shifted to further lower frequency. For TR-6 the intensity of the highest frequency namely M2 is reduced significantly but the intensity and the frequency of the lower frequency mode namely M1 starts to increase. Finally for TR-7, the highest intensity mode is vanished and a single mode namely M1 around 2.5 GHz is only present at the considered frequency range. It is clear from the ground state configuration (see supplemental figure S1) that as the size is reduced the edge effects become prominent and the spins at the vertex perpendicular to the applied magnetic field are mostly affected by this.

The spatial distribution of the power and phase of the spin-wave modes for individual triangles of different sizes are also calculated using the code presented in [43]. For TR-7 which has a base length of 20 nm, only a single mode is present. The power and phase of that mode (M1) is uniformly distributed throughout the triangle as shown in figure 2(b). This indicates that the exchange interactions determine the dynamics of this system, with the static demagnetizing field forming the potential landscape for wave oscillations. For TR-6 (see figure 2(c)), in case of M1 the phase is uniformly distributed but the power

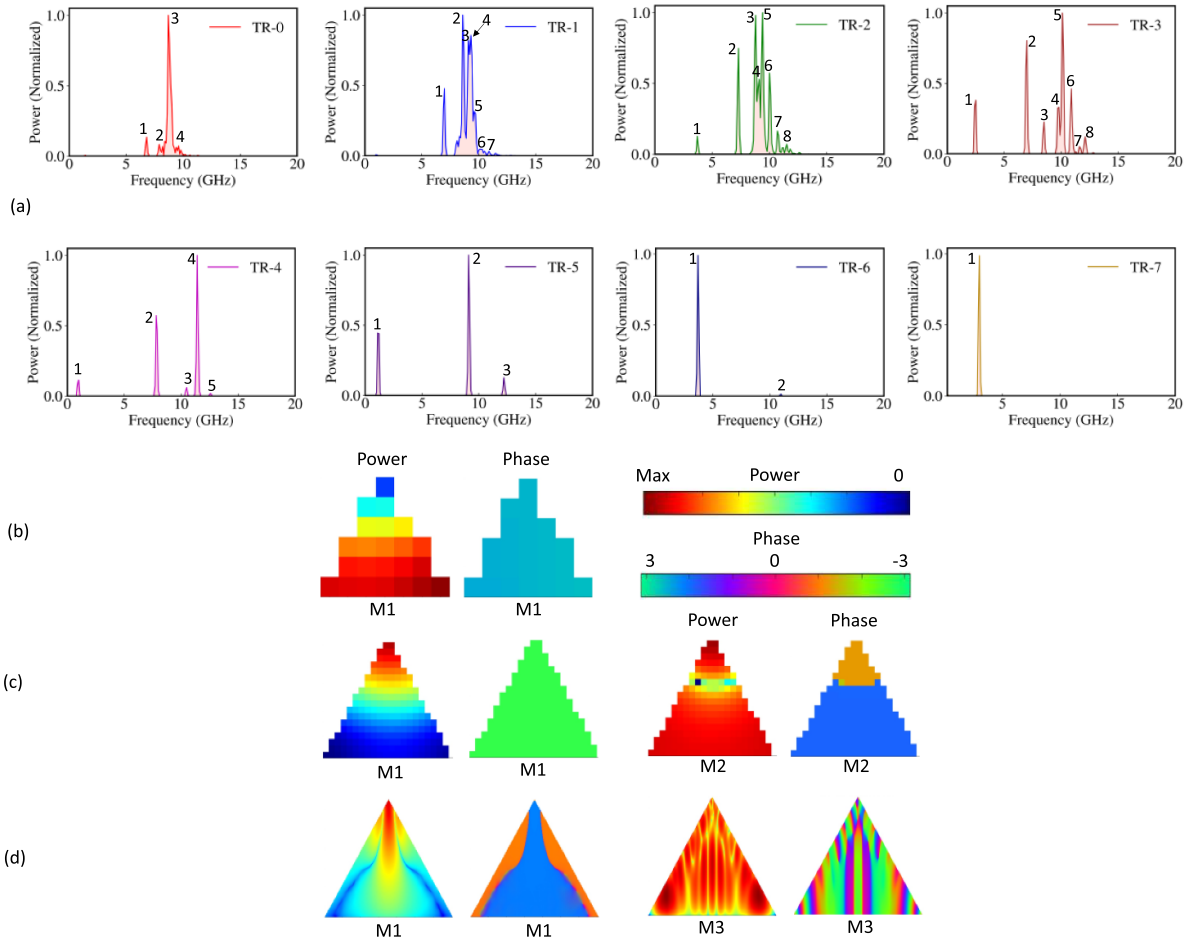

Figure 2. (a) The simulated spin-wave spectra for a single triangular building block of the Sierpinski triangle with different iteration numbers at $\boldsymbol{H}_{\text{ext}} = 0.1$ T and $\varphi = 0°$. The power and phase profile of the spin-wave modes for (b) TR-7, 20 nm, (c) TR-6, 50 nm and (d) TR-0, 2.85 μm triangles. The color scale for power and phase are also shown.

is mainly concentrated at the vertices of the triangle. We named it as an edge mode whereas for M2 the phase within the triangle is changing but the power is almost uniformly distributed throughout the triangle. We called it the bulk mode of the individual triangle. These bulk and edge modes are further modified as the size of the triangle increases because the magnetostatic interactions within the triangle changes with the increase of the size and start prevailing over exchange interactions. For TR-0, as shown in figure 2(d) M1 is an edge mode but the quantization is different, so it is a higher order edge mode, clearly indicating its magnetostatic character. It is observed the number of modes with higher quantization of the power and phase of the bulk spin-wave modes increases with the increase of the size of the triangle. For M3 the phase is changing continuously inside the triangle and the power is also quantized accordingly but overall, the power is distributed throughout the triangle. So, it is a higher order bulk mode. The bulk modes are mainly related to the higher frequency spin-wave modes as the phase changes in a short length and the lower frequency modes are mostly due to the edge modes of the system. The detailed power and phase profiles for all the triangles with different sizes are shown in supplemental figures S2 and S3.

3.1.2. The magnetization dynamics of a Sierpinski triangle with different iteration number. Next, these individual triangular shaped building blocks are arranged to form a Sierpinski triangles and the magnetization dynamics of these Sierpinski triangles with the increase in the iteration number are calculated by using the micromagnetic simulations. The fast Fourier transformation (FFT) spectra of the time-dependent magnetization components $M_z(t)$ are plotted in figure 3. The dynamics of the Sierpinski triangles are completely different with respect to the dynamics of a single triangle. The magnetic environment changes as soon as the single triangles are arranged in a particular pattern as a result the dynamics also get modified. The dynamics also get further modified with the increase of the iteration number. A rich spin-wave spectra is observed for all the samples.

For TRI-1, six modes with same frequency range as TRI-0 are observed. Very careful observation can show that some spin-wave modes start to appear near to 5 GHz. For TRI-0 (TR-0) and TRI-1 there is a large splitting between M1 and M2 shown by a grey rectangle in figure 3 which also provides a frequency gap. For TRI-2, 12 spin-wave modes are observed and the frequency gap of around 7.5 GHz is still present. Additionally, a large splitting between M1 and M2 marked by a blue

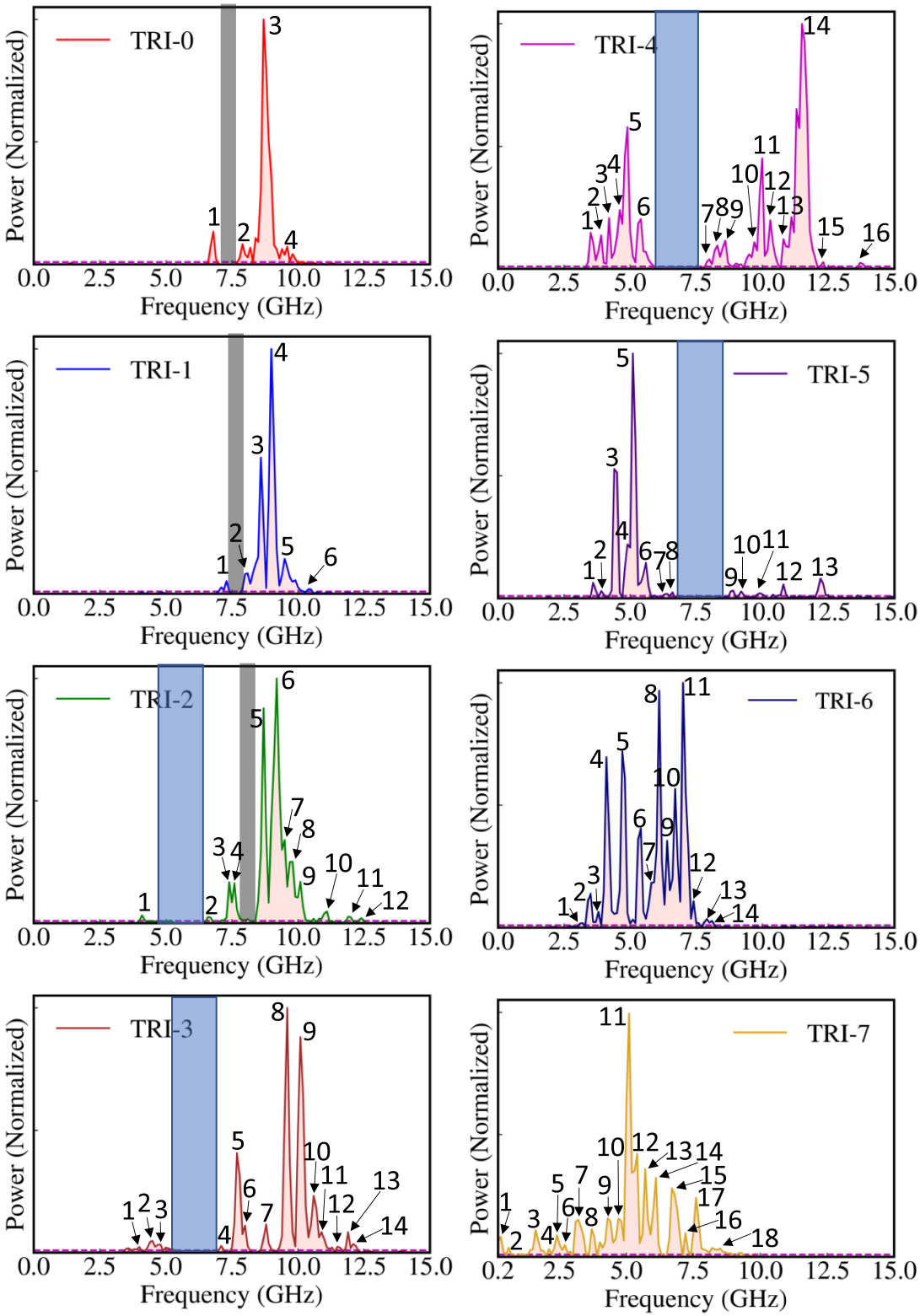

Figure 3. FFT spectra of the simulated time-domain magnetization for different samples at $\boldsymbol{H}_{\text{ext}} = 0.1$ T and $\varphi = 0°$. The mode numbers are shown in the simulated FFT spectra, while the grey and blue rectangle show frequency gaps. All the spin-wave modes which have intensity higher than the magenta dotted line are counted as spin-wave modes.

rectangle starts to appear and a frequency gap is created. As the iteration number increases, due to multiple splitting of the spin-wave modes, two different spin-wave bands are observed separated by this frequency gap (blue) and the frequency gap around 7.5 GHz (grey) vanishes. For TRI-3 and TRI-4, 14 and 16 modes are observed respectively and the high-frequency

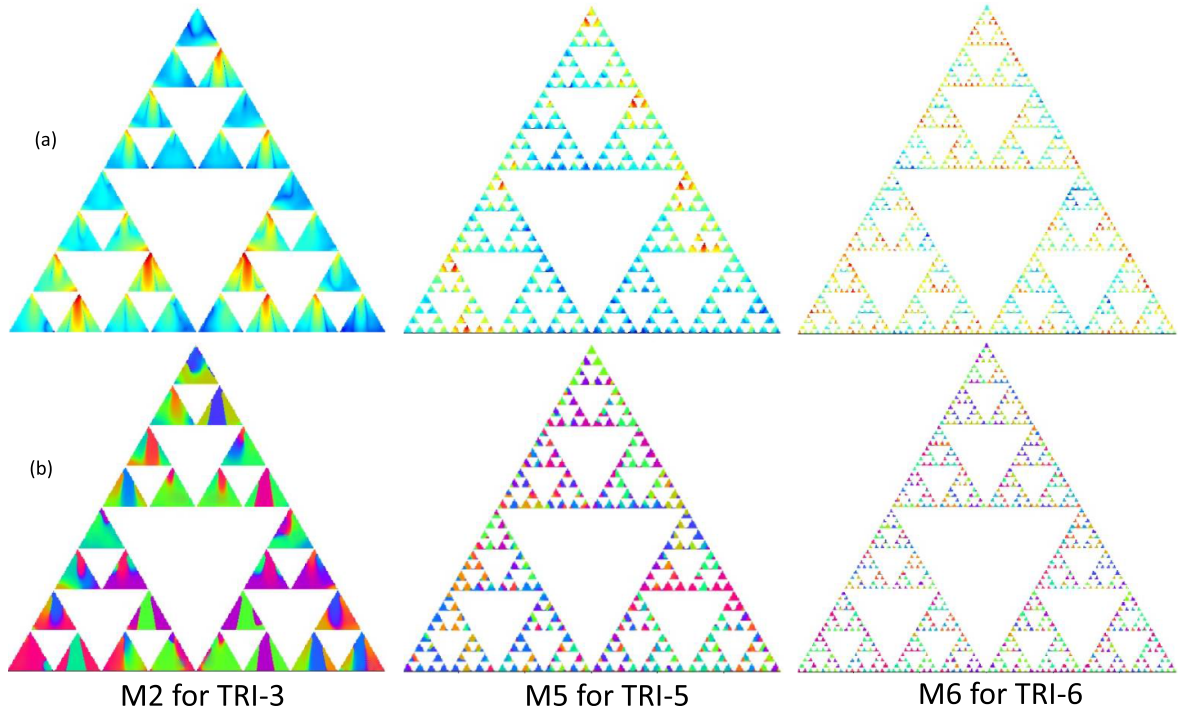

Figure 4. The simulated (a) power and (b) phase profile of the spin-wave mode around 5 GHz, which is M2 for TRI-3, M5 for TRI-5 and M6 for TRI-6 at $\boldsymbol{H}_{\text{ext}} = 0.1$ T and $\varphi = 0^{\circ}$. The similar color scale for power and phase shown in figure 2 are used.

band (M4 to M14 for TRI-3 and M7 to M16 for TRI-4) is present from 7.5 GHz to 12 GHz and the low-frequency band (from M1 to M3 for TRI-3 and M1 to M6 for TRI-4) is observed from 4 to 5.5 GHz. The spin-wave spectra change drastically with a further increase in the iteration number. For TRI-5 the intensity of the lower frequency modes (from M1 to M8) increases significantly whereas the intensity of the higher frequency modes (from M9 to M13) are reduced significantly. For TRI-6 and TRI-7, the frequency gap becomes so wide that it exceeds the considered frequency range, and the higher frequency modes are only present above 15 GHz whereas the lower frequency mode is split into multiple modes due to magnetostatic interactions in the array, and a complex spectrum is observed. A blue shift in the frequency gap is also observed.

The spatial distributions of the spin-wave modes have been calculated for the Sierpinski triangles. The bulk and edge modes of individual triangle are modified when they are arranged in a Sierpinski triangles as the magnetic environment changes. The power and phase profile of the spin-wave mode around frequency $\sim$5 GHz, which is M2 for TRI-3, M5 for TRI-5 and M6 for TRI-6 are shown in figure 4. The phase profile of different spin-wave modes changes significantly as the iteration number increases. The power is distributed randomly throughout the structure. For TRI-3, the power is mainly distributed at the vertices of the triangle, and as the iteration number increases the power starts to distribute uniformly within the triangle. The distribution of the phase as shown in figure 4(b) can explain this nature. For TRI-3, the phase of M2 is continuously changing within the triangle and as the iteration number increases to TRI-5, the phase within the triangle becomes more uniform, and finally for TRI-6 the phase within the triangle is uniform. We found that from TRI-4 to TRI-7 the lower frequency spin-wave modes (in fact in TRI-6 and TRI-7 below 15 GHz) is composed of the fundamental mode of a single triangle (i.e. in-phase oscillations in the single triangle). So, in each small triangle, there is no change of the phase but due to the inter-triangle interactions, the single frequency of the triangle (e.g. TR-7 at 2.5 GHz) split into multiple spin-wave modes and creates a frequency band, similarly to the formation of the bands in crystals. However, the situation results are quite complicated for TRI-0 to TRI-3 because, for a single triangle from TR-0 to TR-3 multiple different kinds of spin-wave modes namely edge, bulk, of different orders of edge and bulk modes are present. These modes are further modified when they are arranged in fractal structures. We propose that two types of magnetostatic interactions are observed for such systems. One is intra-triangular magnetostatic interaction and the other one is inter-triangular magnetostatic interaction. For low iteration number, say from TRI-1 to TRI-4, the spatial distribution shows that the phase changes within individual triangle as the size of the building block is quite large. For such systems intra-triangular magnetostatic interaction is present and dominate (at low frequency part considered in the figure) of the spectra. As the individual triangles are also arranged in a particular fashion, inter-triangular magnetostatic interactions are also present for such systems (TRI-1 and larger), and further modify the spectra. The spatial distribution shows that for TRI-1 to TRI-4 the higher frequency modes are mainly due to the distribution of the bulk modes of the individual triangles and the lower frequency modes are mainly due to the distribution of the edge modes of triangles.

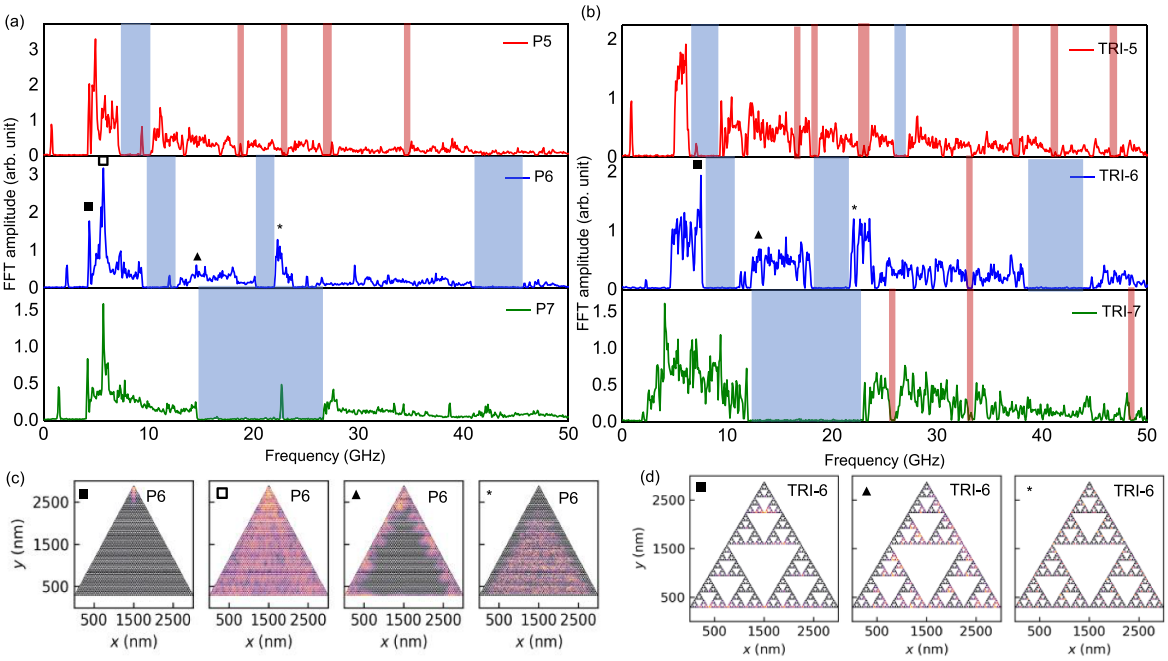

Figure 5. Wide frequency range FFT spectra for different samples: (a) with periodic arrangement of individual triangles: P5, P6 and P7, and (b) Sierpinski triangles: TRI-5, TRI-6 and TRI-7 at $\boldsymbol{H}_{\text{ext}} = 0.1$ T and $\varphi = 0^{\circ}$. The broad frequency gaps are shown by blue rectangles and the mini frequency gaps are shown by red rectangles. The spatial distribution of the marked modes (■, □, ▲ and *) in the FFT spectra for (c) P6 and (d) TRI-6 are shown.

When the iteration number is increased above 4, the size of individual triangles is now below 100 nm, and they can easily form single domain. This is clearly confirmed for TRI-5 and TRI-6, with a nearly uniform (completely uniform for TRI-6) distribution of the phase within the individual triangle at low frequency band (see figure 4). For such a system, mainly the inter-triangular magnetostatic interactions determine the formation of the band. In such a case, we can consider individual triangles connected only at the vertices as three coupled oscillators connected by springs. Such magnetostatically coupled system could have a rich and complex frequency spectrum depending on the phase of their neighbors. As a result, multimode and complex spin-wave spectra are observed for Sierpinski triangles with higher iteration numbers.

3.1.3. The magnetization dynamics of a periodic triangular array with different iteration number. Next, the triangles are arranged in a periodic array as shown in figure 5(b) and the size of the individual triangle is ∼90 nm, 44 nm, and 22 nm respectively, the external size of the structure remains the same. The sizes are similar to the size of individual triangle of TRI-5, TRI-6, and TRI-7 and we named them P5, P6 and P7 respectively. The spin-wave spectra of this periodic structure are also studied by exciting higher-frequency excitation by using Mumax3 [44]. To excite the richer spectrum of spin waves in all triangles we use the Voronoi tessellation algorithm. We divided the system into small random areas, about 30 nm wide each. For each area, we generate a random angle on the y–z plane, which defines the direction of the external microwave magnetic field in that area only. We repeat this for all areas. The exciting field has a sinc time profile and is run for 1 ns. When it is stopped, we start recording the space and time-resolved magnetization every 8.3 ps for 16.6 ns. In these simulations, we extract the maximum value of the spin-wave amplitude over the whole structure and use as the intensity of spin-waves in figures 5 and S4 in supplemental material.

The spin-wave spectra change for the periodic array as compared to the Sierpinski triangles, although the frequency gaps are also present as shown by blue rectangles in figure 5(a). But the spin-wave spectra as well as the frequency gaps of the periodic structure are quite different than the fractal structure. For P5 a single broad frequency gap is present (from 7.5 GHz to 10 GHz), whereas for P6 three broad frequency gaps are observed (gap1: 9.38 GHz to 12.87 GHz, gap2: 20 GHz to 22 GHz, gap3: 41 GHz to 45.5 GHz), and for P7 only one wide frequency gap (from 14.5 GHz to 26.5 GHz) is observed. For P5, there are also a few mini frequency gaps, which are shown by red rectangles in figure 5(a). In the fractal structures, the frequency gaps are more prominent, and there are more mini frequency gaps as compared to the periodic structures, especially at higher iterations. The full frequency spectra for TRI-5, TRI-6 and TRI-7 are also shown in figure 5(b). For TRI-5 two broad frequency gaps (gap1: 6.56 GHz to 9.34 GHz, gap2: 25.57 GHz to 27.44 GHz) and a few mini gaps are present. For TRI-6 three broad frequency gaps (gap1: 7.69 GHz to 11.12 GHz, gap2: 18.09 GHz to 21.62 GHz, and gap3: 38.24 GHz to 44.56 GHz) and one mini gap are

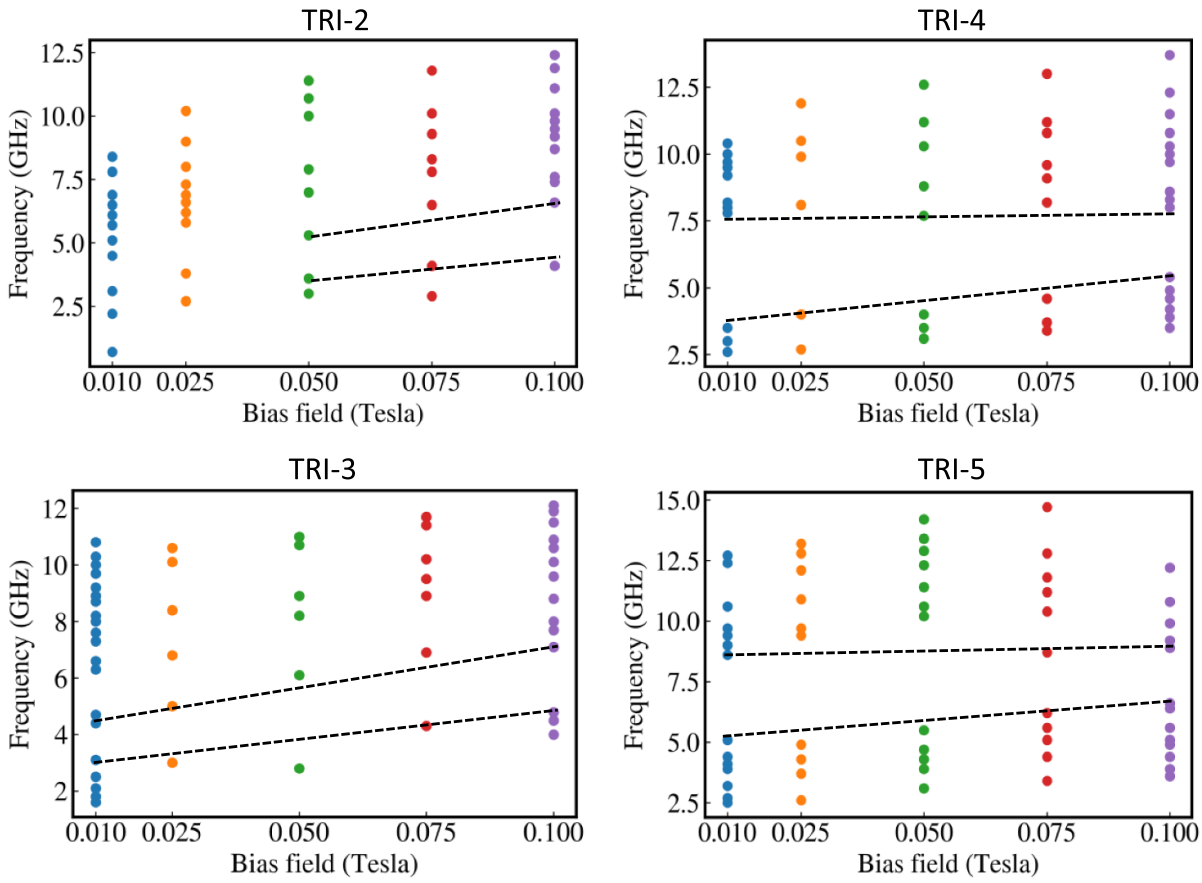

Figure 6. The variation of the precession frequencies for TRI-2, TRI-3, TRI-4 and TRI-5 with the strength of the magnetic field. The frequency gap is shown by the black dotted line.

observed. For TRI-7 one single broad frequency gap (12 GHz to 22.87 GHz) and a few mini gaps are also present. We have compared the spin-wave spectra for P7 and TRI-7, for P7 only the broad frequency gap is present whereas for TRI-7 in addition to a broad frequency gap plenty of mini frequency gaps are present.

The spatial profile of the particular spin wave modes of the periodic and fractal structure for P6 and TRI-6 are also calculated, see figures 5(c) and (d). Similar to the fractal structure, for periodic structure the lower frequency spin-wave modes (from the lower frequency band) are mainly due to the distribution of the mode, where the phase is quite uniform within an individual triangle and the higher frequency spin-wave modes (from the higher frequency bands), which are due to the distribution of the bulk-like mode of the individual triangle. In figures 5(c) and (d), the spatial profile of the spin-wave modes marked by '■', '▲', and '*' from first, second, and third frequency bands, respectively, are shown. For the periodic structure, the spin-wave modes marked by '■', and '▲' are mainly localized at the vertex and edges of the triangle due to the presence of a strong demagnetizing field, and the spin-wave mode marked by '*' is mainly distributed at the center of the array. An additional mode from first frequency band marked by '□', where the intensity of the mode is quite uniformly distributed throughout the array is also shown in figure 5(c). For the periodic structure, the frequencies of all the vertex localized modes (marked by '■') are in the gaps or below the first frequency gap. For the fractal structure, the mode profiles are different, mainly the localized modes are observed at various edges of the Sierpinski triangle (see figure 5(d)). The intensity values of the spin-wave modes for the fractal structure shown in figures 5(a) and (b) are also a few times higher compared to the spin-wave modes in the periodic structure. The localization of the modes is a clear signature of fractal behavior.

3.1.4. Tunning of the frequency gap with the variation of the strength of the magnetic field. Next step is to study and control of the spin-wave spectra with the variation of the strength of the external magnetic field. For that purpose, the magnetization dynamics of TRI-2, TRI-3, TRI-4, and TRI-5 are calculated at the different external magnetic field as shown in figure 6. As mentioned before, rich multimode spin-wave spectra with a clear frequency band gap are present for all the samples at 0.1 T. As the magnetic field decreases the rich spin-wave spectra are present but the frequency of the spin-wave modes decreases systematically with the decrease of the magnetic field. Additional spin-wave modes also start to appear with the decrease of the magnetic field. For TRI-2 and TRI-3 this band gap was reduced systematically with the decrease

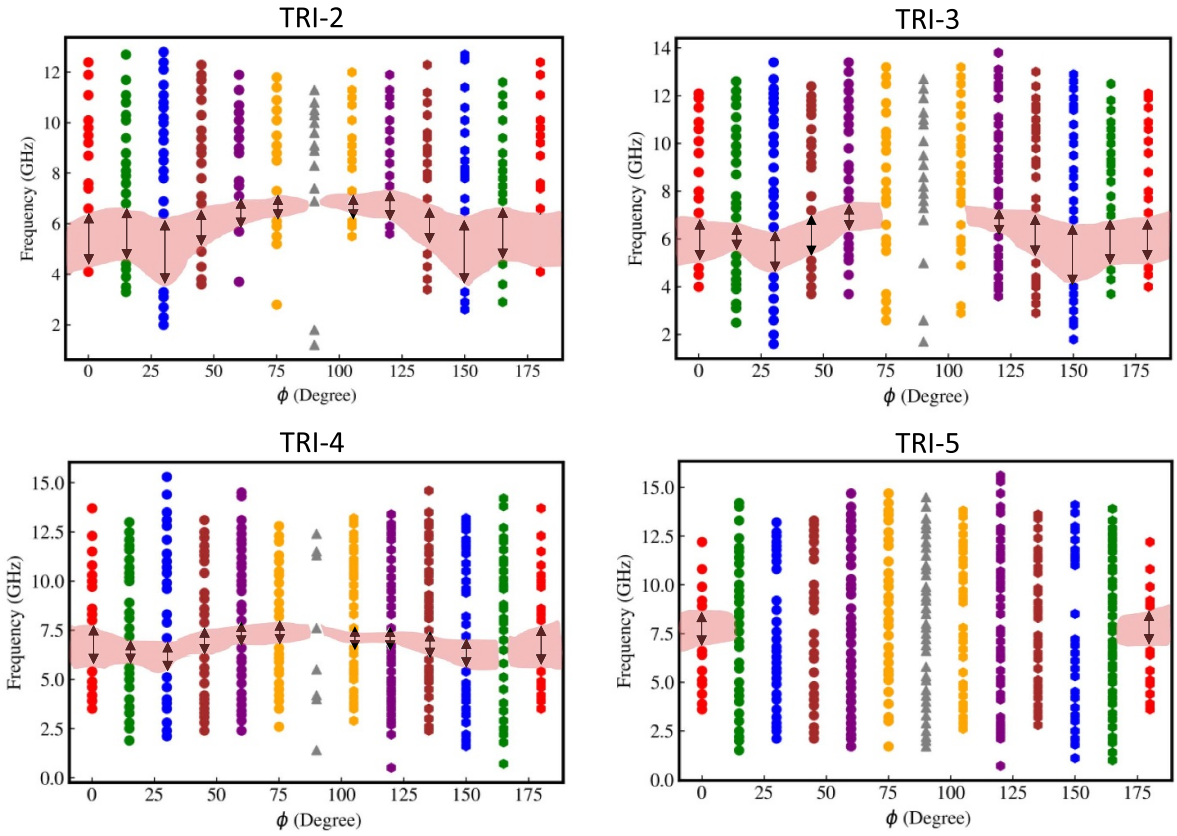

Figure 7. The variation of the precession frequencies for TRI-2, TRI-3, TRI-4 and TRI-5 with the orientation (φ) of the magnetic field ($\boldsymbol{H}_{\text{ext}} = 0.1$ T along $\varphi = 0°$). The frequency gap is shown by pink shaded region and a black arrow.

of the magnetic field, however, for TRI-4, and TRI-5 the frequency band gap increases with the decrease of the magnetic field (shown by the black dotted line in figure 6). For TRI-5, a linear dependence of the frequency gap is observed but the top of the gap a non-monotonous behavior around 0.05 T. The ground state for all the samples at the different magnetic fields is calculated. However, as the magnetic field increases (above saturation magnetic field), the magnetization is aligned along the direction of the applied magnetic field and the ground state is also modified significantly, which affects the modulation of the spin-wave spectra. As the iteration increases, the size of the individual building block of the Sierpinski triangle decreases and the edge effect becomes more prominent for higher iteration number. As a result, at a particular magnetic field bending of the spins increases with the increase of the iteration number (see supplemental figure S1), which modifies the spin-wave spectra.

3.1.5. Tunning of the frequency gap with the orientation of the magnetic field. The spin-wave spectra for TRI-2, TRI-3, TRI-4 and TRI-5 also change with the variation of the azimuthal angle of the external magnetic field as shown in figure 7. For all the samples, the spin-wave spectra are identical for both 0° and 180° but the spin-wave spectra change significantly as the angle changes from 0° to 90°. The splitting in the spin-wave spectra was also modified with the increase of the iteration number as well as with the direction of the applied magnetic field ($\boldsymbol{H}_{\text{ext}}$). As mentioned before that the total effective magnetic field ($\boldsymbol{H}_{\text{eff}}$) of a magnetic element strongly depends on the demagnetizing field ($\boldsymbol{H}_{\text{demag}}$) that arises due to the shape of the element and on the distribution of the magnetostatic stray field which arises due to the arrangement of the elements into an array. This introduces the configurational anisotropy [45] into the system. As the angle changes, the total effective field also changes, which affects the ground state as well as the spin-wave spectra of the systems. But every system has some in-build symmetry due to their boundary, lattice arrangement, and the shape of the individual element. The presence of fourfold, sixfold, eightfold symmetry in configurational anisotropy in circular shaped dot arrays [26] with square, hexagonal, and octagonal lattice symmetry has already been reported. In our case, the basic building block is a triangular shaped magnetic element, which will show a sixfold configurational anisotropy. A small fourfold anisotropy is superposed with the sixfold one due to the square boundary of the image used for simulation. The sixfold anisotropy will further be modified with the increase of the iteration number as the total effective field ($\boldsymbol{H}_{\text{eff}}$) is different for different samples. Next, the frequency gap present for TRI-2, TRI-3, TRI-4 and TRI-5 (shown by the pink shaded region and by the black arrow in figure 7) could also be tuned by varying the direction of the external magnetic field. The frequency gap at 0° is present for all the samples. The spin-wave spectra are not

identical for all supplementary angles (15° and 165° for TRI-3 and TRI-4, 45° and 135° for TRI-5), the gap is also not same for them (see supplementary figure S4). For TRI-2 and TRI-3, the frequency gap increases from 0° to 30° and then reduced from 30° to 60°. At 75° the frequency gap is minimum and at 90° the gap is completely blocked. For TRI-4 a similar behavior is observed but the frequency gap is reduced significantly. For TRI-5, the frequency gap is only present at 0° but the gap completely disappeared with the orientation of the magnetic field. This could be exploited for device applications.

4. Conclusions

In this work, we have investigated the magnetization dynamics of a magnetic Sierpinski triangle, which is a popular example of a deterministic fractal by using micromagnetic simulations. First, the magnetization dynamics of a single triangle of different sizes are studied. A multimode spin-wave spectra is observed for a single triangle with a base length of 2.85 μm and as the size of the triangle reduced to 20 nm only a single spin-wave mode is observed at low frequency range. The phase distribution of the spin-wave modes shows that for a larger triangle the phase changes continuously inside the triangle, whereas for a smaller triangle a uniform distribution of phase is observed because a multidomain system converges to a single domain system with the reduction of the size of the triangle. The magnetization dynamics changes significantly when these triangles are arranged in Sierpinski triangle. A rich complex spin-wave spectra is observed for all the samples and the spin-wave spectra changes significantly with the increase in the iteration number. At 0.1 T a frequency bandgap of $\sim$1.5 GHz is observed for TRI-2 and this gap is present till the iteration number is 5. Beyond iteration number 5, the frequency gap width extends over 15 GHz and only spin-wave modes from the first band are present. The spin-wave dynamics of a periodic triangular array is also studied. Here, the dynamics is quite different compared to the dynamics of a Sierpinski triangle, but the frequency gap is present for both the cases. For such systems both intra- and inter-triangular magnetostatic interactions are present. The inter-triangular magnetostatic interaction is different for a periodic array and Sierpinski triangles, and it is mainly responsible for the modification of the spin-wave spectra in a Sierpinski triangle. The differences between periodic and fractal structures are also visible in the spatial distributions of the spin-wave amplitude, showing localized and extended character, respectively. Next step was to tune the observed frequency gap by changing physical parameter which is one of the important requirements for the application of magnetic fractals as a reconfigurational aperiodic MC. In this case we have tuned it by varying the strength and orientation of the external magnetic field. Interestingly, the variation of the azimuthal angle of the external magnetic field can allow to close the bandgap. This frequency gap could further be tailored to magnonic band structures. The tunability of the frequency gap and existence of the large number of mini-bandgaps could lead to the potential application of the Sierpinski triangles as a nanoscale field-controlled magnonic device, like spin-wave filters or spin-wave splitters.

Data availability statement

The data cannot be made publicly available upon publication because they are not available in a format that is sufficiently accessible or reusable by other researchers. The data that support the findings of this study are available upon reasonable request from the authors.

Acknowledgments

S S gratefully acknowledges the financial support of SERB with file Number SRG/2022/000191 and the Axis Grant at Ashoka University for the funding. S S and R M acknowledge the HPC computer center at Ashoka University. Many thanks to Professor Sabyasachi Bhattacharya, Professor Somendra Mohan Bhattacharya, and Professor Varsha Banerjee for fruitful discussions. M M and M K acknowledges the financial support of NCN Poland Project No. 2020/37/B/ST3/03936.

ORCID iDs

M Moalic https://orcid.org/0000-0002-4562-1543
M Krawczyk https://orcid.org/0000-0002-0870-717X
S Saha https://orcid.org/0000-0001-7832-1072

References

[1] Tehrani S, Chen E, Durlam M, DeHerrera M, Slaughter J M, Shi J and Kerszykowski G 1999 *J. Appl. Phys.* **85** 5822
[2] Kryder M H, Gage E C, Mcdaniel T W, Challener W A, Rottmayer R E, Ju G, Hsia Y-T and Erden M F 2008 *Proc. IEEE* **96** 1810
[3] Parkin S S P, Hayashi M and Thomas L 2008 *Science* **320** 190
[4] Thomson T, Hu G and Terris B D 2006 *Phys. Rev. Lett.* **96** 257204
[5] Allwood D A, Xiong G, Faulkner C C, Atkinson D, Petit D and Cowburn R P 2005 *Science* **309** 1688
[6] Lenk B, Ulrichs H, Garbs F and Münzenberg M 2011 *Phys. Rep.* **507** 107
[7] Kruglyak V, Demokritov O and Grundler D 2010 *J. Phys. D: Appl. Phys.* **43** 260301
[8] Neusser S and Grundler D 2009 *Adv. Mater.* **21** 2927
[9] Kim S K 2010 *J. Phys. D: Appl. Phys.* **43** 264004
[10] Chumak A V, Serga A A, Hillebrands B and Kostylev M P 2008 *Appl. Phys. Lett.* **93** 022508
[11] Vysotskiĭ S L, Nikitov S A and Filimonov Y A 2005 *J. Exp. Theor. Phys.* **101** 547
[12] Demidov V E, Kostylev M P, Rott K, Münchenberger J, Reiss G and Demokritov S O 2011 *Appl. Phys. Lett.* **99** 082507
[13] Kłos J W, Kumar D, Romero-Vivas J, Fangohr H, Franchin M, Krawczyk M and Barman A 2012 *Phys. Rev.* B **86** 184433
[14] Kim S K, Lee K S and Han D S 2009 *Appl. Phys. Lett.* **95** 082507
[15] Au Y, Dvornik M, Dmytriiev O and Kruglyak V V 2012 *Appl. Phys. Lett.* **100** 172408
[16] Kaka S, Pufall M R, Rippard W H, Silva T J, Russek S E and Katine J A 2005 *Nature* **437** 389

[17] Yu H, Duerr G, Huber R, Bahr M, Schwarze T, Brandl F and Grundler D 2013 *Nat. Commun.* **4** 2702
[18] Khitun A, Bao M and Wang K L 2010 *J. Phys. D: Appl. Phys.* **43** 264005
[19] Urazhdin S, Demidov V E, Ulrichs H, Kendziorczyk T, Kuhn T, Leuthold J, Wilde G and Demokritov S O 2014 *Nat. Nanotechnol.* **9** 509
[20] Liu C *et al* 2018 *Nat. Commun.* **9** 738
[21] Saha S, Barman S, Otani Y and Barman A 2015 *Nanoscale* **7** 18312
[22] Mahato B K, Rana B, Mandal R, Kumar D, Barman S, Fukuma Y, Otani Y and Barman A 2013 *Appl. Phys. Lett.* **102** 192402
[23] Ding J, Kostylev M and Adeyeye A O 2012 *Appl. Phys. Lett.* **100** 073114
[24] Vogt K, Fradin F Y, Pearson J E, Sebastian T, Bader S D, Hillebrands B, Hoffmann A and Schultheiss H 2014 *Nat. Commun.* **5** 3727
[25] Krawczyk M and Grundler D 2014 *J. Phys.: Condens. Matter* **26** 123202
[26] Saha S, Mandal R, Barman S, Kumar D, Rana B, Fukuma Y, Sugimoto S, Otani Y and Barman A 2013 *Adv. Funct. Mater.* **23** 2378
[27] Mahato B K, Rana B, Kumar D, Barman S, Sugimoto S, Otani Y and Barman A 2014 *Appl. Phys. Lett.* **105** 012406
[28] Saha S, Barman S, Ding J, Adeyeye A O and Barman A 2013 *Appl. Phys. Lett.* **102** 242409
[29] Lisiecki F *et al* 2019 *Phys. Rev. Appl.* **11** 054061
[30] Watanabe S, Bhat V S, Baumgaertl K, Grundler D, Watanabe S, Bhat V S, Baumgaertl K and Grundler D 2020 *Adv. Funct. Mater.* **30** 2001388
[31] Bhat V S and Grundler D 2018 *Phys. Rev.* B **98** 174408
[32] Lisiecki F *et al* 2019 *Phys. Rev. Appl.* **11** 054003
[33] Dai Y Y, Wang H, Yang T and Zhang Z D 2019 *J. Magn. Mater.* **483** 70
[34] Rychły J, Kłos J W and Krawczyk M 2016 *J. Phys. D: Appl. Phys.* **49** 175001
[35] Shechtman D, Blech I, Gratias D and Cahn J W 1984 *Phys. Rev. Lett.* **53** 1951
[36] Shen X, Li L, Cui W and Feng Y 2018 *Int. J. Heat Mass Transf.* **121** 1307
[37] McMullen C 1984 *Nagoya Math. J.* **96** 1
[38] Alexander S, Laermans C, Orbach R and Rosenberg H M 1983 *Phys. Rev.* B **28** 4615
[39] Nakayama T, Yakubo K and Orbach R L 1994 *Rev. Mod. Phys.* **66** 381
[40] Swoboda C, Martens M and Meier G 2015 *Phys. Rev.* B **91** 064416
[41] Zhou J, Zelent M, Luo Z, Scagnoli V, Krawczyk M, Heyderman L J and Saha S 2022 *Phys. Rev.* B **105** 174415
[42] Donahue M and Porter D G 1999 OOMMF user's guide, version 1.0 *Interagency Report NISTIR 6376* (Gaithersburg, MD: National Institute of Standard and Technology) (available at: http://math.nist.gov/oommf) (Accessed December 2012)
[43] Kumar D, Dmytriiev O, Ponraj S and Barman A 2011 *J. Phys. D: Appl. Phys.* **45** 015001
[44] Vansteenkiste A, Leliaert J, Dvornik M, Helsen M, Garcia-Sanchez F and Van Waeyenberge B 2014 The design and verification of MuMax3 *AIP Adv.* **4** 107133
[45] Cowburn R P, Adeyeye A O and Welland M E 1998 *Phys. Rev. Lett.* **81** 5414

4.5 1D YIG hole-based magnonic nanocrystal

- *1D YIG hole-based magnonic nanocrystal*,
  K.O. Levchenko, K. Davídková, R.O. Serha, **M. Moalic**, A.A. Voronov, C. Dubs, O. Surzhenko, M. Lindner, J. Panda, Q. Wang, O. Wojewoda, B. Heinz, M. Urbánek, M. Krawczyk, A.V. Chumak
  Applied Physics Letters, **127**, 172401 (2025).

4.5.1 Introduction

This study is a collaboration with the experimental group Nanomag of Prof. Chumak from the University of Vienna. We explore how to route and filter spin waves using a one-dimensional magnonic crystal patterned in yttrium iron garnet. Using a nanoscale waveguide with a periodic array of small holes, forming a lattice that shapes the spin-wave spectrum. Using propagating spin-wave spectroscopy and micro-focused Brillouin light scattering, together with micromagnetic simulations, we observe robust transmission over several micrometres and clear stop bands where waves are strongly suppressed. Analysis of the dispersion reveals characteristic mode interactions and anticrossings, with energy transport largely carried by a transverse width mode in the Damon–Eshbach configuration. Altogether, the results point to simple, lithography-friendly building blocks for compact, radio-frequency spin-wave filters and reconfigurable on-chip signal-processing devices.

4.5.1.1 Contribution of the Author

In this publication, I calculated the band structure and transmission spectra using the Amumax software, analysed the resulting data and contributed to the interpretation of experimental results. I helped prepare figure 2 and contributed to the writing and critical review of the manuscript.

Applied Physics Letters

RESEARCH ARTICLE | OCTOBER 27 2025

1D YIG hole-based magnonic nanocrystal

K. O. Levchenko ; K. Davídková ; R. O. Serha ; M. Moalic ; A. A. Voronov ; C. Dubs ; O. Surzhenko ; M. Lindner; J. Panda ; Q. Wang ; O. Wojewoda ; B. Heinz ; M. Urbánek ; M. Krawczyk ; A. V. Chumak

Appl. Phys. Lett. 127, 172401 (2025)
https://doi.org/10.1063/5.0285098

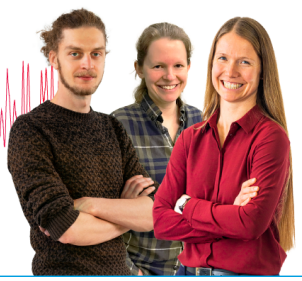

Applied Physics Letters ARTICLE pubs.aip.org/aip/apl

1D YIG hole-based magnonic nanocrystal

Cite as: Appl. Phys. Lett. **127**, 172401 (2025); doi: 10.1063/5.0285098
Submitted: 12 June 2025 · Accepted: 28 September 2025 ·
Published Online: 27 October 2025

K. O. Levchenko,[1,a] K. Davídková,[1,2] R. O. Serha,[1,2] M. Moalic,[3] A. A. Voronov,[1,2] C. Dubs,[4] O. Surzhenko,[4] M. Lindner,[4] J. Panda,[5] Q. Wang,[6] O. Wojewoda,[5] B. Heinz,[7] M. Urbánek,[5] M. Krawczyk,[3] and A. V. Chumak[1]

AFFILIATIONS

[1]Faculty of Physics, University of Vienna, Vienna, Austria
[2]Vienna Doctoral School in Physics, University of Vienna, Vienna, Austria
[3]Department of Physics of Nanostructures, Adam Mickiewicz University, Poznań, Poland
[4]INNOVENT e. V. Technologieentwicklung, Jena, Germany
[5]CEITEC BUT, Brno University of Technology, Brno, Czech Republic
[6]Institute for Quantum Science and Engineering, HUST, Wuhan, China
[7]Fachbereich Physik and Landesforschungszentrum OPTIMAS, RPTU, Kaiserslautern, Germany

[a)]Author to whom correspondence should be addressed: khrystyna.levchenko@univie.ac.at

ABSTRACT

Magnetic media with artificial periodic modulation—magnonic crystals (MCs)—enable tunable spin-wave dynamics and band structure engineering. Nanoscaling enhances these capabilities, making magnonic nanocrystals promising for both fundamental studies and applications. Here, we report on the design, fabrication, and characterization of one-dimensional YIG MCs with nanoholes ($d \approx 150$ nm) spaced $a \approx 1$ μm apart. Microfocused Brillouin light scattering and propagating spin-wave spectroscopy, supported by TetraX and MuMax^3 simulations, reveal spin-wave transmission over 5 μm in the Damon–Eshbach configuration and the formation of pronounced bandgaps with rejection levels up to 26 dB. Detailed analysis of the spin-wave dispersion uncovered complex mode interactions, including two prominent anticrossings at 3.1 and 18.7 rad/μm, between which the spin-wave energy is predominantly carried by the $n = 2$ mode, enabling efficient transmission. The results advance the development of functional MCs and open pathways toward 2D magnonic nanoarrays and magnonic RF nanodevices.

The field of magnonics explores the fundamental and applied potential of the spin waves (SW)—collective oscillations of magnetic moments in a magnetic material. The advantages offered by magnonics include high frequencies, tailored material parameters,[1] low-energy dissipation, and low power consumption, which have been successfully integrated into various prototype circuitry elements,[2,3] with selected concepts surpassing the performance of benchmark conventional devices.[4] Many of them (e.g., filters,[5] transistors,[2] and sensors[6,7]) are realized based on magnonic crystals (MCs)—artificial magnetic materials with a spatially periodic variation of properties.[8–10] The growing potential of nanoscale magnonics for RF applications, including MCs, was highlighted in a recent review.[11] Similar to photonic crystals operating with light, MCs use the wave nature of their quasiparticles—magnons—to achieve propagation characteristics that are inaccessible by other means.[10,12] Key properties of MCs, such as the central frequency and bandgap width, can be tailored by adjusting (often simultaneously) (1) the use of different materials with suitable magnetic properties (e.g., saturation magnetization[13–16]), (2) the choice of the periodic pattern,[17] and (3) external factors, such as the applied magnetic field[18] or temperature.[19] Different combinations of these properties produce a variety of MC designs, including waveguide-[19,20] and thin-film-based[12] structures; one-,[21–25] two-,[26,27] and three-[28,29] dimensional structures; and static,[14,15,17] dynamic,[18,30] and reconfigurable[19,31] MCs.

The simplest and most efficient type of MC is a one-dimensional (1D) structure with geometric patterning. Typically, a 1D MC is fabricated from a waveguide, where patterning enables the structure to act as a wavevector-dependent, mode-selective system.[9,32] 1D MCs can function as standalone devices or serve as building blocks for magnonic directional couplers, transistors, phase shifters, and other RF

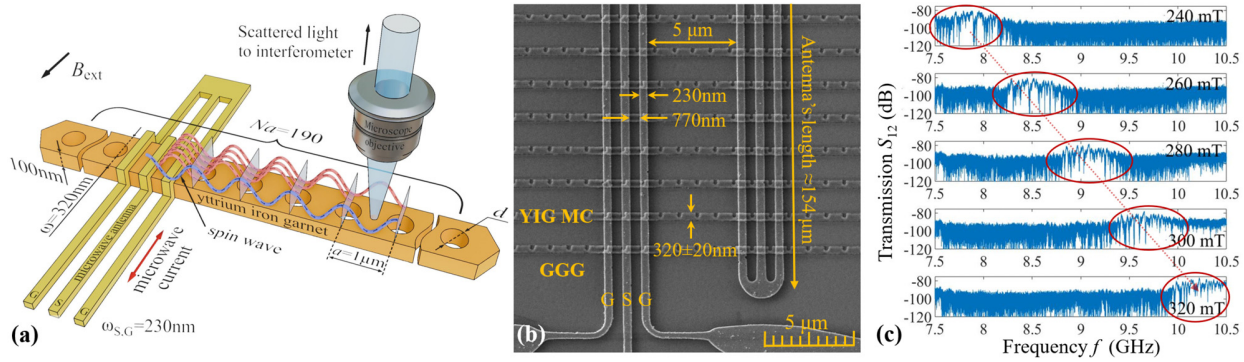

FIG. 1. (a) Sketch of 1D waveguide-based MC periodically modulated with round holes. Spin waves excited by the CPW are shown in blue, while Bragg-reflected waves in red. Key parameters: $\omega = 320$ nm, waveguide's width; $a = 1$ μm, MC's period; $N_a \approx 200$, total number of periods; and $d = 150$ nm, diameter of the holes. (b) SEM image of the typical 1D MC fabricated from a 100 nm-thick LPE-grown YIG/GGG film, with key parameters as in (a). The number of waveguides per antenna is $n_{wg} = 100$, the distance between the antennas is 5 μm. (c) Spin-wave transmission signal S_{12} of MC shown at (b) for varying bias magnetic fields in a frequency range of 7.5–10.5 GHz.

and data-processing components.[2] One of the fundamental works on this topic—a study on a geometrically patterned (notched) microscale Permalloy 1D MC—was realized by Chumak *et al.*,[22] based on a theoretical model by Lee *et al.*[33] and numerical simulations by Ciubotaru *et al.*[34] The authors experimentally demonstrated the propagation of coherently excited SWs through a metallic MC; however, in such macrostructured waveguides, the SW dispersion is inherently multimode,[35] resulting in the simultaneous transmission of waves with different wavelengths at a fixed frequency. In MCs, this leads to bandgap (BG) edges being less defined, forming a gradual slope in the transmission spectra,[22] rendering their operating characteristics less favorable for applications.[36]

To overcome this limitation, MCs based on nanowaveguides can be considered. The effects of downscaling on the SW spectra were explored by Wang *et al.*[37] and Heinz *et al.*[38,39] When the width of an yttrium iron garnet (YIG) waveguide is sufficiently small, exchange interaction dominates over dipolar one, leading to unpinning of SW modes. This alters the quantization condition and shifts higher-order width modes to higher frequencies, effectively providing a single-mode regime.[37] Nanoscale enables key advantages for applications, as shown experimentally by Davídková *et al.*[40] in a multifunctional tunable magnonic nanodevice, or numerically by Ge *et al.*[41] in magnon nanotransistor. In the latter, notably, authors propose to use MC for precise control of the SW propagation and frequency-specific filtering. While nanoscale MCs hold great promise, their potential remains largely unrealized due to the relatively recent advances in nanofabrication.

Here, we report on the experimental realization of a nanoscale 1D waveguide-based MC, geometrically modulated with round holes. Based on our preliminary studies, MCs with optimized geometrical parameters were designed and fabricated. Then, a detailed analysis of the SW transmission in Damon–Eschbach (DE) configuration was performed with the means of propagating spin-wave spectroscopy (PSWS) across different frequency ranges, complemented by TetraX and MuMax^3 simulations of the dispersion relation. Finally, microfocused Brillouin light scattering (μ-BLS) spectroscopy was carried out to demonstrate the spatial behavior of excitations in a single MC waveguide.

Figure 1 presents a sketch of an individual MC waveguide with key parameters (a) and SEM image of a section of the entire fabricated structure (b). The crystal periodicity $a = 1$ μm was selected to align with the maximum excitation efficiency of the antenna[42] (see the supplementary material). The waveguide's width was designed as $\omega = 300$ nm to support a single SW mode in a specific range, e.g., 8–8.2 GHz (<5 rad/μm) under a 262 mT bias field in DE and 10.3–10.9 GHz in a backward volume configuration. After the fabrication, the width was around 320 nm, decreasing a single-mode window to around 100 MHz frequency bandwidth under the same bias field. The total waveguide's length of $\approx$190 μm was chosen to be significantly longer than the estimated SW decay length ($\approx$15.8 μm, see supplementary material Fig. S1) to ensure that SW energy is fully dissipated before reaching the waveguide ends and prevent any edge reflections from interfering with the main signal. The hole diameter d modulates the SW reflection efficiency and thus affects the width and depth of the rejection bands.[10] Based on our simulations of similar structures, $d = 150$ nm was estimated to provide the best ratio of minimized losses to well-defined BGs. The holes' pattern persisted along the whole waveguide. All structures were realized from an LPE-grown 100 nm-thick YIG/GGG (111) film[43,44] using e-beam lithography and ion etching.[38] To estimate the SW propagation length, multiple pairs of coplanar waveguide (CPW) antennas with varying spacings of 1, 2, 5, and 10 μm were fabricated. Considering the small excited magnetic volume and potentially weak PSWS signal, each separate MC structure included up to 100 conduits. Coplanar waveguides were used for coherent SW excitation and detection. Fabrication parameters matched the designed ones, apart from the conduits' width, as mentioned earlier, and the slight upward shift of the holes.

An exemplary propagating SW spectrum, shown in Fig. 1(c), was measured on the 1D MC structure presented in Fig. 1(b). The SW transmission S_{12} was recorded while applying a fixed microwave signal with -10 dBm power to the structure under test in DE configuration (in-plane, $k \perp B_{ext}$). The DE geometry was selected due to its higher excitation efficiency (compared to the backward volume, see the supplementary material), enabled by higher SW group velocity and stronger coupling to the in-plane antenna field. The measured complex propagating SW signal, recalculated to dB magnitude (red circles, motion direction indicated by arrow), was obtained while sweeping the magnetic field from 240 to 320 mT in 20 mT steps across

7.5–10.5 GHz frequencies. Reference background was subtracted as shown in our earlier work;[40] other frequency and power ranges are provided in the supplementary material. The obtained SW spectrum significantly differs from that of a plain film by displaying "bandgaps" or "rejection bands" — regions where propagation is prohibited and the signal's magnitude drops due to the Bragg's scattering of SW from the periodic holes[8–10] ($n_{mc}\lambda = 2\,a \cdot \sin\theta$, where n_{mc} is an integer, λ is a SW wavelength, and θ is an incident SW angle). Only the SWs with wavenumbers $k_a = \pm n_{mc}\pi/a$ satisfy this condition. The BG frequency depends on the material parameters and MC spatial geometry and can be tuned by the applied magnetic field, while the number of gaps is defined by the Fourier distribution of spatial modulators.[10] Here, each hole introduces a sharp magnetic contrast (step-like function), generating multiple periodic bandgaps. Accordingly, in "transmission" or "propagation" bands, where the Bragg condition is not satisfied, SW energy is expected to propagate without interruption, aside from higher insertion losses compared to an unstructured waveguide.[10] Losses at the level of $\approx -80\ldots-85$ dB are rather expected due to the low volume of magnetic material in structurally modulated nanowaveguides. For reference, in a similar experiment by Davídková *et al.*[40] on a 97 nm-thick unstructured YIG film, the PSWS signal displayed losses of $\approx -25\ldots-35$ dB at -10 dBm power level. These losses can be further reduced up to four times through optimization of antennas' SW excitation efficiency.[45] Therefore, having a considerable number of the conduits within one MC structure was crucial for successful signal detection, despite increasing the risk of structural imperfections affecting the transmission.

The results of TetraX[46,47] and Amumax[48] micromagnetic simulations (a fork of MuMax^3 [49,50]) are presented in Figs. 2(a)–2(c), respectively. The waveguide was modeled according to the geometry in Fig. 1(b) with the following YIG parameters: saturation magnetization $M_s = 139$ kA/m, exchange stiffness $A = 3.7$ pJ/m, uniaxial magnetic anisotropy $K_u = 3.58$ J/m^3 ($\perp$ y axis), and Gilbert damping $\alpha = 10^{-4}$. Bias field $B_{ext} = 262$ mT was applied along the x axis. Mode profiles in Fig. 2(a) were calculated for the unstructured waveguide cross section at $k = 0$, considering only the first five ($n = 5$) modes due to the quadratic decrease in dynamic magnetization intensity with increasing n. The real part of the magnetization component m_y in the DE configuration is color-coded with red and blue (more in the supplementary material). In this work, the mode labeling deviates from the standard convention by including edge modes, where SWs are confined to the waveguide's edges. These modes arise from nonuniform internal fields and dipolar interactions in finite-sized structures and are labeled here as $n = 0, 1$. Among them, only the $n = 1$ mode could be excited due to its symmetric mode profile. However, it cannot be resolved in the experiment because of its low amplitude and group velocity. Due to lateral confinement, the profiles show only the width quantization components $k_x = n\pi/\omega$, with the first width mode being $n = 2$. Under direct antenna excitation, only even width modes ($n = 2, 4, \ldots$) are efficiently excited, as odd ones ($n = 3, 5, \ldots$) have no net dynamic magnetization averaged across the width. In practice, slight antenna nonuniformity can excite odd modes, albeit inefficiently. Notably, while the mode profiles appear overall unpinned in a cross section, pinning persists at the waveguide's edges [see Fig. 2(a) $n = 2$], which introduces elastic scattering into higher-order width modes. This occurs because of the larger nanowaveguide's width than required for a complete unpinning of the SW mode profile at the edges.[37,38]

The dispersion relation of the MC is shown in Fig. 2(b). To obtain it, the magnetization's y-components were recorded as functions of position and time, followed by a discrete Fourier transform along both axes for each simulation cell. The absolute value of the resulting complex spectra was computed and summed over the x- and z-axes to yield the final map. Black dashed lines correspond to the intersection of the estimated resonance conditions for Bragg scattering $k_a = \pm n_{mc}\pi/a$ with micromagnetic simulation and experimental SW transmission [left panel of Fig. 2(c)]. To obtain it, "raw" data from Fig. 1(c) were subjected to "time gating"[51] post-processing (details in the supplementary material), improving the signal-to-noise ratio and increasing BG rejection efficiency through the elimination of main spurious signals. The highest signal amplitude originates from SWs with lower wavenumbers, driven by higher group velocity and efficient CPW excitation. Exceptions occur at anticrossing points, where mode hybridization leads to spatial localization and standing wave

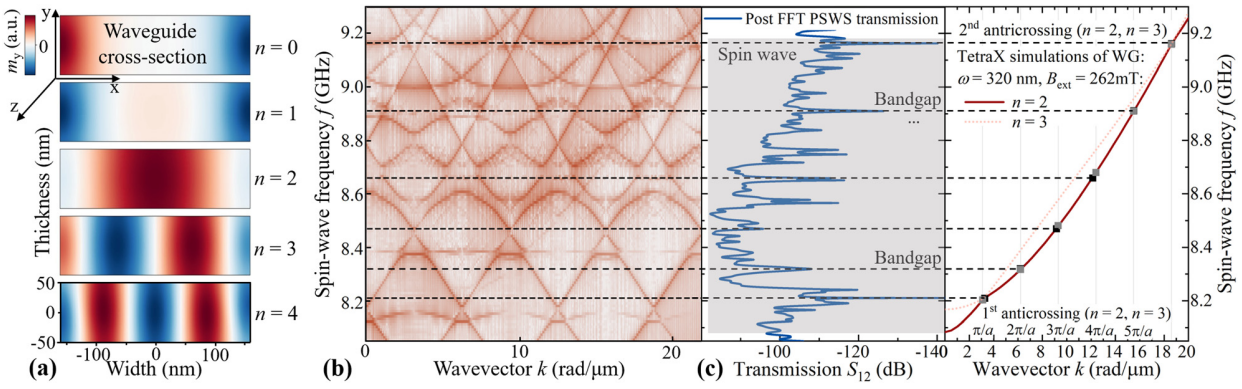

FIG. 2. (a) TetraX simulation of the mode profile amplitudes for the first 5 SW modes of the unstructured waveguide in DE geometry with parameters as shown in Fig. 1(b). The real part of the magnetization dynamic component m_y is calculated for the waveguide cross section at $k = 0$. (b) MuMax^3 micromagnetic simulation of the 1D MC dispersion relation. (c) SW transmission S_{12} at bias field ≈ 262 mT after "time gating" post-analysis vs TetraX-simulated dispersion of a uniform waveguide in DE configuration. Gray squares indicate the intersection of the wavenumbers $k_a = \pm n_{mc}\pi/a$ at the bandgap frequencies with the TetraX-simulated dispersion (crimson solid line), while black squares – the intersection of dispersion with the MuMax^3/experimental data, as shown by the gray solid (c, right panel) and black dashed (b, c) projection lines.

formation, resulting in a transmission drop below 140 dB. Six distinct BGs were identified in a spectrum: five arising from the hole-induced gaps between the antennas ($k = 3.1$ rad/μm, $n_{mc} = 1, .., 5$) and two anticrossings ($k \approx 3.1$ and $k \approx 18.7$ rad/μm), the first coinciding with the structural gap. These anticrossings were revealed with TetraX dispersion simulation [Fig. 2(c) right panel] for the modes $n_{mc} = 2$ and 3 of the unstructured waveguide (crimson solid and peach dotted lines, respectively). Gray squares mark intersections of the BG wavenumbers k_a (thin solid gray lines) with the TetraX simulation of a WG dispersion, while black squares mark the intersection of dispersion with the experimental data/MuMax[3] results (black dashed lines). The rejection efficiency of the bandgaps is between 12.6 and 26.1 dB. The dispersion reveals that the investigated 1D MC operates predominantly in a single-mode within the frequencies 8.08–8.17 GHz (<3.1 rad/μm). Reducing the waveguide width to approximately 280 nm is expected to eliminate mode anticrossings, while further narrowing to 250 nm would expand the single-mode frequency range sevenfold to 7.91–8.56 GHz (up to 12 rad/μm; see the supplementary material). We can also assume that within the linear regime, the majority of the SW energy is effectively carried by $n = 2$ mode in the range 8.2–9.16 GHz (3.1–18.7 rad/μm), since the edge modes $n = 0$, 1 and the odd mode $n = 3$ are not excited effectively. Both the MuMax[3] and TetraX simulations of an individual waveguide showed good agreement with the experiment, considering the cumulative PSWS signal from 100 conduits. The minor misalignment, along with the appearance of multiple weakly defined gaps, is associated with fabrication imperfections. Defect-related variations in hole positioning and etching parameters between different waveguides, as well as within a single waveguide, cause reflections with slightly different amplitudes, phases, and wavelengths, leading to multiple Bragg conditions across the structure(s). This results in SW reflections at slightly different wavevectors and the appearance of a few closely spaced bandpass peaks in the transmission spectrum [e.g., Figs. 2(c) and 3(b)].

After PSWS, coherently excited SWs were probed by μ-BLS spectroscopy.[52,53] An in-plane external field of $\mu_0 H_{ext} = 238.6$ mT was applied along the CPW antenna, ensuring uniform magnetization in DE configuration. Spectral analysis of the scattered light was performed using a 6-pass tandem Fabry–Pérot interferometer and a $\lambda_{Laser} = 457$ nm[54] blue laser. Unlike PSWS, μ-BLS enables probing SW propagation within a single MC nanowaveguide. Figure 3 shows the SW signal, measured ≈ 5 μm away from the CPW antenna (inset) on an MC with identical structural parameters to that analyzed by PSWS. Measurements were performed by sweeping the excitation frequency $f_{ext} = 7 - 7.8$ GHz in $\Delta f = 0.01$ GHz steps at a constant -10 dBm power. The SW signal in the form of BLS detector intensity (counts, Stokes part) is presented as a 2D map [Fig. 3(a)], where each y axis point corresponds to the integrated BLS counts at respective f_{ext}, and as a 3D intensity map [Fig. 3(b)], where the y axis shows the full range of measured frequency f at each excitation f_{ext}; signal intensity color-coded as the z axis. BLS measurements were performed at the waveguide's center. While sweeping the microwave frequency, four periodically spaced passbands were observed (red and green areas in the 3D map), with the first signal appearing at 7.05 GHz and subsequent bands spaced by approximately 0.19 GHz. For clarity, adjacent peaks were Lorentzian-fitted (gray-shaded areas), with the first peak, corresponding to the passband center, located at 7.09 GHz. Regions dominated by the background BLS counts (blue areas on the 3D map)

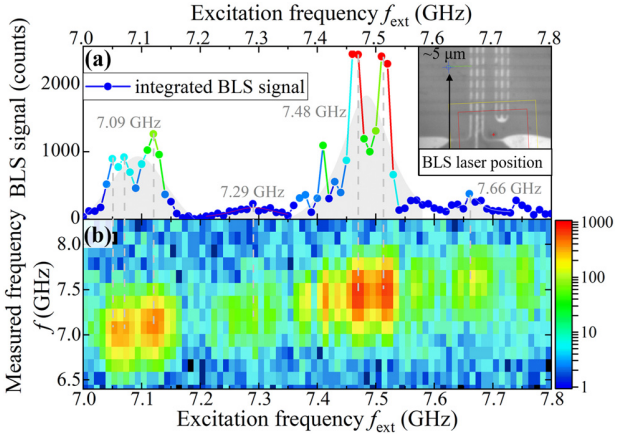

FIG. 3. BLS signal intensity of the propagating SW as a function of coherent excitation f_{ext} (x axis) in a form of: (a) 2D graph, where each y axis point corresponds to the integrated BLS counts over the respective excitation frequency f_{ext}; (b) a 3D intensity map, where the y axis shows the full range of measured frequency f at each excitation frequency f_{ext}, and BLS signal intensity (log scale) is color-coded at z axis. Gray-shaded areas are fitted with a Lorentzian, with the peak frequency highlighted. Measurements were performed 5 μm away from the coplanar waveguide's antenna (inset).

represent five BGs measured 4.5 structural periods from the excitation antenna within a single MC waveguide. The diminishing BLS counts and the appearance of two-three separated peaks in the vicinity of 7.09 and 7.48 GHz indicate structural imperfections.

Finally, we investigated the SW transmission in the passband and bandgap regions by sweeping the laser position from 0 to 5 μm away from the antenna in ≈ 100 nm step. Figure 4 demonstrates the maximum BLS intensity at the passband excitation frequency $f_{ext} = 7.04$ GHz (red circles) and at the bandgap frequency $f_{ext} = 7.2$ GHz (blue squares). The passband signal is an order of magnitude stronger than that of a bandgap, confirming the SW filtering. Linear fitting reveals a smaller slope for the bandgap signal (light-blue dots) compared to the passband (orange dashes), indicating suboptimal excitation efficiency and enhanced signal dissipation due to holes beneath the antenna.

In conclusion, we demonstrated efficient SW propagation in nanoscale one-dimensional YIG magnonic crystal modulated with

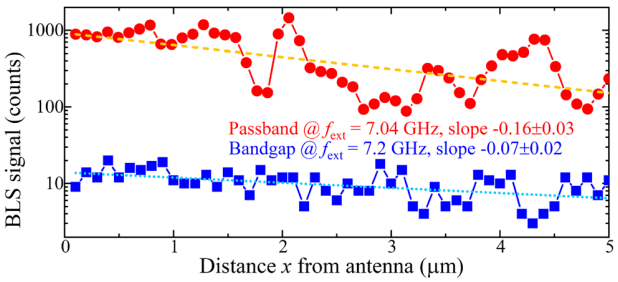

FIG. 4. BLS signal intensity of the propagating spin wave as a function of a laser scan position 0–5 μm from the antenna (x axis); each y axis point corresponds to maximum BLS counts at the respective passband (red) or bandgap (blue) excitation frequency.

holes. PSWS and BLS investigations revealed well-defined magnonic passbands and bandgaps with a rejection efficiency up to 26 dB, corresponding to Bragg scattering from the periodic holes. Single-mode operation is achieved below the first anticrossing (<3.1 rad/μm) within a 100 MHz bandwidth and can be further enhanced by narrowing the waveguides. Between the first and second anticrossings (1 GHz bandwidth, 3.1–18.7 rad/μm), most SW energy is carried by the $n=2$ mode, enabling effective SW transmission. While nanoscaling increases insertion losses and structural defects affecting the spectra, simulations confirm these to be only technical constraints. Future fabrication improvements are expected to firmly establish 1D YIG-based MCs as promising platforms for low-energy, high-frequency RF applications and magnonic computing.

See the supplementary material for details on the fabrication process, analytical calculations performed in MATLAB, micromagnetic simulations using Amumax and TetraX, and the PSWS setup description. Additional content also includes PSWS responses across various frequency ranges and microwave powers, time-gating post-analysis for signal-to-noise enhancement, and extended data from μ-BLS measurements.

The research is funded by the Austrian Science Fund (FWF) project ESP 526-N TopMag (10.55776/ESP526) and by FWF IMEC (10.55776/PAT3864023). M.M. and M.K. acknowledge Grant by the National Science Center of Poland (NCN) No. UMO–2020/37/B/ST3/03936 and 2023/49/N/ST3/03538. The work of M.L. was supported by the German Bundesministerium für Wirtschaft und Energie (BMWI) under Grant No. 49MF180119. B.H. acknowledges funding by the European Research Council within the Starting Grant No. 101042439 "CoSpiN." M.U. acknowledges the support of the Grant Agency of the Czech Republic, Project No. 23-04120L. O.W. acknowledges Project No. CZ.02.01.01/00/22 008/0004594 (TERAFIT). The CzechNanoLab project funded by MEYS CR (LM2023051) is acknowledged for supporting sample fabrication at the CEITEC Nano Research Infrastructure. The authors thank Barbora Koraltan and Sabri Koraltan for the valuable discussions.

AUTHOR DECLARATIONS

Conflict of Interest

The authors have no conflicts to disclose.

Author Contributions

K. O. Levchenko: Conceptualization (lead); Data curation (lead); Formal analysis (lead); Funding acquisition (equal); Investigation (lead); Methodology (lead); Project administration (lead); Software (equal); Validation (lead); Visualization (lead); Writing – original draft (lead); Writing – review & editing (equal). **K. Davídková:** Formal analysis (equal); Investigation (equal); Methodology (equal); Validation (equal); Writing – review & editing (equal). **R. O. Serha:** Formal analysis (equal); Investigation (equal); Methodology (equal); Validation (equal); Visualization (equal); Writing – review & editing (equal). **M. Moalic:** Formal analysis (equal); Funding acquisition (supporting); Investigation (equal); Methodology (equal); Software (equal); Validation (equal); Writing – review & editing (equal). **A. A. Voronov:** Formal analysis (supporting); Investigation (equal); Methodology (equal); Software (equal); Writing – review & editing (equal). **C. Dubs:** Funding acquisition (supporting); Methodology (equal); Resources (equal); Validation (equal); Writing – review & editing (equal). **O. Surzhenko:** Methodology (equal); Writing – review & editing (equal). **M. Lindner:** Funding acquisition (supporting); Methodology (equal); Writing – review & editing (equal). **J. Panda:** Methodology (equal); Writing – review & editing (equal). **Q. Wang:** Methodology (equal); Validation (equal); Writing – review & editing (equal). **O. Wojewoda:** Methodology (supporting); Validation (equal); Writing – review & editing (equal). **B. Heinz:** Funding acquisition (supporting); Validation (equal); Writing – review & editing (equal). **M. Urbánek:** Funding acquisition (supporting); Methodology (supporting); Resources (equal); Validation (equal); Writing – review & editing (equal). **M. Krawczyk:** Formal analysis (equal); Funding acquisition (supporting); Investigation (supporting); Methodology (supporting); Resources (equal); Software (equal); Validation (equal); Writing – review & editing (equal). **A. V. Chumak:** Conceptualization (supporting); Formal analysis (equal); Funding acquisition (supporting); Investigation (supporting); Methodology (supporting); Resources (lead); Supervision (supporting); Validation (supporting); Writing – original draft (supporting); Writing – review & editing (supporting).

DATA AVAILABILITY

The data that support the findings of this study are available from the corresponding author upon reasonable request.

REFERENCES

[1]T. Böttcher, M. Ruhwedel, K. O. Levchenko, Q. Wang, H. L. Chumak, M. A. Popov, I. V. Zavislyak, C. Dubs, O. Surzhenko, B. Hillebrands, A. V. Chumak, and P. Pirro, Appl. Phys. Lett. **120**, 102401 (2022).
[2]A. V. Chumak, A. A. Serga, and B. Hillebrands, Nat. Commun. **5**, 4700 (2014).
[3]G. Talmelli, T. Devolder, N. Träger, J. Förster, S. Wintz, M. Weigand, H. Stoll, M. Heyns, G. Schütz, I. P. Radu *et al.*, Sci. Adv. **6**, eabb4042 (2020).
[4]Q. Wang, M. Kewenig, M. Schneider, R. Verba, F. Kohl, B. Heinz, M. Geilen, M. Mohseni, B. Lägel, F. Ciubotaru *et al.*, Nat. Electron. **3**, 765 (2020).
[5]H. Merbouche, M. Collet, M. Evelt, V. E. Demidov, J. L. Prieto, M. Munoz, J. Ben Youssef, G. de Loubens, O. Klein, S. Xavier *et al.*, ACS Appl. Nano Mater. **4**, 121 (2021).
[6]M. Inoue, A. Baryshev, H. Takagi, P. B. Lim, K. Hatafuku, J. Noda, and K. Togo, Appl. Phys. Lett. **98**, 132511 (2011).
[7]P. J. Metaxas, M. Sushruth, R. A. Begley, J. Ding, R. C. Woodward, I. S. Maksymov, M. Albert, W. Wang, H. Fangohr, A. O. Adeyeye *et al.*, Appl. Phys. Lett. **106**, 232406 (2015).
[8]B. Lenk, H. Ulrichs, F. Garbs, and M. Münzenberg, Phys. Rep. **507**, 107 (2011).
[9]M. Krawczyk and D. Grundler, J. Phys. **26**, 123202 (2014).
[10]A. V. Chumak, A. A. Serga, and B. Hillebrands, J. Phys. D **50**, 244001 (2017).
[11]K. O. Levchenko, K. Davídková, J. Mikkelsen, and A. V. Chumak, arXiv:2411.19212 (2024).
[12]H. Puszkarski and M. Krawczyk, Solid State Phenom. **94**, 125 (2003).
[13]G. Gubbiotti, S. Tacchi, M. Madami, G. Carlotti, A. Adeyeye, and M. Kostylev, J. Phys. D **43**, 264003 (2010).
[14]B. Obry, P. Pirro, T. Brächer, A. V. Chumak, J. Osten, F. Ciubotaru, A. A. Serga, J. Fassbender, and B. Hillebrands, Appl. Phys. Lett. **102**, 202403 (2013).
[15]M. Mruczkiewicz, P. Graczyk, P. Lupo, A. Adeyeye, G. Gubbiotti, and M. Krawczyk, Phys. Rev. B **96**, 104411 (2017).
[16]C. Dubs and O. Surzhenko, Adv. Electron. Mater. **11**(15), e00232 (2025).
[17]Q. Wang, Z. Zhong, L. Jin, X. Tang, F. Bai, H. Zhang, and G. S. Beach, J. Magn. Magn. Mater. **340**, 23 (2013).
[18]A. V. Chumak, T. Neumann, A. A. Serga, B. Hillebrands, and M. P. Kostylev, J. Phys. D **42**, 205005 (2009).

[19]M. Vogel, A. V. Chumak, E. H. Waller, T. Langner, V. I. Vasyuchka, B. Hillebrands, and G. Von Freymann, Nat. Phys. **11**, 487 (2015).
[20]P. Frey, A. A. Nikitin, D. A. Bozhko, S. A. Bunyaev, G. N. Kakazei, A. B. Ustinov, B. A. Kalinikos, F. Ciubotaru, A. V. Chumak, Q. Wang *et al.*, Commun. Phys. **3**, 17 (2020).
[21]Y. Ikezawa, K. Nishimura, H. Uchida, and M. Inoue, J. Magn. Magn. Mater. **272–276**, 1690 (2004).
[22]A. V. Chumak, P. Pirro, A. A. Serga, M. Kostylev, R. Stamps, H. Schultheiss, K. Vogt, S. Hermsdoerfer, B. Laegel, P. Beck *et al.*, Appl. Phys. Lett. **95**, 262508 (2009).
[23]J. W. Kłos, D. Kumar, J. Romero-Vivas, H. Fangohr, M. Franchin, M. Krawczyk, and A. Barman, Phys. Rev. B **86**, 184433 (2012).
[24]H. Qin, G.-J. Both, S. J. Hämäläinen, L. Yao, and S. van Dijken, Nat. Commun. **9**, 5445 (2018).
[25]A. Roxburgh and E. Iacocca, Magnetochemistry **10**, 14 (2024).
[26]S. Tacchi, M. Madami, G. Gubbiotti, G. Carlotti, A. O. Adeyeye, S. Neusser, B. Botters, and D. Grundler, IEEE Trans. Magn. **46**, 172 (2010).
[27]S. Tacchi, P. Gruszecki, M. Madami, G. Carlotti, J. W. Kłos, M. Krawczyk, A. Adeyeye, and G. Gubbiotti, Sci. Rep. **5**, 10367 (2015).
[28]M. Krawczyk and H. Puszkarski, Phys. Rev. B **77**, 054437 (2008).
[29]M. Krawczyk, J. Klos, M. Sokolovskyy, and S. Mamica, J. Appl. Phys. **108**, 093909 (2010).
[30]A. V. Chumak, V. S. Tiberkevich, A. D. Karenowska, A. A. Serga, J. F. Gregg, A. N. Slavin, and B. Hillebrands, Nat. Commun. **1**, 141 (2010).
[31]S. Mantion, A. T. Dias, M. Madami, S. Tacchi, and N. Biziere, J. Appl. Phys. **135**, 053902 (2024).
[32]A. Karenowska, A. Chumak, A. Serga, J. Gregg, and B. Hillebrands, Appl. Phys. Lett. **96**, 082505 (2010).
[33]K.-S. Lee, D.-S. Han, and S.-K. Kim, Phys. Rev. Lett. **102**, 127202 (2009).
[34]F. Ciubotaru, A. Chumak, N. Y. Grigoryeva, A. Serga, and B. Hillebrands, J. Phys. D **45**, 255002 (2012).
[35]V. E. Demidov and S. O. Demokritov, IEEE Trans. Magn. **51**(4), 1 (2015).
[36]Q. Wang, P. Pirro, R. Verba, A. Slavin, B. Hillebrands, and A. V. Chumak, Sci. Adv. **4**, e1701517 (2018).
[37]Q. Wang, B. Heinz, R. Verba, M. Kewenig, P. Pirro, M. Schneider, T. Meyer, B. Lägel, C. Dubs, T. Brächer, and A. V. Chumak, Phys. Rev. Lett. **122**, 247202 (2019).
[38]B. Heinz, T. Brächer, M. Schneider, Q. Wang, B. Lägel, A. M. Friedel, D. Breitbach, S. Steinert, T. Meyer, M. Kewenig *et al.*, Nano Lett. **20**, 4220 (2020).
[39]B. Heinz, Q. Wang, M. Schneider, E. Weiß, A. Lentfert, B. Lägel, T. Brächer, C. Dubs, O. V. Dobrovolskiy, P. Pirro, and A. V. Chumak, Appl. Phys. Lett. **118**, 132406 (2021).
[40]K. Davídková, K. Levchenko, F. Bruckner, R. Verba, F. Majcen, Q. Wang, M. Lindner, C. Dubs, V. Vlaminck, J. Klíma *et al.*, Phys. Rev. Appl. **23**, 034026 (2025).
[41]X. Ge, R. Verba, P. Pirro, A. V. Chumak, and Q. Wang, Appl. Phys. Lett. **124**, 122413 (2024).
[42]V. Vlaminck and M. Bailleul, Phys. Rev. B **81**, 014425 (2010).
[43]C. Dubs, O. Surzhenko, R. Linke, A. Danilewsky, U. Brückner, and J. Dellith, J. Phys. D **50**, 204005 (2017).
[44]C. Dubs, O. Surzhenko, R. Thomas, J. Osten, T. Schneider, K. Lenz, J. Grenzer, R. Hübner, and E. Wendler, Phys. Rev. Mater. **4**, 024416 (2020).
[45]F. Bruckner, K. Davídková, C. Abert, A. Chumak, and D. Suess, arXiv:2501.16553 (2025).
[46]L. Körber, G. Quasebarth, A. Otto, and A. Kákay, AIP Adv. **11**, 095006 (2021).
[47]L. Körber, G. Quasebarth, A. Hempel, F. Zahn, A. Otto, E. Westphal, R. Hertel, and A. Kákay (2022). "TetraX: Finite-element micromagnetic-modeling package," RODARE. https://doi.org/10.14278/rodare.1418
[48]M. Moalic and M. Zelent (2023). "MathieuMoalic/amumax: 2023.10.26," Zenodo. https://doi.org/10.5281/zenodo.10043142
[49]A. Vansteenkiste, J. Leliaert, M. Dvornik, M. Helsen, F. Garcia-Sanchez, and B. Van Waeyenberge, AIP Adv. **4**, 107133 (2014).
[50]J. Leliaert, M. Dvornik, J. Mulkers, J. De Clercq, M. V. Milošević, and B. Van Waeyenberge, J. Phys. D **51**, 123002 (2018).
[51]I. Zdru, F. Ciubotaru, C. Nastase, A. Florescu, A. Abbass Hamadeh, M. Geilen, A. Nicoloiu, G. Boldeiu, D. Vasilache, S. Iordanescu, M. Nedelcu, D. Narducci, M.-C. Ciornei, C. Adelmann, A. Dinescu, M. Weiler, P. Pirro, and A. Müller, IEEE Trans. Ultrason., Ferroelectr., Freq. Control **72**, 30 (2025).
[52]T. Sebastian, K. Schultheiss, B. Obry, B. Hillebrands, and H. Schultheiss, Front. Phys. **3**, 35 (2015).
[53]O. Wojewoda, M. Hrtoň, and M. Urbánek, Phys. Rev. B **110**, 224428 (2024).
[54]B. Hillebrands, Rev. Sci. Instrum. **70**, 1589 (1999).

$$J_{\text{exc}} = \left| \frac{2 \cdot \sin\left(\frac{k_t \cdot l_g}{2}\right)}{k_t \cdot l_g} + \frac{\sin\left(k_t \cdot \left(\frac{l_g}{2} + l_1\right)\right) - \sin\left(k_t \cdot \left(\frac{l_g}{2} + l_1 + l_p\right)\right)}{k_t \cdot l_p} \right|^2$$

where l_g – width of a CPW signal line; l_p – width of a CPW ground line; l_1 – distance between a signal and a ground line; k_t – wavevector.

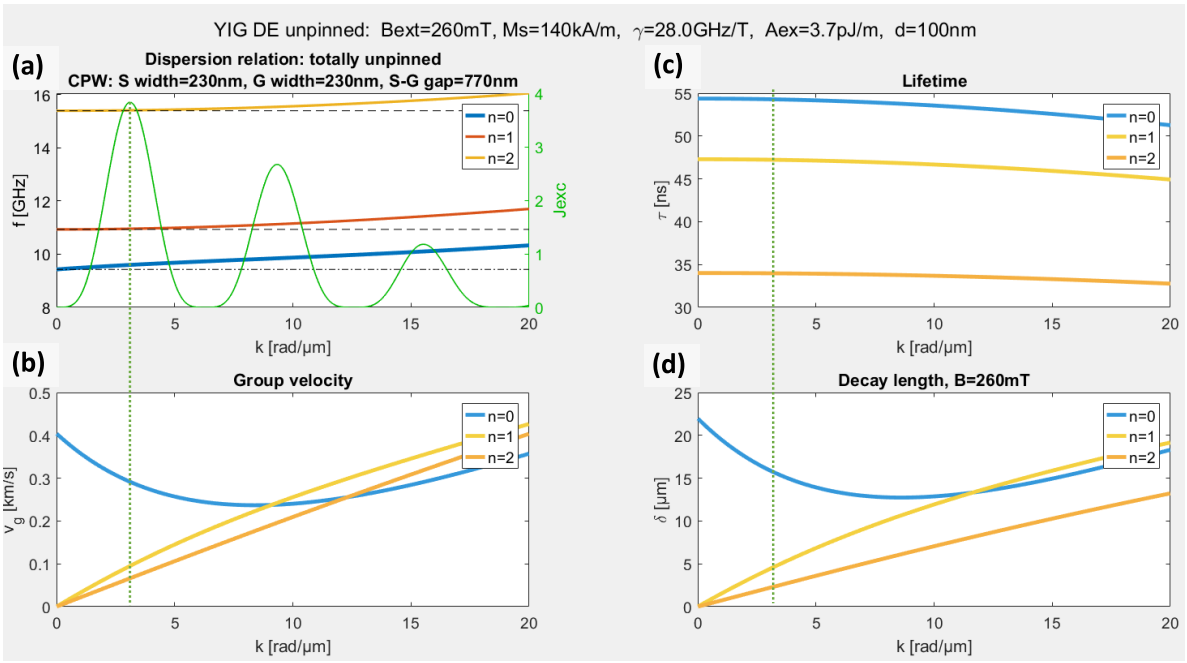

Fig. S1: Analytical calculation of the first three modes in 100 nm-thick YIG unstructured film (M_s =176 mT, $\gamma = 28$ GHz/T, $A_{ex} = 3.7$ pJ/m) in Damon-Eshbach configuration under $\mu_0 H_{ext} = 260$ mT bias field: **(a)** dispersion relation and CPW antenna's (ground-signal-ground, G-S-G, $w_{S,G} \approx 230$ nm, $w_{S-G} \approx 770$ nm) excitation efficiency J_{exc}; **(b)** group velocity v_g (km/s); **(c)** lifetime τ (ns); **(d)** decay length δ (μm). Green dotted line represents a projection of a wavevector $k \approx 3.1 \frac{\text{rad}}{\mu\text{m}}$ corresponding to the lattice period of 1 μm.

The results of the analytical calculation of the dispersion relation for the first three spin-wave modes in an unstructured 100-nm-thick YIG film, together with the excitation efficiency J_{exc} of the CPW antenna, are presented in Fig. S1(**a**). We have considered standard magnetic parameter of the YIG film: $M_s = 176$ mT, $\gamma = 28$ GHz/T, $A_{ex} = 3.7$ pJ/m, Damon-Eshbach (DE) configuration under the 260 mT bias magnetic field. In addition, we have also estimated the group velocity – v_g (Fig. S1(**b**)), lifetime τ (Fig. S1(**c**)), decay length δ (Fig. S1(**d**)). According to Kalinikos and Slavin [S5, S6], the analytical description of the dipole-exchange spin waves in a ferromagnetic film considering the spin pinning condition is:

$$f = \frac{\gamma}{2\pi} \sqrt{\left(B_{ext} + \frac{2A_{ex}}{M_s} k^2\right)\left(B_{ext} + \frac{2A_{ex}}{M_s} k^2 + \mu_0 M_s F_n\right)},$$

where k – total wavevector, $k = \sqrt{k_t^2 + k_n^2}$; k_t – tangential wavevector, which corresponds to the spin-wave propagation in the magnetic film; $k_n = \frac{n\pi}{d}$ – perpendicular wavevector, which is quantized and defined by the film thickness d; μ_0 –vacuum permeability; γ –gyromagnetic ratio; A_{ex} – exchange stiffness; M_s – saturation magnetization; B_{ext} – external magnetic field; F_n – angular and boundary-condition-dependent term:

$$F_n = \sin^2\theta + P_n \left[\cos(2\theta) + \sin^2\theta \cdot \sin^2\phi \cdot \left(1 + \frac{\mu_0 M_s (1 - P_n)}{B_{ext} + \frac{2A_{ex}}{M_s} k^2} \right) \right],$$

where θ is an azimuthal angle, $\theta = \pi/2$ indicates in-plane magnetization; ϕ is the in-plane polar angle between the direction of spin-wave propagation and the direction of an effective field, $\phi = \pi/2$ corresponds

to wavevector perpendicular to magnetization, $P_n -$ spin-pinning condition term, which for unpinned magnetic moments is defined as:

$$P_n = \frac{k_t^2}{k^2}\left[1 - \frac{2k_t(1-(-1)^n e^{-k_t d})}{dk^2(1+\delta)}\right] \text{ with Kronecker's delta } \delta = \begin{cases} 1, & n = 0 \\ 0, & n \neq 0 \end{cases}.$$

Group velocity v_g was evaluated as a derivative of the dispersion relation:

$$v_g(k_t) = \frac{d\omega}{dk} = 2\pi \cdot \frac{df_n}{dk} \approx 0.291 \text{ (km/s)},$$

where $f_n -$ frequency dispersions for the respective quantization number $n = 0, 1, 2, \ldots$; $\omega = 2\pi f -$ angular frequency.

Lifetime was calculated as a field derivative of the dispersion relation:

$$\tau = \left(\alpha\omega \frac{d\omega}{d\omega_H}\right) \approx 54 \text{ (ns)},$$

where $\alpha -$ Gilbert damping constant.

Decay length was calculated according to:

$$\delta = v_g \cdot \tau \approx 15.8 \text{ (μm)}.$$

Maximum excitation efficiency of the planned CPW antenna corresponds to $k \approx 3.1 \frac{\text{rad}}{\mu\text{m}} \rightarrow \lambda \approx 2$ μm. The Bragg scattering condition of a 1D MC in the form of a periodic array of reflecting planes (holes) is defined as $n_{mc}\lambda = 2a \sin\theta_{mc}$, where n_{mc} is integer, $\lambda -$ spin-wave wavelength, a – lattice constant (magnonic crystal period), $\theta_{mc}. -$ incident spin-wave angle. Assuming normal incidence ($\theta_{mc} = \pi/2$), we set the MC period to $a = 1$ μm to achieve optimal excitation.

3. Micromagnetic simulations

3.1 TetraX mode profiles

TetraX micromagnetic simulations were performed for the mode profiles in the DE and Backward Volume (BV) magnetization configuration of an unstructured waveguide cross-section considering (Fig. S2): $M_s = 174.7$ mT, uniaxial magnetic anisotropy $K_u = 3.58$ J/m^3 ($\perp$ x-axis); Gilbert damping $\alpha = 10^{-4}$; waveguide's thickness $d = 100$ nm; waveguide's width $\omega = 320$ nm. Profiles were calculated for $k = 0$, considering only the first five ($n = 5$) modes due to the quadratic decrease in dynamic magnetization intensity with increasing *n*. The real part of the respective magnetization components – m_y for DE, m_x for BV – is color-coded with red and blue.

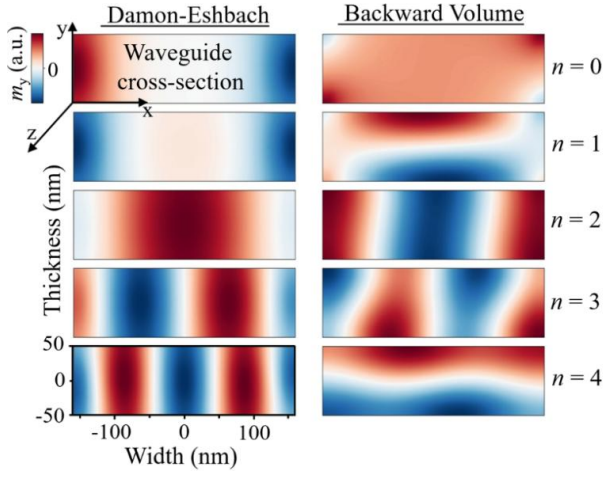

Fig. S2: TetraX simulation of the mode profile amplitudes for the first 5 spin-wave modes of the unstructured waveguide in DE and BV geometry.

Profiles exhibit both width and thickness quantization due to lateral confinement. In the DE configuration, all modes show only width quantization, with components $k_y = n\pi/w$, whereas the BV configuration displays a more complex mix of thickness and width contributions, evident from the horizontal and diagonal color patterns. The DE modes with $n = 0, 1$ are edge modes, where spin waves propagate only along the waveguide edges. Slight non-uniformities in the BV profiles, such as in the $n = 0$ mode, arises from plotting a single magnetization component, while contributions from both dynamic components m_y and m_x are

important. Although the mode profiles are unpinned at the top and bottom surfaces, edge pinning persists, introducing elastic scattering into higher-order width modes. This effect occurs because the waveguide width slightly exceeds the critical threshold required for complete unpinning and single-mode operation. The impact of edge pinning is more pronounced in DE modes due to their intrinsically nonreciprocal and edge-localized nature, which leads to mode anticrossing at lower wavevectors. Nevertheless, simulations confirm that for the selected MC waveguide geometry, the DE configuration provides the clearest understanding and control of spin-wave transmission.

3.2. *MuMax³ dispersion relation of the 1D magnonic crystal waveguide*

The dispersion relation of the MC structure shown in Fig. 2(**b**) of the main article was calculated using Amumax, a fork of MuMax[3]. The simulated geometry had parameters equal to those of the fabricated structures. The computational domain was discretized into 215 × 25 × 1 cells, corresponding to a spatial resolution of 6.1 × 10 × 100 nm along the x-, y-, and z-axes, respectively. The waveguide was modeled using YIG material parameters, with a saturation magnetization $M_s = 174.7$ mT, exchange stiffness $A_{ex} = 3.7 \cdot 10^{-12}$ J/m, and uniaxial magnetic anisotropy $K_u = 3.58$ J/m^3, oriented perpendicular to the x-axis. The Gilbert damping constant was set to $\alpha = 10^{-4}$. A static bias field of $B_{ext} = 260$ mT was applied along the y-axis. To break any residual symmetry that could lead to nonphysical results, additional static fields of 1 mT were applied along the x- and z-axes. Absorbing boundary conditions were implemented by gradually increasing the damping parameter near the edges of the waveguide.

The simulation proceeded in two stages. First, the system was relaxed to its magnetic ground state. Subsequently, spin waves were excited using a sinc-shaped magnetic field applied spatially, ensuring uniform excitation of wavevectors below $10^0 \times 10^6$ rad/m. The temporal profile of the excitation field also followed a sinc function, with a cut-off frequency of 15 GHz and a peak amplitude of 5×10^{-4} T. The excitation was applied over a duration of 100 ns, and the x-component of the magnetization was sampled every 25.6 ps during this period. To compute the dispersion relation, the x-components of the magnetization were recorded as functions of time and position. A discrete Fourier transform was applied along both the time and x-axes using the fast Fourier transform (FFT) algorithm for each simulation cell. The absolute value of the resulting complex spectra was computed and summed over the z- and y-axes to yield the final dispersion map.

The spin-wave dispersion enabled the estimation of the relative positions of the band gaps within the magnonic spectrum and was in good agreement with TetraX dispersion calculation.

3.3. *TetraX simulations*

The dispersion relation as a function of the microwave frequency (Fig. 2(**c**) of the main article) was analytically calculated for a single unstructured MC conduit to match the experimental data. The calculations were performed using an open-source TetraX-based software, developed within the Nanomagnetism and Magnonics group by A. A. Voronov et al., at the University of Vienna (https://www.madivie.at/). Common input parameters for all calculated structures were: Damon-Eschbach configuration, $B_{ext} = 262$ mT; waveguide of width $w = 320$ nm, $t = 100$ nm; $M_s = 174.7$ mT; in-plane anisotropy $K_u = 3.58$ J/m^3; exchange constant $A_{ex} = 3.7 \cdot 10^{-12}$ J/m; Gilbert damping $\alpha = 2 \cdot 10^{-4}$; wavevector range $k = 0...20$ rad/μm; number of k-values = 100; mash cell size $dx, dy = 5$, number of modes $n = 5$.

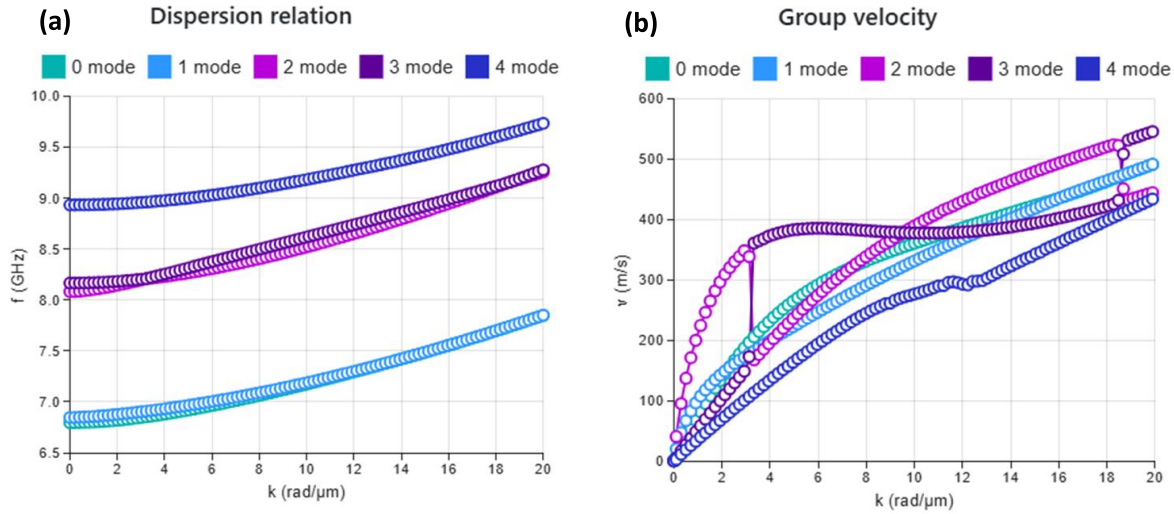

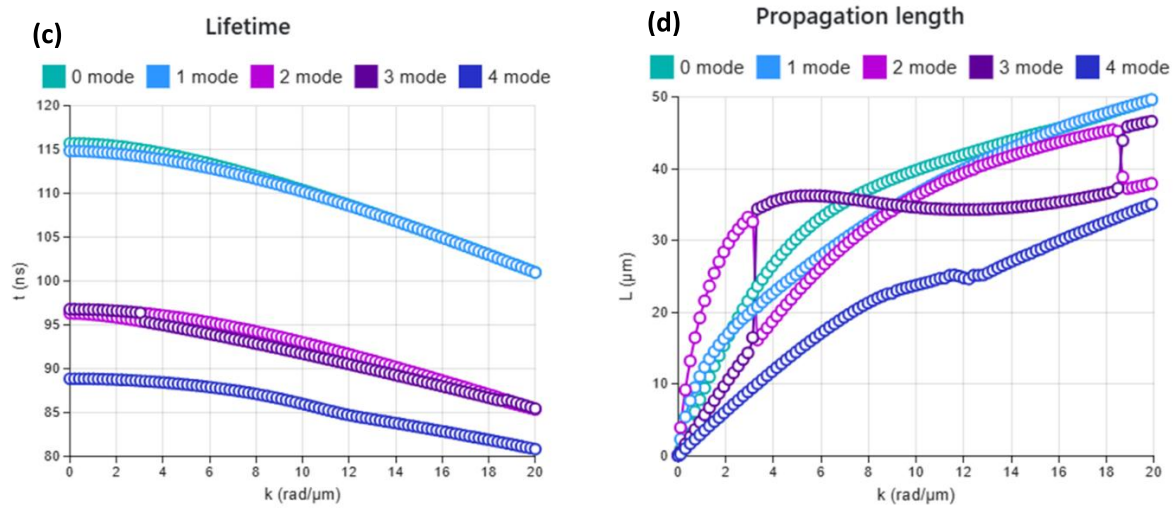

Fig. S3: TetraX micromagnetic simulation of the unstructured waveguide with a width $w = 320$ nm, thickness $t = 100$ nm, saturation magnetization $M_s = 174.7$ mT, and external magnetic field $\mu_0 H_{ext} = 262$ mT for the $n = 5$ modes: **(a)** spin-wave dispersion relation; **(b)** group velocity; **(c)** lifetime; **(d)** propagation length.

Notably, in the main article, only the modes $n = 2$ and 3 of the unstructured waveguide are shown with **crimson solid** and peach dotted lines respectively. In the Supplementary (Fig. S3), all 5 modes are shown in colors according to the program's default palette, with modes 2 and 3 represented with **purple** and **plum** circles, as noted in the figures' legend. First two modes correspond to the edge states, while the lowest fundamental width mode is $n = 2$. The derived parameters for the second mode around $k \approx 3.1$ rad/μm are estimated as: group velocity $v_g \approx 340$ m/s (Fig. S3(**b**)), lifetime $\tau \approx 95.9$ ns (Fig. S3(**c**)), propagation length $l \approx 32.7$ μm (Fig. S3(**d**)). At the $k \approx 3.1$ rad/μm and 18.7 rad/μm spin waves modes $n = 2$ and $n = 3$ are hybridized, forming anticrossing points, where energy is exchanged between the modes.

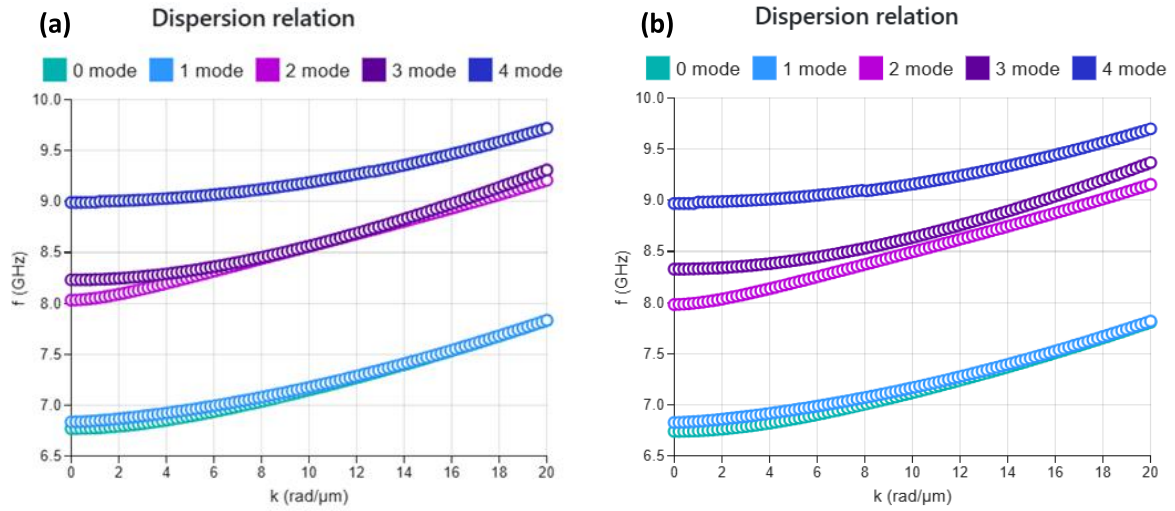

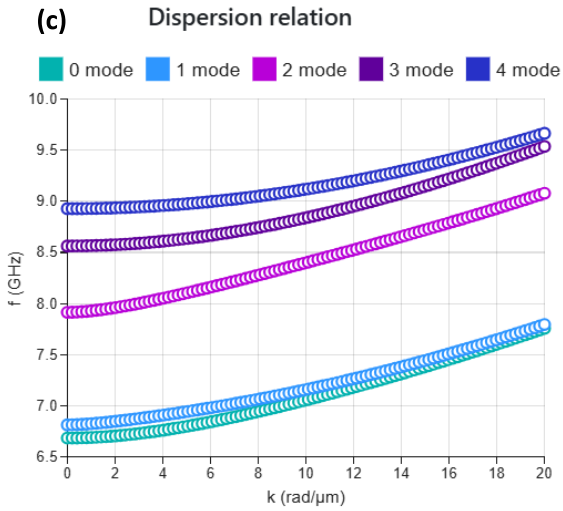

Fig. S4: TetraX micromagnetic simulations of the dispersion relations of an unstructured waveguide with parameters as in Fig. S3, varying in width: **(a)** width $w = 300$ nm; **(b)** width $w = 280$ nm; **(c)** width $w = 250$ nm.

Comparing Fig. S1 to Fig. S3 it is clearly visible how the much the dispersion relation of a thin film differs from the unstructured nanowaveguide. Firstly, a magnon frequency decreases in a waveguide under similar external magnetic field is primarily due to demagnetization field and mode confinement, which alters the effective internal field and dispersion relation. For discussed waveguide's configuration, mode localization ($n = 2, 3$) leads to two anticrossing points – at $k \approx 3.1$ rad/μm and $k \approx 18.7$ rad/μm. Therefore, a single-mode is expected within the frequency bandwidth of 100 MHz ($f \sim 8.08 - 8.17$ GHz, $k < 3.1$ rad/μm). Secondly, tuning of the geometrical parameters of the conduit, primary its width, most prominently affects the shape of the dispersion and modes hybridization.

For example, Fig. S4**(a)** shows the TetraX simulations of the dispersion relation for the waveguide with the same input parameters apart from the width set to originally designed 300 nm, while Fig. S4**(b)** and **(c)** – width set to 280 nm and 250 nm, respectively. It is clearly visible how the decrease of the width to 300 nm leads to the appearance of only 1 anticrossing point at $k \approx 8..11$ rad/μm, increasing the single-mode bandwidth to 200 MHz (8.03 – 8.23 GHz). Reducing the waveguide width to approximately 280 nm eliminates mode anticrossings, while further narrowing to 250 nm expands the single-mode frequency range sevenfold to 7.91 – 8.56 GHz (up to 12 rad/μm). A wider single-mode frequency bandwidth for the original structure is accessible in Backward Volume configuration – from 10.27 GHz to 10.94 GHz for the same input parameters (see Fig. S5). However, the excitation efficiency in such configuration was too low for measurement consideration.

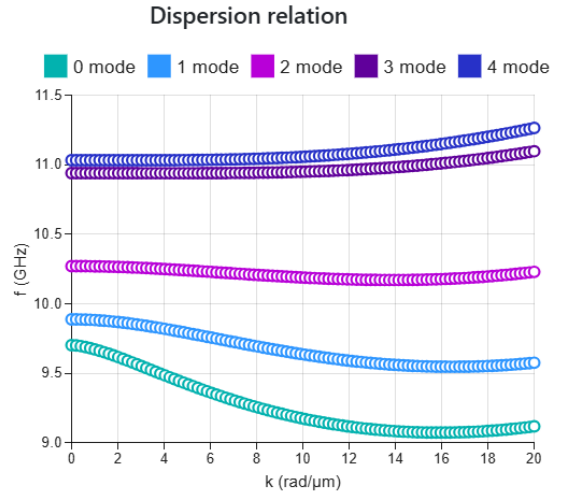

Fig. S5: TetraX micromagnetic simulation of the dispersion relation for an unstructured waveguide with the same parameters as in Fig. S3, but in the Backward Volume geometry.

4. Propagating spin-wave spectroscopy experimental set-up

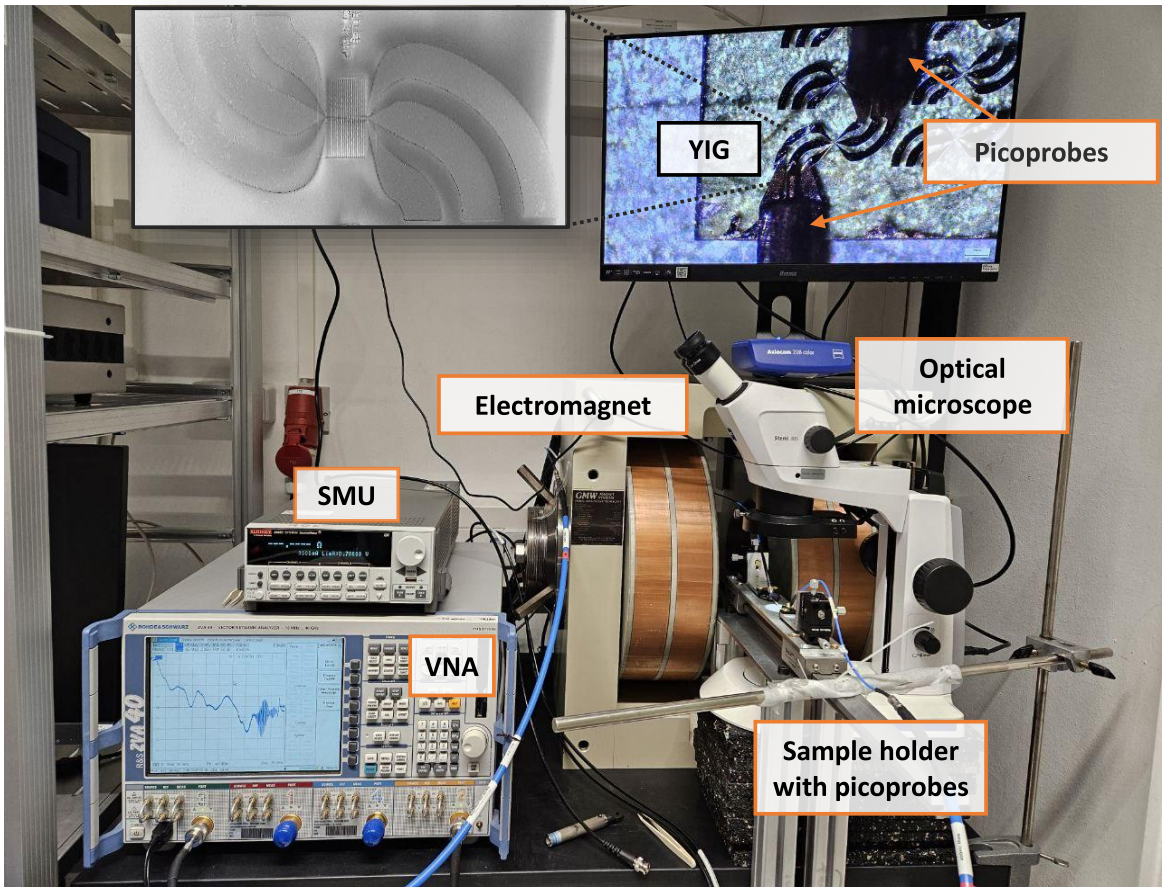

Fig. S6: Experimental setup used in propagating spin-wave spectroscopy (PSWS) measurements, consisting of key equipment: Vector Network Analyzer (VNA), coaxial k-type cables and adapters, 40A-GSG-150-P picoprobes, GMW 3473-70 electromagnet, Source Measurement Unit (SMU) and optical microscope.

All-electrical propagating spin-wave spectroscopy (PSWS) measurements were carried in the set-up shown in Fig. S6. The set-up consists of a Vector Network Analyzer, VNA (4-port Rhode & Schwarz ZVA-40) connected to an H-frame electromagnet GMW 3473-70 with a tunable air gap for various measurement configurations and magnet poles of 15 cm diameter to induce a sufficiently uniform biasing magnetic field ($\mu_0 H_{\text{ext}} = <0.6 \ldots 2.1$ T depending on the air gap). The calibrated VNA signal was transferred via k-type cables/non-magnetic adapters to a pair of 40A-GSG-150-P picoprobes connected to the contact pads of the fabricated CPW antennas. All the measurements were performed at $T_{\text{RT}} \approx 295\,K$. To avoid non-linear contributions from multimagnon scattering processes, preserve the antennas during extended measurements, yet achieve an optimal signal efficiency, we kept the RF power at -10 dBm. Sample is located between the picoprobes on a sample holder, and can be rotated with respect to the required magnetization geometry.

After applying sufficient magnetic field to homogenously magnetize the sample, VNA-generated high-frequency signal is transferred to a CPW antenna fabricated on top of the structure of interest. The applied microwave signal induces an alternating Oersted magnetic field around the antenna. Its components perpendicular to the bias field provide the necessary torque to excite precessional motion of spins in the magnetic medium directly under the antenna. If the correct conditions for the bias magnetic field and frequency are satisfied, this excitation launches propagating spin waves. By symmetry, the spin-wave detection mechanism through the output antenna is the inverse of the excitation. The VNA measures the transmitted and reflected signals, enabling the extraction of key parameters of transmission spectra, such as insertion loss, electromagnetic leakage, attenuation level, etc. VNA parameters used for the measurements were an intermediate frequency bandwidth 0.1-1 kHz, a frequency step 100 kHz and no averaging. Proper connection of picoprobes to sample's contact pads and evaluation of antennas' resistance was done via the Source Measurement Unit (SMU).

5. PSWS – different frequency ranges and 'time gating' for signal-to-noise improvement

Propagating spin-wave spectroscopy transmission signal S_{12} of 100 nm-thick 1D YIG hole-based MC is shown on Fig. S7. The structure under study is same as demonstrated at Fig.1(**c**) of the main article and was measured under same conditions (Damon-Eshbach configuration; microwave signal power level set to -10 dBm). The reference background signal, taken at magnetic fields slightly below the excitation level, was subtracted to improve the signal-to-noise ratio. Most clear signal is demonstrated at Fig. S7(**b**) due to the optimal combination of the preliminary designed antenna's excitation efficiency and high spin-wave group velocity.

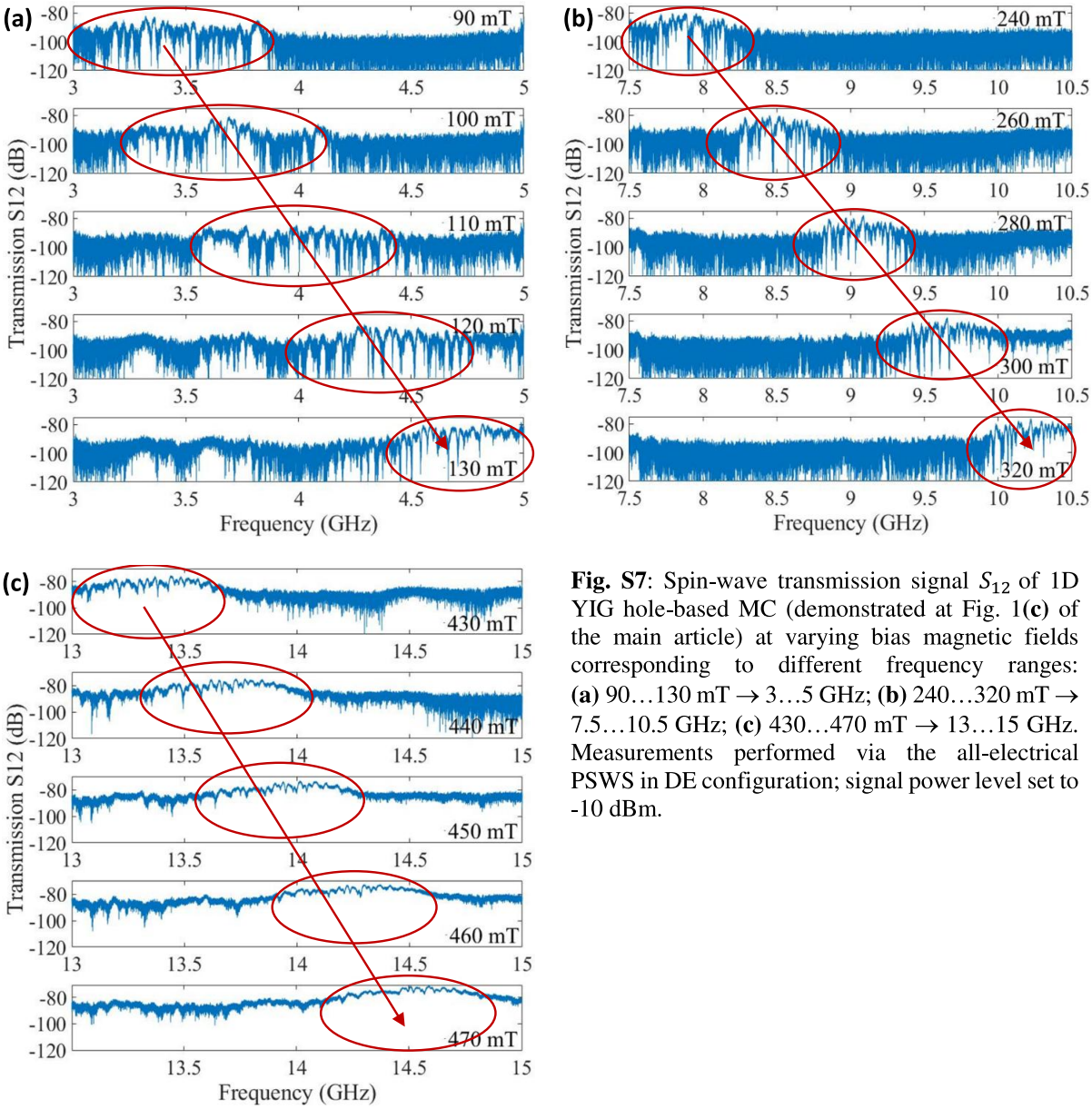

Fig. S7: Spin-wave transmission signal S_{12} of 1D YIG hole-based MC (demonstrated at Fig. 1(**c**) of the main article) at varying bias magnetic fields corresponding to different frequency ranges: **(a)** 90…130 mT → 3…5 GHz; **(b)** 240…320 mT → 7.5…10.5 GHz; **(c)** 430…470 mT → 13…15 GHz. Measurements performed via the all-electrical PSWS in DE configuration; signal power level set to -10 dBm.

To further improve the signal-to-noise ratio and subtract the electromagnetic leakage, we have used 'time gating technique', widely applied in Surface Acoustic Waves (SAW) analysis [S7, S8]. Firstly, the real and imaginary parts of the quasi-continuous S_{12} VNA signal and its reference were respectively subtracted from each other before being subjected to Inverse FFT (IFFT) – Fig. S8(**a**). A significant source of a signal disruption originates from electromagnetic leakage generated by the antenna itself, which propagates between the CPW antennas at a speed of light within a first nanosecond (up to 2 ns considering reflection-induced smearing), and is identified in the time domain as a first pulse of strong amplitude. The SW signal is expected to have a propagation time of around 14.7 ns, considering the ≈ 5 μm distance between the antennas and the

spin-wave velocity of ≈ 340 m/s (according to the TetraX simulations of the unstructured waveguide, *Section 3.3* of the Supplementary materials for the lowest fundamental volume mode $n = 2$ slightly below 3.1 rad/µm). This closely matches the second pulse found in the time-domain data, appearing at 13.6 ns. Therefore, a SW transmission window is further fixed to the time frame 13.6 ns – 90 ns, while setting the rest to zero, to eliminate the parasitic signal and noise. The obtained signal is then transformed back to the frequency domain via the FFT – Fig. S8**(b)**. Note, that we do not differentiate here between the pure SW transmission and reflected components, e.g., triple transit.

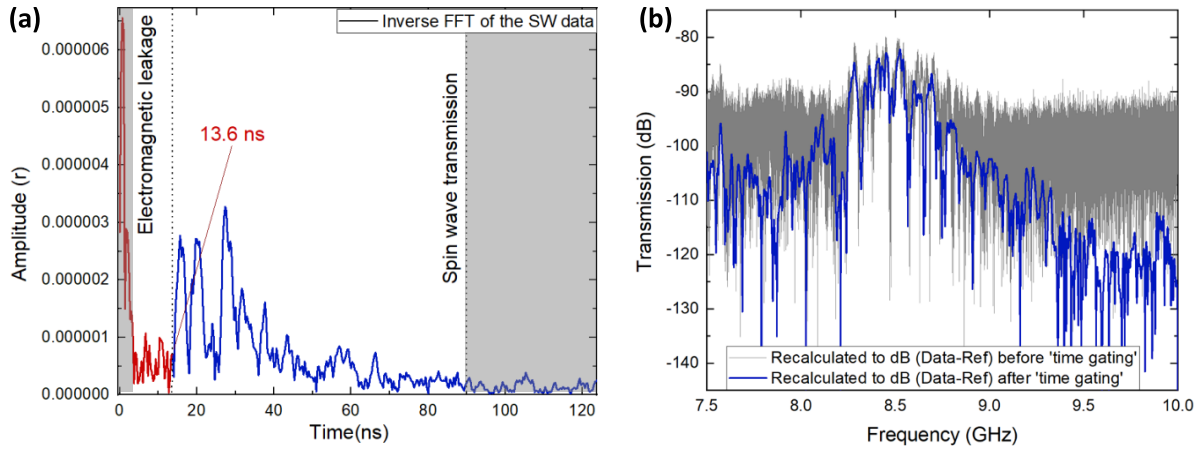

Fig. S8: Exemplary 'time gating' of the S_{12} spin-wave transmission at a bias field of $\mu_0 H_{\text{ext}} = 260$ mT bias magnetic field: **(a)** Distinct peaks of spin-wave transmission and electromagnetic leakage in a time domain (inverse FFT from frequency domain); **(b)** Spin-wave transmission spectra (with a previously subtracted reference signal) before (gray) and after (blue) spurious signal removal. Time domain data in Fig. S3**(a)** conversed back to frequency domain via FFT.

6. PSWS at different power levels

All PSWS measurement discussed in the main article were performed at microwave power of -10 dBm. This value was identified as optimal based on a series of measurements at various VNA power levels, providing the best signal-to-noise ratio while maintaining operation within the linear regime (Fig. S9 **(a)**-**(f)** as indicated in the figures' top caption). Measurements performed on a structure of interest in Damon-Eshbach configuration, with no averaging of the signal and the intermediate frequency bandwidth set to 1 kHz.

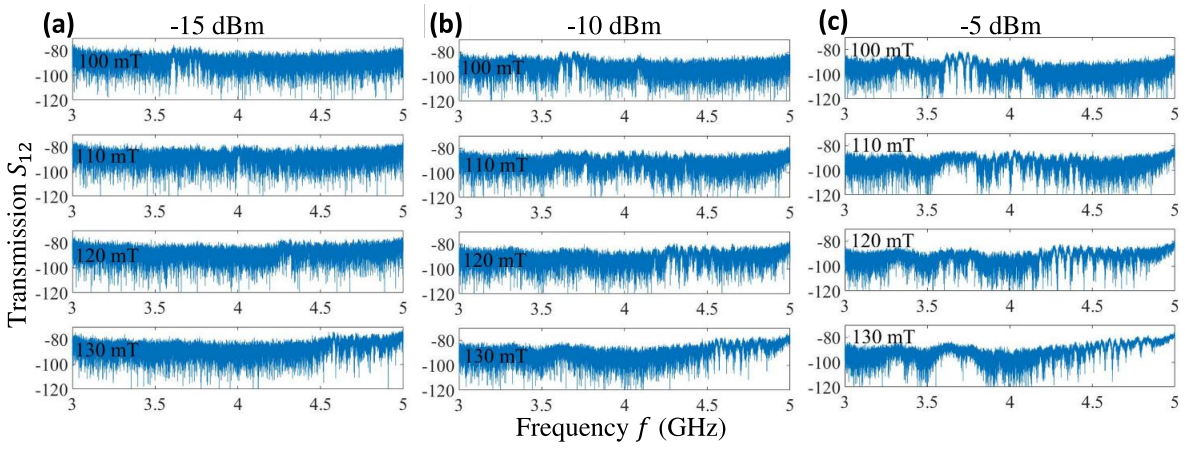

spin-wave velocity of ≈ 340 m/s (according to the TetraX simulations of the unstructured waveguide, *Section 3.3* of the Supplementary materials for the lowest fundamental volume mode $n = 2$ slightly below 3.1 rad/µm). This closely matches the second pulse found in the time-domain data, appearing at 13.6 ns. Therefore, a SW transmission window is further fixed to the time frame 13.6 ns – 90 ns, while setting the rest to zero, to eliminate the parasitic signal and noise. The obtained signal is then transformed back to the frequency domain via the FFT – Fig. S8**(b)**. Note, that we do not differentiate here between the pure SW transmission and reflected components, e.g., triple transit.

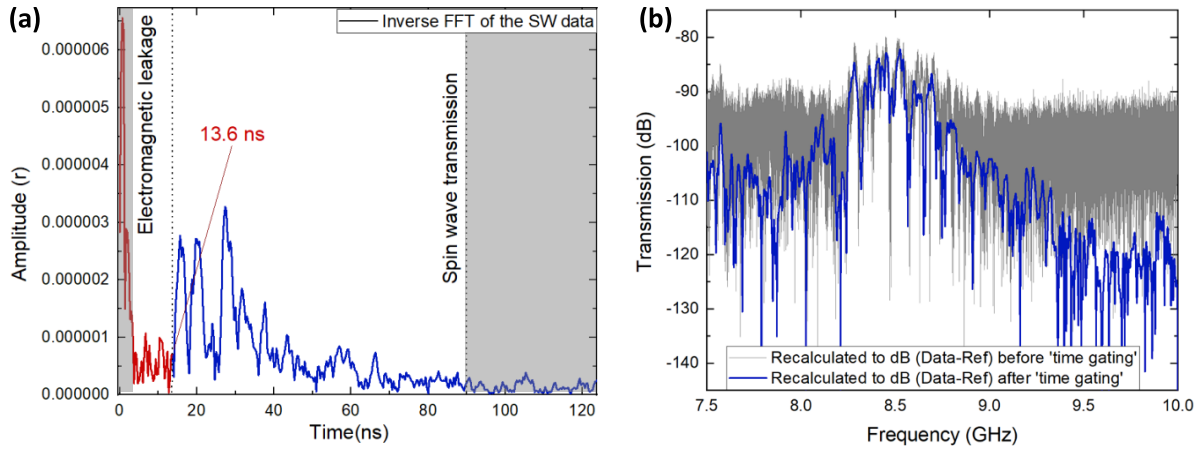

Fig. S8: Exemplary 'time gating' of the S_{12} spin-wave transmission at a bias field of $\mu_0 H_{\text{ext}} = 260$ mT bias magnetic field: **(a)** Distinct peaks of spin-wave transmission and electromagnetic leakage in a time domain (inverse FFT from frequency domain); **(b)** Spin-wave transmission spectra (with a previously subtracted reference signal) before (gray) and after (blue) spurious signal removal. Time domain data in Fig. S3**(a)** conversed back to frequency domain via FFT.

6. PSWS at different power levels

All PSWS measurement discussed in the main article were performed at microwave power of -10 dBm. This value was identified as optimal based on a series of measurements at various VNA power levels, providing the best signal-to-noise ratio while maintaining operation within the linear regime (Fig. S9 **(a)**-**(f)** as indicated in the figures' top caption). Measurements performed on a structure of interest in Damon-Eshbach configuration, with no averaging of the signal and the intermediate frequency bandwidth set to 1 kHz.

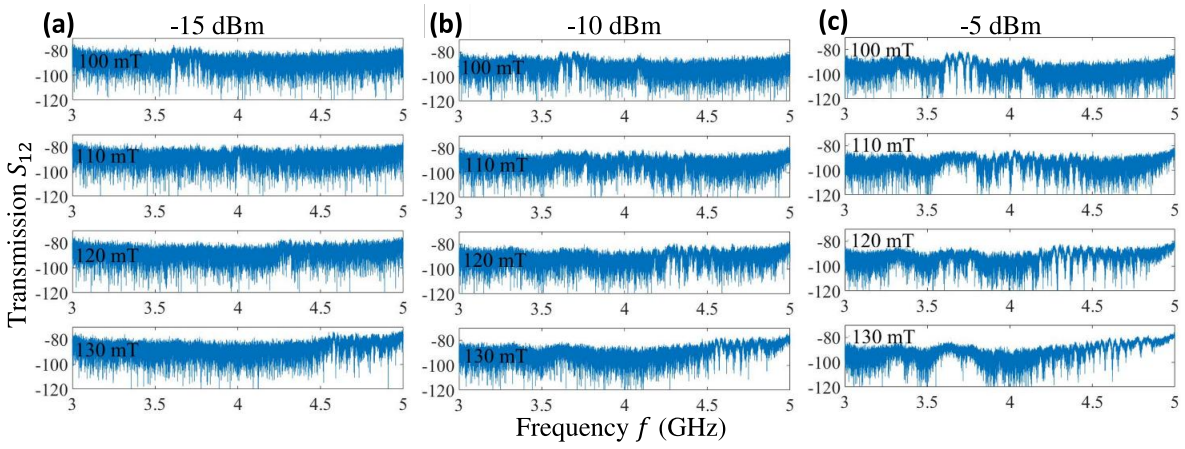

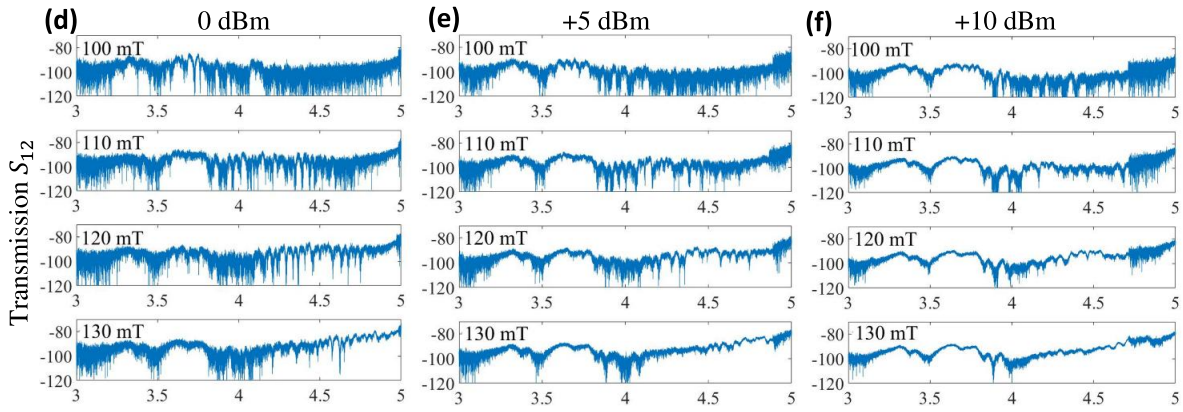

Fig. S9: Six S_{12} transmission spectra of a structure of interest at six different microwave power levels each for four different external magnetic fields, as indicated in the figures.

7. μ-BLS frequency sweep

To study the spin-wave transmission in a single magnonic crystal, we have performed series of microfocused Brillouin light scattering spectroscopy (μ-BLS) measurements. μ-BLS is a crucial technique for current investigation as it provides spatially resolved spin-wave mapping of magnetization dynamics at the submicron scale, with a smallest distinguishable feature ≈ 300 nm. High resolution is achieved at a loss of *k*-resolution, as light is collected from multiple angles, leading to a mixture of different *k*-components in the detected signal. This is unlike *k*-resolved BLS, which uses a collimated laser beam at a defined angle of incidence to selectively probe certain wavevectors, but uses a large laser spot > 50 μm.

The measurements were performed on a different structure than the one used in PSWS analysis, as it was accidentally damaged. However, all relevant geometerical parameters remained the same (i.e., average waveguide's width and the holes' size), just the holes position were more centered. Distance between the antennas was ≈ 2 μm and number of conduits on antennas – 50, which were irrelevant for the BLS measurements.

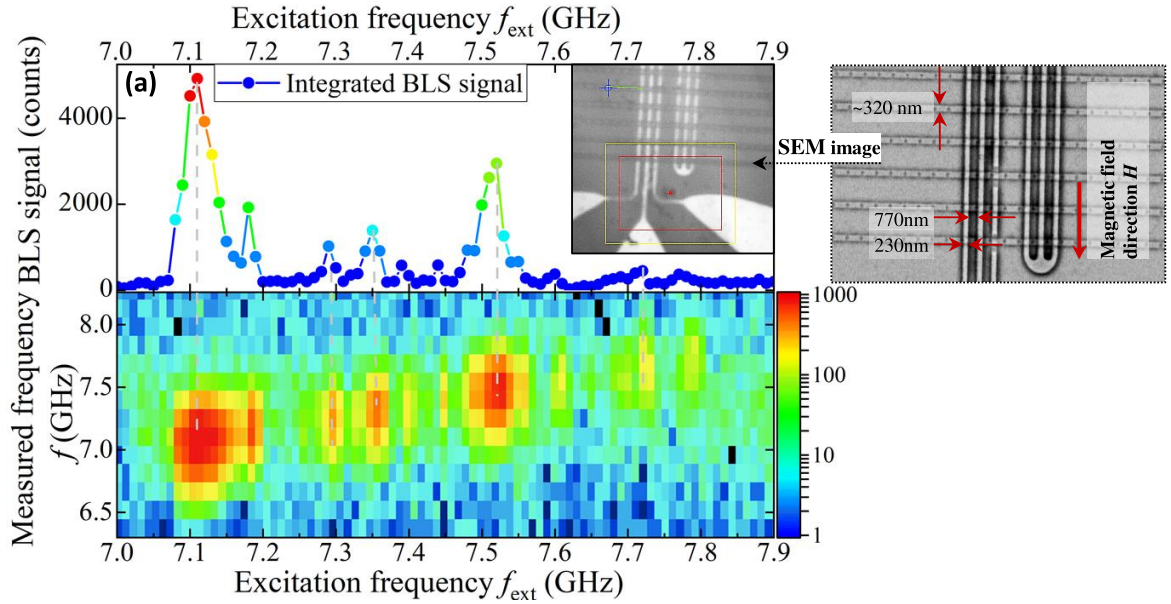

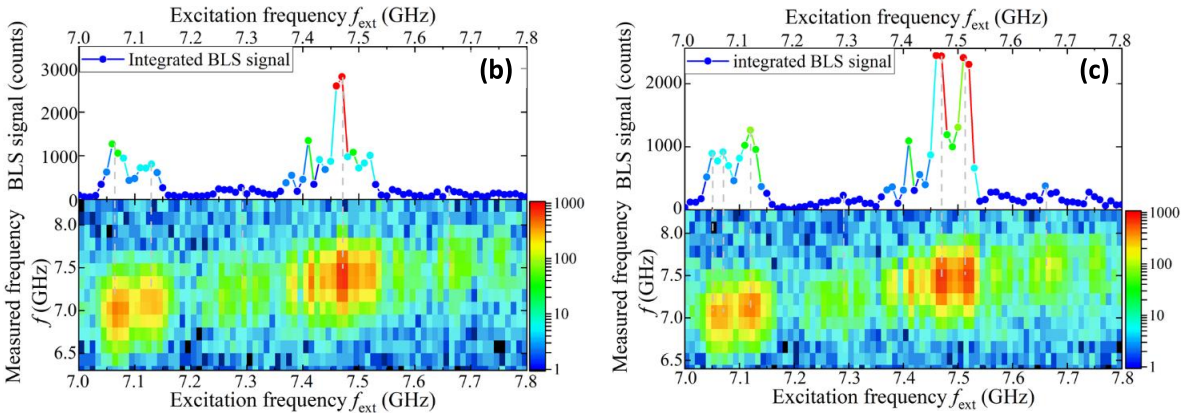

Fig. S10: BLS signal (detector counts) of the propagating spin wave as a function of a coherent excitation f_{ext} (x-axis) in a form of: **(top section of each figure)** 2D graph, where each y-axis point corresponds to the integrated measured frequency f over each respective excitation frequency f_{ext}; **(bottom section of each figure)** 3D intensity map (log scale), where the y-axis shows the full range of measured frequency f at each excitation frequency f_{ext}, and BLS signal intensity is color-coded at z-axis. Three separate measurements **(a)** – **(c)** were performed at slightly shifted laser focus position along the short waveguide axis.

Firstly, we have performed the excitation frequency f_{ext} sweep of a single magnonic crystal conduit at a fixed distance of ≈ 5 μm from coplanar waveguide, as shown at the set-up microscope's photo (Fig. S10**(a)**, inset) and schematically at the SEM image of the investigated structure (Fig. S10**(a)** right panel). The BLS laser was positioned in the middle of the MC waveguide. However, as the waveguide's dimensions are at the resolution limit of the microscope, three measurements (Fig. S10**(a)** – **(c)**) were performed with the same input parameters, but with the laser focus slightly shifted. It is clearly seen how the spin-wave propagation path from the excitation antenna to the detecting laser position is moderately changed, with passband frequency peaks displaying similar periodic pattern, but differ in their amplitude. Also, the spin-wave spectra shown in Fig. S10**(b)** and **(c)** are slightly downshifted in frequencies, as each measurement was taken separately with laser position set every time anew.

The first passband peak appears around 7.05 GHz – 7.12 GHz with subsequent peaks spaced 0.19 GHz from each other (red-green areas on 3D maps). Regions dominated by the background BLS counts (blue areas on the 3D map) represent five band gaps measured 4.5 structural periods from the excitation antenna within a single MC waveguide. In patterned magnetic structures, inhomogeneous demagnetizing fields form at the edges of holes, locally modifying the internal magnetic field and leading to the localization of spin waves. These confined modes are highly sensitive to structural parameters such as hole size, spacing, and film thickness. As a result, fabrication imperfections—common in nanostructured thin films—can lead to variations in these parameters, contributing to the emergence of multiple peaks within one passband region, as well as changes to peaks' amplitude. Additionally, the generally lower signal intensity of propagating spin waves in thin films enhances the visibility of such parasitic modes.

Afterwards, we investigated the spin-wave transmission in the passband and band-gap regions by sweeping the laser position from 0 to 5 μm away from the antenna in around 100 nm step. Note, that Fig. S11 demonstrates the maximum BLS intensity at the passband excitation frequency $f_{\mathrm{ext}} = 7.04$ GHz (red circles) and at the band-gap frequency $f_{\mathrm{ext}} = 7.2$ GHz (blue squares), not integrated as in Fig. S10, for more clear representation. The passband signal is an order of magnitude stronger than that of a bandgap, confirming the SW filtering. Linear fitting reveals a smaller slope for the bandgap signal (light-blue dots) compared to the passband (orange dashes), indicating suboptimal excitation efficiency due to coarse excitation frequency choice, shifted starting position of the linescan from the vicinity of the antenna and enhanced signal dissipation due to holes directly beneath the antenna.

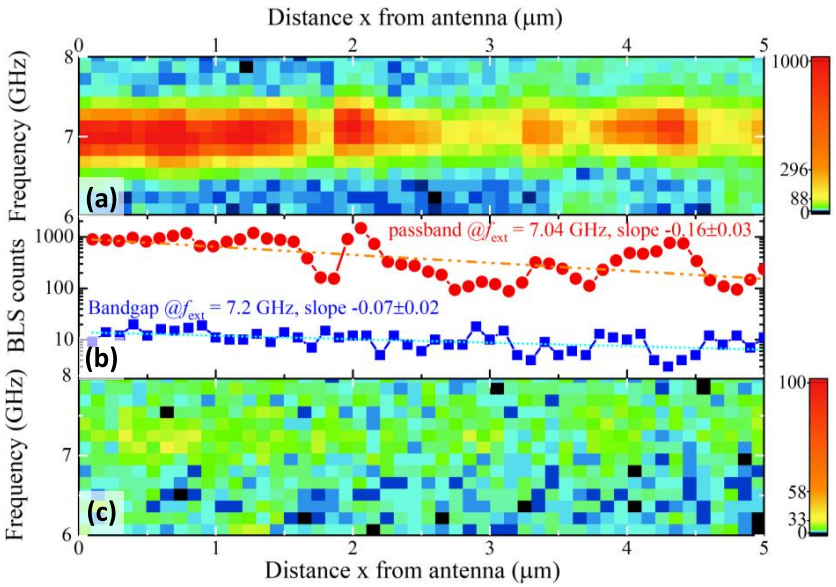

Fig. S11: BLS signal intensity of the propagating spin wave as a function of laser scan position 0-5 μm from the antenna (x-axis) in a form of: a 3D intensity map, where the y-axis shows the measured frequency f at a passband **(a)** or band-gap **(c)** excitation frequencies f_{ext}, while the BLS signal intensity is color-coded on the z-axis; a 2D graph **(b)**, where each y-axis point corresponds to maximum BLS counts at the respective passband and band-gap frequencies.

SUPPLEMENTARY MATERIALS LITERATURE:

[S1] H. Merbouche, et al., "Frequency Filtering with a Magnonic Crystal Based on Nanometer-Thick Yttrium Iron Garnet Films" *ACS Appl. Nano Mat.*, **4**(1), 121–128 (2021). DOI: 10.1021/acsanm.0c02382

[S2] S. Mantion, et al., "Reconfigurable spin wave modes in a Heusler magnonic crystal" *J. Appl. Phys.* **135**(5), 053902 (2024). DOI: 10.1063/5.0189486.

[S3] N. Kanazawa, et al., "The role of Snell's law for a magnonic majority gate" *Sci. Rep.* **7**, 7898 (2017). DOI: 10.1038/s41598-017-08114-7.

[S4] V. Vlaminck and M. Bailleul "Spin-wave transduction at the submicrometer scale: Experiment and modeling" *Phys. Rev. B* **81**, 014425 (2010). DOI: 10.1103/PhysRevB.81.014425.

[S5] B. A. Kalinikos, et al., "The dipole-exchange spin wave spectrum for anisotropic ferromagnetic films with mixed exchange boundary conditions" *J. Phys.: Condens. Matter* **2**, 9861 (1990). DOI: 10.1088/0953-8984/2/49/012.

[S6] B. A. Kalinikos, and A. N. Slavin. "Theory of dipole-exchange spin wave spectrum for ferromagnetic films with mixed exchange boundary conditions" *Journal of Physics C: Solid State Physics* **19**(35), 7013 (1986). DOI: 10.1088/0022-3719/19/35/014.

[S7] C. Heeg "Spin mechanics at radio frequencies" Ph.D. diploma thesis, Technische Universität München (2010).

[S8] I. Zdru, F. Ciubotaru, C. Nastase, A. Florescu, A. A. Hamadeh, M. Geilen, A. Nicoloiu, G. Boldeiu, D. Vasilache, S. Iordanescu, et al., "Interaction of Acoustic Waves With Spin Waves Using a GHz Operating GaN/Si SAW Device With a Ni/NiFeSi Layer Between Its IDTs" *IEEE Transac. Ultras. Ferroelectr. Freq. Contr.* **72**(1), 30 (2025). DOI: 10.1109/TUFFC.2024.3463731.

4.6 Outlook

The work presented in this thesis opens several promising directions for future research. In particular, the antidot-based magnonic systems investigated here—featuring engineered magnetisation textures—offer a rich platform for exploring new spin-wave phenomena (e.g., non-reciprocal edge modes). While the current results are based primarily on micromagnetic simulations, a natural continuation of this work would be the experimental validation of the predicted effects. Techniques such as Brillouin light scattering, time-resolved Kerr microscopy, or propagating spin-wave spectroscopy could be employed to probe the hybridisation between bulk and rim modes, as well as the influence of local anisotropy reduction around antidots.

There is also strong motivation to explore the topological aspects of the observed spin-wave modes. For instance, introducing asymmetry or chiral textures into the rim region could enable the realisation of non-reciprocal or topologically protected edge states[162]. Such configurations could be relevant for the development of programmable magnonic waveguides or logic elements based on edge mode routing[163,164].

In collaboration with other groups, I plan to investigate the interaction between localised textures such as the in plane magnetized rims around antidots and extended spin-wave modes in antidot lattices. Preliminary tests indicate that specific antidot geometries—especially those with broken symmetry—might stabilise Néel-type skyrmions whose dynamics can couple strongly with propagating spin waves. This could provide a pathway toward hybrid devices that combine reconfigurable magnetic textures with directional control of signal transmission.

Furthermore, the numerical tools developed during this thesis—particularly the pyzfn post-processing package—will be extended to allow for automated detection of mode symmetry, group velocity, and topological character. These capabilities could support broader studies of complex geometries and multilayered structures, with potential applications in nanoscale signal processing or neuromorphic computing.

Altogether, this thesis lays the groundwork for a deeper understanding of how magnetisation textures and geometric confinement jointly influence spin-wave dynamics. With continued collaboration, both theoretical and experimental, these insights may pave the way for practical magnonic devices that exploit hybridised, tunable, and topological spin-wave excitations.

4.7 Other research

In addition to the works presented in this Thesis, I have contributed to several projects that broaden my research beyond its main narrative. In **Spin dynamics in patterned magnetic multilayers with perpendicular magnetic anisotropy**, I co-authored a chapter surveying the state of the art in spin dynamics of patterned multilayers with PMA.

Building on this materials–design viewpoint, in **Enhancement of dynamical coupling in artificial spin-ice systems by incorporating a perpendicularly magnetized ferromagnetic matrix** I developed and validated the micromagnetic workflow used to visualise the spin-wave modes in square-lattice artificial spin ice coupled to a PMA film. I also calculated the spin-wave spectra and contributed to the manuscript review. The results show that in-plane-magnetized nanoelements magnetostatically coupled to a PMA matrix exhibit enhanced dynamical interactions, promising for magnonic circuitry.

In **Angle-dependent resonant dynamics of stripes and skyrmions in Re/Co/Pt multilayers**, I created algorithms to detect and count skyrmions from magnetization data, enabling a one-to-one match between experiment and micromagnetic simulation and thereby allowing us to extract the experimental material parameters. The paper shows that, in thin multilayers with Dzyaloshinskii–Moriya interaction (DMI), labyrinth domains transform into skyrmion bubbles and can be stabilized at remanence at specific oblique field angles that increase with Co thickness; broadband FMR resolves four resonant modes with low- (2–18 GHz) and high-frequency (20–35 GHz) branches whose bandwidth narrows as effective anisotropy and interfacial DMI (iDMI) decrease, while the effective Gilbert damping also drops with increasing Co thickness—linking material parameters to tunable stripe/skyrmion dynamics.

In **Stabilization and racetrack application of asymmetric Néel skyrmions in hybrid nanostructures**, I performed relaxation simulations of a nanodot–stripe system separated by a spacer and studied how the skyrmion shape in the dot depends on DMI. The paper shows that magnetostatic coupling between a nanodot-hosted Néel skyrmion and an adjacent in-plane-magnetized stripe deforms the skyrmion into a stable, size-tunable asymmetric ("egg-shaped") state, opens a low-DMI bistability window, and enables straight racetrack transport without the skyrmion Hall effect—establishing a hybrid route to controllable skyrmion devices.

In **Control of vortex chirality in a symmetric ferromagnetic ring using a ferromagnetic nanoelement**, I assisted with post-processing, data interpretation, and manuscript review. The study demonstrates that inserting an asymmetrically placed, single-domain nanoelement inside an otherwise symmetric nanoring biases domain-wall motion during the onion-to-vortex transition, enabling near-deterministic selection of clockwise vs. counterclockwise chirality (>98% control by setting the nanoelement magnetization parallel/antiparallel to the field) that remains robust to grain disorder and variations in the nanoelement's magnetization and position.

In **Unidirectional spin-wave emission by a traveling pair of magnetic-field profiles**, I contributed simulations, post-processing, data interpretation, and wrote the Methods section. The work shows that a pair of parallel, co-moving magnetic-field profiles acts as a compact, switchable unidirectional spin-wave emitter via a Cherenkov-type mechanism: constructive/destructive interference set by the profiles' velocity and spacing selects the emission direction, tunes the frequency, and can confine waves between the profiles.

In **Scattering of spin waves in a multimode waveguide under the influence of a confined magnetic skyrmion**, I analysed the dispersion relations of propagating modes in a Permalloy waveguide, and computed the resonance spectrum of the coupled nanodot–waveguide system with intensities collected from both constituents. In a geometry where a Néel skyrmion in a Co nanodot is positioned 2 nm above a multimode waveguide, we identified three transport regimes—≤6 GHz: reflection without

mode conversion; 6–8 GHz: selective mode mixing; ≥8 GHz: strong, parity-preserving multimode scattering—with transmission overtaking reflection at higher frequencies, enabling skyrmion-mediated control of multimode magnon transport.

Finally, in **Controlling spin textures of magnetic nanodots using an antidot matrix**, I assisted with micromagnetic simulations and manuscript review. The study shows that vertically positioning a soft circular nanodot within or near a perpendicularly magnetized antidot matrix tailors the radial stray field and thus the remanent state, enabling transitions between single-domain, curled-vortex, and radial-vortex textures; optimal placement a few nanometres above/below the matrix maximizes this field and stabilizes vortex ground states for substantially smaller dots (down to 60 nm diameter at 1 nm thickness), and a practical soft/insulator/hard trilayer is proposed to realize this geometry.

Beyond these publications, I contributed to the MANNGA project, where I developed numerical methods to simulate and optimize reservoir computers based on spin-dynamical systems. This included extending the micromagnetic package MuMax3 with efficient routines to reproduce experimental feedback loops and creating custom spatial masks to emulate coplanar-waveguide antennas.

I also lead a PRELUDIUM project on topological magnonics aimed at designing experimentally feasible 2D topological magnonic crystals and demonstrating topologically protected spin-wave transport. The work proceeds in four stages: (i) establishing the computational toolkit (band structures, Berry curvature/Chern-number extraction); (ii) geometry-driven optimization in gallium-doped YIG; (iii) materials-driven tuning—e.g., high-magnetization Co/Pd multilayers that stabilize complex textures affecting topology; and (iv) proof-of-principle demonstrations of robustness to defects with designs tailored for experimental verification. Our primary methodology is finite-difference micromagnetic simulation of Landau–Lifshitz dynamics, complemented by semi-analytical models and collaborations with experimental groups to validate the predicted topological transport.

Chapter 5

About the author

5.1 Conferences

5.1.1 Oral Presentations

- **Intermag 2022** 13 January 2022, New Orleans, USA
  Magnetic coupling between a ferromagnetic stripe and a nanodot
  Mathieu Moalic, Mateusz Zelent, Maciej Krawczyk
- **SolSkyMag 2022** 27 June – 3 July 2022, San Sebastian, Spain
  Dynamic interactions between edge and bulk modes in an antidot lattice with perpendicular magnetic anisotropy
  Mathieu Moalic, Mateusz Zelent, Maciej Krawczyk
- **JEMS 2022** 24 – 29 July 2022, Warsaw, Poland
  Dynamic interactions between edge and bulk modes in an antidot lattice with perpendicular magnetic anisotropy
  Mathieu Moalic, Mateusz Zelent, Maciej Krawczyk
- **SolSkyMag 2023** 18 – 23 June 2023, San Sebastian, Spain
  Antidot lattice with perpendicular magnetic anisotropy: dynamics between edge and bulk modes
  Mathieu Moalic, Mateusz Zelent, Maciej Krawczyk
- **MagiC 2023** 24 – 28 July 2023, Będlewo, Poland
  Antidot lattice with perpendicular magnetic anisotropy: dynamics between edge modes and bulk modes
  Mathieu Moalic, Mateusz Zelent, Maciej Krawczyk

5.1.2 Poster Presentations

- **MagIC+ 2021** Online
  Magnetostatic coupling between a ferromagnetic stripe and a skyrmion inscribed in a nanodot
  Mathieu Moalic
- **Physics of Magnetism 2021** Online
  Mutual magnetostatic coupling between the saturated ferromagnetic stripe and a nanodot
  Mathieu Moalic
- **INTERMAG 2021** Online
  Excitation of short wavelength spin waves in a ferromagnetic conduit with a microwave pumped perpendicularly magnetised nanodot
  Mathieu Moalic
- **736. WE-Heraeus-Seminar 2021** Online
  Excitation of short wavelength spin waves in a ferromagnetic conduit with a microwave pumped perpendicularly magnetised nanodot
  Mathieu Moalic
- **Physics of Magnetism 2023** 26 – 30 June 2023, Poznań, Poland
  Antidot lattice with perpendicular magnetic anisotropy: dynamics between edge modes and bulk modes
  Mathieu Moalic, Mateusz Zelent, Maciej Krawczyk

- **Trends in Magnetism 2023** 2 – 9 September 2023, Rome, Italy
  Antidot lattice with perpendicular magnetic anisotropy: dynamics between edge modes and bulk modes
  Mathieu Moalic, Mateusz Zelent, Maciej Krawczyk
- **JEMS 2023** 27 August – 1 September 2023, Madrid, Spain
  Spin-wave hybridization in a magnonic crystal formed by antidot lattice with perpendicular magnetic anisotropy
  Mathieu Moalic, Mateusz Zelent, Maciej Krawczyk
- **ISIK Symposium 2023** 11 – 13 January 2023, Będlewo, Poland
  Antidot lattice with perpendicular magnetic anisotropy: dynamics between edge modes and bulk modes
  Mathieu Moalic, Mateusz Zelent, Krzysztof Szulc, Maciej Krawczyk
- **Intermag 2024** 5 – 10 May 2024, Rio de Janeiro, Brazil
  Antidot lattice with perpendicular magnetic anisotropy: dynamics between edge modes and bulk modes
  Mathieu Moalic, Mateusz Zelent, Krzysztof Szulc, Maciej Krawczyk
- **International Conference on Magnetism 2024** 30 June – 5 July 2024, Bologna, Italy
  Magnon Interactions in Antidot Lattices with Perpendicular Magnetic Anisotropy
  Mathieu Moalic, Mateusz Zelent, Krzysztof Szulc, Maciej Krawczyk
- **1st Transnational Round Table 2024** 3 June – 5 July 2024, Exeter, UK
  Efficient generation of the second-harmonic propagating spin waves in a thin out-of-plane magnetized ferromagnetic film.
  Mathieu Moalic, Mateusz Zelent, Maciej Krawczyk
- **JEMS 2025** 24 – 29 August 2025, Frankfurt, Germany
  Efficient Second-Harmonic Propagation of Spin Waves in Thin Ferromagnetic Films with Out-of-Plane Magnetization
  Mathieu Moalic, Mateusz Zelent, Maciej Krawczyk
- **Swiss Nanomagnetism Summit 2025** 8 – 9 September 2025, Zurich, Switzerland
  Higher Harmonic Spin Wave Generation Using Out-of-Plane Magnetized Films with Localized In-Plane Magnetization
  Mathieu Moalic, Mateusz Zelent, Maciej Krawczyk

5.1.3 Organization

I helped with the organization of the following conferences, symposia and workshops.

- First Institute of Spintronics and Quantum Information Symposium, Poznań, 2021
- Second Institute of Spintronics and Quantum Information Symposium, Poznań, 2022
- Third Institute of Spintronics and Quantum Information Symposium, Poznań, 2024
- Physics of Magnetism, Poznań, 2023
- MagIC+, Będlewo, 2023

5.2 Awards, grants and scholarships

1. **National Science Center, Poland grant PRELUDIUM 22, Grant No. UMO-2020/37/B/ST3/03936** *Designing an experimentally feasible two-dimensional magnonic crystal for the demonstration of topologically protected spin waves*
2. **Inicjatywa Doskonałości – Uczelnia Badawcza** Recipient of nine internal grants supporting conference travel, research internships, and publication fees
3. **Intermag Sensor Challenge** 1st place (2022), 2nd place (2024)
4. **European Defence Tech Hub Hackathon 2025 in Warsaw** 3rd place

5. **Adam Mickiewicz University Foundation Scholarship** Awarded in 2024

5.3 Research Projects

I have taken part in these following projects during my thesis:

- NCN SHENG, "Spin Waves in Magnetic Skyrmion Crystals", Grant No. UMO-2018/30/Q/ST3/00416.
- NCN OPUS, "New Platform for Study Wave Phenomenon – Reconfigurable Topological Properties and Frustrated Ground States in Magnonics", Grant No. UMO-2020/37/B/ST3/03936
- NCN PRELUDIUM, "Designing an experimentally feasible two-dimensional magnonic crystal for the demonstration of topologically protected spin waves", Grant No. 2023/49/N/ST3/03538
- Horizon Europe, MANNGA, "Magnonic Artificial Neural Networks and Gate Arrays", Grant No. 101070347
- Computational simulations performed at the Poznań Supercomputing and Networking Center (Grant No. pl0095-01).

5.4 Scientific visits

1. **University of Vienna, Austria** 22.01–04.02.2023, group of Dr. Andrii Chumak
2. **University of Porto, Portugal** 01-13.04.2024, group of Dr. Gleb Kakazei

5.5 Student co-supervision

1. **Uladzislau Makartsou**, 2021
2. **Gauthier Philippe**, 2023
3. **Mufti Avicena**, 2023
4. **Joana Hernandez**, 2023
5. **Youenn Patat**, 2024

Bibliography

1. Shalf J. The future of computing beyond Moore's Law. *Philosophical Transactions of the Royal Society A.* 2020;378(2166):20190061.
2. Borkar S, Chien AA. The future of microprocessors. *Communications of the ACM.* 2011;54(5):67-77.
3. Hennessy JL, Patterson DA. A new golden age for computer architecture. *Communications of the ACM.* 2019;62(2):48-60.
4. IEEE International Roadmap for Devices and Systems (IRDS). International Roadmap for Devices and Systems (IRDS): 2023 Update. Published online 2023.
5. Nikonov DE, Young IA. Overview of beyond-CMOS devices and a uniform methodology for their benchmarking. *Proceedings of the IEEE.* 2013;101(12):2498-2533.
6. Chumak AV, Vasyuchka VI, Serga AA, Hillebrands B. Magnon spintronics. *Nature Physics.* 2015;11(6):453-461.
7. Kruglyak V, Demokritov S, Grundler D. Magnonics. *Journal of Physics D Applied Physics.* 2010;43(26):260301.
8. Barman A, Gubbiotti G, Ladak S, et al. The 2021 magnonics roadmap. *Journal of Physics: Condensed Matter.* 2021;33(41):413001.
9. Rana B, Otani Y. Towards magnonic devices based on voltage-controlled magnetic anisotropy. *Communications Physics.* 2019;2(1):90.
10. Csaba G, Papp Á, Porod W. Perspectives of using spin waves for computing and signal processing. *Physics Letters A.* 2017;381(17):1471-1476.
11. Mahmoud A, Ciubotaru F, Vanderveken F, et al. Introduction to spin wave computing. *Journal of Applied Physics.* 2020;128(16):161101.
12. Lachance-Quirion D, Tabuchi Y, Gloppe A, Usami K, Nakamura Y. Hybrid quantum systems based on magnonics. *Applied Physics Express.* 2019;12(7):70101.
13. Jiles D. *Introduction to Magnetism and Magnetic Materials.* 3rd ed. CRC Press; 2016.
14. Needham J, Gwei-Djen L. *Science and Civilisation in China: Volume 4, Physics and Physical Technology, Part 3, Civil Engineering and Nautics.* Cambridge University Press; 1971.
15. Schmidl PS. Two early arabic sources on the magnetic compass. *Journal of Arabic and Islamic Studies.* 1996;1:81-132.
16. Thompson SP, others. *Epistle of Peter Peregrinus of Maricourt to Sygerus of Foncaucourt, Soldier, Concerning the Magnet.* Chiswick Press; 1902.
17. Gilbert W. *On the Loadstone and Magnetic Bodies, And on the Great Magnet the Earth: A New Physiology, Demonstrated with Many Arguments and Experiments.* Wiley; 1893.
18. Ørsted HC. Experiments on the effect of a current of electricity on the magnetic needle. *Annals of Philosophy.* 1820;16:273-277.
19. Faraday M. Experimental researches in electricity. *Philosophical Transactions of the Royal Society.* 1832;122:125-162.
20. Maxwell JC. *A Treatise on Electricity and Magnetism.* Clarendon Press; 1873.

21. Einstein A. Zur elektrodynamik bewegter körper. *Annalen der Physik.* 1905;322(10):891-921.

22. Feynman RP. Space-time approach to quantum electrodynamics. *Physical Review.* 1949;76(6):769-789.

23. Blundell S. *Magnetism in Condensed Matter.* Oxford University Press; 2001.

24. Hund F. Zur deutung der molekelspektren. iii. *Zeitschrift für Physik.* 1925;36:657-674.

25. Pauli W. Über den zusammenhang des abschlusses der elektronengruppen im atom mit der komplexstruktur der spektren. *Zeitschrift für Physik.* 1925;31:765-783.

26. Kittel C. *Introduction to Solid State Physics.* 8th ed. Wiley; 2005.

27. Tinkham M. *Introduction to Superconductivity.* Courier Corporation; 2004.

28. Šmejkal L, Gonzalez-Hernandez R, Turek I, Jungwirth T. Emerging field of altermagnetism. *Physical Review X.* 2022;12(3):31042.

29. Johnson MT, Bloemen PJH, Broeder FJA den, Vries JJ de. Magnetism of permalloy. *Reports on Progress in Physics.* 1996;59(11):1409-1458.

30. Bozorth RM. Ferromagnetism of fe-co alloys. *Physical Review.* 1951;83(5):757-765.

31. Graf T, Felser C, Parkin SSP. Simple rules for the understanding of heusler compounds. *Progress in Solid State Chemistry.* 2011;39(1):1-50.

32. Croat JJ, Herbst JF, Lee RW, Pinkerton FE. Pr-Fe and Nd-Fe-based materials: A new class of high-performance permanent magnets. *Journal of Applied Physics.* 1984;55(6):2078-2082.

33. Strnat K, Hoffer G, Olson J, Ostertag W, Becker J. A family of new cobalt-base permanent magnet materials. *Journal of Applied Physics.* 1967;38(3):1001-1002.

34. Coey JM. Permanent magnet applications. *Journal of Magnetism and Magnetic Materials.* 2002;248(3):441-456.

35. Cherepanov V, Kolokolov I, L'vov V. The exchange stiffness constant of yttrium iron garnet. *Physics Reports.* 1993;229(3):81-144.

36. Hubert A, Schäfer R. *Magnetic Domains: The Analysis of Magnetic Microstructures.* Springer Science & Business Media; 1998.

37. Aharoni A. *Introduction to the Theory of Ferromagnetism.* Vol 109. Clarendon Press; 2000.

38. Cullity BD, Graham CD. *Introduction to Magnetic Materials.* John Wiley & Sons; 2011.

39. Stoner EC, Wohlfarth EP. A mechanism of magnetic hysteresis in heterogeneous alloys. *Philosophical Transactions of the Royal Society of London Series A, Mathematical and Physical Sciences.* 1948;240(826):599-642.

40. Cowburn RP, Koltsov D, Adeyeye A, Welland M, Tricker D. Single-domain circular nanomagnets. *Physical Review Letters.* 1999;83(5):1042.

41. Morrish AH. *The Physical Principles of Magnetism.* IEEE/Oxford University Press; 2001.

42. Chikazumi S, Graham CD. *Physics of Ferromagnetism.* Oxford University Press; 1997.

43. Dzyaloshinsky I. A thermodynamic theory of "weak" ferromagnetism of antiferromagnetics. *Journal of Physics and Chemistry of Solids.* 1958;4(4):241-255.

44. Moriya T. Anisotropic superexchange interaction and weak ferromagnetism. *Physical Review.* 1960;120(1):91.

45. Ruderman MA, Kittel C. Indirect exchange coupling of nuclear magnetic moments by conduction electrons. *Physical Review.* 1954;96(1):99.

46. Kasuya T. A theory of metallic ferro-and antiferromagnetism on Zener's model. *Progress of theoretical physics.* 1956;16(1):45-57.

47. Yosida K. Magnetic properties of Cu-Mn alloys. *Physical Review.* 1957;106(5):893.

48. Slonczewski JC. Current-driven excitation of magnetic multilayers. *Journal of Magnetism and Magnetic Materials.* 1996;159(1–2):L1-L7.

49. Berger L. Emission of spin waves by a magnetic multilayer traversed by a current. *Physical Review B.* 1996;54(13):9353.

50. Brown WF. Thermal fluctuations of a single-domain particle. *Physical Review.* 1963;130(5):1677-1686.

51. Garc\ia-Palacios JL, Lázaro FJ. Langevin-dynamics study of the dynamical properties of small magnetic particles. *Physical Review B.* 1998;58(22):14937.

52. Heisenberg W. Zur theorie des ferromagnetismus. *Zeitschrift für Physik.* 1928;49(9):619-636.

53. Stoner EC. Collective electron ferromagnetism. *Proceedings of the Royal Society of London Series A Mathematical and Physical Sciences.* 1938;165(922):372-414.

54. Hubbard J. Electron correlations in narrow energy bands. *Proceedings of the Royal Society of London Series A Mathematical and Physical Sciences.* 1963;276(1365):238-257.

55. Stancil DD, Prabhakar A. *Spin Waves.* Vol 5. Springer; 2009.

56. Jackson JD. *Classical Electrodynamics.* John Wiley & Sons; 2021.

57. Kittel C. Theory of the structure of ferromagnetic domains in films and small particles. *Physical Review.* 1946;70(11–12):965.

58. Kooy C. Experimental and theoretical study of the domain configuration in thin layers of BaFe. *Philips Res Repts.* 1960;15(7).

59. Kaplan B, Gehring G. The domain structure in ultrathin magnetic films. *Journal of Magnetism and Magnetic Materials.* 1993;128(1–2):111-116.

60. Bogdanov A, Hubert A. Thermodynamically stable magnetic vortex states in magnetic crystals. *Journal of Magnetism and Magnetic Materials.* 1994;138(3):255-269.

61. Muhlbauer S, Binz B, Jonietz F, et al. Skyrmion lattice in a chiral magnet. *Science.* 2009;323(5916):915-919.

62. Nagaosa N, Tokura Y. Topological properties and dynamics of magnetic skyrmions. *Nature Nanotechnology.* 2013;8(12):899-911.

63. Newell AJ, Williams W, Dunlop DJ. A generalization of the demagnetising tensor for nonuniform magnetisation. *Journal of Geophysical Research: Solid Earth.* 1993;98(B6):9551-9555.

64. Fidler J, Schrefl T. Micromagnetic modelling-the current state of the art. *Journal of Physics D: Applied Physics.* 2000;33(15):R135.

65. Donahue M, Porter D. OOMMF User's Guide. *For more information, see website at http://math nist gov/oommf.*

66. Vansteenkiste A, Leliaert J, Dvornik M, Helsen M, Garcia-Sanchez F, Waeyenberge BV. The design and verification of MuMax3. *AIP Advances.* 2014;4(10):107133.

67. Bruno P. Tight-binding approach to the orbital magnetic moment and magnetocrystalline anisotropy of transition-metal monolayers. *Physical Review B.* 1989;39(1):865.

68. Daalderop G, Kelly P, Schuurmans M. First-principles calculation of the magnetocrystalline anisotropy energy of iron, cobalt, and nickel. *Physical Review B.* 1990;41(17):11919.

69. Daalderop G, Kelly P, Schuurmans M. First-principles calculation of the magnetocrystalline anisotropy energy of iron, cobalt, and nickel. *Physical Review B.* 1990;41(17):11919.

70. Osborn JA. Demagnetising factors of the general ellipsoid. *Physical Review.* 1945;67(11–12):351.

71. Aharoni A. Demagnetising factors for rectangular ferromagnetic prisms. *Journal of Applied Physics.* 1998;83(6):3432-3434.

72. Néel L. Anisotropie magnétique superficielle et surstructures d'orientation. *Journal de Physique et le Radium.* 1954;15(4):225-239.

73. Ikeda S, Miura K, Yamamoto H, et al. A perpendicular-anisotropy CoFeB–MgO magnetic tunnel junction. *Nature materials.* 2010;9(9):721-724.

74. Callen E, Callen HB. Magnetostriction, forced magnetostriction, and anomalous thermal expansion in ferromagnets. *Physical Review.* 1965;139(2A):A455.

75. Callen ER, Callen HB. Static magnetoelastic coupling in cubic crystals. *Physical Review.* 1963;129(2):578.

76. Sander D. The correlation between mechanical stress and magnetic anisotropy in ultrathin films. *Reports on Progress in Physics.* 1999;62(5):809.

77. Landau L, Lifshitz E, others. On the theory of the dispersion of magnetic permeability in ferromagnetic bodies. *Phys Z Sowjetunion.* 1935;8(153):101-114.

78. Gilbert TL. A phenomenological theory of damping in ferromagnetic materials. *IEEE Transactions on Magnetics.* 2004;40(6):3443-3449.

79. Lakshmanan M. The fascinating world of the Landau–Lifshitz–Gilbert equation: an overview. *Philosophical Transactions of the Royal Society A: Mathematical, Physical and Engineering Sciences.* 2011;369(1939):1280-1300.

80. Kittel C. On the gyromagnetic ratio and spectroscopic splitting factor of ferromagnetic substances. *Physical Review.* 1949;76(6):743.

81. Sparks M, Loudon R, Kittel C. Ferromagnetic relaxation. I. Theory of the relaxation of the uniform precession and the degenerate spectrum in insulators at low temperatures. *Physical Review.* 1961;122(3):791.

82. Landau L, Lifshitz E. On the theory of the dispersion of magnetic permeability in ferromagnetic bodies. *Physikalische Zeitschrift der Sowjetunion.* 1935;8:153-169.

83. Li Z, Zhang S. Thermally assisted magnetization reversal in the presence of a spin-transfer torque. *Physical Review B.* 2004;69(13):134416.

84. Aharoni A. *Introduction to the Theory of Ferromagnetism.* Clarendon Press; 2000.

85. Cullity BD, Graham CD. *Introduction to Magnetic Materials.* John Wiley & Sons; 2011.

86. Hubert A, Schäfer R. *Magnetic Domains: The Analysis of Magnetic Microstructures.* Springer Science & Business Media; 1998.

87. Kittel C. Physical theory of ferromagnetic domains. *Reviews of Modern Physics.* 1949;21(4):541.

88. Krawczyk M, Grundler D. Review and prospects of magnonic crystals and devices with reprogrammable band structure. *Journal of Physics: Condensed matter.* 2014;26(12):123202.

89. Stancil DD, Prabhakar A. *Spin Waves.* Vol 5. Springer; 2009.

90. Malozemoff AP, Slonczewski JC. *Magnetic Domain Walls in Bubble Materials: Advances in Materials and Device Research.* Vol 1. Academic press; 2013.

91. Bertotti G. *Hysteresis in Magnetism: For Physicists, Materials Scientists, And Engineers.* Academic press; 1998.

92. Bloch F. Zur theorie des austauschproblems und der remanenzerscheinung der ferromagnetika. *Zeitschrift für Physik.* 1932;74(5):295-335.

93. Néel L. Magnetism and local molecular field. *Journal de Physique et le Radium.* 1955;16:265-293.

94. Kittel C, Galt J. Ferromagnetic domain theory. *Solid State Physics.* 1956;3:437-564.

95. Malozemoff AP, Slonczewski JC. *Magnetic Domain Walls in Bubble Materials.* Academic Press; 1979.

96. Shinjo T, Okuno T, Hassdorf R, Shigeto K, Ono T. Magnetic vortex core observation in circular dots of permalloy. *Science.* 2000;289(5481):930-932.

97. Guslienko KY, Ivanov B, Novosad V, Otani Y, Shima H, Fukamichi K. Eigenfrequencies of vortex state excitations in magnetic submicron-size disks. *Journal of Applied Physics.* 2002;91(10):8037-8039.

98. Usov N. Magnetisation curling in soft type ferromagnetic particles with large aspect ratios. *Journal of Magnetism and Magnetic Materials.* 1999;203(1–3):277-279.

99. Thiele A. Steady-state motion of magnetic domains. *Physical Review Letters.* 1973;30(6):230.

100. Pribiag V, Krivorotov I, Fuchs G, et al. Magnetic vortex oscillator driven by dc spin-polarized current. *Nature Physics.* 2007;3(7):498-503.

101. Curcic M, Stoll H, Weigand M, et al. Magnetic vortex core reversal by rotating magnetic fields generated on micrometer length scales. *physica status solidi (b).* 2011;248(10):2317-2322.

102. Yamada K, Kasai S, Nakatani Y, et al. Electrical switching of the vortex core in a magnetic disk. *Nature materials.* 2007;6(4):270-273.

103. Farle M. Ferromagnetic resonance of ultrathin metallic layers. *Reports on Progress in Physics.* 1998;61(7):755.

104. Heinrich B, Cochran J. Ultrathin metallic magnetic films: magnetic anisotropies and exchange interactions. *Advances in Physics.* 1993;42(5):523-639.

105. Bickford Jr L. Ferromagnetic resonance absorption in magnetite single crystals. *Physical Review.* 1950;78(4):449.

106. Harder M, Gui Y, Hu CM. Electrical detection of magnetisation dynamics via spin rectification effects. *Physics Reports.* 2016;661:1-59.

107. Lax B, Button KJ, Hagger H. Microwave ferrites and ferrimagnetics. Published online 1963.

108. Pozar DM. *Microwave Engineering: Theory and Techniques.* John Wiley & Sons; 2021.

109. Schloemann E. Advances in ferrite microwave materials and devices. *Journal of Magnetism and Magnetic Materials.* 2000;209(1–3):15-20.

110. Kittel C. On the theory of ferromagnetic resonance absorption. *Physical Review.* 1948;73(2):155-161.

111. Joseph R, Schlömann E. Demagnetizing field in nonellipsoidal bodies. *Journal of Applied Physics.* 1965;36(5):1579-1593.

112. Kalinikos BA, Slavin AN. Theory of dipole-exchange spin wave spectrum for ferromagnetic films with mixed exchange boundary conditions. *Journal of Physics C: Solid State Physics.* 1986;19(35):7013.

113. Damon RW, Eshbach J. Magnetostatic modes of a ferromagnet slab. *Journal of Physics and Chemistry of Solids.* 1961;19(3–4):308-320.

114. Krawczyk M, Grundler D. Review and prospects of magnonic crystals and devices with reprogrammable band structure. *Journal of Physics: Condensed matter.* 2014;26(12):123202.

115. Nikitov S, Tailhades P, Tsai C. Spin waves in periodic magnetic structures—magnonic crystals. *Journal of Magnetism and Magnetic Materials.* 2001;236(3):320-330.

116. Lee KS, Han DS, Kim SK. Physical origin and generic control of magnonic band gaps of dipole-exchange spin waves in width-modulated nanostrip waveguides. *Physical Review Letters.* 2009;102(12):127202.

117. Kim SK, Lee KS, Han DS. A gigahertz-range spin-wave filter composed of width-modulated nanostrip magnonic-crystal waveguides. *Applied Physics Letters.* 2009;95(8):82507.

118. Tacchi S, Gruszecki P, Madami M, et al. Universal dependence of the spin wave band structure on the geometrical characteristics of two-dimensional magnonic crystals. *Scientific Reports.* 2015;5(1):10367.

119. Gubbiotti G, Montoncello F, Tacchi S, et al. Angle-resolved spin wave band diagrams of square antidot lattices studied by Brillouin light scattering. *Applied Physics Letters.* 2015;106(26):262406.

120. Langer M, Gallardo RA, Schneider T, et al. Spin-wave modes in transition from a thin film to a full magnonic crystal. *Physical Review B.* 2019;99(2):24426.

121. Gallardo R, Schneider T, Roldán-Molina A, et al. Dipolar interaction induced band gaps and flat modes in surface-modulated magnonic crystals. *Physical Review B.* 2018;97(14):144405.

122. Tacchi S, Duerr G, Klos J, et al. Forbidden band gaps in the spin-wave spectrum of a two-dimensional bicomponent magnonic crystal. *Physical Review Letters.* 2012;109(13):137202.

123. Gubbiotti G, Tacchi S, Madami M, et al. Collective spin excitations in bicomponent magnonic crystals consisting of bilayer permalloy/Fe nanowires. *Physical Review B.* 2016;93(18):184411.

124. Fassbender J, Ravelosona D, Samson Y. Tailoring magnetism by light-ion irradiation. *Journal of Physics D: Applied Physics.* 2004;37(16):R179.

125. Fassbender J, McCord J. Magnetic patterning by means of ion irradiation and implantation. *Journal of Magnetism and Magnetic Materials.* 2008;320(3–4):579-596.

126. Obry B, Meyer T, Pirro P, et al. Microscopic magnetic structuring of a spin-wave waveguide by ion implantation in a Ni81Fe19 layer. *Applied Physics Letters.* 2013;102(2):22409.

127. Chumak AV, Pirro P, Serga AA, et al. Spin-wave propagation in a microstructured magnonic crystal. *Applied Physics Letters.* 2009;95(26):262508.

128. Vaz CA. Electric field control of magnetism in multiferroic heterostructures. *Journal of Physics: Condensed Matter.* 2012;24(33):333201.

129. Qin H, Dreyer R, Woltersdorf G, Taniyama T, Dijken S van. Electric-field control of propagating spin waves by ferroelectric domain-wall motion in a multiferroic heterostructure. *Advanced Materials.* 2021;33(27):2100646.

130. Chumak A, Neumann T, Serga A, Hillebrands B, Kostylev M. A current-controlled, dynamic magnonic crystal. *Journal of Physics D: Applied Physics.* 2009;42(20):205005.

131. Serga A, Chumak A, Hillebrands B. YIG magnonics. *Journal of Physics D: Applied Physics.* 2010;43(26):264002.

132. Nikitin AA, Ustinov AB, Semenov AA, et al. A spin-wave logic gate based on a width-modulated dynamic magnonic crystal. *Applied Physics Letters.* 2015;106(10):102405.

133. Dreyer R, Liebing N, Edwards E, Müller A, Woltersdorf G. Spin-wave localization and guiding by magnon band structure engineering in yttrium iron garnet. *Physical Review Materials.* 2021;5:64411.

134. Sud A, Zollitsch C, Kamimaki A, et al. Tunable magnon–magnon coupling in synthetic antiferromagnets. *Physical Review B.* 2020;102(10):100403.

135. Moalic M, Zelent M, Szulc K, Krawczyk M. The role of non-uniform magnetisation texture for magnon–magnon coupling in an antidot lattice. *Scientific Reports.* 2024;14:11501.

136. Dion T, Stenning K, Vanstone A, et al. Ultrastrong magnon–magnon coupling and chiral spin-texture control in a dipolar 3D multilayered artificial spin-vortex ice. *Nature Communications.* 2024;15:4077.

137. Freeman CWF, Youel H, Budniak AK, et al. Tunable ultrastrong magnon–magnon coupling approaching the deep-strong regime in a van der Waals antiferromagnet. *ACS Nano.* 2025;19(16):16024-16031.

138. Sklenar J, Zhang W. Self-hybridization and tunable magnon–magnon coupling in van der Waals synthetic magnets. *Physical Review Applied.* 2021;15:44008.

139. Chumak AV, Vasyuchka VI, Serga AA, Hillebrands B. Magnon spintronics. *Nature Physics.* 2015;11(6):453-461.

140. Shiota Y, Taniguchi T, Ishibashi M, Moriyama T, Ono T. Tunable magnon-magnon coupling mediated by dynamic dipolar interaction in synthetic antiferromagnets. *Physical Review Letters.* 2020;125(1):17203.

141. Liu H, Sun D, Zhang C, Groesbeck M, Mclaughlin R, Vardeny ZV. Observation of exceptional points in magnonic parity-time symmetry devices. *Science Advances.* 2019;5(11):eaax9144.

142. Yu T, Zou J, Zeng B, Rao J, Xia K. Non-Hermitian topological magnonics. *Physics Reports.* 2024;1062:1-86.

143. Wiersig J. Review of exceptional point-based sensors. *Photonics Research.* 2020;8(9):1457-1467.

144. Chumak AV, Kabos P, Wu M, et al. Advances in magnetics roadmap on spin-wave computing. *IEEE Transactions on Magnetics.* 2022;58(6):1-72.

145. Ziegler JF, Ziegler MD, Biersack JP. SRIM—The stopping and range of ions in matter (2010). *Nuclear Instruments and Methods in Physics Research B.* 2010;268(11–12):1818-1823.

146. Sud A, Tacchi S, Sagkovits D, et al. Tailoring interfacial effect in multilayers with Dzyaloshinskii–Moriya interaction by helium ion irradiation. *Scientific Reports.* 2021;11:23626.

147. Beaujour JML, Kent AD, Ravelosona D, Tudosa I, Fullerton EE. Ferromagnetic resonance study of Co/Pd/Co/Ni multilayers with perpendicular anisotropy irradiated with helium ions. *Journal of Applied Physics.* 2011;109(3):33917.

148. Das S, Mansell R, Flajšman L, et al. Tuning of perpendicular magnetic anisotropy in Bi-substituted yttrium iron garnet films by He+ ion irradiation. *Physical Review Materials.* 2024;8:114419.

149. Kiechle M, Papp A, Mendisch S, et al. Spin-wave optics in YIG realized by ion-beam irradiation. *Small.* 2023;19(21):2207293.

150. Kern LM, Pfau B, Deinhart V, et al. Deterministic generation and guided motion of magnetic skyrmions by focused he+ ion irradiation. *arXiv.* Published online 2022.

151. Juge R, Bairagi K, Rana KG, et al. Helium ions put magnetic Skyrmions on the track. *Nano Letters.* 2021;21(7):2989-2996.

152. Moalic M, Zelent M. MathieuMoalic/amumax. Published online October 2023.

153. Vansteenkiste A, Leliaert J, Dvornik M, Helsen M, Garcia-Sanchez F, Van Waeyenberge B. The design and verification of MuMax3. *AIP Adv.* 2014;4(10):107133.

154. Leliaert J, Dvornik M, Mulkers J, De Clercq J, Milošević MV, Van Waeyenberge B. Fast micromagnetic simulations on GPU - Recent advances made with mumax3. *J Phys D: Appl Phys.* 2018;51(12):123002. http://stacks.iop.org/0022-3727/51/i=12/a=123002?key=crossref.9a43adc77840349dbcf0c1ae9cfc9990

155. Harris CR, Millman KJ, Walt SJ van der, et al. Array programming with NumPy. *Nature.* 2020;585(7825):357-362.

156. Dask. https://dask.org/

157. Xarray. https://xarray.dev/

158. Three.js. https://threejs.org/

159. Chart.js. https://www.chartjs.org/

160. cuFFT. https://docs.nvidia.com/cuda/pdf/CUFFT_Library.pdf

161. Moalic M. MathieuMoalic/pyzfn. Published online October 2023.

162. Shindou R, Matsumoto R, Murakami S, Ohe Ji. Topological chiral magnonic edge mode in a magnonic crystal. *Physical Review B—Condensed Matter and Materials Physics.* 2013;87(17):174427.

163. Wang H, Madami M, Chen J, et al. Observation of spin-wave moiré edge and cavity modes in twisted magnetic lattices. *Physical Review X.* 2023;13(2):21016.

164. Moon JH, Seo SM, Lee KJ, et al. Spin-wave propagation in the presence of interfacial Dzyaloshinskii-Moriya interaction. *Physical Review B—Condensed Matter and Materials Physics.* 2013;88(18):184404.